2007

SYNTHESIS AND REACTIVITY OF MEMBRANE-SUPPORTED BIMETALLIC NANOPARTICLES FOR PCB AND TRICHLOROETHYLENE DECHLORINATION

Jian Xu
University of Kentucky, jxu1@engr.uky.edu

ABSTRACT OF DISSERTATION

Jian Xu

The Graduate School

University of Kentucky

2007

SYNTHESIS AND REACTIVITY OF MEMBRANE-SUPPORTED BIMETALLIC NANOPARTICLES FOR PCB AND TRICHLOROETHYLENE DECHLORINATION

ABSTRACT OF DISSERTATION

A dissertation submitted in partial fulfillment of the
requirements for the degree of Doctor of Philosophy in the
College of Engineering
at the University of Kentucky

By
Jian Xu

Lexington, Kentucky

Director: Dr. Dibakar Bhattacharyya, Alumni Professor of Chemical Engineering

Lexington, Kentucky

2007

ABSTRACT OF DISSERTATION

SYNTHESIS AND REACTIVITY OF MEMBRANE-SUPPORTED BIMETALLIC NANOPARTICLES FOR PCB AND TRICHLOROETHYLENE DECHLORINATION

Nanosized metal particles have become an important class of materials in the field of catalysis, optical, electronic, magnetic and biological devices due to the unique physical and chemical properties. This research deals with the synthesis of structured bimetallic nanoparticles for the dechlorination of toxic organics. Nanoparticle synthesis in aqueous phase for dechlorination studies has been reported. However, in the absence of polymers or surfactants particles can easily aggregate into large particles with wide size distribution. In this study, we report a novel in-situ synthesis method of bimetallic nanoparticles embedded in polyacrylic acid (PAA) functionalized microfiltration membranes by chemical reduction of metal ions bound to the carboxylic acid groups. Membrane-based nanoparticle synthesis offers many advantages: reduction of particle loss, prevention of particle agglomeration, application of convective flow, and recapture of dissolved metal ions.

The objective of this research is to synthesize and characterize nanostructured bimetallic particles in membranes, understand and quantify the catalytic hydrodechlorination mechanism, and develop a membrane reactor model to predict and simulate reactions under various conditions. In this study, the PAA functionalization was achieved by filling the porous PVDF membranes with acrylic acid and subsequent in-situ free radical polymerization. Target metal cations (iron in this case) were then introduced into the membranes by ion exchange process. Subsequent reduction resulted in the formation of metal nanoparticles (around 30 nm). Bimetallic nanoparticles can be formed

by post deposition of secondary appropriate metal such as Pd or Ni. The membranes and bimetallic nanoparticles were characterized by: SEM, TEM, TGA, and FTIR. A specimen-drift-free X-ray energy dispersive spectroscopy (EDS) mapping system was used to determine the two-dimensional element distribution inside the membrane matrix at the nano scale. This high resolution mapping allows for the correlation and understanding the nanoparticle structure, second metal composition in terms of nanoparticle reactivity. Chlorinated aliphatics such as trichloroethylene and conjugated aromatics such as polychlorinated biphenyls (PCBs) were chosen as the model compounds to investigate the catalytic properties of bimetallic nanoparticles and the reaction mechanism and kinetics. Effects of second metal coating, particle size and structure and temperature were studied on the performance of bimetallic system. In order to predict reaction at different conditions, a two-dimensional steady state model was developed to correlate and simulate mass transfer and reaction in the membrane pores under convective flow mode. The 2-D equations were solved by COMSOL (Femlab). The influence of changing parameters such as reactor geometry (i.e. membrane pore size) and Pd coating composition were evaluated by the model and compared well with the experimental data.

KEYWORDS: Bimetallic nanoparticles, dechlorination, membrane reactor, polyacrylic acid, chlorinated organics

Jian Xu

October 10, 2007

SYNTHESIS AND REACTIVITY OF MEMBRANE-SUPPORTED BIMETALLIC NANOPARTICLES FOR PCB AND TRICHLOROETHYLENE DECHLORINATION

By

Jian Xu

Dr. Dibakar Bhattacharyya
Director of Dissertation

Dr. Barbara Knutson
Director of Graduate Studies

October 10, 2007
Date

RULES FOR THE USE OF DISSERTATIONS

Unpublished dissertations submitted for the Doctor's degree and deposited in the University of Kentucky Library are as a rule open for inspection, but are to be used only with due regard to the rights of the authors. Bibliographical references may be noted, but quotations or summaries of parts may be published only with the permission of the author, and with the usual scholarly acknowledgements.

Extensive copying or publication of the dissertation in whole or in part also requires the consent of the Dean of the Graduate School of the University of Kentucky.

A library that borrows this dissertation for use by its patrons is expected to secure the signature of each user.

Name	Date

DISSERTATION

Jian Xu

The Graduate School

University of Kentucky

2007

SYNTHESIS AND REACTIVITY OF MEMBRANE-SUPPORTED BIMETALLIC NANOPARTICLES FOR PCB AND TRICHLOROETHYLENE DECHLORINATION

DISSERTATION

A dissertation submitted in partial fulfillment of the
requirements for the degree of Doctor of Philosophy in the
College of Engineering
at the University of Kentucky

By
Jian Xu

Lexington, Kentucky

Director: Dr. Dibakar Bhattacharyya, Alumni Professor of Chemical Engineering

Lexington, Kentucky

2007

ACKNOWLEDGEMENTS

First, I would like to gratefully acknowledge my advisor Prof. Dibakar Bhattacharyya for his guidance, support and friendship during my Ph.D studies. I have worked with him for five years in my graduate education and his unending passion and dedication to the field of membrane & nanomaterials never ceases to stimulate and inspire me to do better. You have been an excellent mentor and I have learned so much from you. I am also grateful for the technical support of my Ph.D committee members, Profs. Douglass Kalika, Bruce Hinds, Michael Jay and Mark Lovell.

I would like to thank Dr. Allan Dozier for the assistance with the TEM analysis. I would like to thank John May and Tricia Coakley from UK Environmental Research and Training Laboratory (ERTL) for their help with the analytical support. I would also like to acknowledge everyone in the DB lab, Aaron, Abhay, Ajay, Andrew, Dave, Deepak, Morgan, Melody, Nathan, Noah, Peter, Saurav, Scott, Tee, Vasile and Yongchao for all of your support and help throughout the years.

Finally, I would like to thank my wife, Wenting Xi, for her support throughout the completion of this degree. We were so happy and excited with the arrival of our son, Ethan Xu during my Ph.D studies. I would like to thank my parents, Chengxu Xu and Guozhen Chen for support in our lives.

This work was funded by the National Institute of Environmental Health Science (NIEHS-SBRP), US Environmental Protection Agency (USEPA-STAR) and Department of Energy (DOE-KRCEE).

Table of Contents

List of Tables

List of Figures

Chapter 1 Introduction

This chapter highlights the research interest addressed in this dissertation. It starts with a brief background review of the chlorinated organic degradation in general followed by the focus on the reductive dechlorination by nanosized zero valent metals. Then it introduces the traditional membrane separation processes and discusses the advantages of combination of membrane and highly reactive nanosized materials for the toxic organic dechlorination application. The research objectives are presented at the end of this chapter.

1.1 Remediation of Chlorinated Organics

Chlorinated organics, such as trichloroethylene (TCE), carbon tetrachloride (CT), chlorophenols, and polychlorinated biphenyls (PCBs) etc. are among the most common contaminants in soil and groundwater (Westrick et al., 1984). Most of these chloro-organics were widely used in industry during the past half century as solvents, pesticides, electric fluids and introduced into soil and groundwater by direct and indirect release. Due to the hydrophobic nature and resistance to biological degradation, the degradation is fairly slow under natural conditions and thus the species accumulate in the environment (Vogel et al., 1987). Many of these compounds are highly toxic and potent carcinogens even at low concentrations. The conventional degradation methods for the remediation of water or soil contaminated with these chlorinated organics are microbial transformations (Morris et al., 1992), carbon adsorption (Nakano et al., 2003) followed by incineration (Shaub and Tsang 1983), chemical oxidation including ozonation (Nakano et al., 2003), UV photolysis, or supercritical water oxidation, and chemical reduction at elevated temperature. However, these traditional methods are usually expensive or require high temperature and long reaction times. For example, dechlorination of PCBs by zero-valent iron requires temperatures of 400 °C (Chuang et al., 1995). Thus, it is important to develop effective methods for degradation of chlorinated organics at ambient conditions. Oxidative Fenton reaction is an effective way for detoxification of chlorinated organics at room temperature (Basu and Wei 1998; Kwan and Voelker 2003; Teel et al., 2001;

Pignatello et al., 2006). Free hydroxyl radical-OH• generated by ferrous ion (Fe^{2+}) and hydrogen peroxide (H_2O_2) in the reaction is a very powerful oxidant for the degradation of chlorinated organic pollutants at room temperature (Kiwi et al., 2000; Perez et al., 2002; Zepp et al., 1992). The primary degradation products are non-toxic organic acids and free chloride. The main drawback of the traditional Fenton's reaction is that pH must be in the acidic region for rapid and efficient contaminant destruction. Specifically, the problems for groundwater treatment at neutral pH include rapid, localized reagent (Fe^{2+}, and H_2O_2) decomposition, localized temperature increase, and iron hydroxide ($Fe^{2+} \rightarrow Fe^{3+} \rightarrow Fe(OH)_3$) precipitation resulting in fouling of injection equipment.

In contrast to the oxidative pathway, chlorinated organics can also be degraded by the reductive pathway at room temperature. The reduction pathway involves replacement of chlorine with hydrogen in the presence of free electrons or catalyst to achieve dechlorination process. Zero valent metals (Fe^0, Zn^0, and Sn^0) have been extensively reported in the literature as effective reductants for dechlorination of many chlorinated organics at room temperature (Matheson et al., 1994; Orth and Gillham 1996; Gotpagar et al., 1997 and 1998; Boronina et al., 1998; Scherer et al., 1998; Arnold et al., 1998 and 1999; Tarr 2003). Bulk size zero valent iron (ZVI) particles in permeable reactive barriers have been employed at many remediation sites for degradation of chlorinated aliphatics in the United States (Powell et al., 2002). In general, the reductive dechlorination with ZVI can be described by the following reaction (Zhang et al., 1998):

$$C_xH_yCl_z + zH^+ + zFe^0 \rightarrow C_xH_{y+z} + zFe^{2+} + zCl^-$$

However, bulk size ZVI has only shown limited reactivity. Reductive degradation by bulk size ZVI usually requires long reaction time (days to months) and results in incomplete dechlorination with dominating chlorinated intermediates. It is know that PCB dechlorination by ZVI does not take place at room temperature (Lowry and Johnson 2004). Many studies have been conducted to enhance the ZVI's reactivity by coating the secondary catalyst metal such as Pd and Ni on the surface of Fe (bimetallic system) (Wang and Zhang 1997; Schrick et al., 2002; Kim and Carraway 2003; Lowry and Johnson 2004; Xu et al., 2005a; Xu and Bhattacharyya 2005b and 2006). The presence of the secondary metal brings novel catalytic properties that are absent in the monometallic particles (Mandal et al., 2003). The deposition of second metal can also enhance chemical

reactivity by changing the electronic properties of surface. It is believed that the presence of the secondary metal alters the reduction pathway from electron transfer (ZVI system) to catalytic hydrodechlorination and thus greatly increases the reaction rate. Furthermore, the formation of chlorinated intermediates is inhibited in the bimetallic system (Zhang et al., 1998). Recently, the creation and development of nanosized materials have brought important and promising techniques into the field of chloro-organics degradation. It is well know that reductive dechlorination by ZVI or bimetallic system is a heterogeneous reaction which only takes place at the particle surface. Therefore, reducing the particle size can greatly enhance the reaction rate due to the high surface area. For example, the transformation rate for chlorinated ethylenes by nanoparticles was calculated to be two orders of magnitude higher than those commercial-grade iron particles (Wang and Zhang 1997; Lien and Zhang 2001). The extraordinary performance of the nanoscale particles was attributed not only to high surface area to volume ratio (ten to hundred times higher than those of commercial-grade particles) but to the higher surface reactivity. Henry (1998) reported that significant changes of the topology found on the nanoparticle surface result in various facets, edges, corners and defects, which could create additional reactive sites. Small metal particles having a high binding energy of their core electrons can influence the interaction between the surface sites with the reactants and products.

1.2 Membrane Supported Bimetallic Nanoparticles

Membranes are known for separation and have been widely used in different industries for over 40 years (Ho and Sirkar, 1992; Bhattacharyya and Butterfield, 2003; Meyer et al., 2006). Membrane separation involves separating a mixture of two or more components by a semipermeable barrier (the membrane) through which one or more of the species transfer faster than another or other species. Since membrane separation usually does not require phase change, it is more energy efficient than the conventional separation such as distillation and evaporation. Generally, polymeric membrane structure consists of two basic types: porous and non-porous membranes. Porous membranes are mainly used for microfiltration (MF) and ultrafiltration (UF) application which is based on the size exclusion mechanism. Gas separation and pervaporation require non-porous

membrane structure which involves the solution-diffusion mechanism, i.e. the separation is based on the solubility and diffusivity variance of different molecules. Recently, many studies have been focused on modification of membrane pores or surface with functional groups such as carboxylic acid, sulfonic acid etc to achieve new applications such as heavy metal capture, bioreaction, catalysis and protein purification. In contrast to the traditional membrane separation processes, these new membranes are known as the functionalized membrane. The main advancement of the functionalized porous membrane is the versatile applications at high mass transfer rate and at low pressure. Different functional groups bring different potential applications, while the porous membrane structure provides high pore surface area and accessibility under convective flow. This work deals with the functionalization of porous membranes with transitional metal nanoparticles to provide a promising and novel way to perform catalytic reactions.

Nanosized metal particles have become an important class of materials due to the unique physical and chemical properties other than those from the bulk size metals. Substantial studies for metal nanoparticles synthesis have been reported in the field of catalysis (Scott et al., 2005), optical (Jain et al., 2006), electronic (Paul et al., 2003), magnetic (Yakushiji et al., 2005) and biological devices (Patolsky et al., 2004; Jiang et al., 2004). In these cases, to avoid the agglomeration and aggregation, nanoparticles were usually stabilized by polymers or ligands in solution phase, or immobilized on solid supports (Worden et al., 2004; Fukasawa et al., 2005; Liu et al., 2004). Much attention has been given to the preparation of metal nanoparticles embedded in polymer films or membranes by a stepwise approach of ion-exchange/reduction (Ikeda et al., 2004; He et al., 2002 and 2003; Pivin et al., 2006; Damle et al., 2001; Xu et al., 2005a; Xu and Bhattacharyya, 2005b and 2007). In this method, ion-exchange ligands created in the thin films can bind metal cations from aqueous solution. Post reduction or precipitation produces nanoparticles from bound metal cation precursors. The advantage of this process is the creation of controllable nanostructure properties during nanoparticle synthesis by utilizing these ion exchange ligands. The nanostructure properties include the particle size and distribution, particle concentration and interparticle spacing. The amount of metal cations loaded is controlled by the amount of ligand sites and ion-exchange conditions such as the pH and competitive ions (He et al., 2002). The distance

between bound cations which determines the final particle size is also controlled by the space between ion-exchange ligands (Wang et al., 2002). For example, Wang and co-workers reported that silver nanoparticles with various size and concentration have been produced in the polyelectrolyte multilayer film (Wang et al., 2002).

Various ligands and chelating groups can be used for the synthesis of metal nanoparticle by the ion-exchange/reduction method. Especially, polyelectrolytes (Rivas et al., 2003) containing multifunctional chelating agents provide a great number of side functional ligands such as amines, carboxylic acids, amides, alcohols, aminoacids, pyridines, thioureas, iminos, etc. These side functional groups can have strong interaction with metal ions to establish stable polymer-ion complexes. Attachment procedures of these chelating polymers and polypeptides on membrane internal pore surfaces have been extensively studied for metal ions sorption (Konishi et al., 1996; Bhattacharyya et al., 1998; Ritchie et al., 1999 and 2001; Hestekin et al., 2001). These functionalized membranes incorporating metal ions have the possibility to be the precursors for nanoparticle synthesis. MF and UF membranes are no doubt the ideal base for functionalization due to the open structure and large pore size which are essential to attain high efficient utilization of available sites as well as the easy accessibility to the nanoparticles immobilized inside the membrane matrix.

Polyacrylic acid (PAA), a water soluble chelating polyelectrolyte, has been extensively used for metal capture and ion-exchange process because of the carboxylic acid group (Rivas et al., 2003). Generally, there are three different ways to functionalize MF/UF membrane with PAA: (1) dip or spin coating PAA on the membrane support; (2) layer by layer assembly of polycations (polyallylamine hydrochloride (PAH), polyethyleneimine (PEI)) and PAA on membrane surface or pores; (3) in-situ polymerization of acrylic acid (PAA monomer) inside membrane pores. Literature results have also included PAA as the membrane selective layer to prepare pervaporation membrane (PV) (Xu and Huang 1988; Choi et al., 1992; Rhim et al., 1993 and 1996; Ohya et al., 1994) because of the highly preferential water permeation characteristics of PAA. PAA functionalization on MF/UF membrane (polyvinylidene fluoride (PVDF) polysulfone (PS), polyacrylonitrile (PAN), etc) is a well-known process for preparing PV, nanofiltration (NF) (Gabriel and Gillberg 1992) and reverse osmosis (RO) membrane

(Huang et al., 1998). Incorporating the PAA coating layer with metal ions (Al^{3+}) as additives was investigated to increase the hydrophilicity of the layer and restrict the swelling of the membrane by forming cross-linking structure with metal ions (Choi et al., 1992; Ohya et al., 1994; Rhim et al., 1996). However, few studies have been conducted for the immobilization of nanoparticles in microporous membranes modified with PAA. Microporous membranes functionalized with highly reactive metal nanoparticles are quite novel. The advantages of immobilization of metal nanoparticle in porous membrane in this work include prevention of nanoparticle agglomeration, control of particle, structure and assembly, convective flow to eliminate the diffusion resistance, recapture of dissolved metal ions.

1.3 Research Objectives

Zero valent iron-based system has exhibited significant success on the remediation of chlorinated organics in water by reductive degradation pathway. However, the reaction mechanisms and rate models for membrane supported iron-based nanoparticles have not been reported in the literature for the remediation of water contaminated with chlorinated organics. Immobilization of metal particles in membrane phase avoids aggregation and agglomeration and allows for the controllable nanoparticle synthesis by using the functional ion-exchange groups. The reductive dechlorination mechanism and the role of second dopant metal, and the correlation between reactivity and particle structure have not been fully clarified in the literature. Our overall objective of this work is not only to develop highly reactive membrane-supported nanosized bimetallic materials for reductive dechlorination of selected chlorinated organics but also to understand and quantify the role of second dopant metal, particle size (nano vs. bulk size) in the reactive properties of bimetallic nanoparticles, and reaction pathway/reaction rate changes through high resolution X-ray mapping and reaction product distribution. Specific objectives of this research involve:

- To develop and establish methods of modifying microporous membrane pore/surfaces with polyelectrolytes (PAA) as the functional groups for capture of metal ions as the nanoparticle precursor.

- To study and quantify the extent of chelation between ferrous ions and carboxylic acid ion exchange groups.
- To establish direct in-situ synthesis of bimetallic nanoparticles with controlled structure and size in the microporous membrane supports derived from polyelectrolyte functionalization and ion exchange.
- To characterize membrane and bimetallic nanoparticle by scanning electron microscopy (SEM), transmission electron microscopy (TEM), scanning transmission electron microscopy (STEM), X-ray Mapping techniques.
- To establish methods of bimetallic nanoparticles characterization in the presence of a polymer support using electron microscopy to quantify the role of the second metal during bimetallic reduction mechanisms of chlorinated organics
- To understand the reaction mechanism and to quantify the reaction kinetics with product and intermediates analysis for the dechlorination of TCE and selected PCBs by membrane-based nanostructured bimetallic particles.
- To study and correlate the composition of the second dopant metal and the nanoparticle structure with catalytic reactivity by high resolution X-ray mapping.
- To establish a convective flow membrane reactor model incorporating mass transfer reaction kinetics and membrane partitioning for prediction and simulation at various system and operating conditions.
- To enhance Fe/Pd nanoparticles reactivity by understanding the oxidation of iron using various methods such as X-ray mapping and quantification of hydrogen production.

Chapter 2 Background

This chapter reviews the literature studies on the destruction of toxic chlorinated organics. It starts with the chlorinated organics degradation by the oxidative pathway. Then it draws attention to the zero valent iron based reductive pathway by highlighting the reaction mechanism, current drawbacks, reactivity improvement based on nanostructured materials and second dopant metal. Finally, it discusses the background and theory of nanoparticle synthesis and membrane separation processes. It highlights the advantages of synthesizing bimetallic nanoparticles in membrane phase in terms of stabilization of nanoparticles, high reactivity, and minimization of mass transfer resistance.

2.1 Chemical Degradation of Chlorinated Organics

Generally, chemical degradation of chlorinated organics in water at room temperature can be achieved by two different reaction pathways: oxidation and reduction. Oxidative dechlorination processes include UV light, ozone, ozone + hydrogen peroxide, Fenton's reaction, etc., whereas the reductive processes include various zero-valent metals, such as Fe, Zn, Fe/Pd, Fe/Ni, etc. The main difference between oxidative and reductive processes is complete reaction in the former leads to the formation of organic acids and CO_2, while for the latter results in formation of the non-chlorinated analog of the parent compound (e.g., ethylene/ethane from TCE). Oxidative processes are usually based on the generation of free radicals as the oxidant (e.g. OH• from Fenton's reaction). Oxidative process by free radical reaction involves three pathways: hydroxylation (by substitution), oxidation, and aromatic ring cleavage (if aromatics are involved). The mechanism for reductive pathway is electron transfer for single metal system (Fe^0 or Zn^0) or catalytic hydrodechlorination for bimetallic system (Fe/Pd, Fe/Ni).

2.1.1 Oxidative Pathway

Chemical oxidation is an important technique for the remediation ground water and soil contaminated with toxic organics. Various oxidizing agents such as permanganate, ozone, persulfate can be used for this process. For example, the use of permanganate has been extensively studied for the treatment trichloroethylene (TCE) and perchloroethylene (PCE) (Schnarr et al., 1998). Hydrogen peroxide is another important oxidant source. The advantage of using hydrogen peroxide is easy to use, low cost and suitable for wide organic contamination. Although hydrogen peroxide is a strong oxidant, the rate of direct oxidation for many organic pollutants is very slow. Practically, hydrogen peroxide is combined with UV, ozone or ferrous ions in the wastewater treatment. These processes are based on the highly reactive hydroxyl radicals (OH•), which is the primary oxidizing species and can be utilized to destroy many organic contaminants at fast rates. The hydroxyl radical based processes are known as advanced oxidation processes (AOPs) (Watts et al., 2005).

Among AOPs, Fenton's reaction has been known as an efficient technique for degradation of many chlorinated organics (Ahuja et al., 2007; Pera-Titus et al., 2004). The Fenton's system consists of ferrous ions combined with hydrogen peroxide under acidic conditions. Fenton (1894), as the inventor, first found the high reactivity in the study of oxidation of tartaric acid by hydrogen peroxide. However, the hydroxyl radical mechanism of the Fenton's reaction was not proposed until 1934 by Haber and Weiss. This mechanism can be described by the following equations:

Initiation:

$$H_2O_2 \rightarrow H_2O + \frac{1}{2}O_2 \quad \text{(E2.1)}$$

$$H_2O_2 + Fe^{2+} \rightarrow Fe^{3+} + HO^- + OH\bullet \quad \text{(E2.2)}$$

$$H_2O_2 + Fe^{3+} \rightarrow Fe(OOH)^{2+} + H^+ \leftrightarrow Fe^{2+} + HO_2\bullet + H^+ \quad \text{(E2.3)}$$

$$OH^- + Fe^{3+} \rightarrow Fe(OH)^{2+} \leftrightarrow Fe^{2+} + OH\bullet \quad \text{(E2.4)}$$

Propagation:

$$OH\bullet + H_2O_2 \rightarrow HO_2\bullet + H_2O \quad \text{(E2.5)}$$

$$HO_2\bullet + H_2O_2 \rightarrow OH\bullet + H_2O + O_2 \quad \text{(E2.6)}$$

$$HO_2\bullet + HO_2^- \rightarrow OH\bullet + HO^- + O_2 \quad \text{(E2.7)}$$

Termination:

$$OH\bullet + Fe^{2+} \rightarrow Fe^{3+} + HO^- \quad \text{(E2.8)}$$

$$HO_2\bullet + Fe^{3+} \rightarrow Fe^{2+} + H^+ + O_2 \quad \text{(E2.9)}$$

$$HO_2\bullet + OH\bullet \rightarrow H_2O + O_2 \quad \text{(E2.10)}$$

$$OH\bullet + OH\bullet \rightarrow H_2O_2 + O_2 \quad \text{(E2.11)}$$

Chlorinated Organics (RCl) Degradation

$$RCl + H_2O_2 \rightarrow Intermediates + H_2O \quad \text{(E2.12)}$$

$$RCl + OH\bullet \rightarrow Intermediates \quad \text{(E2.13)}$$

$$Intermediates + H_2O_2 \rightarrow H_2O + CO_2 + Cl^- \quad \text{(E2.14)}$$

$$Intermediates + OH\bullet \rightarrow H_2O + CO_2 + Cl^- \quad \text{(E2.15)}$$

The characteristic oxidizing reactivity of hydroxyl radical is due to a deficit of one electron in the valence orbit (unpaired electrons). The standard reduction potential for OH• is +2.73 V. This make it capable of oxidizing a variety of chlorinated organics, which usually have reduction potential of +0.5 V~+1.5 V. The most common mechanisms for hydroxyl radical reactions are hydroxylation, oxidation, and ring cleavage (Watt et al., 2005). For example, oxidation of benzene by OH• starts with the formation of phenol by hydroxylation onto the ring. Subsequent substitution by another hydroxyl radical forms a catechol. Subsequently, ring cleavage results in the formation of cis-1,2-muconic acid. Further hydroxylation produces various β-keto acids.

The solution pH has a great effect on the Fenton's reaction. The classic Fenton's reaction is carried out at pH of 2~4. At pH high than 4, the degradation rate of chlorinated organics will decrease with the increase of pH. This is due to the precipitation of iron as ferric hydroxide at pH above 5. The regeneration of Fe^{2+} by the reaction of Fe^{3+} with H_2O_2 (E 2.3) also requires low pH. Thus, Fenton's reaction is usually modified to extend its application at neutral pH for groundwater remediation. Extensive studies have been reported using chelating agent for this purpose. By adding the chelating agent into the Fenton's reaction system, the precipitation of iron hydroxide at neutral pH can be

inhibited due to the formation of Fe (II)/Fe (III)-chelate complex. The chelate Fenton's system also allows higher utilization of hydroxyl radicals and longer reactivity by controlled release of free ferrous ions. The chelating agents that have been studied for modified Fenton's reaction includes: EDTA, citric acid (Li et al., 2005), polyacrylic acid (PAA), gluconic acid (Ahuja et al., 2007) etc.

2.1.2 Reductive Pathway

In contrast to the oxidative pathway, the reductive pathway at room temperature utilizes hydrogen to replace chlorine in the presence of electrons or hydrogenation catalyst to achieve the dechlorination process. Generally, electronegative metals in the bulk phase, such as Zn and Fe, have been used for the reductive dechlorination of chlorinated organics (Orth and Gillham, 1996; Gotpagar et al., 1997 and 1998; Boronina et al., 1998; Scherer et al., 1998; Arnold et al., 1998 and 1999; Tarr 2003). Although the degradation of chlorinated organics is often referred to as zero-valent metal catalysis, it is not strictly catalytic but rather an electrochemical corrosion process. Extensive literature exists on dechlorination kinetics and reduction rates by Fe^0, but the presence of impurities in the source of iron (Tamara and Butler, 2004) size differences, and surface area variations (Helland et al, 1995), including surface treatment methodologies, have led to wide variability in reported results (Burrow et al., 2000). The surface chemistry and particle morphology of the metal also affect rates of dechlorination because of increased oxide layer and diffusion resistance for electron transfer.

The reductive dechlorination by single zero valent metal particle (Fe, Zn, Sn, Mg) is a redox reaction. The reaction mechanism is generally recognized as direct electron transfer. The indirect reduction by H_2 (hydrogenation) is more favorable at low hydrogen overpotential metals such as Pd or Pt than Fe (high hydrogen overpotential). Since the electrons released from metal particles usually have a short life and can only transmigrate a short distance, the chlorinated organics must be located at the particle surface for the electron transfer. Thus, it is a heterogeneous reaction, which involves adsorption on the particle surface, reaction on surface and desorption. The reductive dechlorination reaction can be described in the following equations (Matheson and Tratnyek, 1994):

$$Fe^0 \rightarrow Fe^{2+} + 2e^- \quad \text{(E2.16)}$$

$$RCl + 2e^- + H^+ \rightarrow RH + Cl^- \quad \text{(E2.17)}$$

$$RCl + Fe^0 + H^+ \rightarrow Fe^{2+} + RH + Cl^- \quad \text{(E2.18)}$$

In this redox reaction, iron is the reducing agent, which is oxidized to form ferrous ions in aqueous solution and release two electrons. The standard reduction potential for iron is -0.440 V (Matheson and Tratnyek, 1994). This makes the ZVI thermodynamically suitable for reducing various chlorinated alkyls which have estimated standard reduction potential ranges from +0.5 to +1.5 V (Roberts et al., 1996). Without the presence of chlorinated organics (RCl), equation E2.18 becomes a well known iron corrosion reaction:

$$2H_2O + Fe^0 \leftrightarrow Fe^{2+} + H_2 + 2OH^- \quad \text{(E2.19)}$$

In the presence of chlorinated organics, RCl serves as the oxidizing agent. The iron corrosion reaction in water is a complex process. There are other side reactions except for the above main corrosion reaction (E2.19). For example, in the case of absence of strong oxidant at near neutral pH, the main iron corrosion reaction (E2.19) is coupled with two other side reactions:

$$O_2 + 2H_2O + 4e^- \rightarrow 4OH^- \quad \text{(E2.20)}$$

$$O_2 + 2H_2O + 2Fe^0 \leftrightarrow 2Fe^{2+} + 4OH^- \quad \text{(E2.21)}$$

The presence of dissolved oxygen enhances iron corrosion based on equation E2.21. Further oxidation of Fe^{2+} by O_2 results in the formation of ferric hydroxide precipitation. This may dramatically inhibit the corrosion reaction and thus deactivate the zero valent iron by forming $Fe(OH)_3$ rust on the particle surface due to the extremely low water solubility.

Extensive studies have been conducted to understand dechlorination mechanisms and pathways (Matheson and Tratnyek, 1994; Roberts et al., 1996; Arnold and Roberts 1998, Arnold et al., 1999). However, the precise reaction pathways and intermediates formed for chlorinated organics reduction by zero valent metals have not been fully clarified. Generally, the reductive dechlorination based on electron transfer can have two different pathways (Macalady et al., 1986; Schwarzenbach et al., 1993; Roberts et al., 1996): hydrogenolysis (replacement of one chlorine by one hydrogen) and reductive β-elimination (two chlorines are released).

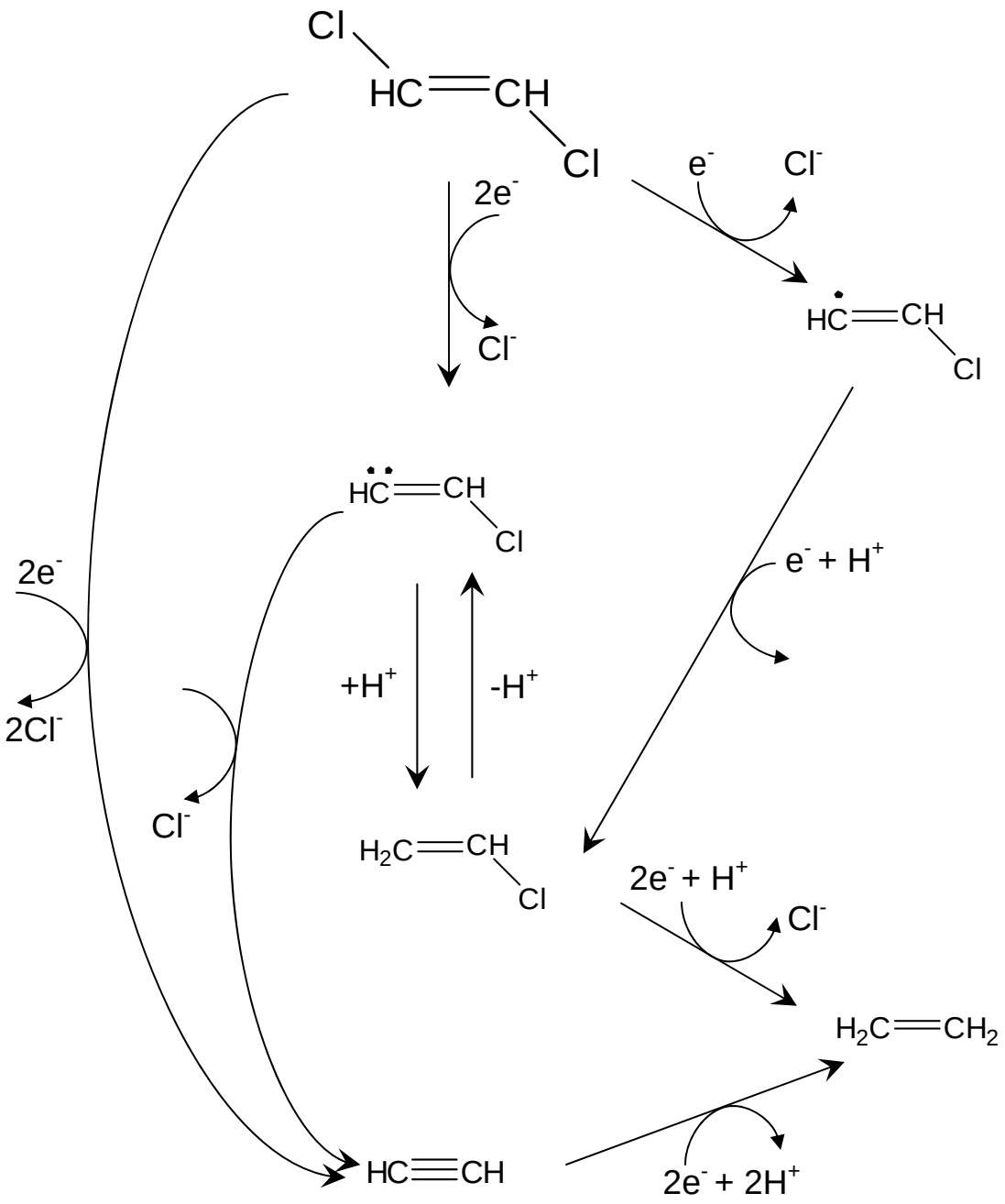

Figure 2.1 Proposed reduction pathways for trans-dichloroethylene by zero valent metals (adapted from Roberts et al., 1996)

A net transfer of two electrons is required for both pathways. Figure 2.1 shows proposed the reduction pathway for trans-dichloroethylene (DCE) by Fe^0 (Roberts et al., 1996). Sequential hydrogenolysis of trans-DCE results in vinyl chloride (VC) as the intermediate and ethylene as the final product. While the reductive β-elimination yields acetylene which can be further reduced to ethane by hydrogenation.

Although zero valent metals have been widely used in the past for the remediation of water contaminated with various chlorinated organics, there are some problems that need to be addressed: (1) slow reaction rate which require long reaction time or high concentration of metals; (2) incomplete dechlorination and formation of toxic chlorinated intermediates; (3) zero or limited reactivity towards chlorinated aromatics, especially for PCBs and (4) loss of reactivity with the time due to the formation of iron hydroxide precipitates on the particle surface.

Thus, extensive studies have been contributed to enhance the reactivity and stability of zero valent particles for the degradation of chlorinated organics in water. The creation and development of nanosized materials have brought important and promising techniques into ZVI based degradation due to the heterogeneous reaction nature. The transformation rate for chlorinated ethylenes by nanoparticles was calculated to be two orders of magnitude higher than those commercial-grade iron particles (Wang and Zhang, 1997; Lien and Zhang, 2001). The extraordinary performance of the nanoscale particles was attributed to high surface area to volume ratio (ten to hundred times higher than those of commercial-grade particles).

It has been demonstrated that the addition of a second catalytic metal such Ni or Pd (bimetallic nanoparticles) can dramatically increase the dechlorination reaction rate (Grittini et al. 1995, Zhang et al. 1998, Schrick et al. 2002, Kim and Carraway, 2000, Lowry and Johnson 2004, Tee et al., 2005; He et al. 2007). In this case, the chlorinated organics are reduced to non-chlorinated hydrocarbons on the second catalytic metal surface (Pd or Ni) by substitution of chlorine with hydrogen generated from Fe^0 corrosion. Compared to the electron transfer in ZVI system, the dechlorination mechanism for bimetallic system is catalytic hydrodechlorination. The presence of a second catalytic metal results not only in enhanced reaction rates but the elimination of toxic chlorinated intermediates formation. The common practice is to compare pollutant degradation in

terms of surface area normalized reaction rates (k_{SA}, L m^{-2} h^{-1}). For example, the k_{SA} for 2,2'-dichlorobiphenyl (DiCB, PCB 4) by nano Fe/Pd (Pd = 1 wt%) systems is 1.3×10^{-2} L m^{-2} h^{-1} (Xu and Bhattacharyya, 2005b) with complete biphenyl formation, which is about 100,000 fold higher than nano Fe^0 systems (k_{SA} = 1.1×10^{-7} L m^{-2} h^{-1}) (Lowry and Johnson 2004). Without the second Pd coating, the nano Fe^0 system results in incomplete dechlorination with 2-chlorobiphenyl dominating as the chloro-intermediate. The destruction of 2, 2'-dichlrobiphenyl with Fe/Pd is a catalytic hydrodechlorination process involving the following reactions (Figure 2.2). Nutt et al. (2006) reported the use of Pd-Au nanoparticles in the catalytic hydrodechlorination of TCE with supplied H_2 gas. The effect of Pd coating density on the reactivity was studied and compared in terms of initial turnover frequencies. However the role of the secondary dopant metal Pd and the relationship between reactivity and dopant coating density for Fe/Pd system have not been fully understood. It is speculated (Nutt et al 2005, 2006) that two-dimensional ensembles of Pd atoms rather than individual Pd atoms are the active sites. It should be noted bimetallic Fe/Pd systems do not require external H_2 gas supply. More specifically, the correlation between reactive properties and the nanoparticle structure, the distribution of first and second metal, the composition of second metal, and particle size (nano size versus bulk size) have not been fully clarified in the literature.

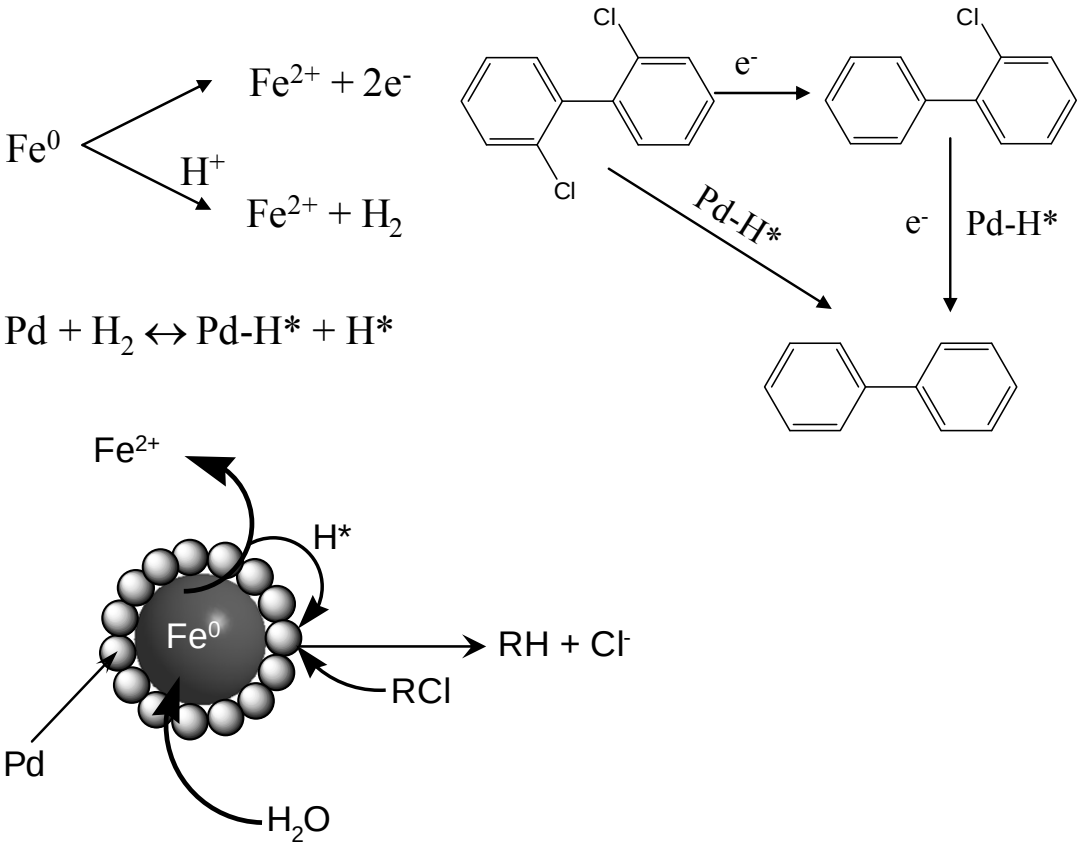

Figure 2.2 Proposed catalytic hydrodechlorination pathways for 2,2'-dichlorobiphenyl by Fe/Pd nanoparticles.

2.2 Nanoparticle Synthesis

Generally, preparation of nanoparticles can be divided into four primary physical and chemical methods (Aiken and Finke, 1999): (1) mild chemical reduction of metal salts in solution phase; (2) thermal decomposition of metal carbonyls (Tannenbaum, 1998; Gonsalves et al., 2000); (3) ligand reduction and displacement from organometallics in solvent phase (Gonsalves et al., 2000; Philippot et al., 2003; Corbierre et al., 2004); (4) metal vapor deposition (CVD) (Akamatsu and Deki, 1997; Hierso et al., 1998). For all these cases, initially zero-valent metal atoms are produced and then aggregate themselves to form nanoclusters which may agglomerate and grow to micron scale or larger. This agglomeration reduces the specific surface area and the interfacial free energy, which can result in the loss of nanoparticle reactivity. Chemical reduction of metal ions in solution phase is the most common method for the preparation of metal nanoparticles (Fe^{2+}, Cu^{2+}, Ag^{+}, and Pd^{2+} etc). For example, nanoscale Fe^0 particles are prepared by reduction of Fe^{2+} or Fe^{3+} with sodium borohydride ($NaBH_4$) in the aqueous phase (Glavee et al., 1995). This aqueous phase based nano ZVI synthesis method is more environmentally friendly than other solvent-based synthesis. It is also important to point out that the reaction between Fe^{2+} and sodium borohydride is a complex process. Various products such as Fe^0, Fe_2B, Fe_3B and HBO_2 have been reported (Glavee et al., 1995; Shen et al., 1993). It is well known that the reaction is controlled by several factors such as pH, molar ratio and concentration of reactants, and ways of mixing the reactants. All possible overall reactions for producing Fe-B nanoparticles using borohydride in aqueous solution were suggested by the following reactions (Shen et al., 1993).

$$2Fe^{2+} + BH_4^- + 2H_2O = 2Fe^0 + BO_2^- + 4H^+ + 2H_2 \quad \text{(E2.22)}$$

$$2Fe^{2+} + 2BH_4^- + 2H_2O = Fe_2B + HBO_2 + 2H^+ + 4.5H_2 \quad \text{(E2.23)}$$

$$6Fe^{2+} + 5BH_4^- + 6H_2O = 2Fe_3B + 3HBO_2 + 7H^+ + 11H_2 \quad \text{(E2.24)}$$

It is known previously that the standard reduction potential for Fe^{2+}/Fe^0 is -0.44v (E2.16). According to the literature (Shen et al., 1993), BH_4^- gives $8e^-$ at alkaline conditions by the following half reactions.

$$BH_4^- + 2H_2O \rightarrow HBO_2 + 3H^+ + 2H_2 + 4e^- \quad E^0 = -0.98\text{v} \quad \text{(E2.25)}$$

$$BH_4^- + 4OH^- \rightarrow BO_2^- + 2H_2O + 2H_2 + 4e^- \quad E^0 = -1.67v \qquad (E2.26)$$

The strong reducing power of BH_4^- make it favorable for making various zero valent metal particles such as Co, Cu, Ni, Ag, etc. Both the addition rate and concentration of BH_4^- solution influence the boron content in the metal particle products. Iron particle agglomeration usually can not be avoided in this case without using a stabilizer. Typically, agglomeration of nanoparticles is caused by interparticle interactions such as Vander Waals forces. Fe^0 as a magnetic metal can result in more intense agglomeration due to the strong magnetic interactions.

This atom agglomeration usually can be controlled by using various stabilizers such as polymers, ligands, or surfactants. In this case, particle stabilization is achieved by surrounding or combining the metal center with sterically bulky materials (Gonsalves et al., 2000). For instance, steric stabilization can be obtained by coating the particles with polybutadiene (Gonsalves et al., 2000), poly (N-vinyl-2-pyrrolidone) (Teranishi and Miyake, 1999; Papp et al., 2004) or polyvinylpyridine (Tsutsumi et al., 1999). Li et al (2003) reported the preparation of 10 nm iron nanoparticles using CTAB as the protection agent. The nanoparticle agglomeration can also be prevented through electrostatic repulsion by using charged stabilizing agents. Adsorption of charged molecules on nanoparticles provide electrical double layer and thus enhance the Coulombic repulsion between nanoparticles.

Ligands, ion exchange and chelating groups can also be used to trap metal ions which are subsequently reduced to form stable nanosized metal particles. Polyelectrolytes containing multifunctional groups such as amines, sulfonic acid and carboxylic acids, etc have been extensively studied for metal nanoparticle synthesis. These side functional groups can have strong interaction with metal ions to establish stable polymer-ion complexes. In this case, metal ions will interact with these stabilizing polyelectrolytes to form polymer-metal ion complex which plays a critical role to protect metal particles from agglomeration. The interactive force includes electrostatic force, coordinate bonding, and hydrogen bonding.

2.3 Membrane Immobilized Nanoparticles

Membrane separation is well known as a good alternative process for traditional separation such as distillation and evaporation. The advantages of membrane separation are the low energy consumption and the compact system. The membrane process usually does not involve phase change which requires high amount of energy in the traditional separation process. Generally, membrane separation mechanism can be divided into two categories: sieving mechanism and solution-diffusion (Figure 2.3). Microporous membranes used in the liquid separation such as microfiltration (MF), ultrafiltration (UF) and nanofiltration (NF) separate by sieving mechanism determined by the pore diameter and particle size. The pores in the porous membrane may vary between 1 nm to 500 nm. Gas separation and pervaporation process require a dense (non-porous) selective structure. The separation mechanism is known as the solution and diffusion achieved by the variation of solubility and diffusivity of different molecules in the polymer matrix.

The traditional size exclusion based membrane process such as MF, UF and NF do not require the pore surface be active in the separation. It is promising to utilize and modify membrane pores with functional groups to obtain special separation and reaction functions. Many studies have been reported on functionalizing the MF membrane pores with -OH, $-NH_2$, $-SO_3H$, -COOH, or $-CONH_2$ groups by using chemical modification (Bhattacharyya et al., 1998), polymerization (Ulbricht and Yang 2005; Geismann and Ulbricht 2005), and layer by layer assembly (LBL) methods (Hong and Bruening, 2006a; Smuleac et al., 2006). The functionalized membrane has been studied for various applications such as NF type separation (Hong et al., 2006b), heavy metal removal (Bhattacharyya et al., 1998; Ritchie et al., 1999 and 2001; Hestekin et al., 2001), protein recovery (Avramescu et al., 2003), bioreaction (Smuleac et al., 2006), and catalysis (Shah and Ritchie 2005). The advantages of using functionalized porous membrane are high mass transfer capacity, low operating pressure due to the open structure and many versatile applications (Figure 2.4).

Membrane supported nanoparticles is a new type of functionalized membrane. It has been reported that silica and zeolite nanoparticles immobilized in the polymer membrane matrix can enhance the gas separation and reverse osmosis separation

performance. Membrane supported transitional metal nanoparticles can also be used to carry out catalytic reactions. Nanosized metal catalysts are usually immobilized and dispersed in solid supports such as active carbon, metal oxides (Tada et al., 2004), zeolites (Legrand et al., 2004). Tremendous studies have been focused on the synthesis of nanocomposites containing metal nanoparticles in polymeric matrix for optics, sensor, and catalysis application. The main advantage of synthesizing metal/polymer composites is the control of nanoparticle size and distribution. In addition, the polymers may also have a great influence on the nanoparticle activity by modifying the access to the sites (Kiadambi and Bruening, 2005). However, immobilization of nanoparticles in solid dense matrix may cause a diffusion resistance during the catalytic reaction because the reactants now need to diffuse to the nanoparticles if the support has a dense structure. To overcome this problem, it is advantageous to synthesize and immobilize nanoparticles in an open matrix. Microfiltration (MF) membranes are of great interest for this purpose due to the open structure and 100 – 500 nm pore size. This is essential for attaining highly efficient utilization of available sites as well as the easy accessibility to the nanoparticles immobilized inside the membrane matrix. Membranes functionalized with bimetallic nanoparticles offers great advantages for the catalytic reaction because diffusion limitation can be minimized under convective flow.

A. Porous polymer membrane

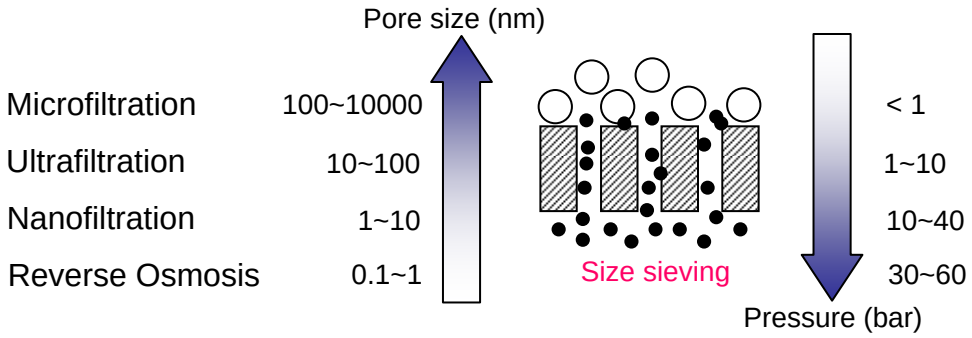

B. Nonporous polymer membrane

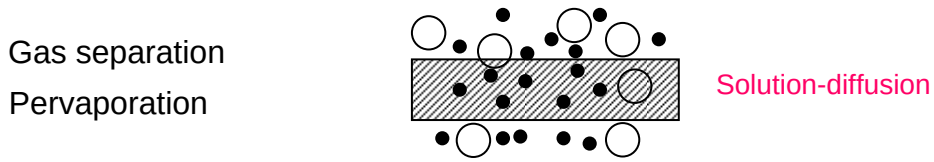

Figure 2.3 Membrane structure and separation mechanism

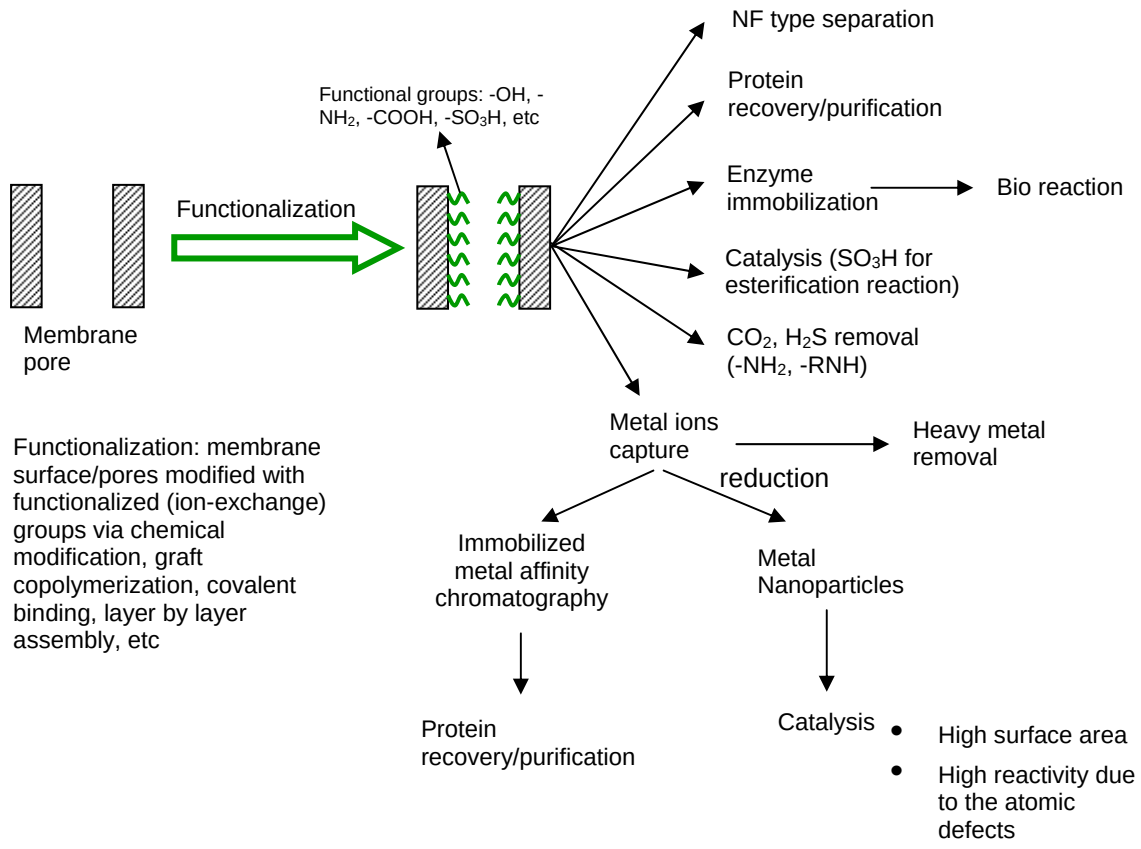

Figure 2.4 Porous membrane functionalization and application

Chapter 3 Experimental Section

3.1 Introduction

This chapter includes descriptions and procedures for all the chemicals, membranes, set-ups used in the research. In addition, the preparation of membrane functionalization, nanoparticle synthesis and dechlorination reaction set-ups will be discussed in detail. The membranes were characterized by scanning electron microscopy (SEM), thermogravimetric analyzer (TGA), and Fourier transform infrared (FT-IR). Nanoparticles were characterized by SEM, transmission electron microscopy (TEM), X-ray energy dispersive spectroscopy (EDS), scanning transmission electron microscopy (STEM), and high resolution transmission electron microscopy (HRTEM). The analysis techniques performed for organic and metal ions quantification are: gas chromatography equipped with mass spectrometry (GC/MS), ion chromatography (IC), inductively coupled plasma atomic emission spectrophotometry (ICP-AES), atomic adsorption (AA), total organic carbon (TOC).

3.2 Materials

Acrylic acid (AA), benzoyl peroxide, 1,1,1-trimethylolpropane triacrylate (TMPTA), toluene anhydrous, ferrous chloride tetrahydrate ($FeCl_2 \cdot 4H_2O$), potassium tetrachloropalladate (K_2PdCl_4), sodium borohydride ($NaBH_4$), ethanol anhydrous and hexane were obtained from Aldrich. Ferrous chloride, nickel chloride, sulfuric acid (1N), ethylene glycol, $FeSO_4 \cdot 7H_2O$, and trichloroethylene were obtained from Fisher Scientific. Halogenated ethane standard, naphthalene-d8 (5000 mg L^{-1} in methyl chloride), decachlorobiphenyl (PCB209), 3,3',4,4'-tetrachlorobiphenyl (PCB77), 2,3,2',5'-tetrachlorobiphenyl (PCB44), 3,4,4'-trichlorobiphenyl (PCB37), 3,3',4-trichlorobiphenyl (PCB35), 2,2',5-Trichlorobiphenyl (PCB18), 2,2',3-Trichlorobiphenyl (PCB16), 4,4'-dichlorobiphenyl (PCB15), 3,4'-dichlorobiphenyl (PCB13), 3,4-dichlorobiphenyl (PCB12), 3,3'-dichlorobiphenyl (PCB11), 2, 2'-dichlorobiphenyl (PCB4), 4-chlorobiphenyl (PCB3), 3-chlorobiphenyl (PCB2), 2-chlorobiphenyl (PCB1) and

biphenyl were obtained from Ultra Scientific. Palladium acetate ($[Pd(C_2H_3O_2)_2]_3$) was from Alfa. Polyacrylic acid (MW 50,000) was obtained from Polysciences. Dextran (MW 144,000; 482,000; 670,000; 1,400,000; 2,000,000) was obtained from Sigma. Commercial polyether sulfone MF membrane (PES, 0.22μm pore size, 4.7 cm diameter, 150~200μm thickness), PVDF MF membrane (0.22 μm pore size, 4.7 cm diameter, 125 μm thickness and 75% porosity) and hydrophilized PVDF MF membrane (0.1 μm pore size, 4.7 cm diameter, 110 μm thickness) were purchased from Millipore.

3.3 Preparation of PAA-Functionalized Membrane

3.3.1 PAA Dip Coating

Two types of MF membranes were used as the support for PAA modification by dip-coating: hydrophobic PES membrane and hydrophilized PVDF membrane.

PAA/PES Membrane Preparation

PES microfiltration membrane obtained from Millipore was used as the support membrane layer. The PAA coating layer was attached to the surface of PES support membrane by a dip-coating process (Choi et al., 1992; Ohya et al., 1994; Huang et al., 1998). A PES MF membrane was immersed in a dilute aqueous coating solution of PAA. After removal from the immersion bath, a thin adherent layer was left on the membrane. Aqueous coating solution was prepared by diluting 25 wt% PAA solutions to 12.5 wt% solution with 2 wt% ethylene glycol as the crosslinking agent and 7.8 wt% $FeCl_2 \cdot 4H_2O$ as the precursor of iron nanoparticles. The molar ratios of PAA repeat unit (~COOH) to ethylene glycol and the ratio to Fe^{2+} were both 4:1. The crosslinked PAA/PES composite membrane was finally obtained by thermally heating the membrane in the oven under vacuum at 110~120°C for 3 hours. The ether bond formed between carboxylic group and ethylene glycol generate the crosslinking PAA network structure. Figure 3.1 illustrates that two PAA chains are cross-linked due to the esterification reaction between the

carboxylic group in PAA and the hydroxyl group in EG. It is important to only do a partial (about 50%) cross-linking to leave free carboxylic groups for metal entrapment.

PAA/PVDF Membrane Preparation

A similar procedure was used to prepare PAA/PVDF composite membranes by dip-coating. Briefly, hydrophilized PVDF MF membrane (0.1 μm pore size, 4.7 cm diameter, 110 μm thickness, Millipore) was also used as another support membrane layer. Aqueous coating solution was prepared by diluting 25 wt % PAA (MW 50,000) solutions to 12.5 wt % solution with 2.3 wt % ethylene glycol as the crosslinking agent and 10.5 wt % $FeSO_4 \cdot 7H_2O$ as the precursor of iron nanoparticles. The crosslinked PAA/PVDF composite membrane was finally obtained by thermally heating the membrane in the oven under vacuum at 110~120°C for 3 hours (Figure 3.1).

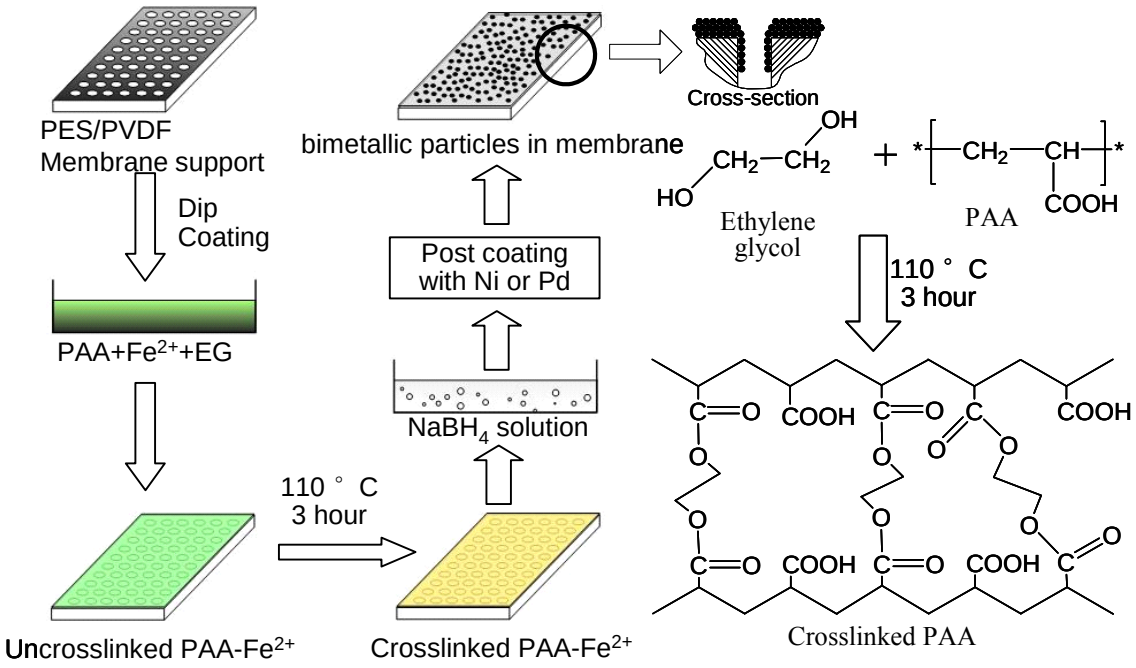

Figure 3.1 Schematic diagram for preparation of nanoscale Fe/Pd or Fe/Ni particles in the PAA/PES or PAA/PVDF membrane and cross-linking reaction between EG and PAA (Xu and Bhattacharyya, 2005a).

3.3.2 In-situ Polymerization of Acrylic Acid

The PVDF MF membranes functionalized with PAA were prepared by filling the membrane pores with the acrylic acid monomer solution, followed by literature reported (for polyethylene MF membrane) in-situ free radical polymerization via thermal treatment (Gabriel and Gillberg, 1993). The typical procedure is described in Figure 3.2. In order to achieve the ability of wetting out the hydrophobic PVDF membrane, toluene was chosen as the solvent medium. The monomer solution was prepared by mixing the acrylic acid (30 wt %), benzoyl peroxide (0.5 wt %, initiator), TMPTA (1 wt %, cross-linking agent) in toluene. Benzoyl peroxide as the initiator was first dissolved in toluene. The solutions were purged with ultra high purity nitrogen for 2 hours to remove any dissolved oxygen that can act as an inhibitor. The PVDF membranes were immersed into the monomer solution for 2 min and quickly placed between two teflon plates that were subsequently clamped together. The membranes immobilized in the two teflon plates were then placed into the oven at 90 ± 2 °C with nitrogen purge. The TMPTA served as the crosslinking monomer due to the trifunctional double bonds (Figure 3.3). This high branch structure offers high cross-linking density during free radical polymerization (Gabriel and Gillberg, 1993). After 4 hours, the membranes were released from teflon plates and washed in 200 mL ethanol to remove unreacted monomers. Finally, the PAA/PVDF membranes were rinsed with deionized water and kept in deionized water for nanoparticle synthesis.

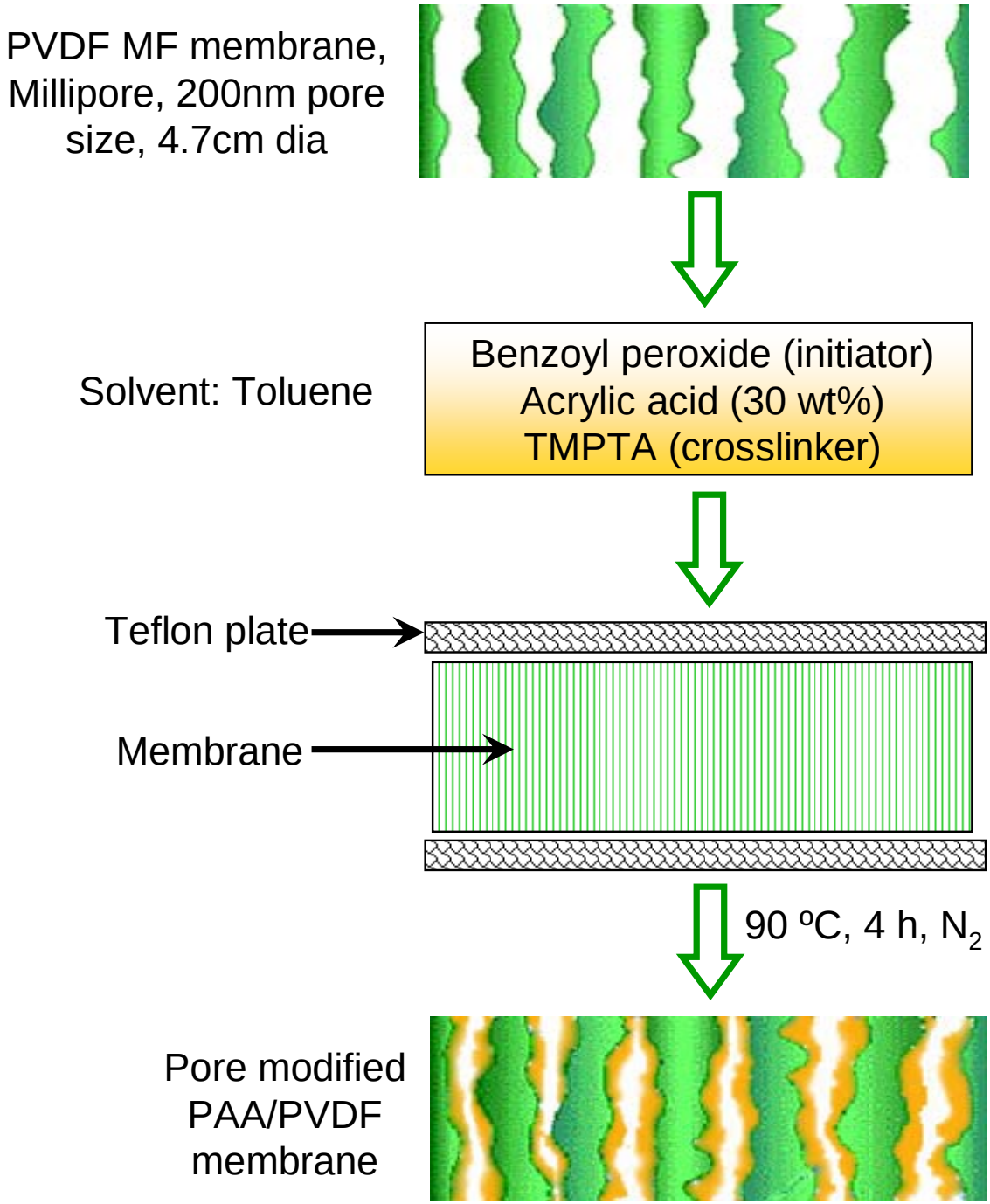

Figure 3.2 Schematic diagram of PAA functionalized PVDF MF membranes using in-situ polymerization of acrylic acid via thermal treatment (Xu and Bhattacharyya, 2007).

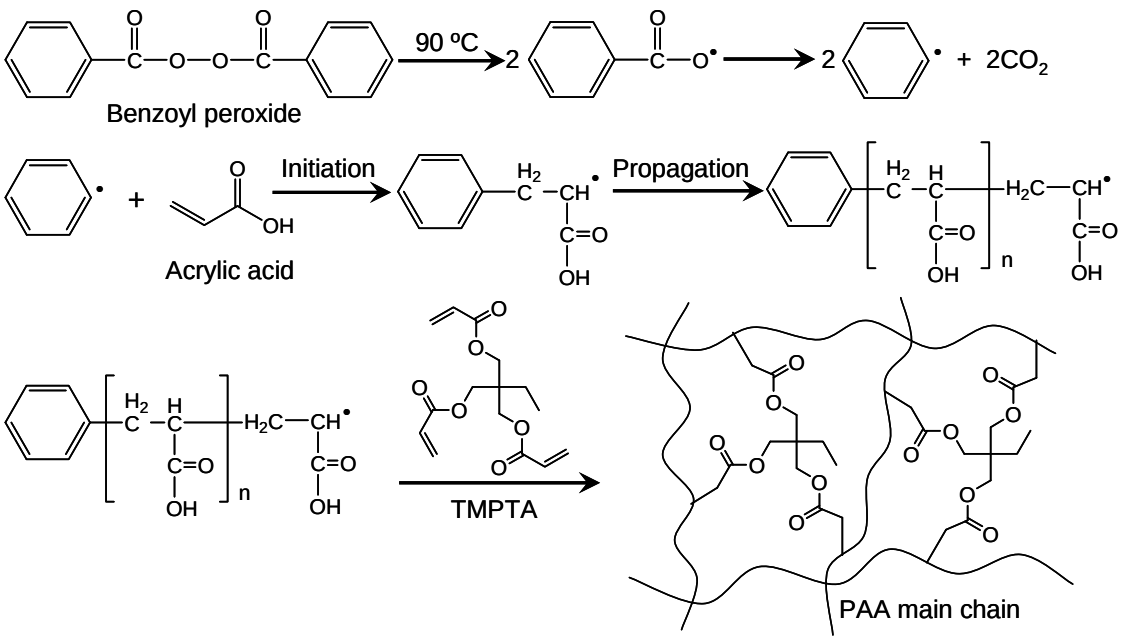

Figure 3.3 Thermal induced free radical polymerization reaction of acrylic acid using benzoyl peroxide as the initiator. PAA is cross-linked during polymerization by TMPTA (Xu and Bhattacharyya, 2007).

3.4 Bimetallic Nanoparticle Synthesis in Membrane Phase

3.4.1 Synthesis of Bimetallic Nanoparticles in PAA/PES (Dip-coating) Membranes

Figure 3.1 shows the typical procedure for the synthesis of nanoscale metal particles inside the PAA membrane domain. There are two steps involved in the procedure: (1) Crosslinked PAA/PES composite membrane preparation; (2) Reduction of metal ions inside membrane matrix. Since PAA is a water-soluble polymer, it has to be crosslinked to form network structure which is insoluble in water.

Nanoscale Fe^0 particles were prepared by soaking 5 samples (each 4.7 cm dia) of PAA/PES composite membranes in the $NaBH_4$ (0.4M) aqueous solution for 10 minutes. Fe^{2+} in the PAA layer was reduced and immobilized inside the polyelectrolyte membrane matrix which can inhibit agglomeration of newly formed Fe atoms. Excess $NaBH_4$ was used to prevent oxidation of iron particles. The membrane surface was rinsed by large amount of deoxygenated DIUF water for three times to remove the residual reactant and product.

Generally, bimetallic nanoparticles can be prepared by two different methods (Figure 3.4): post coating and simultaneous reduction. Preparation of bimetallic nanoparticle by the post coating method involves sequential formation of first and second metal. After forming the single metal (Fe) nanoparticles in the previous section, the second metal are formed and deposited on the first metal surface to form bimetallic nanoparticles. The formation of second metal can be achieved by reduction of second metal ions with first zero valent metal nanoparticles. For example, Pd^{2+} can be reduced by Fe^0 and deposited on the Fe^0 surface to from Fe/Pd nanoparticles if less than a stoichiometric amount of Pd^{2+} is used (Figure 3.4). Additional reducing agent may be required if the reduction potential energies of first and second metal are close. For example, $NaBH_4$ is usually required to reduce Ni^{2+} in the presence of Fe^0 to form Fe/Ni nanoparticles. Since the first and second metal are formed sequentially, the bimetallic nanoparticles synthesized by post coating method have the core shell structure. The first metal is in the core region and the second metal is in the shell region. The second method to prepare bimetallic nanoparticles is to reduce the two metal ions simultaneously (Figure

3.4). Since the two metals are formed at the same time, bimetallic nanoparticles have alloy structure. The first and second metal atoms are homogenously dispersed inside the whole particle. The two types of bimetallic nanoparticle structure (core-shell vs alloy) were characterized by high-resolution X-ray mapping. And the bimetallic nanoparticle structure on the catalytic reactivity will be discussed later.

Fe/Ni Nanoparticles

Bimetallic Fe/Ni nanosized particles were produced by two different methods:

(1) **Formation of Fe Nanoparticles by Reduction followed by Ni Deposition**: 5 samples of PAA/PES composite membranes containing Fe nanoparticles were immersed in 50mL $NiCl_2 \cdot 6H_2O$ (0.1 wt%, pH = 4.8) for 10 minutes (Figure 3.5A). Upon deprotonation of COOH in the PAA repeating unit, Ni^{2+} was picked up by PAA layer and immobilized on the top of membrane surface. Subsequent immersion of the membrane into the same $NaBH_4$ aqueous solutions (0.4 M) again for 5 minutes results in nickel precipitation on the iron surface to form Fe/Ni bimetallic nanoparticles by the electroless metal plating process (Delaunois et al., 2001). In order to quantify metal content inside the PAA/PES composite membrane, a Varian SpectrAA 220 Fast Sequential atomic adsorption spectrometer equipped with a Fisher Scientific data coded hollow cathode lamp was used to do soluble metal analysis by immersing one PAA/PES membrane containing Fe/Ni particles into 40 mL sulfuric acid (1N) for an hour. It was observed that the color of membrane changed from black to white, while the color of sulfuric acid solution changed form white to light-brown, suggesting that iron and nickel nanoparticles were dissolved in the sulfuric acid. Based on the AA analyses, each 4.7 cm dia PAA/PES membrane contained 7.2mg Fe and 1.8mg Ni nanoparticles (Fe: Ni = 4:1). According to known sample analysis each time, the maximum error for AA was determined to be 5%.

(2) **Simultaneous Reduction of Fe^{2+} and Ni^{2+} in Membrane**: By adding $NiCl_2 \cdot 6H_2O$ (2.4wt %) as the precursor of Ni nanoparticles into the PAA coating layer solution, Fe/Ni particles can be produced simultaneously (Figure 3.5B) from $NaBH_4$ reduction with the membrane containing both iron and nickel ions (Fe: Ni=4:1). Based on

the AA analyses, each PAA/PES membrane contains 9 mg metal nanoparticles (Fe: Ni = 4:1).

After reduction, both membranes were rinsed by large amount of deoxygenated DIUF water and then dried at room temperature for further dechlorination experiments. As shown in Figure 3.5B, reducing Fe and Ni simultaneously by sodium borohydride could cause the formation of iron and nickel particles in separate domain. However, reducing Ni^{2+} with $NaBH_4$ after iron particles are present in the membrane matrix causes the deposition of Ni on the surface of iron particles, which forms nickel-coated iron particles (Carpenter et al., 2003). In this case, iron should be ideally covered by Ni, which will be proven by the particle characterization and dechlorination results.

1. Post coating of second metal (Core-shell structure)

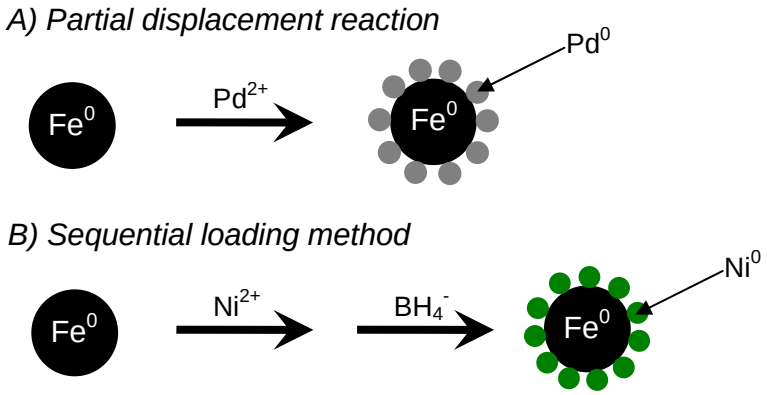

2. Simultaneous reduction of two metal ions (Alloy structure)

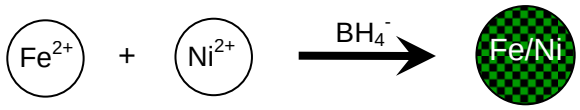

Figure 3.4 Schematic diagram for bimetallic nanoparticle synthesis

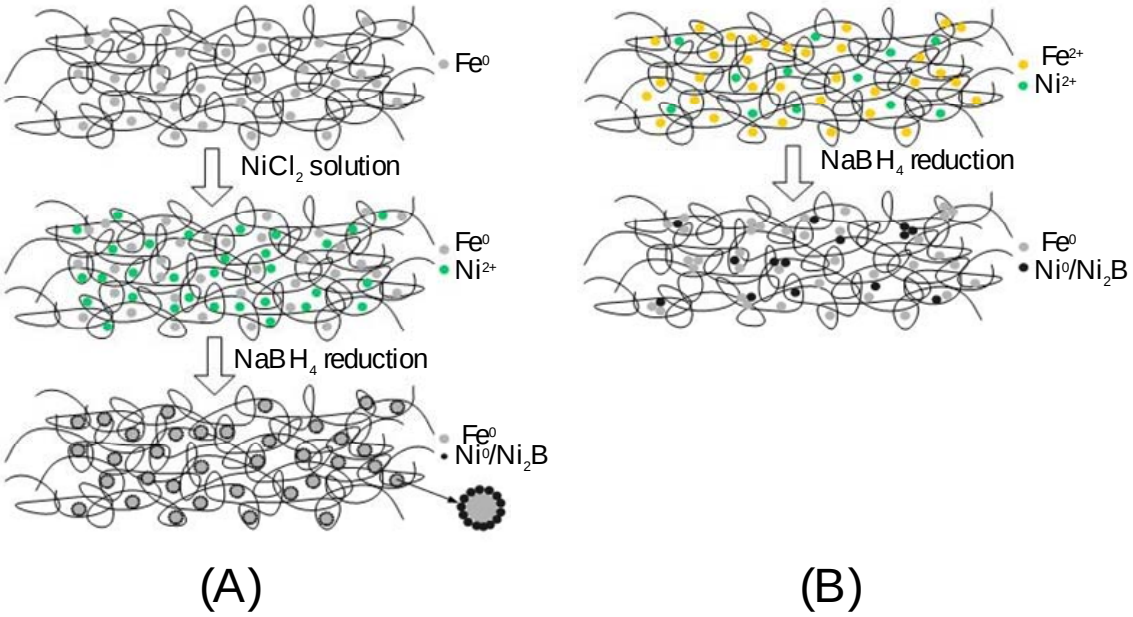

Figure 3.5 Schematic of diagram for synthesis of nanoscale Fe/Ni particles inside PAA membrane domain (A) Reducing Fe particles followed by Ni deposition; (B) Simultaneous reduction of Fe and Ni salts.

Fe/Pd Nanoparticles

Fe/Pd bimetallic nanoparticles were prepared by soaking 5 samples of PAA/PES membranes immobilized with Fe nanoparticles in a 50 mL ethanol solution containing 0.1 wt% palladium acetate ($[Pd(C_2H_3O_2)_2]_3$). Pd^{2+} was reduced to Pd^0 by Fe^0 and subsequently deposited on the Fe surface (Zhang et al., 1998; Lien and Zhang, 2001). By AA analyses and using Pd mass balance the calculation showed that 4 mg of Pd was deposited on 36 mg of nanoscale iron particles (Fe: Pd = 9:1) in each 4.7 cm membrane.

3.4.2 Synthesis of Bimetallic Nanoparticles in PAA/PVDF (Dip-coating) Membranes.

Fe^0 nanoparticles were prepared by soaking 10 samples (each 4.7 cm dia) of PAA/PVDF composite membranes containing Fe^{2+} in 200 ml 0.5 M $NaBH_4$ aqueous solution for 10 minutes. Fe^{2+} in the PAA layer was reduced and immobilized inside the polyelectrolyte membrane matrix. Ten samples of PAA/PVDF composite membranes containing Fe^0 nanoparticles were immersed in 100 mL $NiSO_4 \cdot 6H_2O$ (0.07 wt %, pH = 4.8) for 10 minutes. Upon deprotonation of COOH in the PAA repeating unit, Ni^{2+} was adsorbed by PAA. Subsequent immersion of the membrane into the same $NaBH_4$ aqueous solutions (0.5 M) again for 5 minutes results in nickel precipitation on the iron surface to form Fe/Ni nanoparticles.

Fe/Ni alloy nanoparticles were synthesized in PAA/PVDF Membrane by adding $NiSO_4 \cdot 6H_2O$ (2.5 wt %) as the precursor of Ni nanoparticles into the PAA coating layer solution, Fe/Ni particles can be produced simultaneously from $NaBH_4$ (0.5 M) reduction with the membrane containing both iron and nickel ions.

Fe/Pd nanoparticles were prepared by soaking 5 samples of PAA/PVDF membranes containing Fe nanoparticles in a 50 ml ethanol solution containing 0.015 wt % of palladium acetate ($[Pd\ (C_2H_3O_2)_2]_3$). Pd^{2+} was reduced to Pd^0 by Fe^0 and subsequently deposited on the Fe surface. The Fe and Pd content inside the membrane was also determined by soluble metal analysis in AA.

3.4.3 Synthesis of Fe/Pd Nanoparticles in Pore Modified PAA/PVDF Membranes

The flowchart for the membrane supported nanoparticle synthesis is described in Figure 3.6. Briefly, the ferrous ions were first loaded into membranes by ion exchange, and Fe nanoparticles were formed followed by reduction of Fe^{2+} with $NaBH_4$. Prior to the ion exchange, the PAA/PVDF membrane (4.7 cm in dia) was soaked in 100 mL sodium hydroxide (0.1 M) overnight (12~14 h) to convert PAA from hydrogen form (–COOH) to the sodium form (–COONa). After the excess sodium hydroxide was rinsed from the membrane with deionized water, the membrane was shaken in 100 mL deoxygenated solution of ferrous chloride (5.5 mM) at pH 4.8~5 with nitrogen purge for 12 h. During this process, the ferrous ions were bound with PAA in the membrane by ion exchange with Na^+. The membrane was then washed with deoxygenated deionized water.

Subsequent immersion into 200 mL solution of sodium borohydride (0.07 M) yielded Fe nanoparticles embedded in the PAA/PVDF membrane. It has been found in the literature that boron is present at ~ 4 wt % as FeB in the iron nanoparticles when Fe^{2+} is reduced by $NaBH_4$ (Liu et al., 2005). The boron and iron contents were determined by digesting the nanoparticles in 25 wt % nitric acid solution and measuring the dissolved Fe and B concentration through inductively coupled plasma atomic emission spectroscopy (ICP-AES). After rinsing with deoxygenated deionized water and ethanol sequentially, the membrane supported iron nanoparticles were soaked into 50 mL solution (90/10 vol.% ethanol/water) of K_2PdCl_4 (0.12 mM) for 30 min. This resulted in the deposition of Pd on the Fe surface through the following redox reaction (He and Zhao, 2005):

$$Pd^{2+} + Fe^0 \rightarrow Fe^{2+} + Pd^0 \quad (1)$$

Due to the high reactivity of Fe nanoparticles, 90 vol.% ethanol were used to minimize the Fe corrosion reaction and other side reactions. After rinsing with ethanol three times, the prepared Fe/Pd nanoparticles in PAA/PVDF membrane were stored in ethanol solution for further dechlorination study. The Pd deposition content was also determined by digestion of nanoparticles in 25 wt % nitric acid and followed by ICP-AES analysis. Different Pd loading Fe/Pd nanoparticles in PAA/PVDF membrane were prepared using various K_2PdCl_4 (0.012 mM ~ 0.2 mM) solutions to investigate the effect of Pd deposition content.

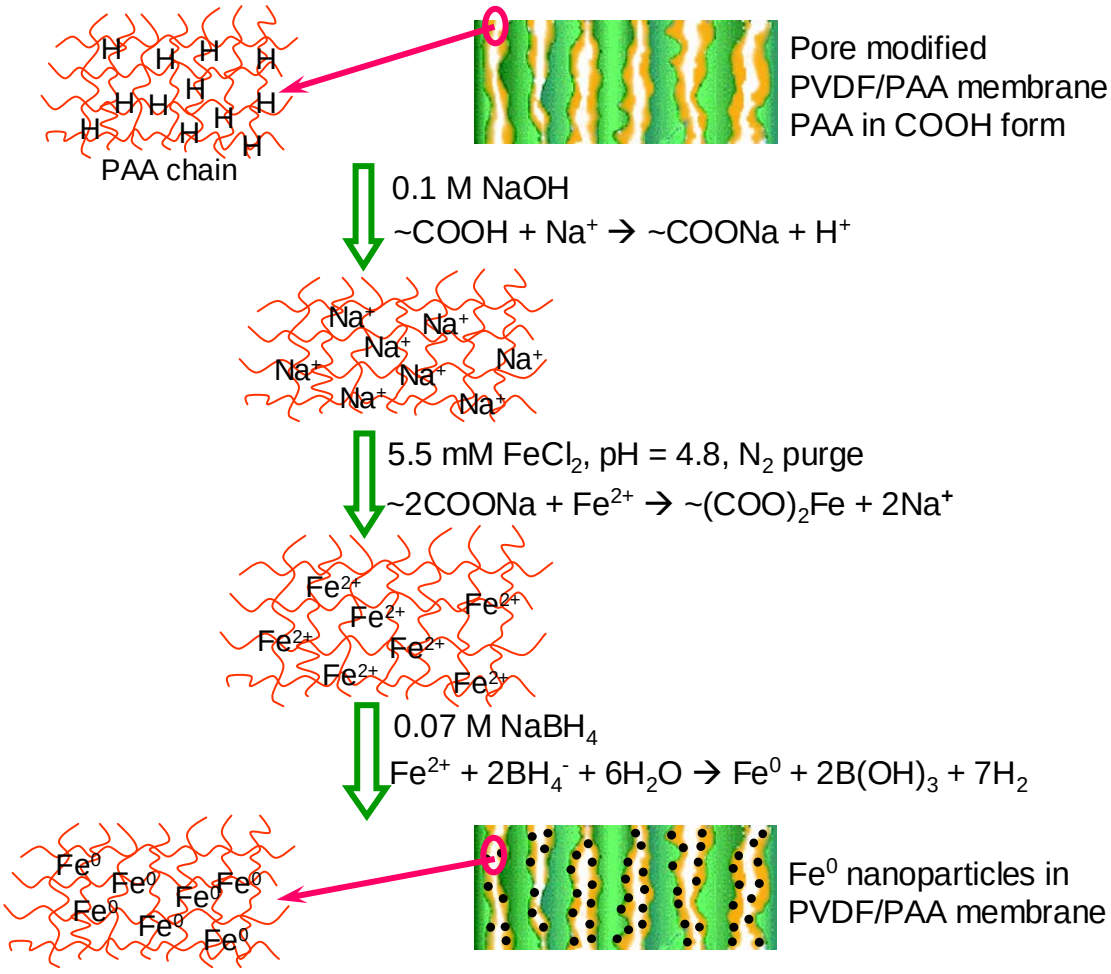

Figure 3.6 Schematic diagram of iron nanoparticles synthesized in pore modified PAA/PVDF membranes (Xu and Bhattacharyya, 2007)

3.5 Solution Phase Synthesis

Solution phase (no membrane) synthesis of Fe/Ni Particles was also prepared for comparison purposes. The procedure consisted of dissolving 3.63 g $FeCl_2 \cdot 4H_2O$ and 1.0 g $NiCl_2 \cdot 6H_2O$ in 50 mL deoxygenated DIUF water. After adding 3 g $NaBH_4$ into the solution, the metal salts were reduced to black particles. Fe/Ni particles were washed by deoxygenated DIUF water, and then rinsed by ethanol and acetone to remove residual water. The particles were finally dried at room for further dechlorination experiments.

Commercial Fe particles were used for Ni and Pd coating in order to compare results with nanoparticle system. Iron particles (~120 μm, from Fisher Scientific) were washed with 1M HCl and then rinsed with deoxygenated deionized water and ethanol sequentially. Aqueous solutions of $NiSO_4$ and K_2PdCl_4 were prepared by deoxygenated deionized water (pH = 2) and used respectively to deposit Ni and Pd on the iron particle surface. The Fe/Ni and Fe/Pd particles were then rinsed with deoxygenated deionized water and ethanol sequentially. The rinsed Fe/Ni and Fe/Pd particles were stored in ethanol solution for the dechlorination study. The Pd and Ni coverage was also determined by digestion in 25 wt% nitric acid and followed by ICP-AES analysis.

3.6 Characterization of Membranes and Fe/Pd Nanoparticles

Surface and cross sections of membranes containing metal nanoparticles were examined using the Hitachi S-900 Scanning Electron Microscope (SEM). A Hitachi S-3200 SEM equipped with an energy dispersive spectrometer (EDS) was also used to obtain information regarding the elements present in the nanoparticles. The EDS was operated under high vacuum conditions (20kV voltage) where an electron beam was focused on the particles. Membranes were coated with gold and palladium for imaging purposes. In the case of cross-sectional images, membranes were freeze-fractured under liquid N_2 prior to sputter coating with gold and palladium.

The structure and composition of the nanoscale metal particles were also studied at nano scales using bright field transmission electron microscopy (TEM), EDS, and dark field scanning transmission electron microscopy (STEM). A JEOL 2010F with a field

emission gun (FEG) and accelerating voltage of 200 kV was employed. EDS Line profile analysis was performed to study the Fe and Ni compositions in the nano domain. In the EDS line profile analysis, the electron beam was scanned along a designated line across the sample while x-rays were detected for discrete positions along the line. The analysis of the x-ray energy spectrum at each position provided plots of the relative elemental concentration versus position along the line. This type of analysis was performed with the microscope operating in STEM mode. The computer control and data acquisition system used is the Emispec EsVision. One 0.5 nm spot was used to provide a strong x-ray signal. Typically 20 to 30 steps were taken along each profile with a range of 14 to 27 nm. The step size was chosen to be smaller than any observable feature. The dwell time chosen was ten seconds. This provided high quality and low noise x-ray spectra. When the Fe and Ni profiles were computed, full width half max (FWHM) integration windows were chosen about the K alpha peaks to maximize the signal to noise ratio.

STEM-EDS mapping was utilized to image the elemental distribution inside the membrane matrix. The size of the focused electron beam was about 0.5 nm in diameter. The X-rays induced by the electron beam from the specimen were detected simultaneously with the scanning of the electron beam and form EDS mapping images of selected elements. The dwelling time was chosen as 500 ms. The tilt angle was increased to 15 degrees which significantly increased our count rate.

To obtain a thin film for TEM imaging, the membrane sample containing metal nanoparticles was prepared by the same procedure in the particle synthesis step except that a minute droplet of PAA was dropped and coated directly on a gold TEM grid (200 Mesh Square) instead of the PES or PVDF support membrane. For bimetallic nanoparticle synthesized in pore modified PAA/PVDF membranes, the membrane samples for TEM observation were prepared by ultra sectioning into about 50 nm thickness slices using a conventional microtome technique with a diamond knife. The cut slices were loaded on a copper TEM grid coated with lacey carbon film.

The thermal stability of the pore modified PAA/PVDF membranes was examined using a TGA 2050 thermogravimetric analyzer (TA Instrument, USA). About 15 mg sample was used. The scanning temperature range for the TG analysis was between 25 and 1000 °C with the heating rate of 10 °C/min under nitrogen atmosphere.

The Fourier transform infrared (FT-IR) spectra of the pore modified PAA/PVDF membranes were obtained on a Nicolet Magna IR 860 Instrument in the range of 4000-500 cm^{-1}.

3.7 Dechlorination Reactions

Bimetallic Nanoparticles in PES Membranes Dip-coated with PAA

Batch experiments for dechlorination of trichloroethylene (TCE) with Fe/Ni nanoparticles in PAA/PES membranes were conducted in 42 mL serum glass vials. In each batch vial, 45 mg metal particles (Fe/Ni) at the mass ratio of 4:1 immobilized on 5 samples of membranes were loaded into the vial containing 40 mL 10±1 mg/L TCE and 2-mL headspace. The serum glass vials were sealed with Teflon-lined silicon septa and placed on a wrist-action shaker throughout the duration of the experiment. Parallel blank experiments without membranes and metal particles, and control experiments with only PES support membrane were also performed. For comparison, experiments were also conducted with the nanoscale Fe/Ni particles produced directly in the solution, and membrane-based nanoscale Fe/Pd particles (40 mg/40 mL, Fe: Pd=9:1).

Bimetallic Nanoparticles in PVDF Membranes Dip-coated with PAA

The reactivity of bimetallic nanoparticles synthesized in PAA/PVDF membranes was studied towards dechlorination with 2, 2'-Dichlorobiphenyl (PCB4) and TCE. Batch experiments for dechlorination of PCB4 and TCE were both conducted in 24.5 ml serum glass vials. For dechlorination of PCB4, 22 mg Fe/Pd nanoparticles (Pd=1 wt %) immobilized in 4 samples of PAA/PVDF membranes were loaded into the vial containing 8.1 mg/L PCB4 in 20 ml of 50/50 vol.% ethanol/water. For TCE dechlorination, 8 mg of Fe/Ni nanoparticles immobilized in 2 samples of PAA/PVDF membranes were loaded into the vial containing 20 mg l^{-1} TCE in 20 ml deoxygenated water. All the serum glass vials were sealed with Teflon-lined silicon septa and placed on a wrist-action shaker

throughout the duration of the experiment. Parallel control experiments with only support membrane (no metal particles) were also performed.

Fe/Pd Nanoparticles in Pore Modified PAA/PVDF Membranes

The reactivity of Fe/Pd nanoparticles prepared in pore modified PAA/PVDF membranes were investigated towards dechlorination of 2, 2'-dichlorobiphenyl. Batch experiments for dechlorination of 2, 2'-dichlorobiphenyl (PCB4), 3,3',4,4'-tetrachlorobiphenyl (PCB77), 2,3,2',5'- tetrachlorobiphenyl (PCB44). The batch dechlorination reaction was conducted in 24.5-mL serum glass vials. In each batch vial, one piece of PAA/PVDF membrane (47cm in dia) embedded with 16 mg Fe/Pd nanoparticles was loaded into 20 ml solution of PCBs. All the serum glass vials were sealed with teflon-lined silicon septa and placed on a wrist-action shaker throughout the duration of the experiment. At predetermined time intervals, a 2-mL aqueous solution was withdrawn from the selected reaction vial and transferred to a 4-mL vial containing 2-mL hexane for the extraction of PCBs. After removing all the residual solution, 10 ml hexane was added into the reaction vial for membrane phase extraction. The 4-ml and reaction vials were both placed on a wrist-action shaker and mixed for 2 hours to achieve extraction equilibrium. Duplicated experiments were conducted at each sampling time. Some experiments were also conducted in convective flow (0.5-5 bar pressure)

3.8 Analytical Methods

3.8.1 TCE Analysis

TCE analysis was performed using a gas chromatography (GC, Varian-3900) equipped with an ion-trap mass spectrometry (MS, Saturn-2100T). A Tekmar-Dohrmann 3100 purge-and-trap (PT) with the autosampler (Varian Archon) was coupled to the GC/MS and used for direct organic analysis of the aqueous phase (50 $\mu g\ l^{-1}$ 1,4-difluorobenzene was used as the internal standard). External haloethanes mixture standards containing 200 mg/L TCE, cis-DCE, tans-DCE and 1, 1-DCE in methanol (Ultra Scientific) were used to prepare calibration curves (Concentration range: 25-500

μg l^{-1}). According to known sample analysis each time, the maximum error was determined to be less than 15%.

3.8.2 Ethane and Ethylene Analysis

Hydrocarbon products for TCE dechlorination experiments in the headspace were measured by GC (HP 5890)/MS (Series 6150) equipped with a cryo-cooling system using liquid CO_2 as the coolant. External standards of ethane, ethylene (Scott Specialty Gas, 1% in N_2) were used to prepare calibration curves. According to known sample analysis each time, the maximum error for both ethane and ethylene was determined to be less than 15%.

3.8.3 PCBs Analysis

The concentration of PCB44, PCB18, PCB16, PCB4, PCB1, and biphenyl were measured by gas chromatography (GC: Varian-2800) equipped with mass spectrometry (MS: Varian-6100). For each 24.5 ml experimental sample vial, 4 ml of hexane as the extractant for PCBs was added to an 8 ml vial containing 4 ml of aqueous solution which was removed from the reaction vial. After removing all the residual solution, 10 ml hexane was added into the reaction vial for membrane phase extraction. The 8-ml and reaction vials were both placed on a wrist-action shaker and mixed for 2 hours to achieve extraction equilibrium. From each extraction vial, a 1 ml aliquot of the extraction solvent layer was transferred to a 1 ml GC autosampler vial for analysis using GC/MS. Ten microliters of naphthalene (5000 mg/L in methyl chloride) was added into the GC sample vial as an internal standard. External standards of PCB44, PCB18, PCB16, PCB4, PCB1, and biphenyl in hexane (Ultra Scientific) were used to prepare calibration curves. The calibration curves were linear over the concentration range of 0.5-20 mg l^{-1} (($R^2 > 0.999$, regressions were based on the 7-point calibration). According to known sample analysis each time, the maximum error was determined to be less than 10%. The detection limit for all the PCBs was 0.1 mg L^{-1}.

PCB77 and degradation products were analyzed by gas chromatography (GC: Agilent-6890) equipped with an inert mass selective detector (MSD: Agilent-5975). analysis for PCB77 dechlorination experiments were conducted by transferring 100 µl aliquot of the extraction solvent to a 100-µl glass insert with a polymer bottom spring in a 1-mL GC autosampler vial for. Ten microliters of decachlorobiphenyl (PCB209) (1 mg L^{-1} in hexane) were added into the 100-µl glass inert as the internal standard (IS). External standards of 3,3',4,4'-tetrachlorobiphenyl (PCB77), 3,4,4'-trichlorobiphenyl (PCB37), 3,3',4-trichlorobiphenyl (PCB35), 4,4'-dichlorobiphenyl (PCB15), 3,4'-dichlorobiphenyl (PCB13), 3,4-dichlorobiphenyl (PCB12), 3,3'-dichlorobiphenyl (PCB11), 4-chlorobiphenyl (PCB3), 3-chlorobiphenyl (PCB2) and biphenyl in hexane were used to prepare calibration curves. The calibration curves for all PCBs analyzed were linear over the concentration range of 0.1~5 mg L^{-1} ($R^2 > 0.999$, regressions were based on the 7-point calibration). It should be noted that PCB12 and PCB13 were unresolved under the chromatographic conditions. PCB12 and PCB13 were analyzed together as the total amount. The detection limit for all the PCBs was 0.1 mg L^{-1}. According to known sample analysis each time, the maximum error was determined to be less than 10%.

3.8.4 Hydrogen Analysis

Analysis of hydrogen gas generated from the corrosion of iron reaction during the dechlorination reaction with bimetallic nanoparticles was conducted using a GC (Agilent 6890N , Carboxen 1004 micropacked column from Supelco Inc.) equipped with a thermal conductivity detector (TCD). The GC System interfaced with ChemStations software. The temperature program used was: One min holding at 50 °C followed by a ramping rate of 5 °C /min to 120 °C and remained at 120 °C for another minute (Tee 2006). Ultra high purity argon was used as the carrier gas. External standard hydrogen gas (1 mol% H_2 in N_2, analytical accuracy: ±0.02 %) from Scott Specialty was used to prepare the calibration curve. The calibration curves were linear over the concentration range of 1.15 ~ 5.73 mini mole ($R^2 = 0.994$, regressions were based on the 5-point calibration). A Hamilton air-tight lock syringe was used to withdraw 0.1 ~ 1 ml of headspace volume

from the reaction vials and injected directly to the manual injection port. The total mole of hydrogen generated was correlated with a five-point calibration curve. Based on the known sample analysis each time, the maximum error was less than 15%.

3.8.5 Chloride Analysis

The concentration of chloride ion in the aqueous solution was determined by ion chromatograph (Dionex ICS-2500, column: Ionpac AS18, eluent: KOH, current: 100 mA, flow: 0.95 mL/min) with a conductivity detector. Based on the known sample analysis each time, the maximum error was less than 5%.

3.8.6 Metal Ions Analysis

All the concentrations of metal ions (iron, sodium, palladium, boron) were quantified by ICP-AES (Varian: VISTA-PRO). In all cases, the instrument calibration was based on commercial standards (Fisher Scientific) containing 1000 mg L^{-1} of the desired metal serially diluted with 5% nitric acid. Yttrium chloride (1 mg L^{-1}) was used as the internal standard. Based on the known sample analysis each time, the maximum error for all the elements was less than 8%. The batch TCE dechlorination solution used for the analysis of iron and nickel ions by AA was first passed through a Millipore regenerated cellulose ultrafiltration membrane (Ultracel Amicon YM10, MWCO 10,000).

3.8.7 TOC Analysis

Neutral dextran (MW 144,000; 482,000; 670,000; 1,400,000; 2,000,000) rejection was monitored via total organic carbon (TOC) measurements of the feed and permeate solutions (experimental error <2%) to determined the effective pore size of pore modified PAA/PVDF membranes.

Chapter 4 Results and Discussions

4.1 Introduction

This chapter includes results and discussions for reductive dechlorination using various bimetallic nanoparticles immobilized in different PAA functionalized membrane matrix. The first area discussed is the scientific reasons for using membrane supported bimetallic nanoparticles in the degradation of chlorinated organics. Next, the membrane functionalization by PAA was characterized using SEM, permeation, thermal analysis, dextran rejection, and STEM mapping. The successful PAA functionalization and characterization is necessary for the metal capture and subsequent nanoparticle synthesis. The binding interaction between PAA and ferrous ions was studied by EDS and STEM mapping to understand the role of PAA in stabilizing nanoparticles and controlling the particle size. The bimetallic nanoparticles were then characterized by SEM, TEM, STEM, and HRTEM. This gives important information of nanoparticle distribution, size and structure, which can be further correlated with reaction kinetics. Extensive experimental results of TCE and PCB dechlorination were present to understand and quantify reductive dechlorination mechanism, the composition of second dopant metal (Pd or Ni), role of water, particle size (nano size versus bulk size) and temperature effect in the catalytic reactivity. The dechlorination reaction rates are evaluated in terms of surface normalized rate (k_{SA}) to compare the reactivity of various bimetallic nanoparticles. Normalizing the variation of k_{SA} as a function of dopant metal content was performed to understand the reaction mechanism and quantify the role of the dopant metal. Finally, a steady state two-dimensional reactor model was developed to describe the reaction inside the membrane pores.

4.2 Bimetallic Nanoparticles in Functionalized Membranes: Reasons and Advantages:

As discussed previously in the background, the aqueous phase synthesis results in the agglomeration and aggregation of nanoparticles, which can greatly reduce the specific area and particle reactivity. The agglomeration is more intense for iron atoms due to the strong magnetic interactions. Various stabilizers such as polymers and surfactants have been successfully used to prevent nanoparticles (Au, Ag, and Pd) from agglomerations in solvent phase. But not all these stabilizers are suitable for environmental applications. And some stabilizers may not function properly in the aqueous phase. The iron nanoparticle protected by the stabilizer in aqueous phase may tend to aggregate again at the dry state.

Immobilization of nanoparticles in solid supports provides another approach for nanoparticle stabilization. Much attention have been given to the preparation of metal nanoparticles embedded in thin and dense films or gels by a stepwise approach of ion-exchange/reduction (Ikeda et al., 2004; He et al., 2002 and 2003; Pivin et al., 2006; Damle et al., 2001). In this method, ion-exchange ligands created in the thin films can bind metal cations from aqueous solution. Post reduction or precipitation produces nanoparticles from bound metal cation precursors. The advantage of this process is the controllable nanostructure properties during nanoparticle synthesis by utilizing these ion exchange ligands. The nanostructure properties include the particle size and distribution, particle concentration and interparticle spacing. However, the accessibility of the nanoparticles may be limited due to the dense structure of the solid support. The chlorinated organics must diffuse through the dense film before they can be adsorbed on the nanoparticle surface. Thus, the use of open structured supports such as MF or UF membranes containing functional ion-exchange groups provides an ideal approach for ordered and stable nanoparticle formation as well as the highly effective dechlorination technique. The diffusion limitation can be avoided by applying convective flow. Furthermore, the membrane supports functionalized with ion exchange groups have the capability of capturing dissolved metal ions (Fe^{2+}, Fe^{3+}, Ni^{2+}). The recaptured metal ions by membranes can be subsequently regenerated using $NaBH_4$.

4.3 Membrane Characterization

As discussed in the experimental section, there are two types of methods used in this study to functionalize MF membranes (PES, PVDF) with PAA: (1) PAA dip-coating; (2) in-situ polymerization of acrylic acid inside membrane pores (pore-filled PAA/PVDF membranes).

4.3.1 PES/PVDF Membranes Dip-coated with PAA

Degree of PAA Cross-linking

The degree of PAA cross-linking was determined by the entrapment capacity of Ca^{2+} by free carboxylic group in PAA. Table 4.1 shows the sorption of Ca^{2+} by uncross-linked and cross-linked PAA. For uncross-linked PAA, the molar ratio of entrapped Ca^{2+} to the COOH was 0.124. This ratio decreased to 0.049 in the cross-linked PAA due to the loss of free carboxylic groups. Theoretically, 50% of carboxylic group in PAA should have been cross-linked with ethylene glycol according to the molar ratio of 0.5 (OH: COOH). Because of the cross-link of PAA chains, however, some free carboxylic groups may be far enough not to capture calcium ions, which explain that less than 50% free carboxylic groups of cross-linked PAA can pick up Ca^{2+} in the Table 4.1.

Membrane Permeability

Table 4.2 shows the pure water flux in the PES support membrane and cross-linked PAA/PES membrane with iron and nickel nanoparticles. After the PES support membrane was coated with cross-linked PAA and nanoparticles, the membrane permeability (A) was found to decrease significantly from the initial value of 77×10^{-4} cm^3 cm^{-2} bar^{-1} s^{-1} to 3.03×10^{-4} cm^3 cm^{-2} bar^{-1} s^{-1} for cross-linked PAA composite membrane and to the final value of 0.27 cm^3 cm^{-2} bar^{-1} s^{-1}. Obviously, the permeation flux decline was attributed to the resistance from PAA coating layer and the nanoparticles

immobilized inside the membrane-pore matrix which could significantly decrease membrane pore size as well as membrane porosity.

Table 4.1 The interaction between free and cross-linked PAA with Ca^{2+} at pH 5.0

	Initial Ca^{2+} (mM)	Repeat unit of PAA (mM)	Captured Ca^{2+}(mM)	Ca^{2+}/(repeat unit) molar ratio	Degree of cross-link
Uncross-linked PAA[a]	0.450	0.94	0.117	0.124	-
Cross-linked PAA[b]	0.373	0.50	0.0247	0.0494	60%

a. 0.0677g PAA (MW 50,000) was added in 50 ml 363 mg/L $CaCl_2$ solution and mixed for 60 minutes. The solution was filtered by a Millipore centrifuge membrane cell (MWCO 10,000) for the free Ca^{2+} analysis with AA. **b.** 0.0362g PAA (MW 50,000) was cross-linked by 0.0078g EG (OH/COOH molar ratio is 0.5) to form PAA/PES composite membrane. The membrane was mixed with 373 mg/L $CaCl_2$ solution. Free Ca^{2+} in the solution was measure by Atomic Adsorption (AA).

Table 4.2 Pure water Permeability (10^4) (cm^3 cm^{-2} bar^{-1} s^{-1})

	Permeability (10^4)(cm^3 cm^{-2} bar^{-1} s^{-1})
PES Support Membrane	76.9
PAA/PES Membrane	3.03
PAA/PES Membrane with Fe/Ni Nanoparticles (2 wt% metal loading)	0.27

4.3.2 Pore-Filled PAA/PVDF Membranes

Figure 4.1 compares the SEM surface images of the unmodified PVDF support membrane and the PAA functionalized PVDF membrane in the dry state. The PVDF MF support membrane (Figure 4.1a) shows a highly porous microstructure. The pores are mostly circular in shape but highly non-uniform in size (0.2~2 μm). As expected, the modified membrane shows less porosity with small number and size of pores. This indicates that PAA has been filled into the pores to create smaller pores. As can be seen in Figure 4.1b, the PVDF support is not completely covered and the pores are partially blocked after the pore modification with 30 wt % acrylic acid (AA) in toluene. It has been reported that high pore coverage can be achieved by increasing the concentration of acrylic acid (Gabriel and Gillberg, 1993). In this study, complete pore filling may not be desirable due to the high diffusion resistance for the hydrophobic chlorinated organic molecules and also for nanoparticle synthesis. Based on the studies by Gabriel and Gillberg (1993), AA concentration of 30% is sufficient to obtain a completely wettable membrane in the presence of cross-linker. The cross-section images of these membranes are shown in the Figure 4.2. By contrast, different regions of cross-sections clearly show the structure difference between PAA modified membrane and unmodified substrate membrane. As shown in the Figure 4.2c and d, the pores inside the PVDF substrate are filled with small grains, suggesting that PAA modification has taken place throughout the PVDF substrate. EDS mapping analysis of oxygen atom was also performed in the STEM mode to verify that the observed structure change was due to the PAA modification. The EDS mapping results will be discussed latter.

The chemical structure of PVDF membranes functionalized with PAA by in-situ polymerization of AA was studied using FT-IR. The FT-IR spectra of the unmodified PVDF membranes and the PAA functionalized PVDF membranes are shown in the Figure 4.3. The characteristic absorption band appeared at 1730 cm^{-1} is the ester (-COO-) bond (Rhim et al., 2004; Ying et al., 2004) which comes from the carboxylic acid group of PAA. The strong intensity of the –C=O-in the ester bond confirms the successful PAA modification. The characteristic absorption band for CF_2 of PVDF appears at 1120-1280 cm^{-1} (Ying et al., 2004).

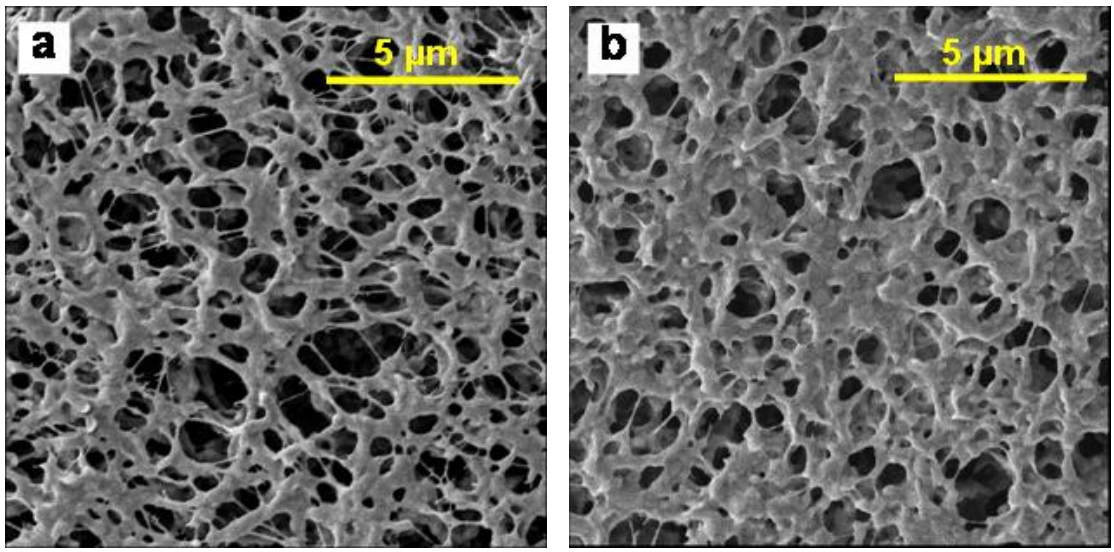

Figure 4.1 SEM images of membrane surface: (a) unmodified PVDF support membrane; (b) pore-filled PAA/PVDF membrane (Xu and Bhattacharyya, 2007)

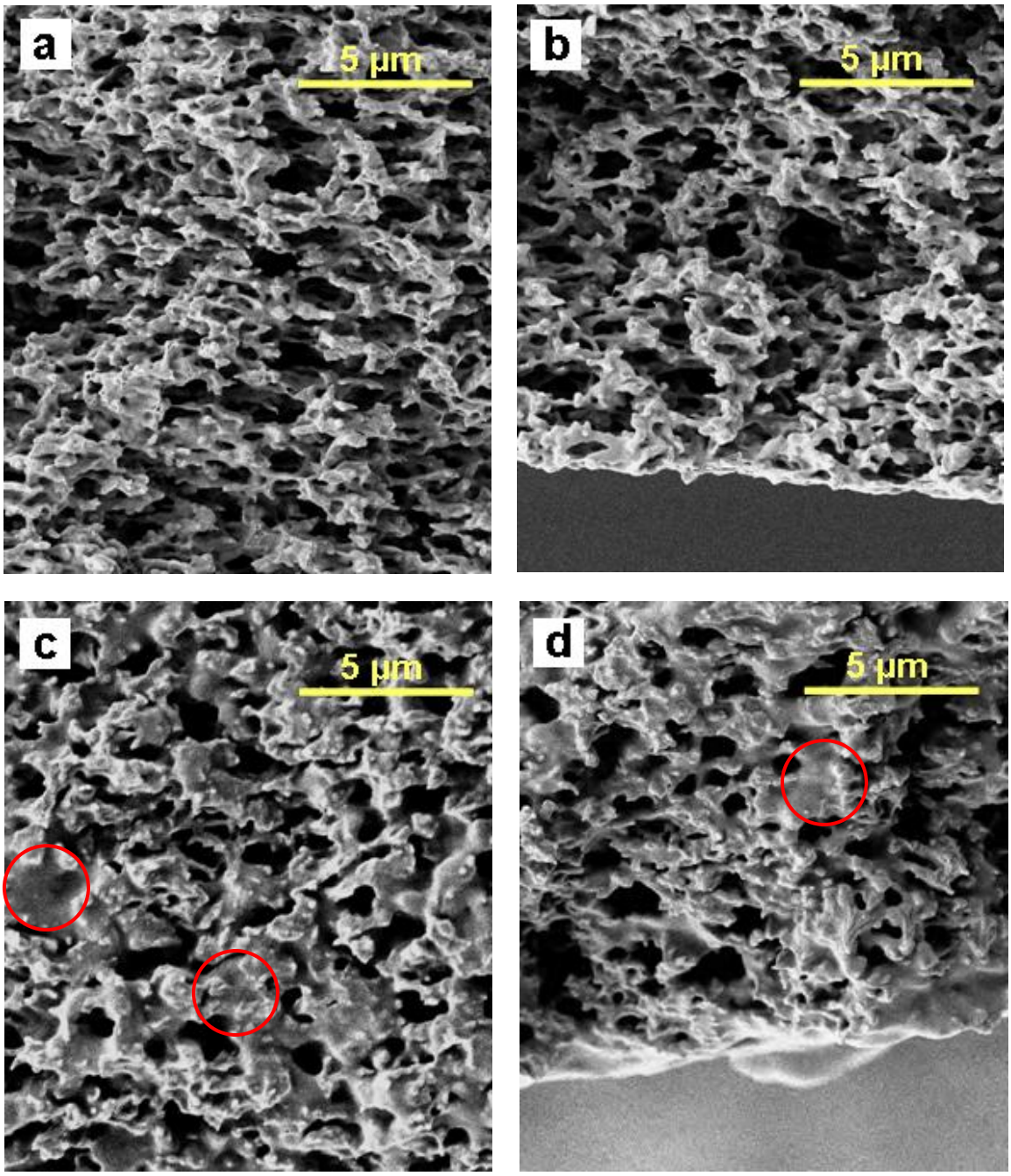

Figure 4.2 SEM images of membrane cross-sections. Unmodified PVDF support membrane: (a) middle of the cross-section; (b) bottom of the cross-section. Pore-filled PAA/PVDF membrane: (c) middle of the cross-section; (d) bottom of the cross-section. The circles in (c) and (d) represent the location of PAA.

The thermal stability of the pore-filled PAA/PVDF membranes (containing Fe/Pd nanoparticle) was investigated by TG analysis. By monitoring the sample weight change with temperature, the TG analysis can provide important information of membrane thermal stability, PAA decomposing temperature and PAA content. Figure 4.4 shows the TG analysis curves for unmodified PVDF membrane, pore-filled PAA/PVDF membrane (PAA in –COOH form), and PAA powder. The unmodified PVDF membrane only shows one-step weight loss at 455 °C which corresponds to the degradation of CF_2 chain (Ying et al., 2004). The PAA/PVDF membrane (-COOH form) exhibits a distinct three-step degradation process. The first weight loss is at the temperature range of 225~301 °C due to the formation of anhydride (Moharram and Khafagi, 2006). The second weight loss is observed at the temperature range from 301~441 °C corresponding to further decomposition of polyacrylic anhydride (Moharram and Khafagi, 2006). The last weight loss occurs over the temperature at 455 °C, which is attributed to the decomposition of PVDF side chains.

4.3.3 Membrane Permeability

The pure water flux through the PVDF membrane before and after membrane modification is shown in Figure 4.5 and Figure 4.6. By comparing Figure 4.5 and Figure 4.6, the membrane permeability decreased significantly from initial value of 127×10^{-4} cm^3 cm^{-2} bar^{-1} s^{-1} to 3.03×10^{-4} cm^3 cm^{-2} bar^{-1} s^{-1} for the membrane after PAA functionalization and nanoparticles immobilization. The flux drop is expected due to the presence of PAA chains inside the pores, which significantly reduces the effective pore size and the porosity. Since PAA is a highly hydrophilic polymer, it can greatly absorb water and create a highly swelling layer within the pores to decrease the flux.

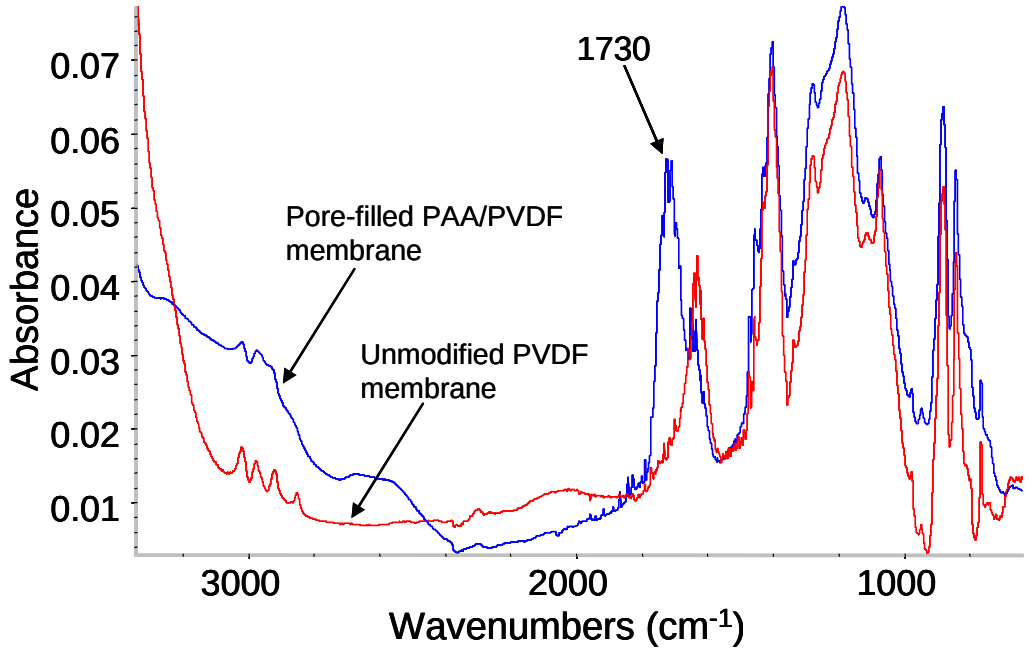

Figure 4.3 FT-IR spectra of unmodified PVDF membrane and pore-filled PAA/PVDF membrane.

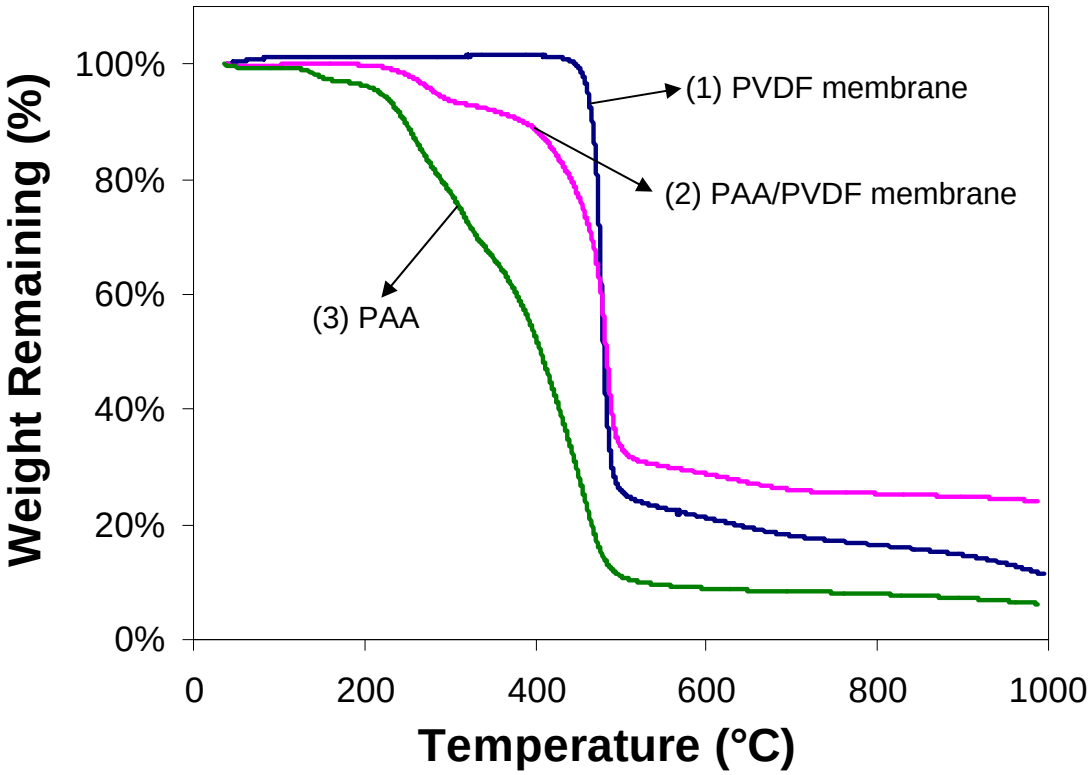

Figure 4.4 TG analysis curves of (1) unmodified PVDF membrane, (2) pore-filled PAA/PVDF membrane, (3) PAA. The heating rate is 10 °C per minute.

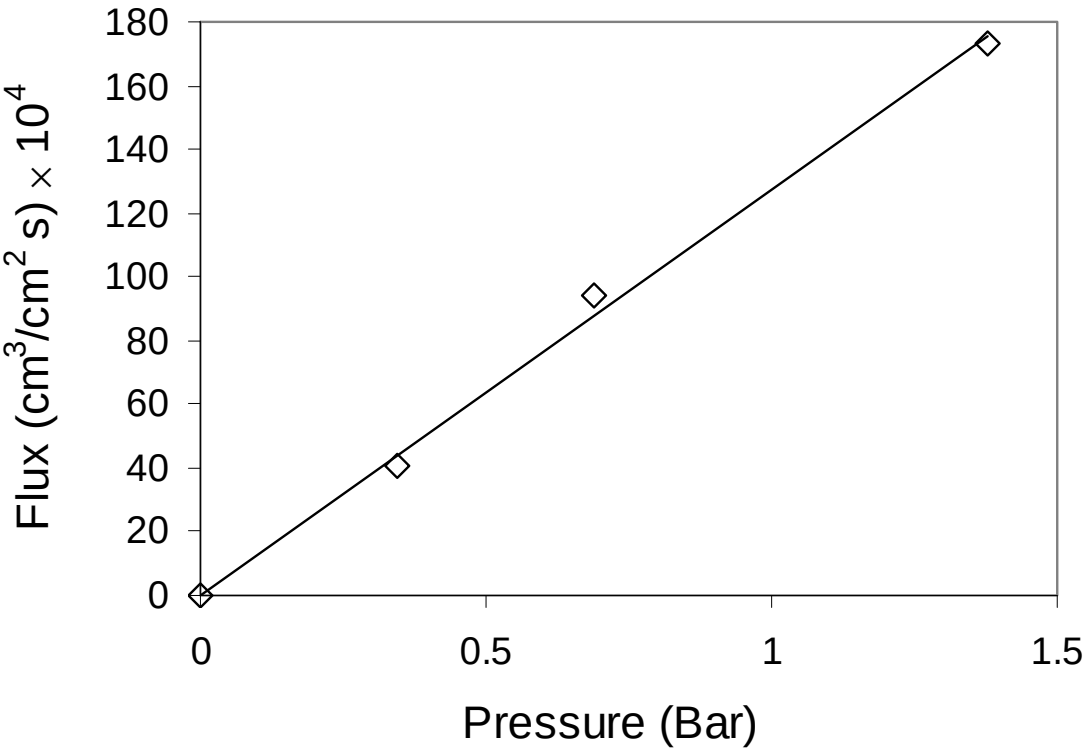

Figure 4.5 Pure water flux through unmodified PVDF (pore diameter = 220 nm) membrane at different pressure.

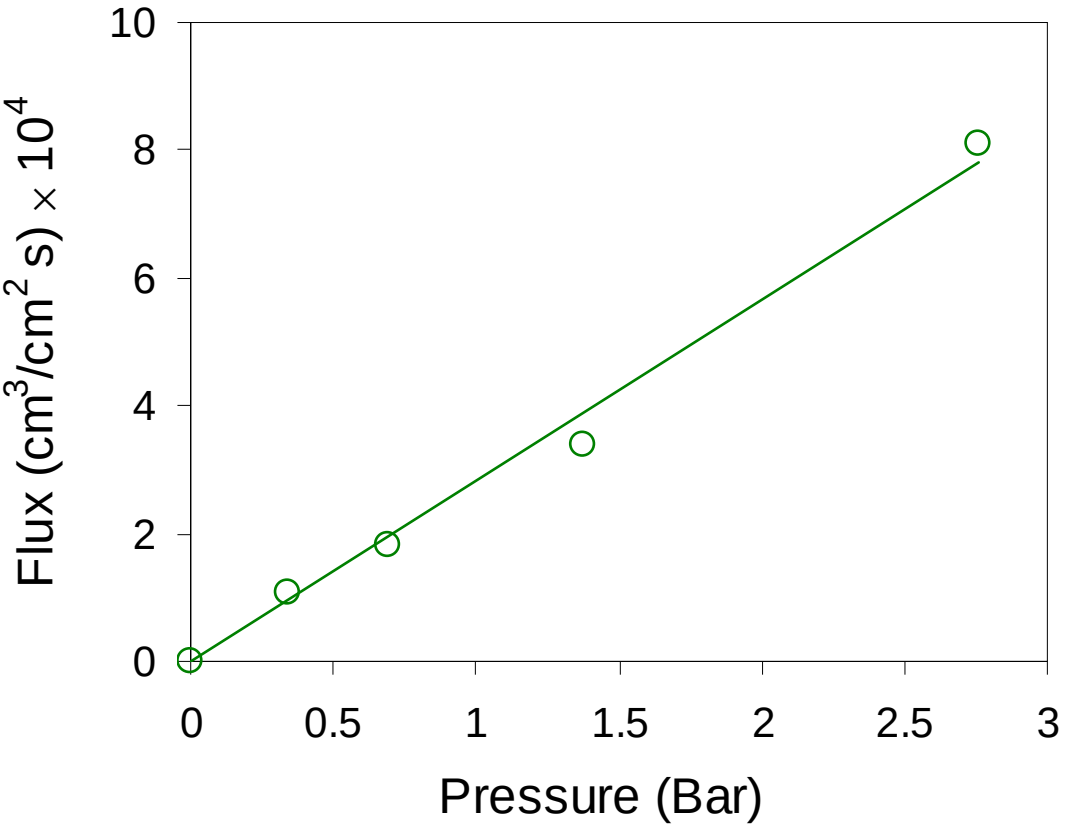

Figure 4.6 Pure water flux at different pressure through pore-filled PAA/PVDF membranes containing Fe/Pd nanoparticles (6 wt% metal loading).

4.4 Nanoparticle Characterization

4.4.1 Bimetallic Nanoparticle in PES Membranes Dip-coated with PAA

To reveal the structure difference between the support membrane and the composite PAA/PES membrane deposited with nanoscale Fe/Ni particles, the morphology of membrane surface and cross-section was observed by SEM. As shown in Figure 4.7 A and C**,** the PES MF support membrane has about 200 nm pore size and high porosity. After the support membrane coated with PAA solution and subsequent reduction with $NaBH_4$, the membrane surface and pores are all covered with Fe/Ni nanoparticles (Figure 4.7 B and D). Figure 4.7 D shows a two-layer structure image of Fe/Ni nanoparticles immobilized in the PAA/PES composite membrane. The top layer is the Fe/Ni nanoparticles in PAA, while the bottom layer has the similar structure and morphology to the PES support membrane (Figure 4.7 C). As it can be seen from the figure, there are few nanoparticles located inside the membrane. This indicates no obvious penetration of PAA inside the membrane due to the high viscosity and high molecule weight of PAA. The PAA layer is mainly deposited on the PES support membrane surface. The two layer structure is consistent with the results reported in the literature (Choi et al., 1992; Ohya et al., 1994; Huang et al., 1998) on the preparation of composite membranes by the dip-coating method for pervaporation, reverse osmosis, and gas separation. The two layer asymmetric structure with a thin dense top layer supported by a porous sub-layer allows for high separation selectivity as well as the high permeation flux. The nanoparticles-PAA layer thickness was estimated from the cross-section image as about 0.2μm.

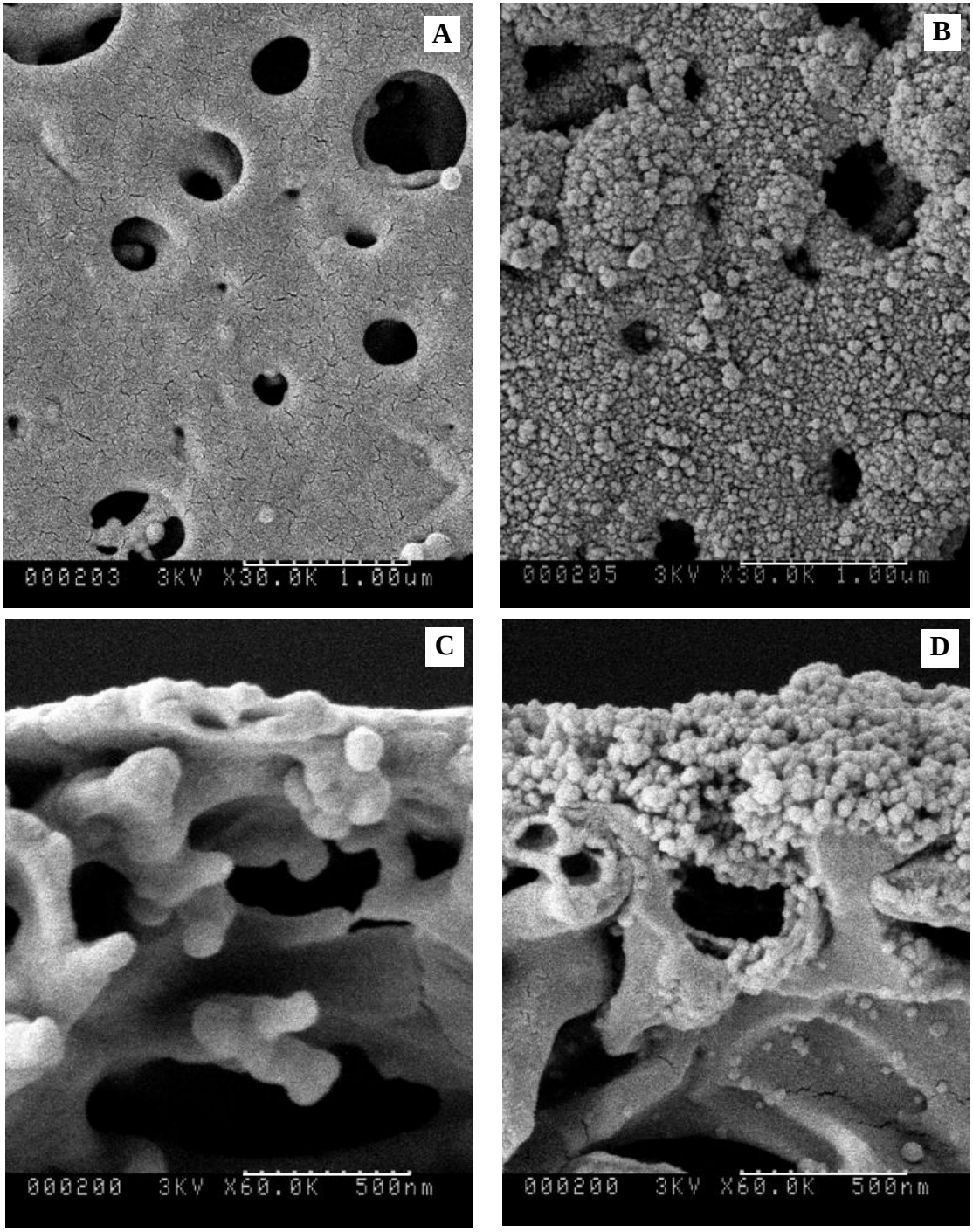

Figure 4.7 (A) SEM image of PES support membrane surface (30,000×); (B) SEM surface image of nanoscale Fe/Ni particles immobilized in PAA/PES composite membrane (reducing Fe followed by Ni deposition, 30,000×); (C) SEM cross-section image of PES support membrane (60,000×); (D) SEM cross-section image of PAA/PES composite membrane containing nanoscale Fe/Ni particles (reducing Fe followed by Ni deposition, 60,000×) (Xu and Bhattacharyya, 2005a).

A SEM energy-dispersive spectrum (SEM-EDS) analysis of the Fe/Ni particles at membrane surface and cross-section is also illustrated in Figure 4.8 A and B. Qualitative analysis using EDS is a procedure to determine the presence or absence of one or more elements in a sample. For x-ray spectrometry, elements that are present produce characteristic x-ray peaks, while elements that are absent obviously do not produce any peaks. Furthermore, a quantitative SEM-EDS analysis shows atomic composition of all present elements. It is important to point out that when using the EDS for bulk specimens in the SEM, accurate chemical analyses can only be obtained from a large area (0.5~30μm diameter) due to electron beam spreading on the bulk specimen (Williams and Carter, 1996). Therefore, the EDS quantitative results were obtained from an area containing several particles not a single particle. Both surface and cross-section analysis reveal about 4:1 metal atomic ratio of Fe to Ni. Since Ni was reduced in the second step and deposited on Fe particles, most of Ni should be located at the surface of the Fe particle. As expected, the ratio of Fe to Ni was lower at the surface than cross-section, suggesting higher amount of Ni at the membrane surface. The EDS results also show that both Fe and Ni composition are higher at membrane surface than cross-section, which is consistent with the two-layer structure (0.2μm Fe/Ni nanoparticle layer compared to 150μm support membrane layer).

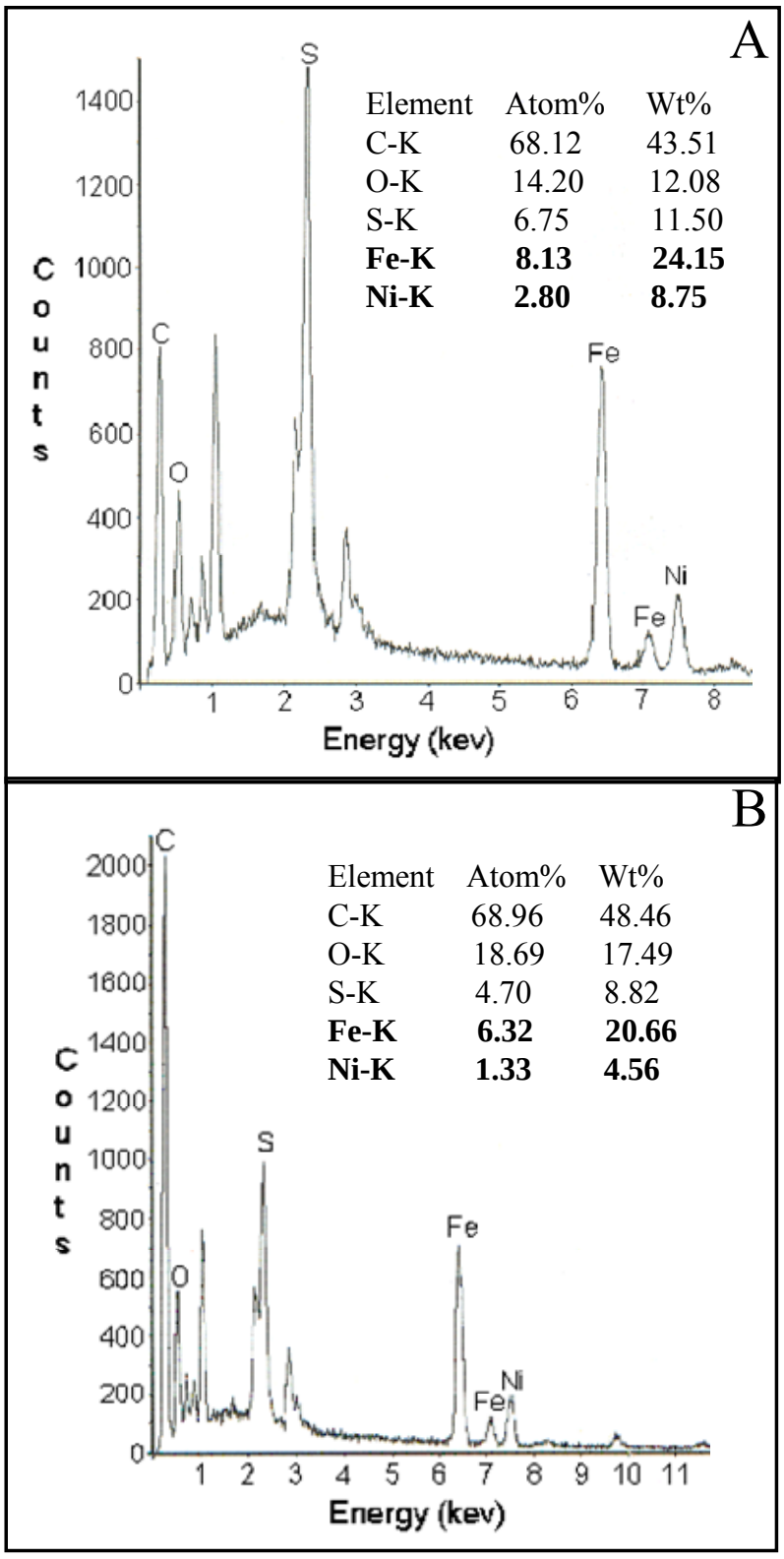

Figure 4.8 EDS spectrum of nanoscale Fe/Ni (reducing Fe followed by Ni deposition) inside PAA/PES A: membrane surface (Corresponding to Figure 4.7B) and B: cross-section (Corresponding to Figure 4.7D) (Xu and Bhattacharyya, 2005a).

A SEM image of nanoparticle on the membrane surface was taken at higher magnification (100k) to obtain particle size and size distribution. As shown in Figure 4.9A, the SEM image consists of well-dispersed Fe/Ni nanoparticles. A statistical analysis of the image (Figure 4.9B) yielded an average particle size of 28 nm, with the size distribution standard deviation of 7 nm. As a comparison, a SEM image of nanoscale Fe/Ni particles synthesized directly in the solution phase without polymer is shown in

Figure **4.10**A. Compared to the individual particles that can be easily distinguished in Figure 4.9A, agglomeration of particles is high in

Figure **4.10**A and present in the form of chains of beads. The reason is that newly formed metal atoms in the solution easily aggregate and combine with each other without the protection of polymer or membrane matrix. Based on a statistical analysis for 150 particles, the average particle size is 31 nm, with the size distribution standard deviation of 9 nm.

Figure **4.10**B is the SEM-EDS spectrum for particles synthesized without membrane. The boron peak suggests that some nickel particles were present as Ni_2B. Boron is a very light element which can be identified by EDS only at relatively high concentration. The reason for the absent boron peak in other EDS spectrum is due to the relatively low boron concentration in particles immobilized in membrane domain.

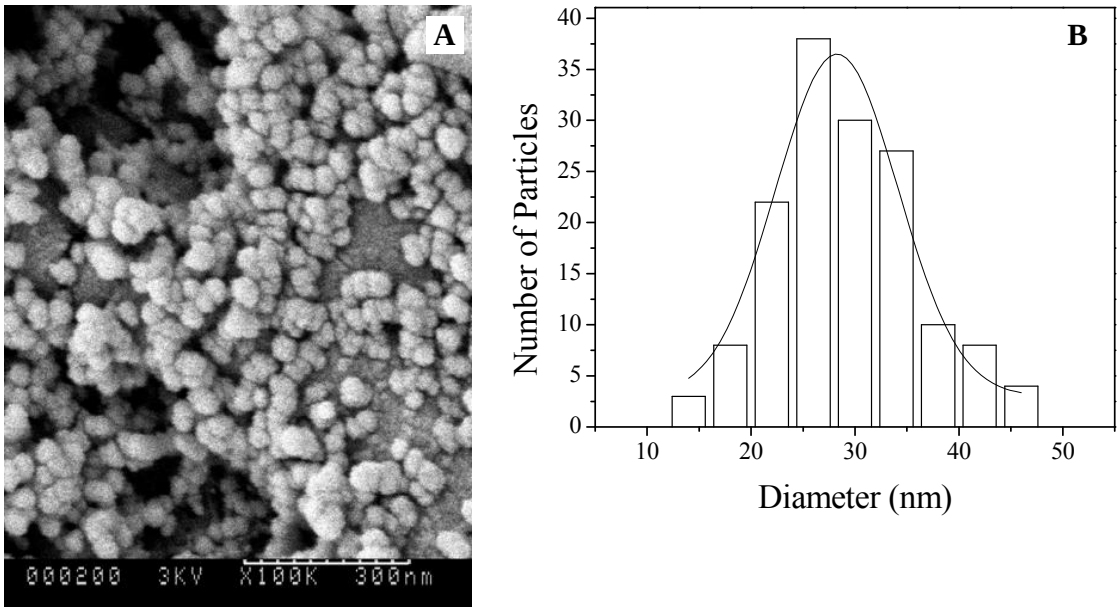

Figure 4.9 (A) SEM surface image of nanoscale Fe/Ni particles immobilized in PAA/PES composite membrane (reducing Fe followed by Ni deposition) (100,000×); (B) Histogram from the left SEM image of 150 Fe/Ni nanoparticles. The average particle size is 28 nm, with the size distribution standard deviation of 7 nm (Xu and Bhattacharyya, 2005a).

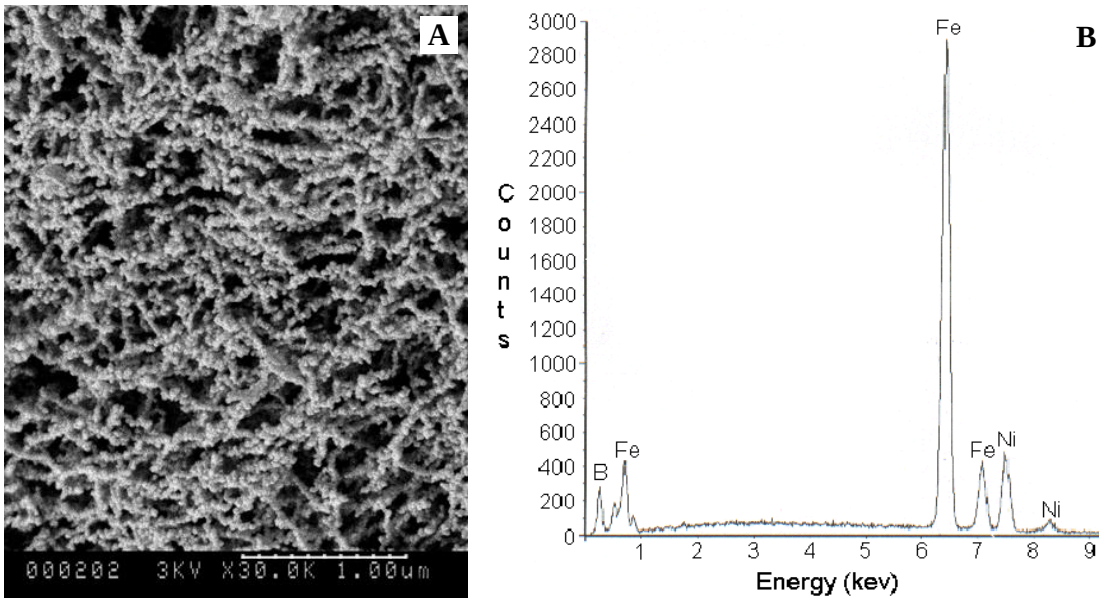

Figure 4.10 (A) SEM image of Fe/Ni particles reduced simultaneously in solution phase (30,000×); (B) EDS spectrum of Fe/Ni particles synthesized in the solution phase.

Because of the limitation of SEM, transmission electron microscopy (TEM) and scanning transmission electron microscopy (STEM) with energy dispersive x-ray spectroscopy (STEM-EDS) was also used to obtain the structure and composition information of the metal particles at nano scales. Figure 4.11 shows a typical bright field TEM image of the nanoscale Fe/Ni particles in the PAA membrane domain. A statistical analysis based on 150 particles of the image yielded an average particle size of 5±0.8 nm. It should be noted that for this TEM imaging particles in a very thin membrane (total thickness about 100 nm) were formed directly in the TEM grid. Because of fast drying in this membrane film, particle agglomeration was minimal. The smaller particle size in TEM image was observed due to the thinner film formed on the TEM grid and high resolution of TEM which is capable of resolving individual particle in nano domain. On the contrary, because of the low resolution of SEM, only clusters of individual particles or relatively large particles can be identified in SEM image which results in increase of particle size. The main purpose of using TEM and STEM here is to obtain elemental compositions of nanoparticles at nano scale. In STEM mode, EDS Line profile analysis was performed and the results are shown in Figure 4.12A (reducing Fe followed by Ni deposition) and Figure 4.12B (simultaneous reduction of Fe and Ni). In Figure 4.12C, the compositional line profiles probed with EDS show relatively constant Fe and Ni intensities across the particles, suggesting uniform Fe and Ni composition (Fe: Ni=4:1) across the particles. However, highly fluctuating Fe and Ni intensities were observed across the particles in Figure 4.12D, indicating varying Fe and Ni composition of simultaneously reduced Fe/Ni particles. The varying Fe and Ni composition shown implies that iron was not uniformly covered by nickel, and some Fe particles and Ni particles are present in separate domain.

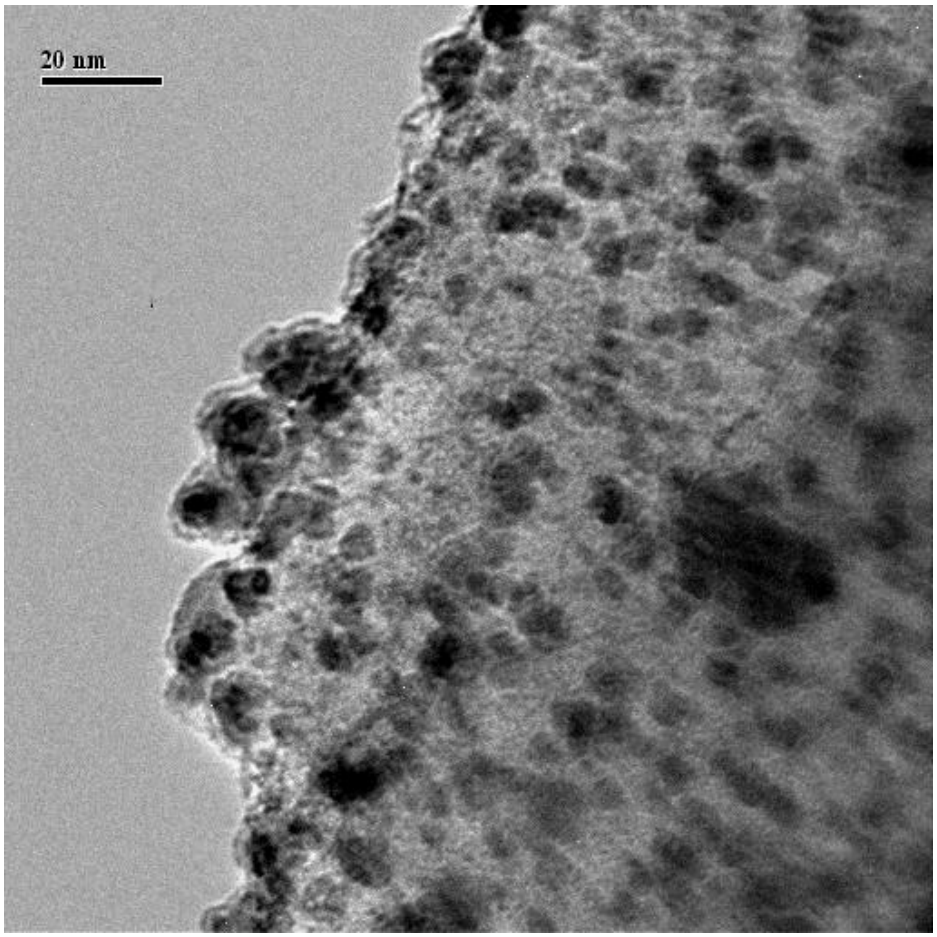

Figure 4.11 Typical bright field TEM image of nanoscale Fe/Ni particles in the PAA membrane domain prepared in a Au coated TEM grid (reducing Fe followed by Ni deposition).

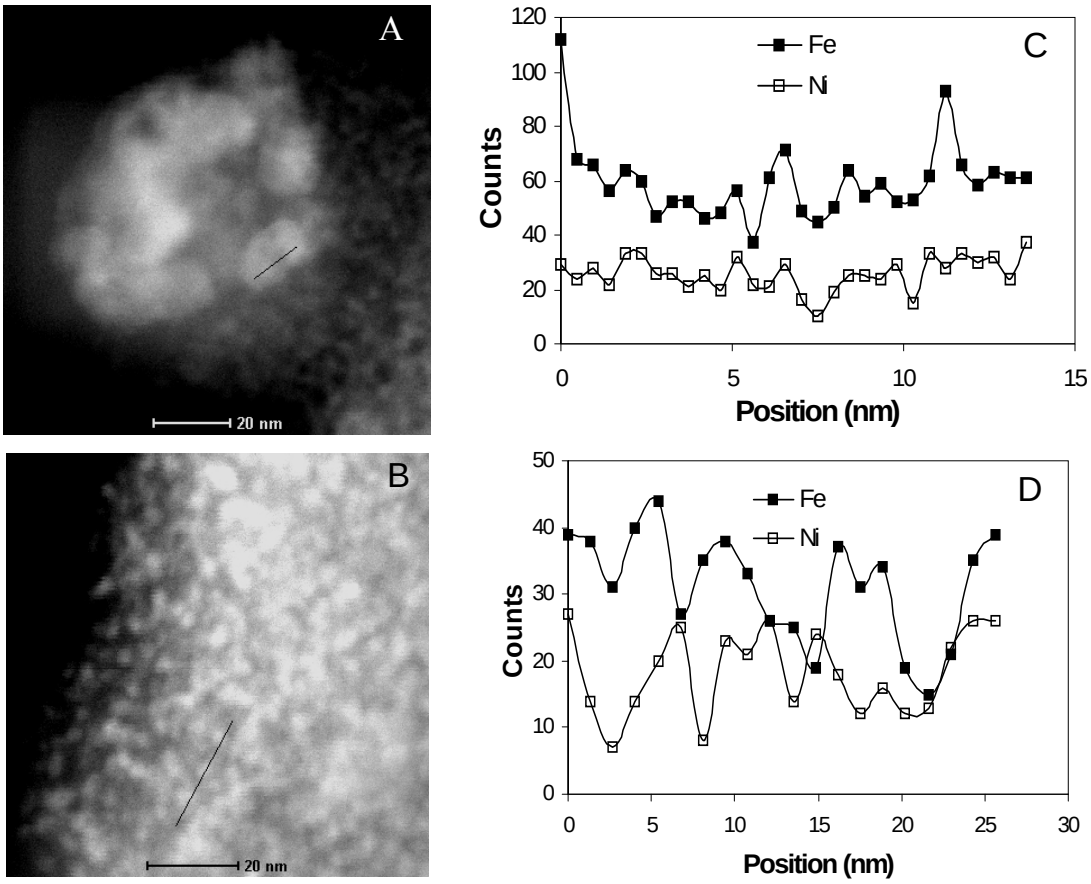

Figure 4.12 Dark field STEM image of Fe/Ni inside PAA membrane (A): reducing Fe followed by Ni deposition and (B): simultaneous reduction of Fe and Ni; Compositional line profiles probed by STEM EDS (C): along the black line in (A) and (D): along the black line in (B) (Xu and Bhattacharyya, 2005a).

Furthermore, STEM-EDS mapping was performed to determine the two-dimensional Fe/Ni element distribution inside PAA membrane. Figure 4.13 presents the STEM-EDS mapping images of (A): reducing Fe followed by Ni deposition (B): simultaneous reduction of Fe and Ni. As shown in Figure 4.13A, all Fe and Ni were dispersed together inside the membrane matrix, indicating Fe was homogeneously covered by Ni. On the other hand, some regions which show separation of Fe and Ni particles are observed in Figure 4.13B. Based on the proof of STEM-EDS mapping data which is consistent with the EDS line profile analysis, it can be concluded that reduction of iron followed by nickel produces more evenly dispersed Fe/Ni nanoparticles than those in which Fe and Ni are reduced simultaneously. The distribution and composition of Fe and Ni in the nano domain can play an important role in the degradation of chlorinated organics.

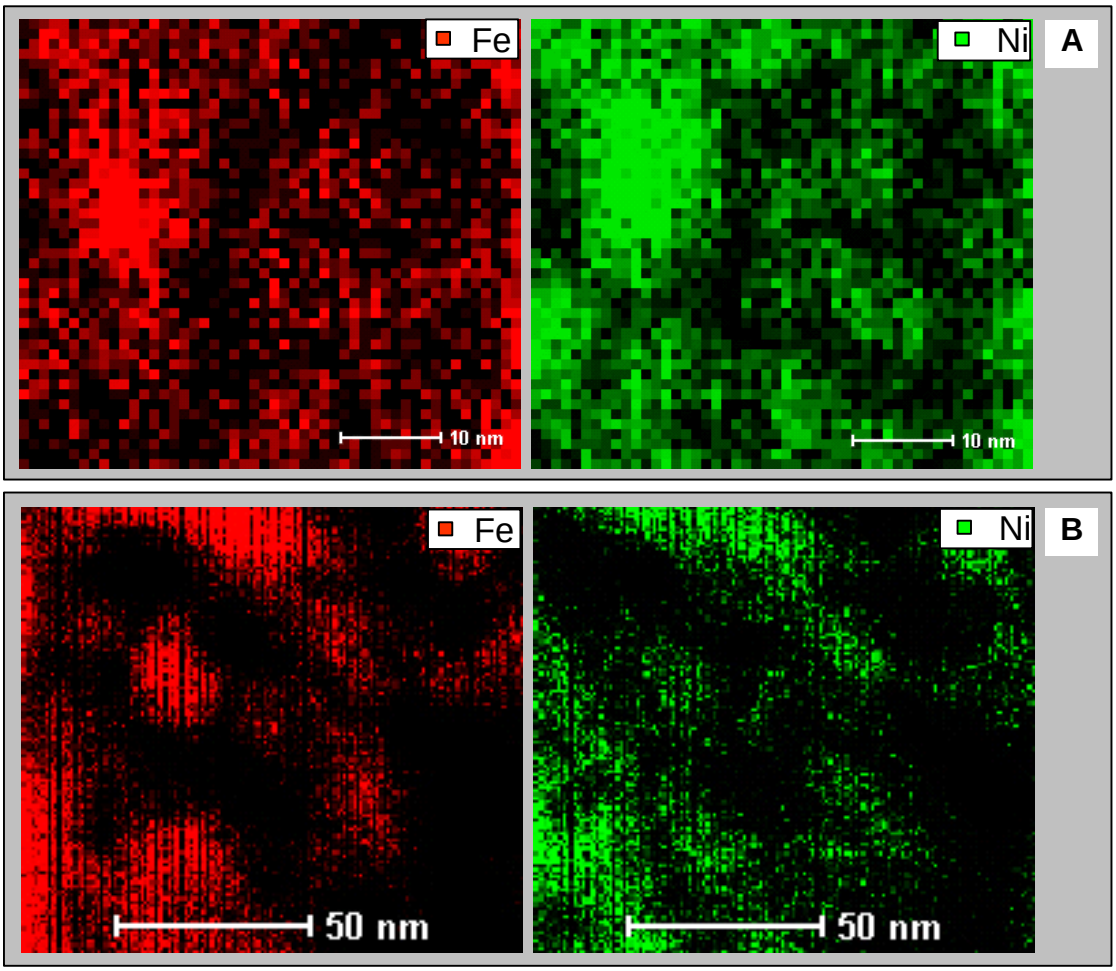

Figure 4.13 STEM EDS mapping images of Fe/Ni nanoparticles distribution inside PAA membrane (A): Reducing Fe followed by Ni deposition; (B): Simultaneous reduction of Fe and Ni (Xu and Bhattacharyya, 2005a).

4.4.2 Bimetallic Nanoparticle in PVDF Membranes Dip-coated with PAA

There are two main steps in the preparation of membranes containing metal nanoparticles: firstly, The PAA-Fe^{2+} (pH = 2.0) layer is attached to the surface of PVDF MF membrane by a dip-coating process. PVDF support membranes (commercial) were already hydrophilized using hydroxy propyl acrylate and tetra ethylene glycol deacrylate (Steuck 1990). The presence of hydrophilic layer on PVDF membrane pores has a strong interaction with PAA, which can enhance the stability of coating layer. Ethylene glycol (EG) is added as the crosslinking agent for PAA. Crosslinked PAA layer is obtained after heating the membrane at 110 °C for 3 hours and this results in the formation of an ether bond between the carboxylic group and ethylene glycol. Partial (about 50%) crosslinking was necessary to leave free carboxylic groups for metal cations entrapment. Subsequently, Fe^{2+} is reduced by $NaBH_4$ to form nanoscale Fe^0 particles.

Bimetallic nanoparticles can be prepared by consecutive reduction of the second metal ions and subsequent deposition on first metal particles. This can be achieved either by a partial displacement reaction on the first metal surface or using an additional reducing agent. Consecutive reduction of one metal ion over another usually causes the formation of core/shell structure nanoparticles (Mandal et al., 2003; Son et al., 2004; Sao-Joao et al., 2005; Yang et al., 2005; Nutt et al., 2005). For example, when Fe particles are immersed into insufficient amount of Pd^{2+}, Fe is partially oxidized to Fe^{2+} and Pd^{2+} is reduce to Pd^0, resulting in the formation of core/shell Fe/Pd nanoparticles. For Fe/Ni nanoparticles synthesis, additional $NaBH_4$ usually is required to reduce Ni^{2+} to Ni^0 because the standard electrode potential ($E°$) of Fe and Ni are quite close ($E°$ [Fe^{2+}/Fe] = -0.44 V, $E°$ [Ni^{2+}/Ni] = -0.26 V, $E°$ [Pd^{2+}/Pd] = +0.99 V). Another convenient way for preparation of bimetallic nanoparticles is by simultaneous reduction of two metal ions, which usually results in the formation of alloy structure nanoparticles (Mandal et al., 2003).

As shown in the SEM images (Figure 4.14a and b**)**, both bimetallic Fe/Ni and Fe/Pd particles are roughly spherical with an aggregate size of about 120 nm. Examination of the particles at higher resolution indicates that each particle consists of

many smaller particles of size 20-30 nm. The SEM-EDS analysis identifies the presence of Fe/Ni and Fe/Pd particles as well as the compositions of all present elements.

The interaction between metal cations and carboxylic groups in PAA is critical in the prevention of particle aggregation, which can greatly influence the nanoparticle size. The interaction mechanisms consist of ion exchange, chelation and electrostatic binding (counterion condensation). In order to investigate the role of PAA in nanoparticle synthesis, membrane-based Fe nanoparticles were prepared by varying the ratio of PAA to $FeSO_4$ (constant PAA, varying $FeSO_4$). In all these cases, only the free carboxylic groups (about 50%) are available to participate in binding Fe cations. Although the PAA crosslinking reaction was conducted at low pH but the borohydride reduction step ($Fe^{2+} \rightarrow Fe^0$) was in alkaline pH condition and thus the COOH groups were ionized for metal cation binding. The formation of network structure after crosslinking also affects the metal cations binding (Xu and Bhattacharyya, 2005a). As shown in Figure 4.15, Fe particle size increases with the decrease of molar ratios of PAA to Fe^{2+}. At low Fe^{2+} concentration, because of ion exchange Fe^{2+} in the PAA layer are spatially arranged. Hence, aggregation of Fe atoms is inhibited due to the low mobility of bound Fe^{2+}. While with the decrease of PAA/Fe ratio, both bound (with COO^-) and free form (mobile Fe salt) will be present inside the PAA matrix. So, the aggregation of Fe atoms is enhanced (Figure 4.15).

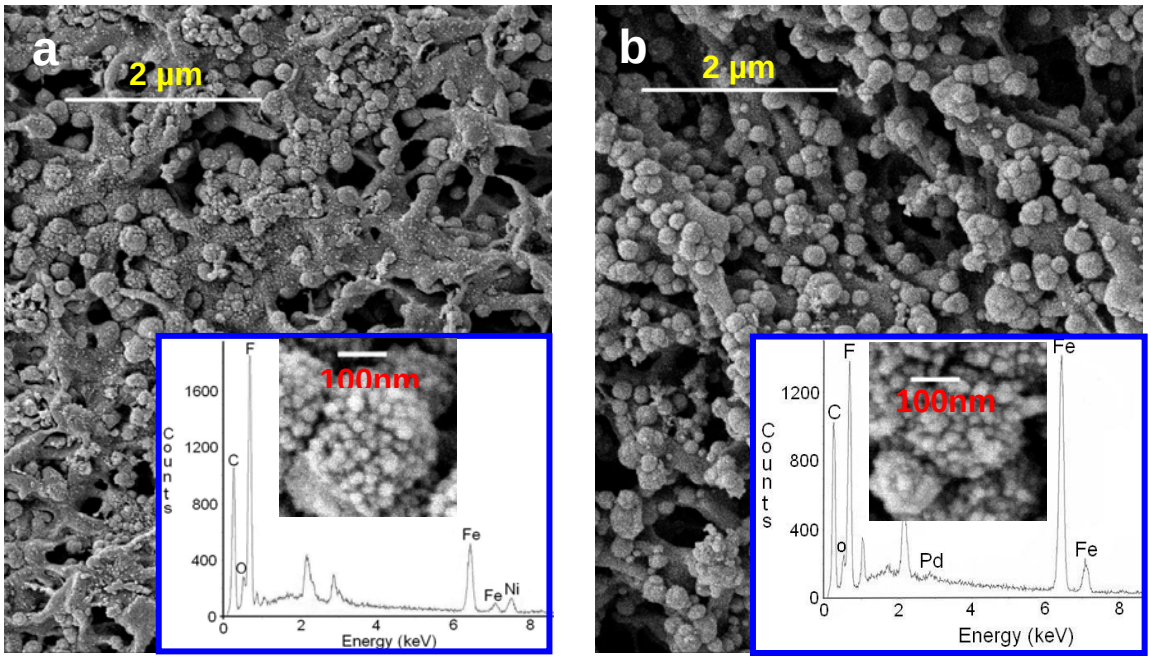

Figure 4.14 SEM images of bimetallic nanoparticles in PAA/PVDF membrane: (a) Fe/Ni (Ni = 25 wt%); (b) Fe/Pd (Pd = 1 wt%). [PAA monomer unit]: [$FeSO_4$] = 4 (Xu and Bhattacharyya, 2005b).

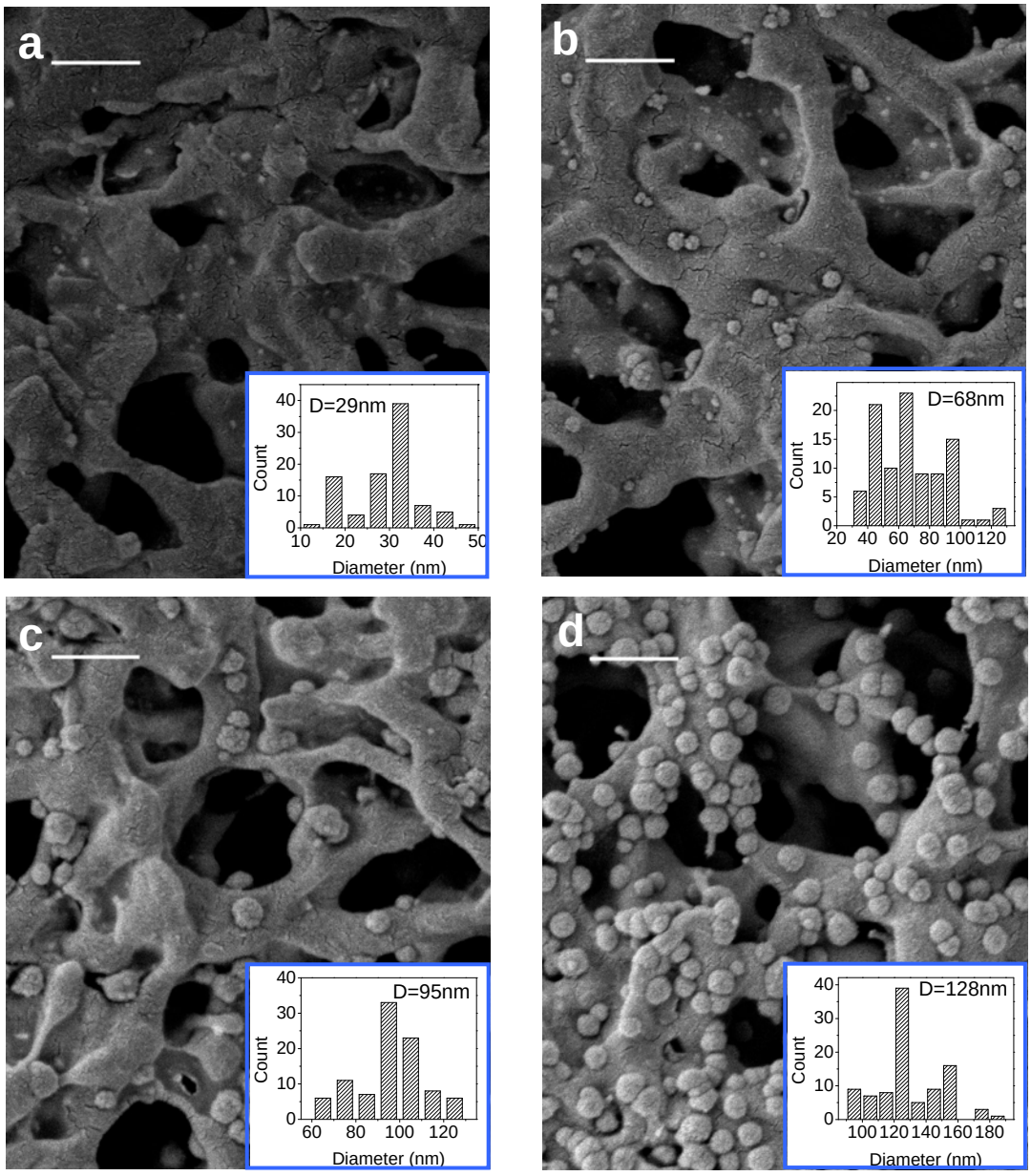

Figure 4.15 SEM images of Fe nanoparticles in PAA/PVDF membranes synthesized with different molar ratio of PAA (monomer unit) to $FeSO_4$: (a) 100; (b) 50; (c) 8; (d) 4. $NaBH_4$ concentration = 0.5 M for all cases. The scale bar is 500 nm (Xu and Bhattacharyya, 2005b).

4.4.3 Interaction between Ferrous Ions and PAA in Pore-Filled PVDF Membranes

In the study of pore-filled PAA/PVDF membranes, we prepared iron nanoparticles in three steps: polymerization of acrylic acid in PVDF microfiltration membrane pores, subsequent ion exchange of Fe^{2+}, and chemical reduction (by borohydride) of ferrous ions bound to the carboxylic acid groups. By using this PAA metal ions binding interaction (Fe^{2+} and COO^-) followed by the borohydride reduction method, we created iron nanoparticles well dispersed inside membranes because the ferrous ions are bound and distributed along the PAA chains. The surrounding polymer chains also can prevent ion migration and nanoparticle agglomeration, which plays a critical role in stabilizing nanoparticles and controlling the particle size (Wang et al., 2002). Therefore, it is necessary to understand the binding interaction between ferrous ions and PAA. First, the mass balance of Na^+ and Fe^{2+} is calculated based on the ICP analysis of the $FeCl_2$ solution before and after loading of Fe^{2+} on the membrane. According to the ICP results, the atom ratio of Na^+ released from the PAA/PVDF membrane over the ferrous ions bound to the membrane is 1.9 ± 0.1. In theory, binding one Fe^{2+} from solution results in two sodium ions released from the membrane due to the charge balance. This indicates that the ferrous ions are well chelated with PAA (no physical adsorption). An elemental analysis was performed on the PAA/PVDF membrane loaded with Fe^{2+}, and the result is shown in the Figure 4.16. It has been found that coordination number for PAA-divalent metal complex is 2 (Tomida et al., 2001). Therefore, one ferrous cation is satisfied with two carboxyl anions containing four oxygen atoms. As shown in the Figure 4.16, the EDS analysis gives the atom ratio of 3.5 (oxygen over iron). This value agrees well with the established PAA-metal binding stability constant.

Secondly, the bound ferrous ion proximity in the membrane plays an important role in controlling the size of nanoparticle (Wang et al., 2002; Xu and Bhattacharyya, 2005). It has been reported that the average particle size is larger when metal cation concentrations in membrane are higher (Wang et al., 2002; Xu and Bhattacharyya, 2005). This is due to the enhanced aggregation of Fe atoms because of the shorter distance between Fe^{2+} at the higher loading density. In order to reveal the distribution of Fe and

PAA at nanoscale, EDS elemental maps of the membrane cross-section were acquired using STEM. A region of the membrane sample at lower magnification is shown in a STEM bright field image (Figure 4.17a). The EDS mapping was performed at the selected area on the left STEM image (Figure 4.17a) and reveals the position of elemental atoms of iron, fluorine (F) and oxygen (O) in Figure 4.17b, c and d respectively. The map is generated by placing white dots on the image when an X-ray count of a particular element is received. As shown in the Figure 4.17b and c, the dots for oxygen appear strongly in the map and oxygen atoms are mainly found in the regions where little fluorine atoms were identified. This indicates the presence of PAA inside the membrane because oxygen only comes from carboxylic acid group. And it also confirms the assumption that the small grains observed in the SEM cross-sections are PAA. By comparing iron, fluorine and oxygen map, the iron and oxygen atoms are combined together and located in the same phase separated from the phase where fluorine atoms are present. This indicates that PVDF substrate has no affinity to Fe^{2+} and ferrous cations are strongly bound with PAA carboxylic acid groups.

Next, an EDS map was acquired at higher magnification to obtain a better understanding of the interaction between Fe^{2+} and PAA. As shown in the Figure 4.17e~g, all the iron atoms are associated with oxygen atoms and the Fe map matches perfectly with oxygen map. The black dots appear in the iron map are believed to be the gaps between chelated ferrous ions. It is important to point out that these images and maps were obtained under the completely dry state due to the requirement of sample preparation and TEM analysis. This can change the morphology of the membrane because PAA is an extremely swellable polyelectrolyte.

Using ICP analysis results and mass balance, 95 % yield of Fe nanoparticle was achieved after reduction of bound Fe^{2+} with $NaBH_4$. This indicates insignificant leaching of nanoparticle from the membrane phase during the reduction process. According to the ICP analysis, about 4 wt% boron was found in the Fe nanoparticles. Obviously $Fe^{2+} \rightarrow Fe^{0}$ conversion will lead to Na^{+} binding with COO^{-} sites. Na analysis by SEM-EDS confirmed this case. It has been reported that the reduction of Fe^{2+} with borohydride in aqueous solution involves three independent reactions. The boron content in the Fe-B

nanoparticles is determined by the pH, the addition rate and the concentration of $NaBH_4$ solution.

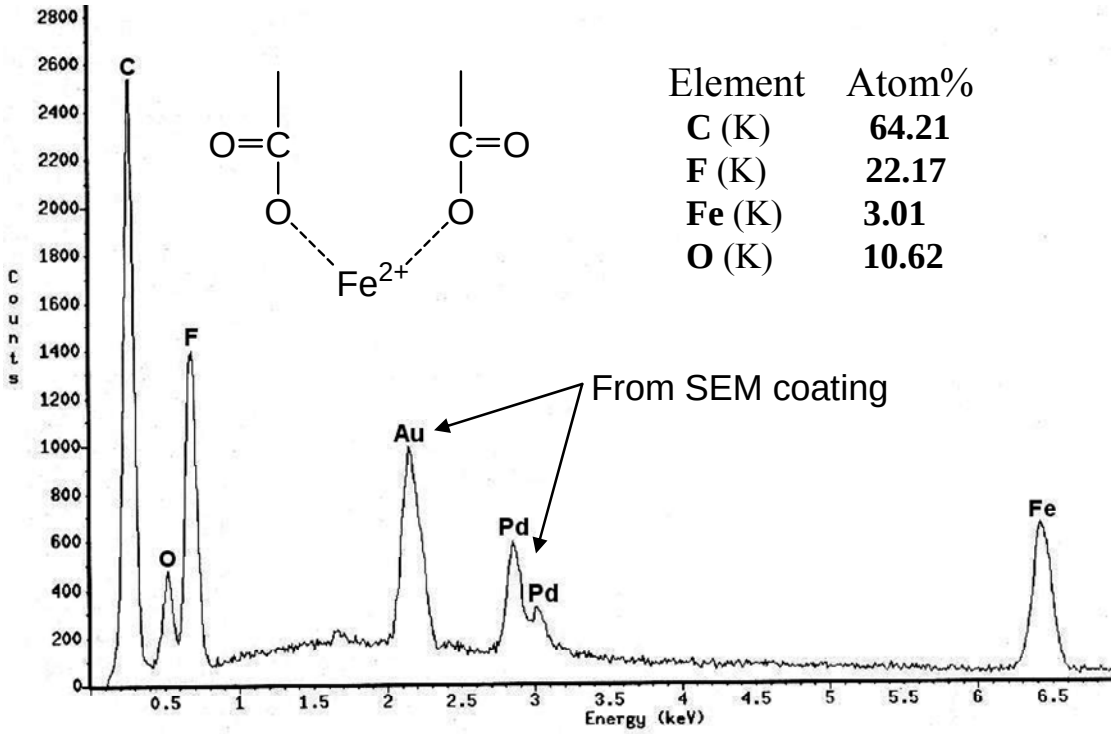

Figure 4.16 SEM-EDS spectra of PAA pore-filled PVDF membranes loaded with ferrous ions (Xu and Bhattacharyya, 2007).

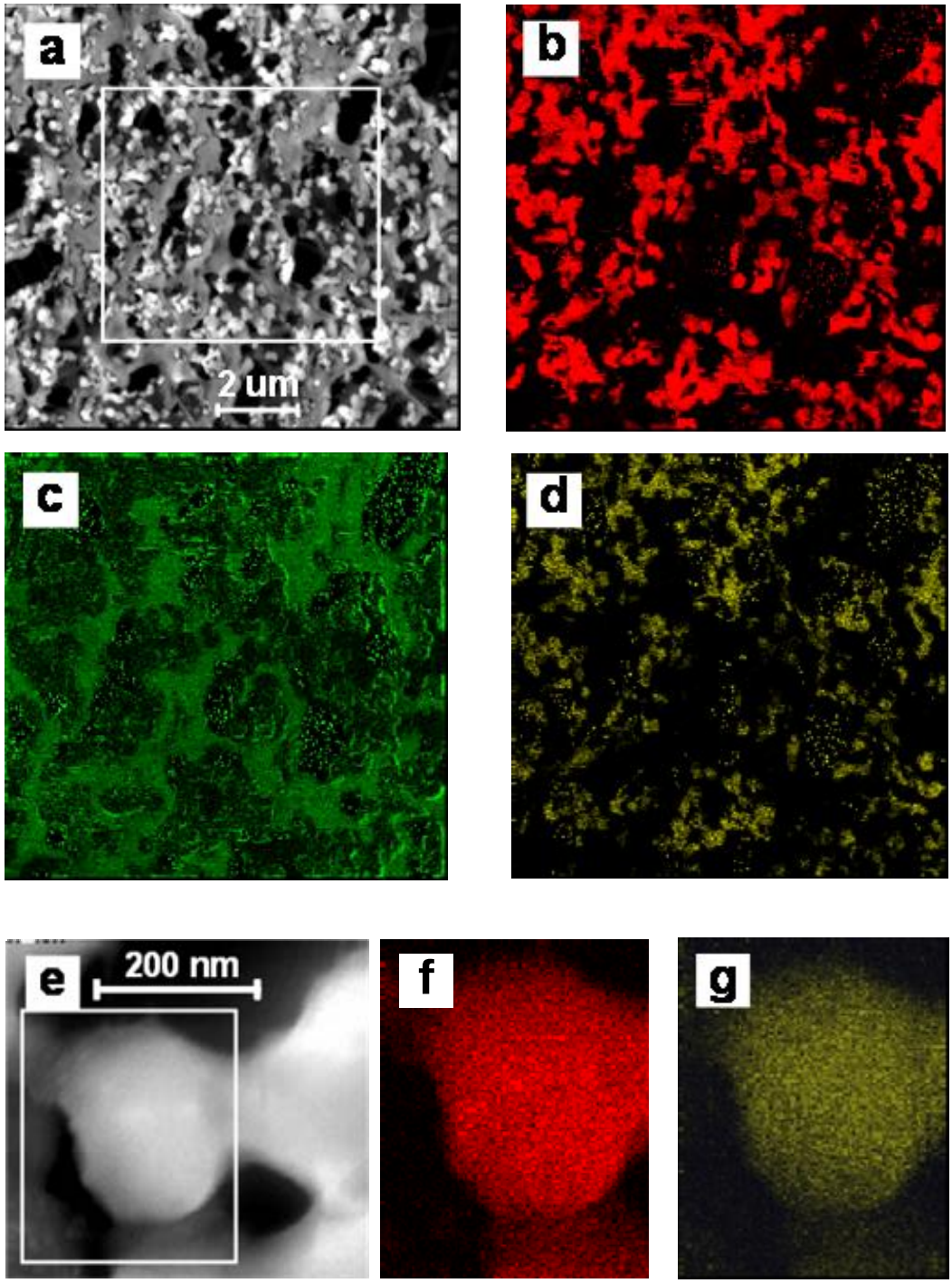

Figure 4.17 STEM-EDS Mapping of PAA/PVDF membranes chelated with Fe^{2+}. (a): Low magnification STEM image of membrane cross-section; (b): Fe map from (a); (c): F map from (a); (d): O map from (a); (e) High magnification STEM image of membrane cross-section; (f): Fe map from (e); (g): O map from (e) (Xu and Bhattacharyya, 2007).

4.4.4 Fe/Pd Nanoparticle in Pore-Filled PAA/PVDF Membranes

TEM analysis at low magnification was performed to verify the nanoparticle formation and distribution inside PAA/PVDF membranes. As shown in the Figure 4.18, Fe/Pd nanoparticles in spherical shape are homogeneously dispersed in the PAA phase over the membrane cross-section. While the regions containing no nanoparticles are believed to be the PVDF substrate phase. A statistical analysis of the image yielded an average particle size of 30 nm in diameter, with the size distribution standard deviation of 5.7 nm. Based on the mean diameter of 30 nm, the external surface area for nanoparticles was calculated to be ~ 25 $m^2 g^{-1}$. The EDS analysis was also conducted during the TEM observation using a 2-nm electron beam spot to determine the elements present in the nanoparticles. The composition of nanoparticles identified in the TEM image was also quantified by EDS (Figure 4.18c). The Pd content was found to be 1.9 wt%, which is consistent with the previous ICP analysis results. Boron as a light element at low content was not detected by EDS due to the low energy sensitivity (Williams and Carter, 1996).

Next, the nanostructures and element distribution of the Fe/Pd nanoparticles were observed by HRTEM and STEM-EDS mapping. Figure 4.19 shows a STEM bright field image and the elemental mapping images of the corresponding area for Fe and Pd. The probe size used was 1 nm in diameter. The mapping images clearly demonstrate a core/shell structure for the Fe/Pd nanoparticle with Fe in the core region and Pd in the shell region. This is as expected because Pd was post reduced by Fe^0 and deposited on the iron surface.

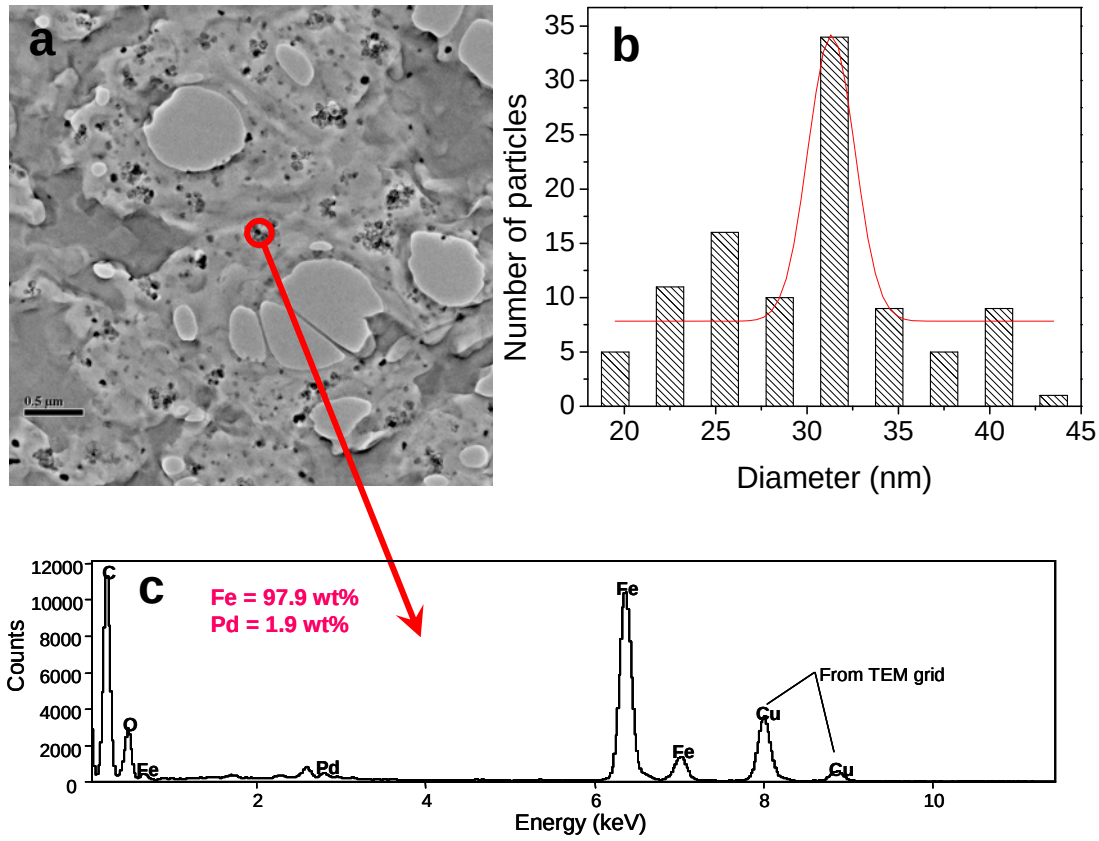

Figure 4.18 (a): TEM image of PAA/PVDF membrane cross-section containing Fe/Pd nanoparticles; (b): Histogram from the left TEM image of 100 Fe/Pd nanoparticles; (c): EDS spectrum acquired from the nanoparticles in the TEM image (Xu and Bhattacharyya, 2007).

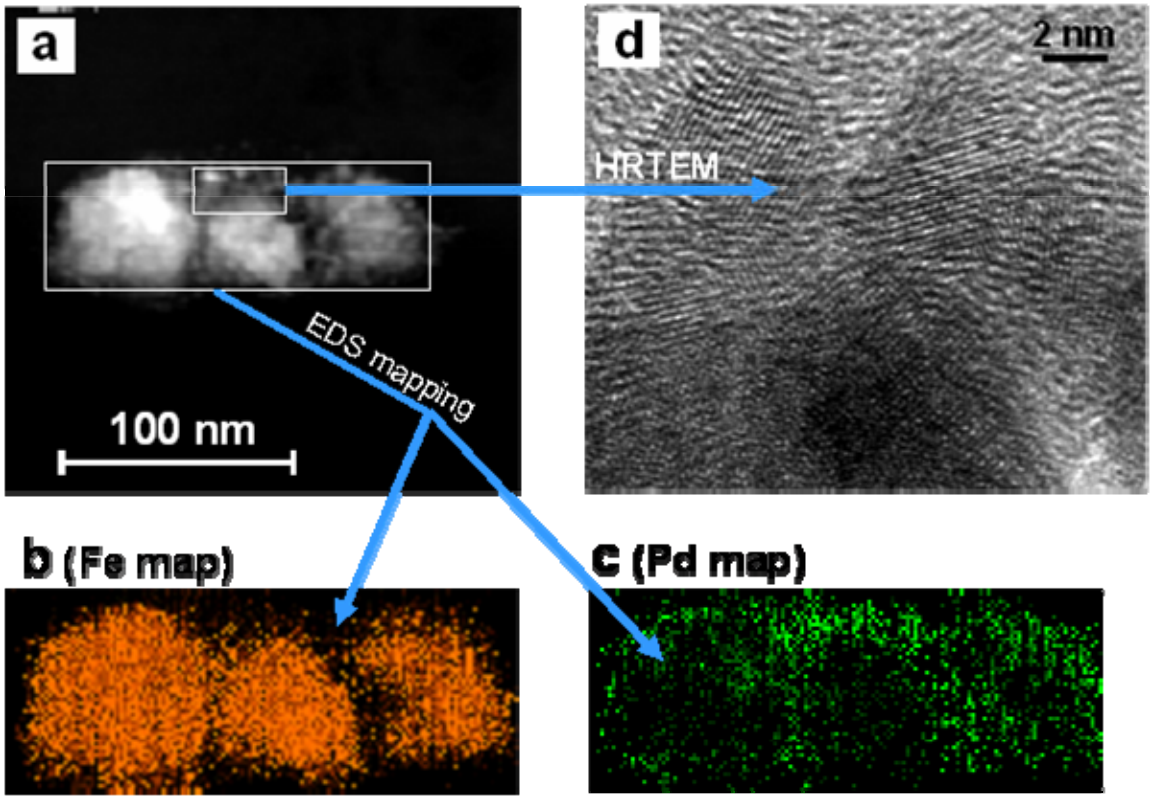

Figure 4.19 Characterization of Fe/Pd nanoparticles. (a) STEM image of Fe/Pd (Pd = 2.3 wt%) nanoparticles; (b) EDS mapping image of Fe; (c): EDS mapping image of Pd; (d): High Resolution TEM image of Fe/Pd nanoparticles (Xu and Bhattacharyya, 2007).

4.5 Dechlorination of TCE and PCBs by Bimetallic Nanoparticles

4.5.1 TCE Dechlorination by Bimetallic Nanoparticles in PAA/PES Membranes (Dip-coating)

Various nanoparticles systems were evaluated for dechlorination rates using 10 mg L^{-1} TCE feed solution. Figure 4.20 shows experimental data for the degradation of TCE with various nanoscale Fe/Ni particles and Fe/Pd nanoparticles: (1) solution phase synthesis (no membrane) Fe/Ni particles (2) simultaneous reduction of Fe and Ni in the PAA/PES membrane phase; (3) reducing Fe followed by Ni deposition in the PAA/PES membrane phase, (4) nano Fe/Pd particles in the PAA/PES membrane phase, and (5) bulk Ni_2B particles (30 mesh) purchased from Sigma-Aldrich. In all the batch experiments, initial TCE concentration was 10 mg L^{-1}, and metal loading to solution ratio was 45 mg/40 mL for all Fe/Ni (4:1), 40 mg/40 mL for Fe/Pd (9:1), and 45 mg/40 mL for commercial Ni_2B respectively. TCE concentrations in the figure are expressed as the ratio of TCE at time t / TCE in feed (C/C_0). The amounts of TCE in blank control samples (without membrane and metal particles) and membrane control (without metal particles) samples remained relatively constant within a period of 2 hour, suggesting insignificant TCE transformation by PAA/PES membrane.

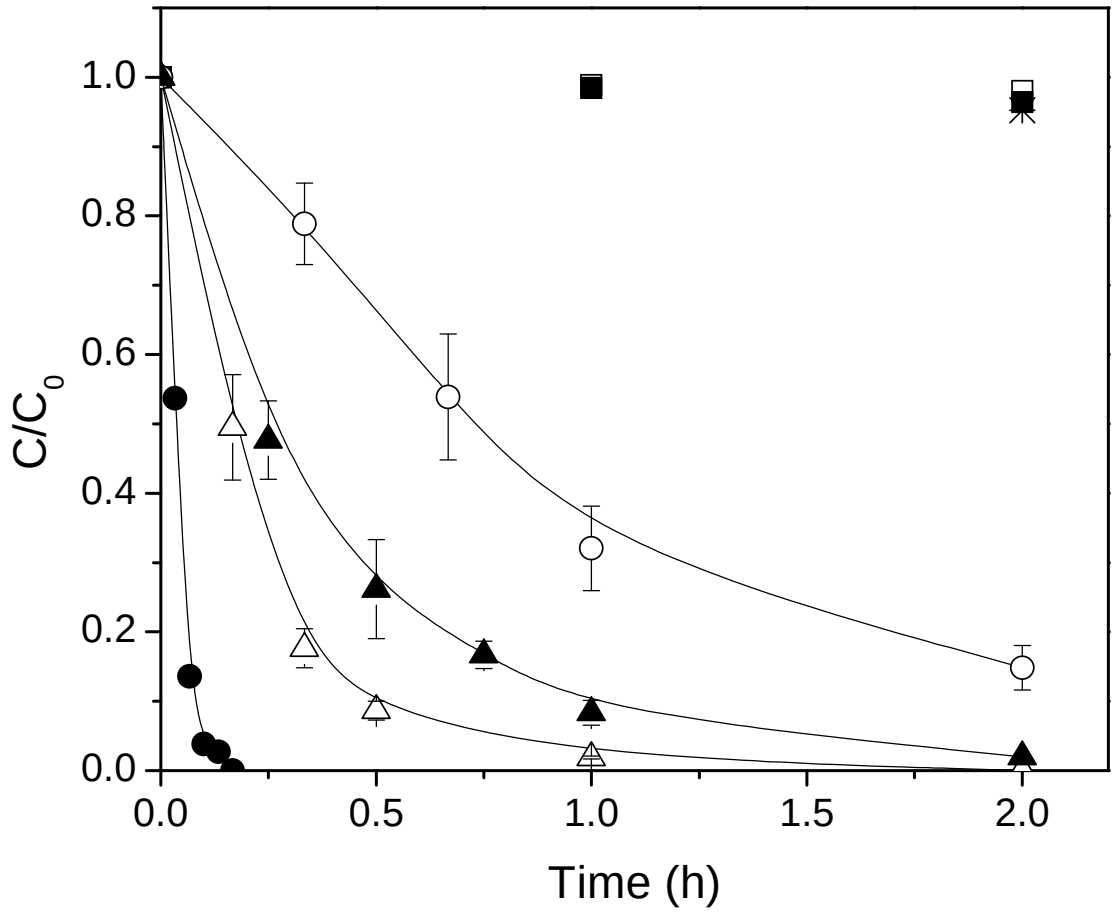

Figure 4.20 Reactions of TCE with (□) blank control (no membrane and particles); (■) PAA/PES membrane (no particles); (∗) Ni_2B (45mg)obtained from Sigma-Aldrich; (●) Fe/Pd in PAA/PES (total metal = 40 mg, Fe/Pd ratio = 9) membrane; (△) Fe/Ni (total metal = 45 mg, Fe/Ni ratio = 4) in PAA/PES membrane (reducing Fe followed by Ni deposition); (▲) Fe/Ni in (total metal = 45 mg, Fe/Ni ratio = 4) PAA/PES membrane (simultaneously reduction of Fe and Ni); (○) Fe/Ni (total metal = 45 mg, Fe/Ni ratio = 4) (reduced simultaneously in solution phase).Initial TCE = 10 mg/L (Xu and Bhattacharyya, 2005a).

As shown in Figure 4.20, nanoscale Fe/Pd system which has a higher initial iron corrosion rate and hydrogenation efficiency than Fe/Ni system exhibited highest dechlorination rate. TCE was completely degraded in less than 0.25 hours. Fe/Ni (reducing Fe followed by Ni deposition) gave 98% TCE dechlorination within 1 hour. Production of ethane was identified in the headspace in both Fe/Pd and Fe/Ni system, and a relative ethane analysis obtained by GC peak area is shown in Figure 4.21. TCE degradation resulted in ethane formation. No other intermediate chlorinated products were seen in both aqueous and headspace phase. Another product, chloride ion, was also analyzed in aqueous phase for the independent check of dechlorination reaction. Assuming that for each degraded TCE molecular three chloride ions are released, 8.1mg/L chloride ions will be produced at the end of 10mg/L TCE dechlorination reaction. But only 3.0 mg/L Cl^- (37% Cl^- recovery) was formed at the end of reaction. Lower Cl^- concentrations observed can be explained by the sorption of chloride ions on membranes and nanoparticles (Schrick et al., 2002). In the dechlorination study of TCE with nanoscale Fe^0 (single metal system) (Choe et al., 2001), only a small amount of intermediates were identified and ethane was observed as the main product. However, chlorinated intermediates such as cis-1,2-dichloroethylene, 1,1-dichloroethylene, and vinyl chloride were found as main products in the dechlorination with bulk iron particles. Further degradation to form ethane is a really slow process. Thus, compared to the bulk system, the fast and complete destruction of TCE in nano system is probably due to the high surface energy of nanosized particles which could change the mechanism of dechlorination with bulk particles.

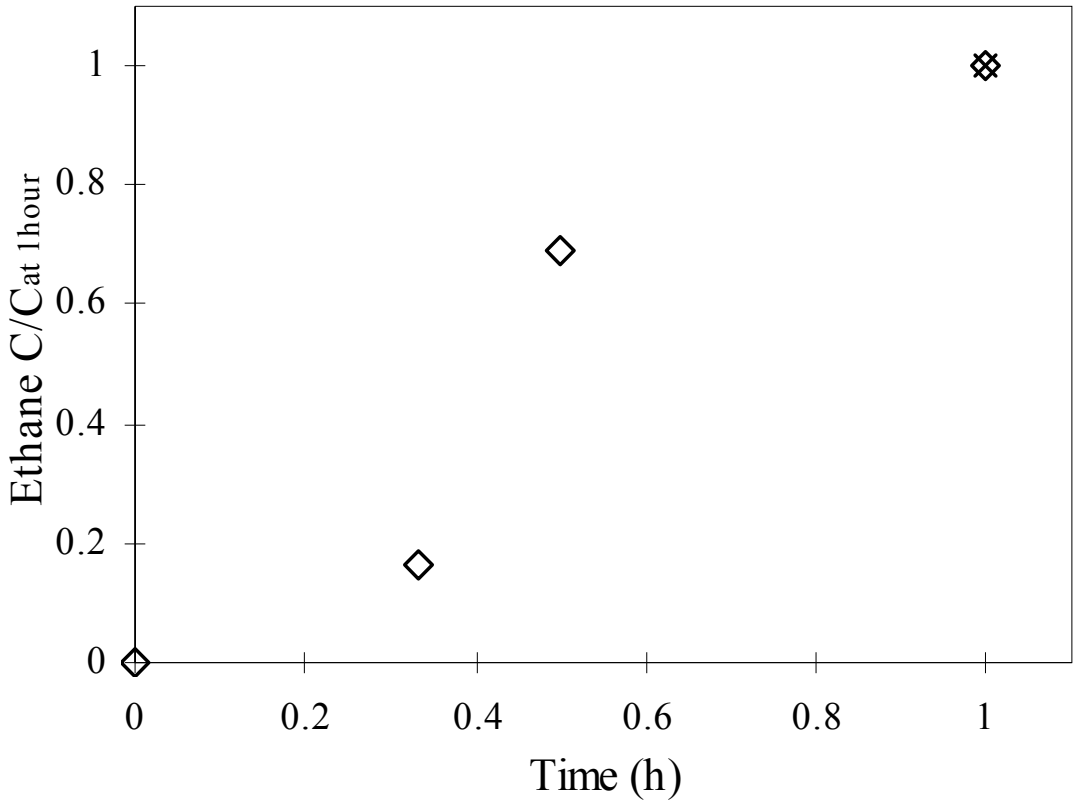

Figure 4.21 Ethane production in 0.5mL headspace from (◇) dechlorination of 10mg/L TCE by nano Fe/Ni (reducing Fe followed by Ni deposition) in PAA/PES membrane; (×) 30mL pure TCE dechlorination by nano Fe/Pd in PAA/PES membrane in the presence of 5 μL water. The amount of ethane was expressed as the peak area ratio to the 1 hour dechlorination by Fe/Ni (Xu and Bhattacharyya, 2005a).

In bimetallic nano system (Fe/Ni, Fe/Pd), the dechlorination rate is further promoted by the catalytic hydrogenation as well as enhanced iron corrosion because of secondary electropositive metal (Ni or Pd). Both Ni and Pd are well known catalysts for hydrogenation reaction (Ciebien et al., 1999; Brown and Brown, 1963; Brown 1970). The presence of a second electropositive metal could accelerate the dissolution of iron and provide a less fouling surface for reductive reaction (Gotpagar et al., 1999). The standard oxidation reduction potentials of these metals relative to a hydrogen electrode are +0.987 (Pd), -0.250 (Ni), -0.440(Fe).

Nanoscale Fe/Ni particles immobilized in the membrane matrix showed a higher reaction rate than those prepared in solution phase. Within 1 hour, more than 90% TCE was degraded by Fe/Ni in PAA/PES membrane, while only 50% TCE was dechlorinated by Fe/Ni prepared without membrane under the same metal loading. The corrosion of Fe^0 during the dechlorination reaction implies the release of ferrous ions and increase of pH in solution which can form iron hydroxide film on particles. Therefore, the unreactive hydroxide coating could decrease the reaction rate due to the loss of reactive sites (Matheson and Tratnyek, 1994). In the presence of PAA membrane, however, the formation of iron metal hydroxide film can be prevented because ferrous ions were recaptured by carboxylic group of PAA. This is one of the important advantages of using polyelectrolyte membranes containing nanoparticles. For Ni_2B system, no obvious TCE degradation was observed within two hours, indicating that Ni_2B as a poor electron donor at room temperature and is unable to dechlorinate TCE without active hydrogen provided by iron corrosion.

Dechlorination of Pure TCE and Role of Water

In order to investigate the role of H_2O in the TCE dechlorination with the bimetallic metal system, pure TCE dechlorination in the absence of water with bimetallic particles in membrane platform was performed. Fe/Pd (40 mg) particles immobilized in PAA/PES membranes were added into 30 mL pure TCE. Although the PES support membrane was partially dissolved in TCE, the metal particles were still immobilized inside the cross-linked PAA matrix. No ethane and other intermediate chlorinated

compounds were detected in the gas phase after 1 hour, indicating no dechlorination reaction took place in pure TCE without water which is the donor of active hydrogen and corrosion of Fe. Subsequently, 5μL DIUF water (water concentration in TCE = 9mM) was deliberately added into the 30 mL pure TCE solution, and ethane was identified in the gas phase after 1 hour. The peak area of ethane production was roughly the same as that in dechlorination of 10mg/L TCE in aqueous solution (Figure 4.21), suggesting the dechlorination reaction requires the presence of some water to facilitate the corrosion of the primary metal (Fe) to generate active hydrogen for the catalytic dechlorination. It is well known that both Pd and Ni could promote dechlorination of TCE. In the bimetallic system, iron serves primarily as electron donor which provides hydrogen by the reduction of water (corrosion of iron), while the second metal Ni or Pd acts as a catalyst [2,6] which has the ability to adsorb hydrogen into its lattice and maintain high surface concentration of hydrogen. In the presence of the second catalytic metal Pd or Ni, TCE was adsorbed and preferentially dehalogenated on the bimetallic Fe/Pd (or Ni) surface by active hydrogen, which can greatly increase the transformation rate of TCE.

Dechlorination Reaction Rates

In order to get better comparison of the reaction rates at different conditions, it is necessary to normalize the reactivity per unit metal surface area as originally proposed by Tratnyek. The dechlorination rate in a batch system can be described by the pseudo-first-order model (Lien and Zhang, 2001; Zhang et al., 1998).

$$\frac{dC}{dt} = -k_{SA} a_s \rho_m C \qquad \text{(E4.1)}$$

Where C is concentration of total organic compound (mg/L); k_{SA} is surface-area-normalized reaction rate coefficient (L h^{-1} m^{-2}); a_s is specific surface area of metal particles (m^2 g^{-1}); ρ_m is mass concentration of metal (g L^{-1}); and t is time (h). For each specific batch experiments, a_s, and ρ_m can all be considered as constants. Assuming all particles are spherical and discrete, the available particle surface area per unit weight can be calculated based on the particle diameter which was obtained from the statistical analysis of the SEM image (Fe/Pd and Fe/Ni particles in membrane domain). The particle

distribution analysis showed similar size. This is to be expected for the case when Pd or Ni was post deposited after forming the Fe particles. Best linear fit values of the k_{SA} were obtained in Figure 4.22 by using the experimental dechlorination results of Figure 4.20. Logarithmic values of TCE concentrations are plotted versus time and k_{SA} value of at various reaction conditions were given in the Table 4.3.

As discussed before, the reaction rate of Fe/Pd was the highest (k_{SA} = 0.948 L h^{-1} m^{-2}), suggesting Pd has higher catalytic reactivity than Ni in the bimetallic system. For TCE dechlorination by Fe/Ni particles, the k_{SA} value varied with the method used to prepare them. The k_{SA} value of Fe/Ni prepared inside membrane domain was higher than that synthesized in solution phase.

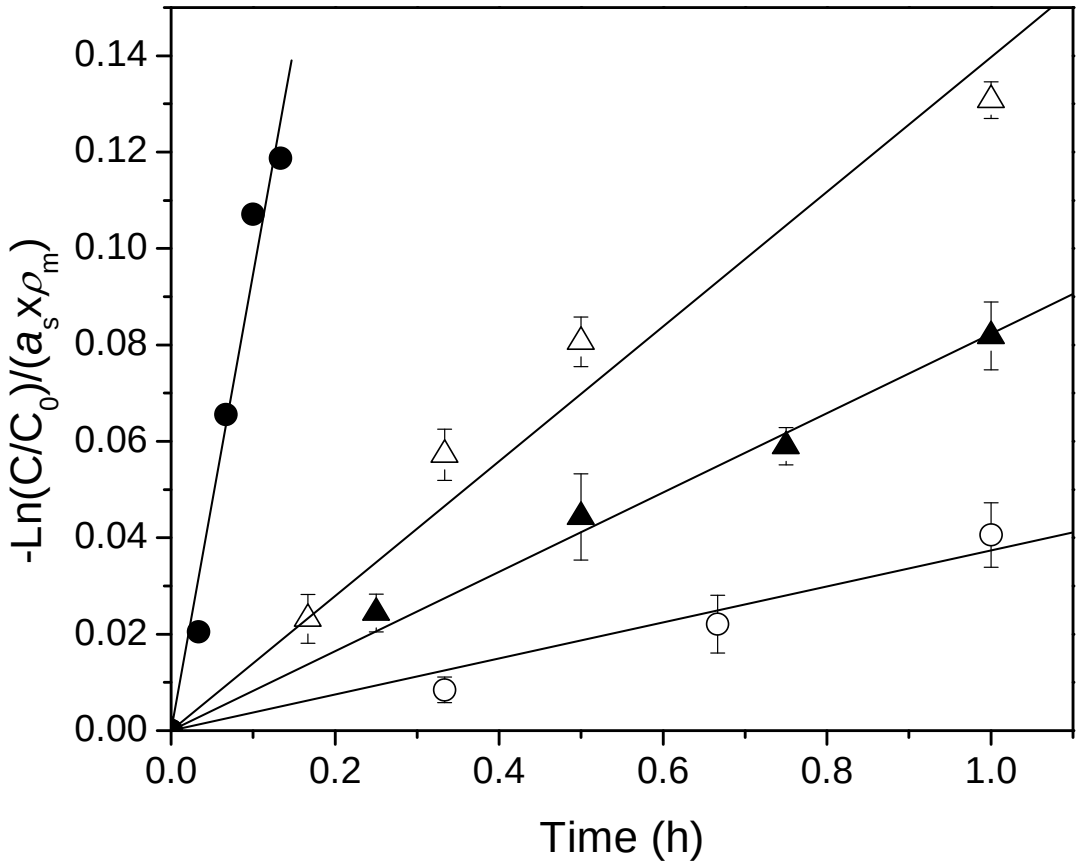

Figure 4.22 Best linear fit of k_{SA} for dechlorination results with (●) nanoscale Fe/Pd in PAA/PES membrane; (△) Nano Fe/Ni in PAA/PES membrane (reducing Fe followed by Ni deposition); (▲) Nano Fe/Ni in PAA/PES membrane (simultaneous reduction of Fe and Ni); (○) Nano Fe/Ni reduced simultaneously in solution phase (Xu and Bhattacharyya, 2005a).

Table 4.3 Values of Surface-Area-Normalized Rate Coefficients k_{SA} (L h^{-1} m^{-2}) (Xu and Bhattacharyya, 2005a)

Reaction system	Synthesis method	k_{SA} (L h^{-1} m^{-2})	R^2
Fe/Pd	Pd deposition on Fe in membrane domain	0.948±0.05	0.969
Fe/Ni	Reducing Fe followed by Ni deposition in membrane domain	0.1395±0.006	0.983
Fe/Ni	Simultaneous reduction of Fe and Ni in membrane domain	0.0813±0.002	0.989
Fe/Ni	Simultaneous reduction Fe and Ni in solution phase	0.0378±0.003	0.962

Beside the deactivation by iron hydroxide film formed on metal surface in the absence of PAA membrane, the difference in reaction rate is probably due to the small and discrete particles formed in the membrane phase. Nanoparticles prepared in the solution phase without stabilizing polymer forms innumerable chains of beads because of the excessive agglomeration of metal atoms. The dechlorination rate of TCE is a strong function of the total surface area of metal particles. Since the surface area is calculated under the assumption that all particles are discrete, excessive aggregation of nanoclusters in solution phase will cause less surface area or loss of the available reactive sites which results in the decrease of k_{SA}.

On the other hand, the membrane matrix can also play an important role in the overall rate of destruction of TCE. The reaction rate discussed here is the overall (or observed) reaction rate which includes the intrinsic reaction rate and adsorption rate of TCE to reactive sites (nanoparticles). It is well know PES is a highly hydrophobic polymer and thus one would expect a strong interaction with hydrophobic compound such as TCE, i.e. a higher partitioning rate for TCE. Based on the TCE analysis of the PES/PAA membrane control, 90% TCE was adsorbed by the membrane matrix after 2 hours. Figure 4.23 shows the schematic diagram for degradation of TCE by nanosized bimetallic particles immobilized in the PAA/PES membrane. TCE adsorption on reactive sites can be achieved by transfer in aqueous phase or diffusion in membrane matrix. TCE diffusion rate inside membrane matrix is higher than the rate in aqueous phase because of the hydrophobic property of the PES. This could enhance the overall dechlorination rate due to the lower transfer resistance of TCE in membrane domain.

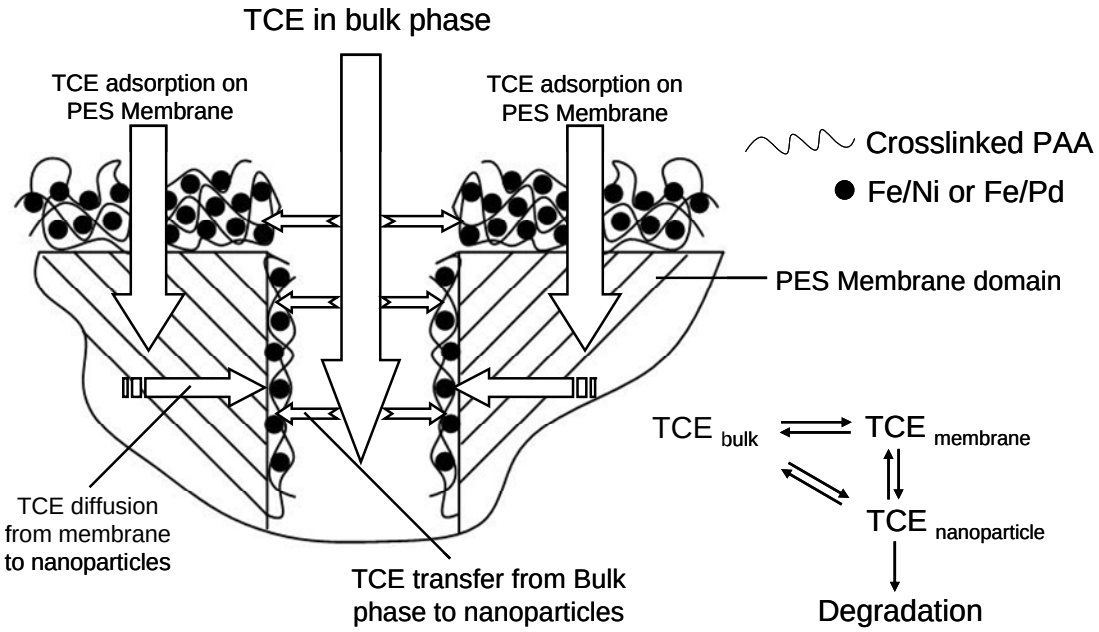

Figure 4.23 Schematic diagram for degradation of TCE by nano bimetallic particles immobilized in the PAA/PES membrane.

However, even for Fe/Ni synthesized in the same membrane domain, the reaction rate was different from the method to prepare bimetallic Fe/Ni particles. As shown in the Table 4.3, reducing Fe followed by Ni deposition gives a higher k_{SA} value than the system where iron and nickel are reduced simultaneously inside membrane. It is believed that in a bimetallic Fe/Ni complex system, Fe needs to be in close contact and covered by Ni in order for catalysis to be effective. Physically mixed Fe/Ni particles or Ni particles covered by Fe provided no better dehalogenation of TCE than Fe alone (Schrick et al., 2002). When Fe and Ni were reduced simultaneously, some of Fe particles may be isolated from Ni which has been proven in the STEM EDS line profile (Figure 4.12) and STEM EDS mapping images (Figure 4.13). Thus, reducing Fe particles followed by Ni deposition provides a better way to produce ideal Fe/Ni bimetallic particles in which significant numbers of iron particles are covered by Ni.

According to the definition of the surface-area-normalized reaction rate coefficient, k_{SA} should be ideally the same in different metal systems if the reaction rate is only dependent on the surface area. This is true only when surface reactive sites are independent of particle size and/or dopant (such as Ni, Pd) materials are absent. However, the variations of k_{SA} in Figure 4.22 suggest that overall TCE dechlorination rate in bimetallic system is also affected by other factors such as the catalytic reactivity of the secondary metal, elemental distribution of primary and secondary metal or concentration of reactive sites, adsorption rate of TCE to reactive sites. The reaction model developed by Johnson (Johnson et al., 1996) provides a better way to explain and quantify the effect of variation in reactivity of different metal system

$$\frac{dC}{dt} = -k_2 \Gamma a_s \rho_m C \qquad \text{(E4.2)}$$

Where k_2 is the second order rate constant (including intrinsic rate and mass transfer rate) and Γ is the surface concentration of reactive sites (catalytic sites in bimetallic system). In this model, k_{SA} is expressed as the product of k_2 and Γ, which is more reasonable when dechlorination reaction preferentially occurs at the reactive catalytic surface sites (Fe/Ni, Fe/Pd). For dechlorination with Fe/Ni system inside membrane domain, reducing Fe followed by Ni deposition gives faster reaction rate because of higher Γ (reactive sites) where Fe and Ni are in close contact. This elemental

distribution of Fe and Ni in nano domain has been proven by STEM EDS line profile (Figure 4.12) and EDS mapping image (Figure 4.13). Further more, the ratio of Γ in two different Fe/Ni systems inside membrane matrix can be calculated based on the k_{SA} value because k_2, a_s, and ρ_m are the same in both cases. According to the value in Table 4.3, the reactive sites of Fe/Ni (Ni deposition on Fe) are 1.7 times higher than that of Fe/Ni (simultaneous reduction of Fe and Ni). The faster rate obtained by Fe/Pd than Fe/Ni is due to the larger k_2 which is dependent on the higher catalytic reactivity of Pd. The slower rate by Fe/Ni synthesized in solution phase is probably due to the slower adsorption rate which decrease k_2, and the formation of hydroxide precipitates on the metal surface, which would reduce Γ. Further studies are required for the quantification of Γ in dechlorination with bimetallic systems.

4.5.2 TCE Dechlorination by Bimetallic Nanoparticles in PAA/PVDF Membranes (Dip-coating)

The reactive properties of the bimetallic Fe/Ni nanoparticles in PVDF membranes dip-coated with PAA were examined by reduction of TCE in water at room temperature. TCE contamination of groundwater is widely reported in the literature. Figure 4.24 shows the batch reaction (at pH 6) of TCE with Fe/Ni (Ni = 25 wt%) nanoparticles in PAA/PVDF membranes. The TCE transformation rate can be described by a simple pseudo-first-order model (E4.1). Complete dechlorination of TCE was achieved within 2 hours. Ethane and Cl^- were formed as the only products in the headspace and aqueous phase respectively. No chlorinated intermediates were detected and 92% carbon balance and 93% Cl balance were obtained in the whole system, indicating a direct reaction pathway from TCE to ethane for bimetallic Fe/Ni (Ni = 25 wt%) nanoparticles.

The complete conversion of TCE to ethane with bimetallic nanoparticles is totally different from the sequential reductive dechlorination with monometallic Fe system. For the Fe system TCE is transformed to dichloroethylene (DCE) to vinyl chloride (VC) and finally to ethylene and ethane (Orth and Gillham, 1996). The presence of the secondary metal on nanosized Fe changes the reaction pathway dramatically (Schrick et al., 2002; Zhang et al., 1998). In the monometallic Fe system, the dechlorination mechanism is

preferably explained by dissociative electron transfer resulting in the formation of less chlorinated radicals as intermediates (Matheson and Tratnyek, 1994). While in the bimetallic system, Fe is considered as the reductant for water to generate hydrogen and TCE is dechlorinated by catalytic hydrodechlorination (Liu et al., 2005) in the presence of Ni, resulting in the direct reduction to ethane. Another advantage of coating the secondary metal is to prevent the conversion of the Fe^0 to an oxide form (Fe_xO_y) which can deactivate the nanoparticle surface (Matheson and Tratnyek, 1994).

It has been reported in earlier studies that dechlorination reaction can be described by a pseudo-first-order kinetic model. The TCE degradation rate by Fe based bimetallic nanoparticles is considered as first order in terms of both TCE concentration and the concentration of metals available in the solution. Therefore, E4.1 was used in many literatures (Johnson et al., 1996) to describe this pseudo-first-order reaction model.

$$\frac{dC}{dt} = -k_{SA} a_s \rho_m C \tag{E4.1}$$

Regression of the kinetic data can be used to determine the surface area normalized reaction rate constant k_{SA}. Since k_{SA} is the characterized first-order reaction rate, it should be independent of variance of reaction conditions such as initial TCE concentration, metal mass and the volume of reaction system. In order to confirm the independence of k_{SA} and pseudo-first-order reaction assumption, TCE dechlorination by Fe/Ni nanoparticles (Ni = 25 wt%) in PAA/PVDF membranes were conducted at various conditions such as different TCE concentration, metal loading, and the volume of the reaction system. Figure 4.25 shows the Logarithmic values of TCE degradation versus time and the best linear fit regression at various reaction conditions. As shown in the figure, the Logarithmic TCE concentration data divided by corresponding metal surface area at different reaction conditions generally overlap and appear equivalent expected value. This indicates that the independence k_{SA} for the TCE dechlorination at different conditions. k_{SA} is a unique value for the same type of metal particles regardless of the reaction conditions. Therefore, k_{SA} can be used to compare the reactivities of different types of metal particles.

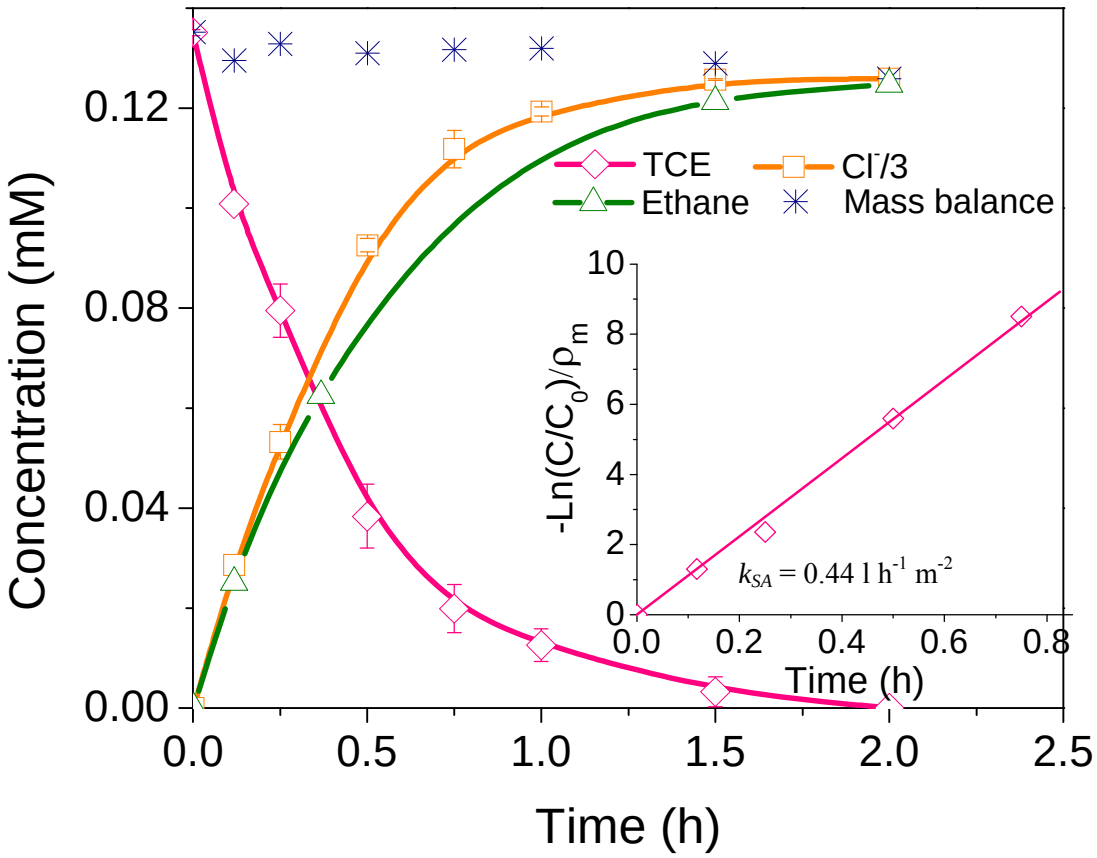

Figure 4.24 Batch reaction of TCE dechlorination and products formation (ethane and chloride) with Fe/Ni (Ni = 25 wt%, post coat Ni) nanoparticles in PVDF membranes dip-coated with PAA. $\rho_m = 0.2$ g l^{-1} (Xu and Bhattacharyya, 2005b).

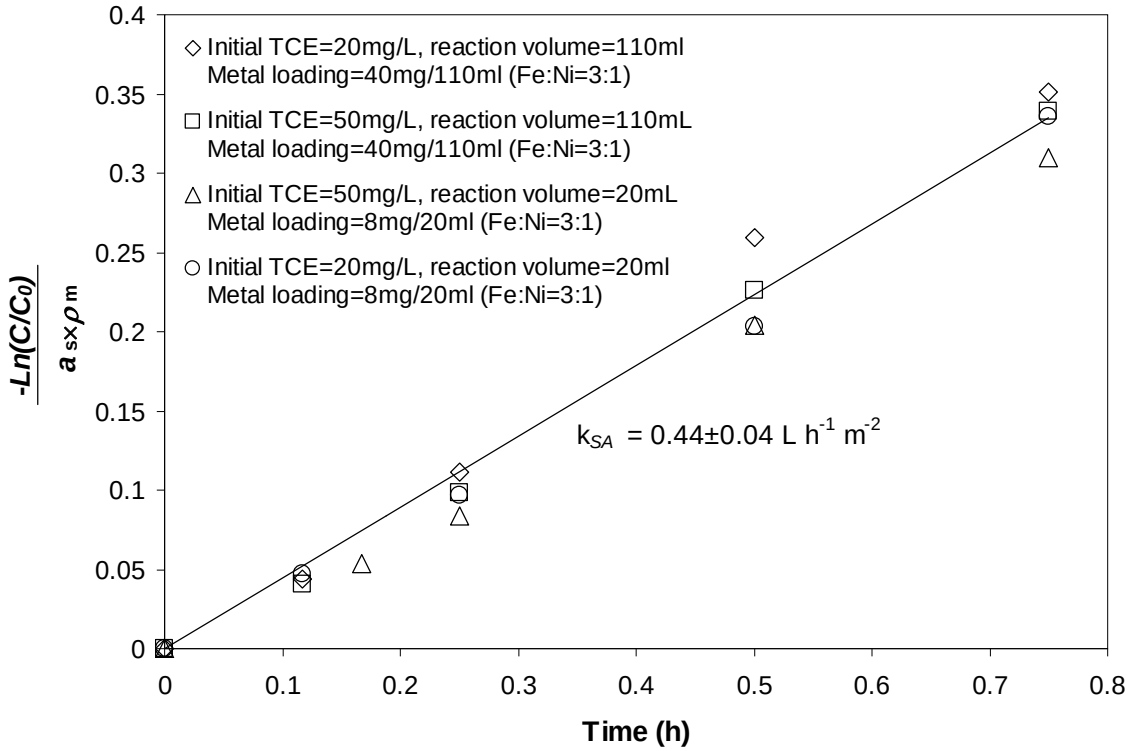

Figure 4.25 Independence of surface-area-normalized dechlorination rate (k_{SA}) on reaction volume, initial organic and concentration. Best linear fit of k_{SA} for dechlorination results with Fe/Ni (Ni=25 wt%, post coating Ni) nanoparticles in PVDF membranes dip-coated with PAA at different reaction conditions.

Effect of Ni coating composition on the reactivity

Shrick et al. (2002) reported that physical mixture of nano Fe and nano Ni particles also decrease the catalysis efficiency, indicating that only close contact of Fe and Ni can be considered a catalytic reactive site (Schrick et al., 2002; Zhang et al., 1998). Thus the Ni coating amount or the Ni layer thickness of the core/shell nanoparticles is extremely critical to obtain maximum reactive sites. Insufficient or excessive coating of Ni may cause the formation of Fe-rich surface or Ni-rich surface, which lowers the catalytic efficiency.

TCE dechlorination experiments with bimetallic nanoparticles were also conducted to understand the effect of Fe and Ni distribution on reactive properties. It has been recognized that Fe atoms and Ni atoms located at the particle surface need to be in close contact in order to become a catalytic cell. The EDS mapping results (not shown here) of Fe/Ni nanoparticles with 2 wt% Ni content showed large amount of surface sites containing isolated Fe atoms where no catalytic hydrodechlorination occurs, which reduce catalytic sites dramatically. This has been proven by the lower TCE degradation rate (k_{SA} = 0.04 l h^{-1} m^{-2}, Figure 4.26). The formation of ethylene found in the products (Figure 4.27) also confirms the presence of isolated Fe atoms where TCE can only be reduced by dissociative electron transfer. The EDS mapping results showed a dominating Ni distribution at the surface of Fe/Ni nanoparticles with 80 wt% Ni. The high amount of Ni coating can inhibit the formation of hydrogen from the Fe^0 corrosion reaction and thus lower the efficiency of catalytic hydrodechlorination which requires the presence of hydrogen. This has been also confirmed by the lower TCE degradation rate (k_{SA} = 0.032 l h^{-1} m^{-2}) in Figure 4.26.

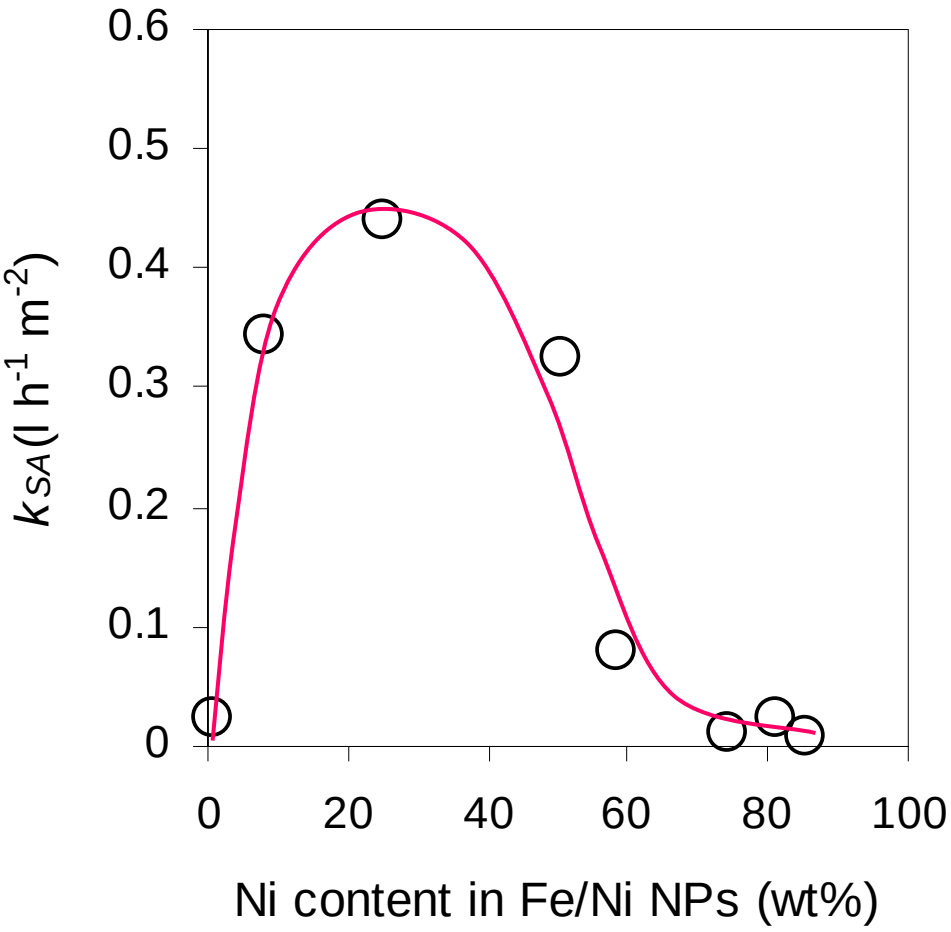

Figure 4.26 TCE dechlorination rate constant variation of Fe/Ni nanoparticles with different Ni composition in PVDF membrane dip-coated with PAA (Xu and Bhattacharyya, 2005b).

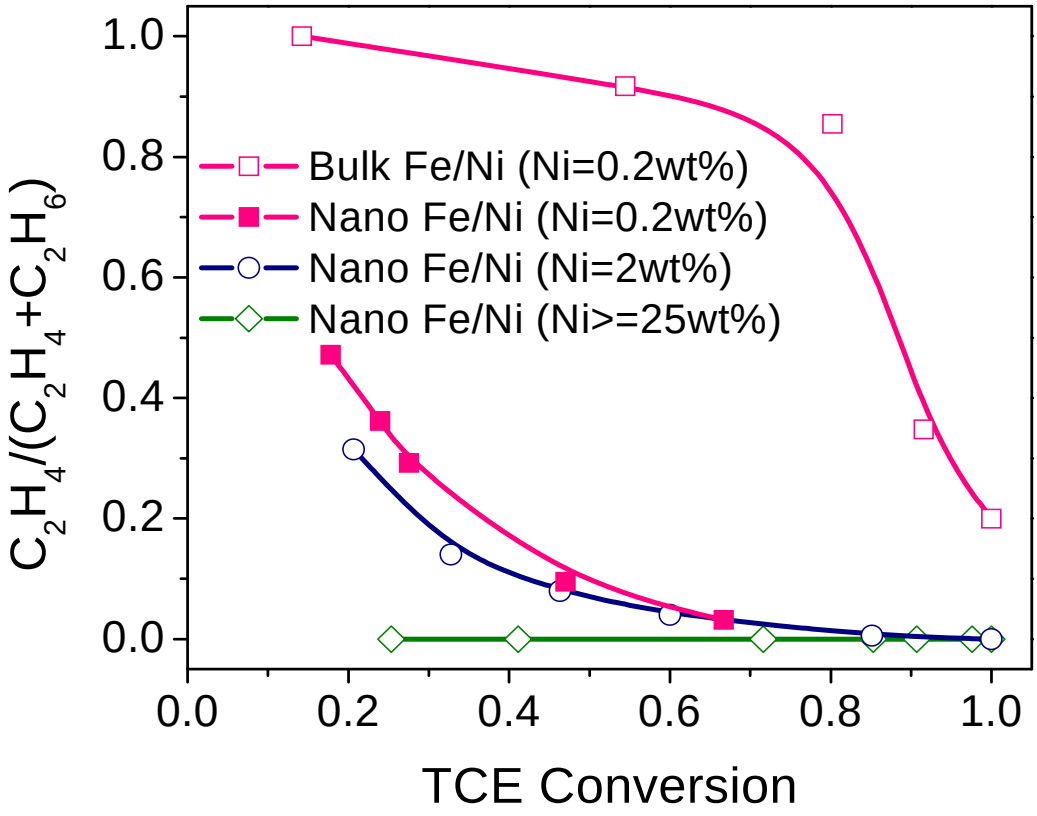

Figure 4.27 Ethylene and ethane formation from TCE dechlorination with various Fe/Ni nanoparticles in PVDF membranes dip-coated with PAA and bulk Fe (commercial, about 150 μm) particles post-coated with Ni (Xu and Bhattacharyya, 2005b).

It is important to point out that Fe/Ni nanoparticles containing 2 wt% Ni and 80 wt% Ni show similar TCE degradation rates, but the dechlorination products are different. Only ethane was obtained for the TCE dechlorination by Fe/Ni nanoparticles with 80 wt% Ni, indicating a direct reduction pathway. However, Fe/Ni nanoparticles with 2 wt% Ni exhibit a combination of catalytic hydrodechlorination by Fe/Ni and dissociative electron transfer by Fe^0 due to the formation of ethylene and ethane.

EDS mapping results of Fe/Ni nanoparticles with 25 wt% Ni showed the optimum metal distributions. The high TCE transformation rate (k_{SA} = 0.44 l h^{-1} m^{-2}) observed in the Figure 4.26 verifies the presence of high amount catalytic reactive sites. The absence of ethylene in the products also implies negligible formation of isolated Fe atoms at the nanoparticle surface.

We also investigated the impact of particle size (nano versus bulk) on the reactive properties by comparing the TCE dechlorination with nano Fe/Ni and bulk Fe/Ni (no membrane) at the same amount Ni content (0.2 wt%). The TCE transformation rate of nano Fe/Ni (~ 30 nm) was found to be about 13 times higher than that of bulk Fe/Ni, which is expected due to the higher surface area of nanoparticles. The dechlorination products (Figure 4.27) were also analyzed to understand the reaction pathway in these two different systems. In the bulk Fe/Ni system, cis-DCE (not shown in the Figure 4.27) and ethylene were the main products at low TCE conversion rate, and more ethylene was converted to ethane with the increase of TCE degradation. This indicates that TCE is mainly dechlorinated in the sequential reduction pathway (electron transfer), and the presence of Ni enhances the hydrogenation of ethylene to ethane. While in the nano Fe/Ni system, no formation of chlorinated intermediates was observed and ethylene was only formed at low TCE conversion rate. Ethane appeared as the main product even at low TCE conversion rate and become the dominating compound at high TCE conversion (> 50%). Hence, in the nano Fe/Ni system, TCE is mainly degraded by direct reduction pathway according to the products information.

TCE dechlorination with various bimetallic nanoparticles

In order to further understand the catalytic dechlorination mechanism and bimetallic nanoparticle reactivity, TCE dechlorination experiments were conducted with bimetallic nanoparticles with different type of dopant metal and different structure. Figure 4.28 shows the normalized rate constant (k_{SA}) of TCE dechlorination using PAA/PVDF membrane based Fe/Cu nanoparticles, alloy Fe/Ni nanoparticles (simultaneous reduction of Fe and Ni), and core-shell Fe/Ni nanoparticles (post coating Ni). The second metal composition was kept the same (25 wt%) for all the three reaction systems. As expected, the core-shell Fe/Ni nanoparticles exhibit higher TCE degradation rate than the alloy Fe/Ni nanoparticles. k_{SA} for core-shell nano Fe/Ni is about four times higher than that of alloy nano Fe/Ni. It has been demonstrated that the most Ni atoms are located at the out side of iron surface for the core-shell structure. The alloy structure has a homogenous distribution of iron and nickel atoms inside particle, which results in lesser amount of Ni atoms on the surface. Since the Ni is the active sites for the catalytic hydrodechlorination reaction and the reaction only takes place at the particle surface, the lower k_{SA} for alloy Fe/Ni nanoparticles is due to the less active sites (Ni atoms) on the surface.

Compared to the Fe/Ni nanoparticles, Fe/Cu nanoparticles show a much slower reaction rate. k_{SA} for core-shell Fe/Cu nanoparticles is about 30 times lower than core-shell Fe/Ni nanoparticle at the same dopant composition. In order to understand the reactivity difference between Cu and Ni, the product formation was measured for TCE degradation with Fe/Cu and Fe/Ni nanoparticles. As shown in the Figure 4.29, the dominating product for Fe/Cu system is ethylene, suggesting the main reduction pathway is by electron transfer. In contrast, ethane is the only product formed in the Fe/Ni system due to the catalytic hydrogenation mechanism. This observation is consistent with the result reported in the literature (Cwiertny et al., 2007) for the cis-dichloroethylene (cis-DCE) dechlorination by Fe/Ni and Fe/Cu particles. Ni and Pd are proven the most active dopant for the reductive dechlorination reaction due to the high hydrogenation activity.

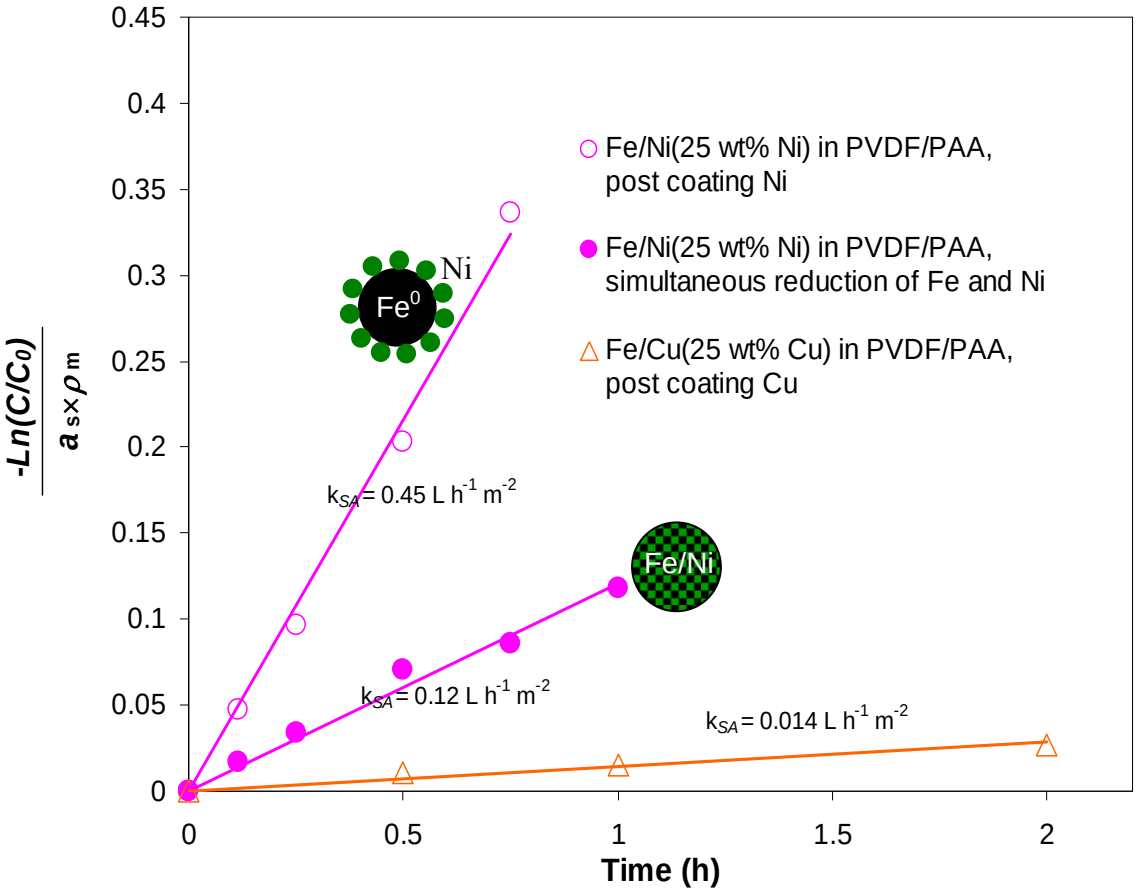

Figure 4.28 Best linear fit of k_{SA} for dechlorination results with (○) Fe/Ni (Ni=25 wt%, post coating Ni) nanoparticles in PAA/PVDF membranes; (●) Fe/Ni (Ni=25 wt%, simultaneous reduction of Fe and Ni) nanoparticles in PAA/PVDF membranes; (△) Fe/Cu (Cu=25 wt%, posting coating Cu) in PAA/PVDF membranes.

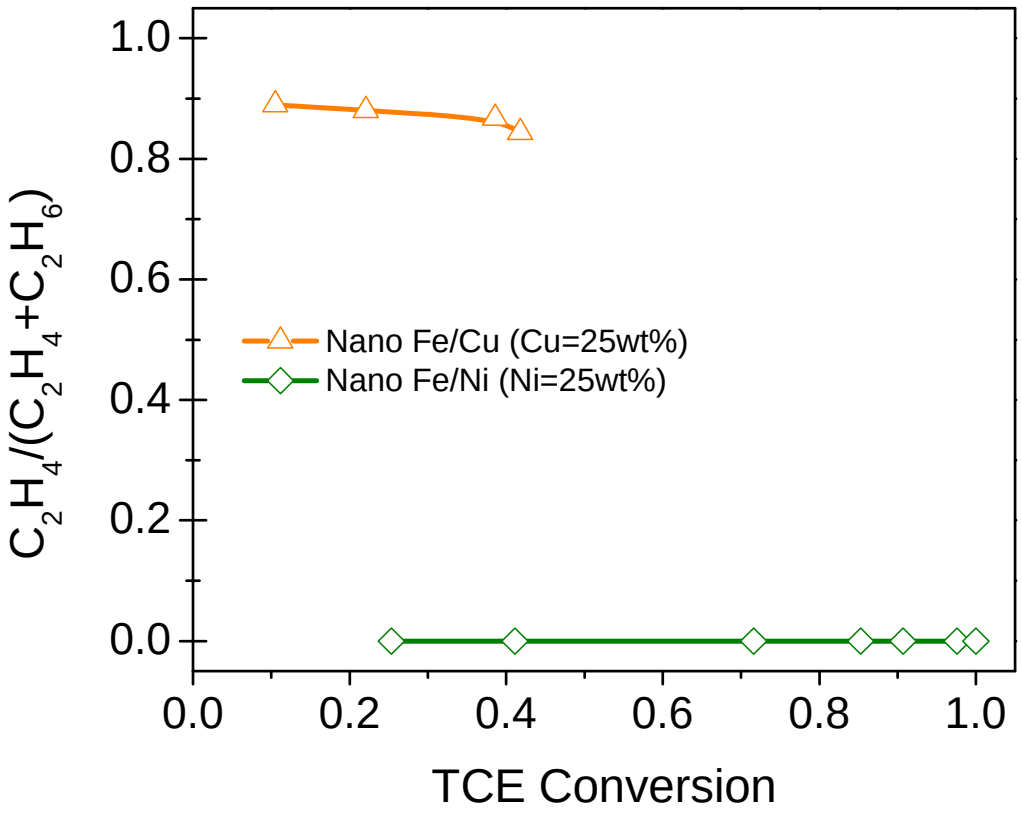

Figure 4.29 Ethylene and ethane formation from TCE dechlorination with Fe/Ni (Ni = 25 wt%, post coating Ni) nanoparticles and Fe/Cu nanoparticles (Cu = 25 wt%, post coating Cu) in PVDF membranes dip-coated with PAA.

Effect of pH

The reductive dechlorination with zero valent metals is initialized by the corrosion reaction of Fe^0 which produces the electrons and hydrogen gas. Since the iron corrosion reaction is highly dependent of the solution pH, pH has a great effect on the reductive degradation of TCE. The solution pH also affects the status of ferrous ions formed from corrosion reaction. At higher pH values, ferrous ions form ferrous hydroxide or ferric hydroxide if O_2 is present which can be deposited on the Fe^0 surface and deactivate the nanoparticles. Low pH promotes the corrosion reaction and H_2 generation, and allows Fe^0 surface to remain active for the reaction by preventing the formation of iron hydroxide. But the fast corrosion reaction at low pH may consume Fe^0 and Ni^0 nanoparticles so quickly that the reaction stops in short time.

Figure 4.30 shows the effect of the solution pH on the dechlorination of TCE by Fe/Ni nanoparticles in PVDF membranes dip-coated with PAA. Since the dechlorination and iron corrosion reaction increase solution pH by consuming H^+, sodium acetate (NaAC, 0.5 M) was used to as the buffer to maintain the pH. As it can be seen from the figure, the TCE dechlorination at initial pH of 5.85 without buffer shows the highest the reaction rate. Since no buffer was used, the final pH increased to 10.05. In the presence of 0.5 M NaAC, the reaction rate at initial pH of 6.65 is about two times higher than that at initial pH of 8.50. This result is consistent with the general trend of decreasing reaction rate with increasing pH observed for the other TCE reduction studies reported in the literature (Liu and Lowry, 2006). The lower rate could be explained by low hydrogenation efficiency because less hydrogen was produced at higher pH. The lower rate at higher initial pH is also due to the formation of iron hydroxide which can be deposited on the nanoparticle surface and deactivate the nanoparticles. For the TCE dechlorination without using buffer, the reaction rate remained highest even at pH 10.05 which is the highest in all the cases. The high reaction rate at high pH is due to the ion-exchange function of PAA. Previously, PAA was attached to membrane to capture Fe^{2+} for iron nanoparticle synthesis. In the dechlorination reaction, PAA can also act as the ion-exchanging polymer to recapture the ferrous or ferric ions generated in solution to avoid the precipitation of iron hydroxide. This can prevent the deactivation of

nanoparticle surface and extend the reactivity. However, in the presence of 0.5 M NaAC, PAA loses the ion-exchange capability due to the high concentration of Na^+. PAA is preferentially bound with Na^+. In order to prove the recapture of Fe^{2+}/Fe^{3+}, dissolved iron concentration after the dechlorination reaction was analyzed by ICP and the results are shown in the Table 4.4. It can be seen that 1.47 mg Fe in solution was observed at the initial pH of 5.81 in the presence of 0.5 M NaAC. In contrast, only trace amount of Fe (0.032 mg) was detected at the same pH 5.85 without NaAC, indicating the recapture of dissolved Fe by PAA.

TCE dechlorination at the initial pH of 4.25 shows a high initial rate but the reaction rate decreased rapidly. The reaction stops only after 15 mins. The short reaction time is mainly due to the fast consumption of Fe^0 and Ni^0 at low pH, although low pH promotes the hydrogen production and prevents the formation of iron hydroxide. As shown in the Table 4.4, more than 50% Fe^0 was dissolved within 1 hour, while less than 5% Fe was consumed within 1 hour at pH above 7. This confirms the short life time of Fe/Ni nanoparticles at low pH. Therefore, it is advantageous to perform the dechlorination reaction at near neutral pH to obtain and remain high reactivity of bimetallic nanoparticles.

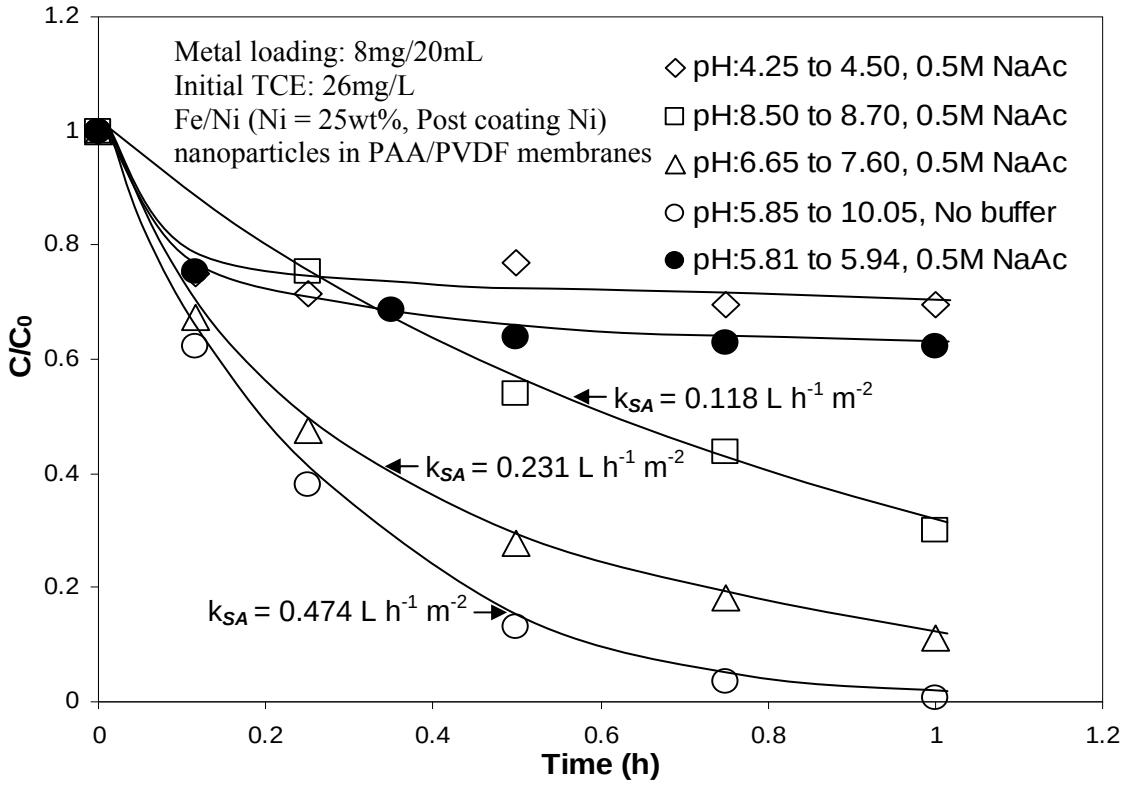

Figure 4.30 TCE dechlorination with PAA/PVDF (dip-coating) membrane supported Fe/Ni (Ni = 25 wt%, post coating Ni) nanoparticles at different pH in 0.5M sodium acetate buffer.

Table 4.4 Dissolved iron concentration in the TCE dechlorination by Fe/Ni (Ni =25 wt%) nanoparticles in PAA/PVDF (dip-coating) membranes at different pH. Metal loading = 8 mg/20 ml

Initial pH	Fe concentration in solution after 1h (mg)
4.25 (0.5M NaAC)	4.3
5.81 (0.5M NaAC)	1.47
6.65 (0.5M NaAC)	0.21
8.50 (0.5M NaAC)	0.10
5.85 (No Buffer, final pH=10.05)	0.032

Stability and Longevity of Fe/Ni Nanoparticle Reactivity

In the reductive dechlorination of TCE or PCBs with iron-based bimetallic particles, iron is also a reactant which is consumed with the reaction. Side reactions such as the oxidation of iron by dissolved O_2 and iron water corrosion also result in the additional loss of Fe. Hence, the durability and longevity of the membrane-based bimetallic nanoparticles are essential for the environmental remediation applications. According to the stoichiometric equation ($C_2HCl_3 + 4Fe^0 + 5H^+ \rightarrow C_2H_6 + 4Fe^{2+} + 3Cl^-$), complete dechlorination of one mole TCE requires four moles of iron. But, the actual amount of iron needed depends on the fraction of Fe^0 in the particle which is available for reaction (Fe^0 in the inner core may not be available), the selectivity of the reaction for TCE dechlorination, and efficiency of hydrogen (from Fe^0 corrosion reaction) utilization (Liu et al., 2005)

In order to examine the long-term performance of Fe/Ni nanoparticles, a multicycle dechlorination experiment was conducted in a 20 ml batch solution containing 80mg Fe/Ni nanoparticles (Ni = 25 wt%) in PAA/PVDF membranes with repeated TCE spiking. TCE concentration in the bath solution was raised from approximate zero to 10.6 mg l^{-1} after each spike of concentrated TCE solution (40 µl 5000 mg l^{-1} TCE in ethanol). As shown in the Figure 4.31, complete degradation of TCE spiked in each cycle was achieved within 15 minutes. After first 12 cycles, PAA/PVDF membranes containing Fe/Ni nanoparticles were stored in batch solution for 48 hours with no TCE spiking. Further four cycles of TCE dechlorination (repeated TCE spiking) were conducted with the same Fe/Ni nanoparticles after 48 hours storation. There is no obvious decline of TCE reduction rate after a period of 16 cycles, and complete conversion to ethane in headspace with no formation of other chlorinated intermediates was also achieved for the last cycle. This indicates insignificant loss of reactivity of membrane-based Fe/Ni nanoparticles for a long period of reaction time. AA analysis of the solution was also performed after 16 cycles of reaction. The final metal ion concentrations in the solution were found to be 0.5 mg l^{-1} for iron and less than 0.1 mg l^{-1} for nickel. Over the 16 cycles of reaction, a total of 0.024 mmol TCE was completely transformed to ethane, which requires at least 0.098 mmol dissolution of Fe^0 based the stoichiometric equation. This could result in the

formation of 275 mg l^{-1} Fe ions in solution even at the absence of other side reactions of iron. Therefore, the lower concentration detected in the solution confirms the recapture of Fe ions by PAA in membranes. The insignificant loss of reactivity of membrane-based Fe/Ni nanoparticles in Figure 4.31 is probably due to the recapture of Fe ions by the membrane which can prevent the nanoparticle surface fouling.

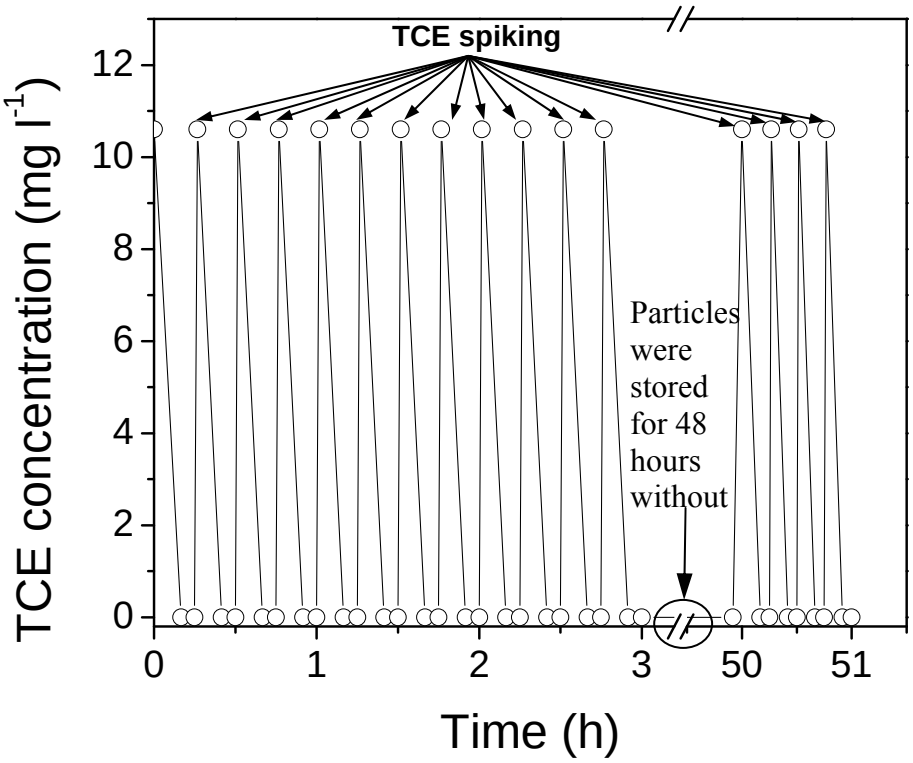

Figure 4.31 The stability and longevity of Fe/Ni nanoparticles in PVDF membranes dip-coated with PAA. TCE degradation with core/shell Fe/Ni (Ni =25 wt%) nanoparticles (in PAA/PVDF membrane) in a repeated spiking experiment. Concentrated TCE solution was spiked into a 20 ml batch solution containing 80 mg Fe/Ni nanoparticles. TCE concentration was raised from 0 to 10.6 mg l^{-1} after each spike. After first 12 cycles, PAA/PVDF membranes containing Fe/Ni nanoparticles were stored in batch solution for 48 hours with no TCE spiking. Further four cycles of TCE dechlorination (repeated TCE spiking) were conducted with nano Fe/Ni particles after 48 hours storation (Xu and Bhattacharyya, 2005b).

4.5.3 Dechlorination of 2, 2'-Dichlorobiphenyl (PCB 4) by Bimetallic Nanoparticles in PAA/PVDF Membranes (Dip-coating)

The Fe/Pd core/shell nanoparticles in PVDF membranes dip-coated with PAA were characterized using TEM and STEM mapping. The reactivity of Fe/Pd nanoparticles were tested through the degradation with environmentally important, toxic PCBs. Figure 4.32 shows the dark field STEM image of Fe/Pd NPs inside PAA membrane. To obtain a thin film for STEM imaging, the membrane sample containing metal nanoparticles was prepared by the same procedure in the particle synthesis step except that a minute droplet of PAA was coated directly on the gold TEM grid (lacey carbon film) instead of the PVDF support membrane. The main purpose of using STEM here is to understand the nanostructure of Fe/Pd nanoparticles by analyzing elemental distribution in the nano domain.

In order to identify the formation of core/shell structure, EDS mapping was performed in STEM mode with Fe/Pd nanoparticles with 1 wt% Pd. (Figure 4.32). The mapping images clearly demonstrate that bimetallic Fe/Pd nanoparticles having a Fe-rich core and a Pd-rich shell. Even for the bimetallic nanoparticles containing only 1 wt% Pd, the core/shell structure is clearly illustrated in the Figure 4.32B. It is important to point out that the STEM-EDS mapping presents us a 2-D image of 3-D sample in transmission (Williams and Carter, 1996).

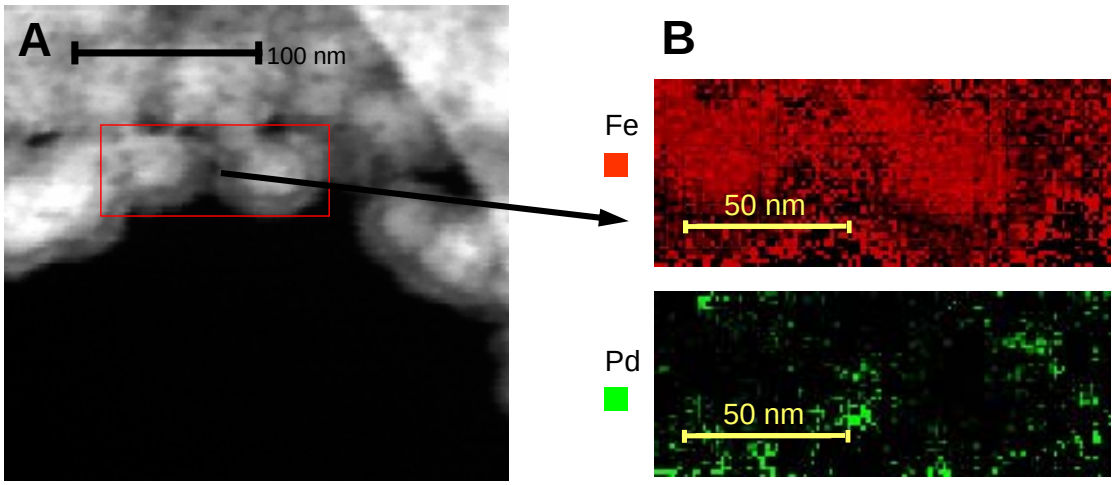

Figure 4.32 Characterization of Fe/Pd nanoparticles. (A) STEM image of Fe/Pd in PAA membrane; (B) EDS mapping image of Fe/Pd (Pd = 1 wt%) in PAA membrane (Xu and Bhattacharyya, 2005b).

The reactive properties of Fe/Pd nanoparticles were then tested toward dechlorination of 2, 2'-dichlorobiphenyl (DiCB, PCB 4) as a model compound at room temperature (~ 25^{o}C). Figure 4.33 shows the batch reaction (at pH 6) results of 8.1 mg l^{-1} PCB 4 in 50/50 vol.% ethanol/water solution with Fe/Pd nanoparticles (Pd = 1 wt%) in PVDF membranes dip-coated with PAA. Complete PCB 4 degradation by Fe/Pd nanoparticles was achieved within 1 hour. Biphenyl was formed as the main dechlorination product. 2-chlorobiphenyl (PCB 1) as the chlorinated intermediate was only identified in the low concentration level. The predominance of final product biphenyl indicates the dechlorination rate of the intermediate was much faster than that of the parent compound. Although the Fe/Pd for the dechlorination of PCB 4 is often referred as metal catalysis, it is not strictly catalytic because Fe is a reactant to generate hydrogen by corrosion reaction. Pd serves as catalyst, and the chlorine atom in PCB 4 is replaced by hydrogen on the Pd surface.

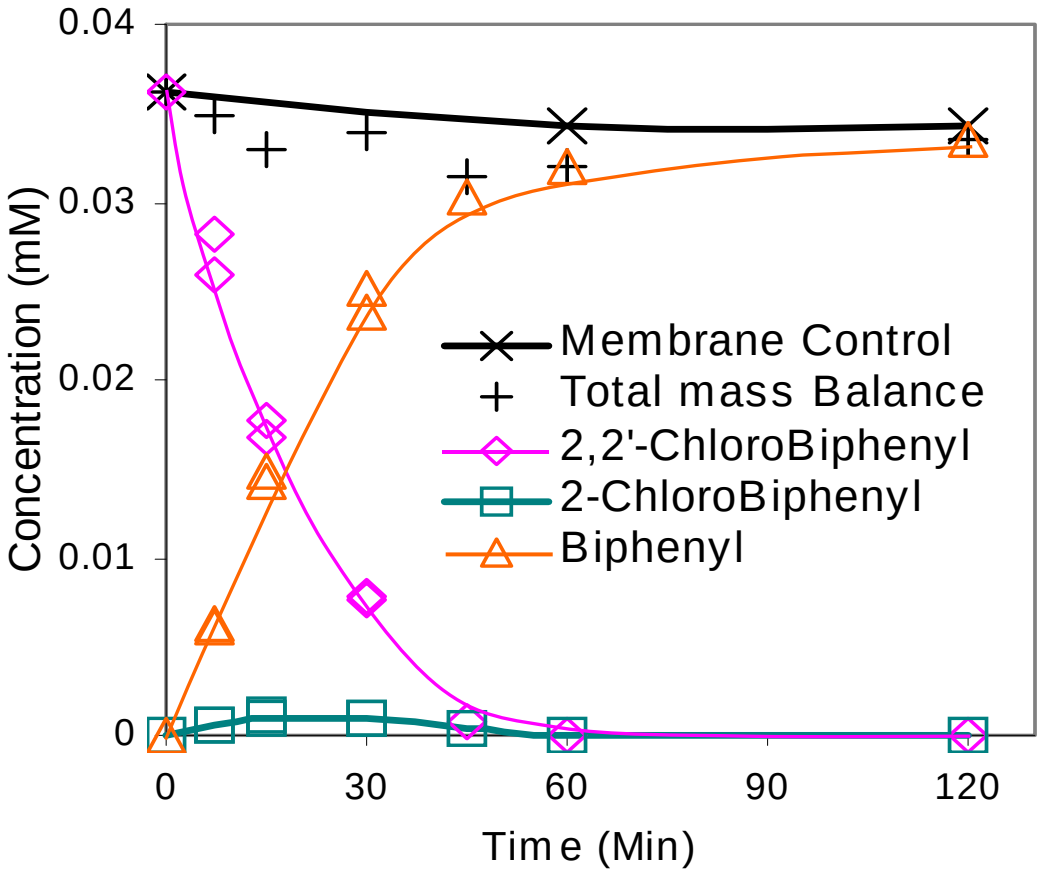

Figure 4.33 Batch reaction of 2, 2'-chlorobiphenyl (PCB 4) dechlorination with Fe/Pd (Pd = 1 wt%) in PVDF membrane dip-coated with PAA at room temperature. Metal loading (ρm) = 1.1 g l^{-1} (Xu and Bhattacharyya, 2005b).

4.5.4 Dechlorination of 2, 2'-Dichlorobiphenyl (DiCB, PCB 4) by Bimetallic Nanoparticles in Pore-filled PAA/PVDF Membranes

To investigate the catalytic properties of Fe/Pd nanoparticles synthesized in pore-filled PAA/PVDF membranes, we studied the reductive hydrodechlorination of PCB 4 using the bimetallic nanoparticles. PCBs are among the most important chlorinated aromatic compounds that cause a stringent environmental problem due to their hydrophobic nature and excellent chemical stability. The dechlorination mechanism and kinetic rates were investigated using pore-filled membrane supported Fe/Pd nanoparticles. In order to understand and quantify the role of second dopant metal, we studied the dechlorination rates as a function of Pd content on Fe as well as the reaction temperature.

Kinetics rates and mechanism

Figure 4.34 shows the concentration profiles for the batch reaction of PCB 4 with Fe/Pd (Pd = 2.3 wt%) nanoparticles in pore-filled PAA/PVDF membranes at 25 °C. The membrane supported Fe/Pd nanoparticles exhibit extremely fast DiCB degradation rate. More than 90% dechlorination of PCB 4 only with 0.8 g L^{-1} metal loading was achieved within 2 hours. Biphenyl was formed as the dominating product. 2-chlorobiphenyl (PCB 1) as the chlorinated intermediate was only identified in the trace level. This indicates a direct reductive pathway due to the higher degradation rate for the chlorinated intermediate. The carbon mass balance based on the sum of PCB 4, PCB 1 and biphenyl was about 91%~95% of the initial amount of PCB 4. The 5%~ 9% mass losses is due to the extraction equilibrium. It has been established that the PCBs dechlorination with Fe/Pd nanoparticles can be described by equation E4.1

$$-\frac{dC}{dt} = k_{obs}C = k_{SA}\rho_m a_S C \qquad \text{(E4.1)}$$

Based the 30 nm average diameter of Fe/Pd nanoparticles identified by TEM, a_S is calculated to be 25 m^2 g^{-1}. ρ_m is the loading of nanoparticles (g L^{-1}). k_{obs} is the observed rate constant (h^{-1}). Based on the best linear fit to the experimental data (R^2 = 0.996), the k_{obs} and k_{SA} determined to be 1.36 h^{-1} and 0.068 L h^{-1} m^{-2}. Complete conversion to

biphenyl was achieved and only trace amount of the intermediate (PCB 1) was detected, which indicates the direct formation of biphenyl pathway for the Fe/Pd nanoparticle system.

Batch experiments of PCB 4 dechlorination with PAA/PVDF supported Fe/Pd nanoparticles were also performed at no mixing conditions to study the effect of external mass transfer on the reaction. As shown in the Figure 4.35, PCB 4 dechlorination rate is much lower than the rate at normal mixing conditions due to the great effect of external mass transfer. After 2 hours, less than 50% conversion of PCB 4 was achieved compared to the complete conversion of PCB 4 at normal mixing condition. The k_{SA} is determined to be 0.014 L h^{-1} m^{-2}, which is about 5 times lower than that at the mixing condition. This indicates the overall dechlorination by Fe/Pd nanoparticles maybe mass transfer limited or mass transfer can not be neglected at least. It should be noted that even at normal mixing conditions, the internal mass transfer resistance inside membrane pore may still exist because of the cross-linked PAA layer. Quantification of mass transfer resistance effect on the PCB dechlorination under convective flow mode will be discussed in the next Chapter.

In order to understand the role of particle size in terms of reactivity and reaction pathway shift, we studied dechlorination of PCB 4 with bulk Fe particles (~120 μm) coated with Pd (Pd = 1.5 wt%). At very high metal loading of 87.5 g L^{-1}, only about 10% dechlorination of PCB 4 was achieved and 2-chlorobiphenyl and biphenyl both appeared at the same concentration level within 8 h (not shown). The slow observed reaction rate is not just due to the lower surface area of the bulk size particles (2 m^2 g^{-1} based on BET analysis). However, the surface normalized rate constant k_{SA} of bulk Fe/Pd particles calculated based on the degradation of PCB 4 is only 0.00011 L h^{-1} m^{-2} which is over 600 times lower than that of membrane supported nanosized Fe/Pd particle. The great difference in k_{SA} indicates the higher reactivity of nanosized Fe/Pd particles. The enhanced reactivity is believed due to the various facets, edges, corners and defects which provide additional sites with high catalytic properties (Henry, 1998). The bulk Fe/Pd system showed a sequential reaction pathway with significant formation of chlorinated intermediates in contrast to direct biphenyl formation pathway for nano Fe/Pd system.

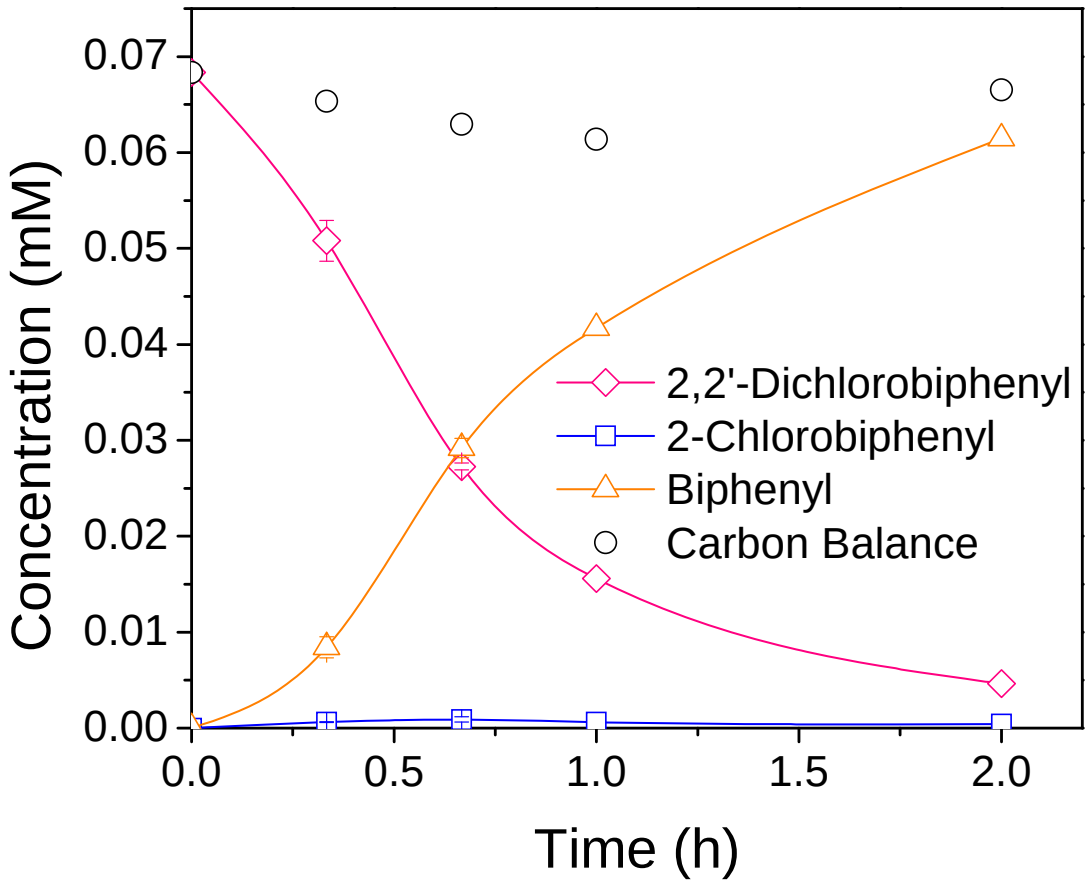

Figure 4.34 Batch reaction of 2, 2'-chlorobiphenyl (PCB 4) with Fe/Pd (Pd = 2.3 wt %) in pore-filled PAA/PVDF membrane at room temperature. Metal loading: 0.8 g L^{-1}. Initial organic concentration: 16 mg L^{-1} (Xu and Bhattacharyya, 2007).

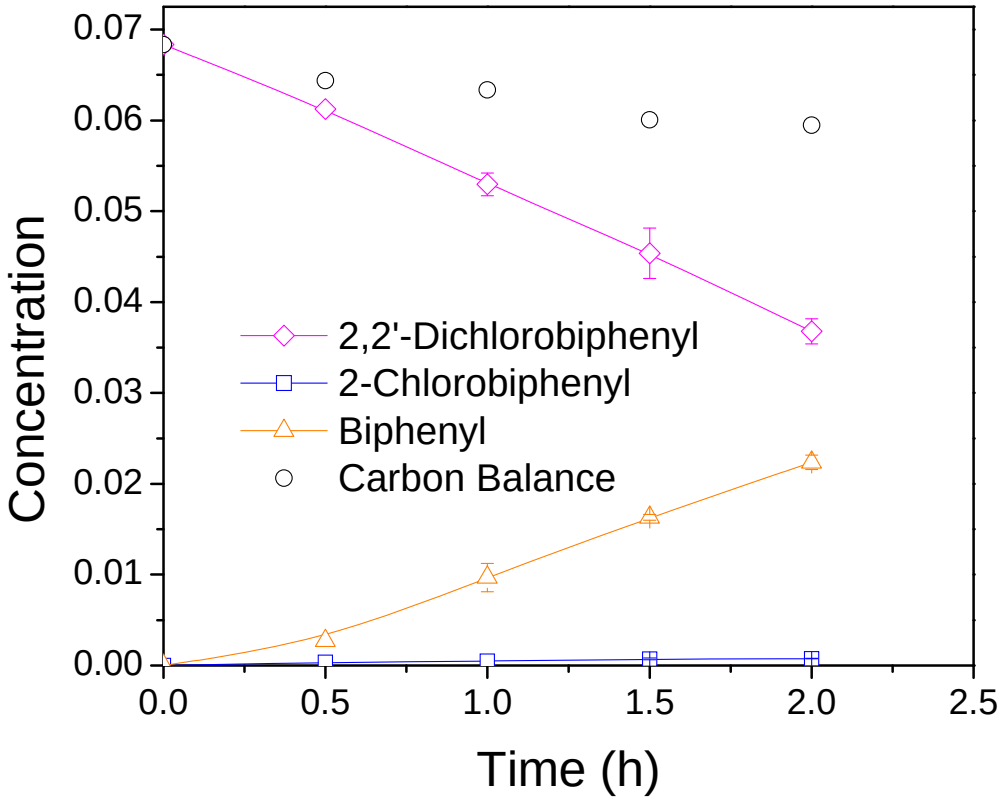

Figure 4.35 Batch reaction of 2, 2'-chlorobiphenyl (DiCB, PCB 4) with Fe/Pd (Pd = 2.3 wt %) in pore-filled PAA/PVDF membrane at room temperature without mixing. Metal loading: 0.8 g L^{-1}. Initial organic concentration: 16 mg L^{-1}.

Reaction mechanism and the role of water

In order to understand the dechlorination mechanism and the role of H_2O in the PCB 4 dechlorination with the bimetallic metal system, PCB 4 dechlorination in batch mode was performed in the absence of water with membrane immobilized Fe/Pd nanoparticles. One piece of PAA/PVDF membrane containing 16 mg Fe/Pd nanoparticles was added into 20 mL solution of PCB 4 (20 mg L^{-1} in pure ethanol). No degradation of PCB 4 and formation of PCB 1 and biphenyl were detected after 2 hours, indicating no dechlorination reaction took place in the absence of water which is the donor of hydrogen from Fe corrosion reaction. Subsequently, 10 μL DIUF water (water concentration = 27 mM) was deliberately added into the 20 mL PCB 4 solution. PCB 1 and biphenyl was identified after 2 hours (Table 4.5). This indicates the hydrodechlorination reaction requires the presence of some water to facilitate the corrosion of the primary metal (Fe) to provide hydrogen and electrons which can be utilized to replace chlorine at the Pd (dopant metal) surface. In the bimetallic system, iron serves primarily as electron donor which provides hydrogen by the reduction of water (corrosion of iron), while the second metal Pd acts as a catalyst (Xu and Bhattacharyya, 2005a; 2005b). The hydrogen gas generated from iron corrosion is adsorbed on the palladium lattice and dissociated into atomic H which is one of the strongest reductant. It is well known that chlorinated organics are strongly adsorbed on the palladium surface by forming Pd-Cl bonds (Bodnariuk et al., 1989; Park et al., 1997). In the Fe/Pd bimetallic system, catalytic hydrodechlorination of dichlorophenol has been reported over the palladium surface by atomic H atoms and electrons provided by Fe-Pd galvanic cells (Wei et al., 2006).

Table 4.5 PCB 4 dechlorination after 2 hrs in pure ethanol and 27 mM water (Xu and Bhattacharyya, 2007)

	PCB 4 (mM)	PCB 1 (mM)	Biphenyl (mM)	Total carbon balance (mM)
Pure ethanol	0.089	*	*	0.089
27 mM water in ethanol	0.08	0.0015	0.0033	0.085

- Initial PCB 4 concentration: 0.089mM (20 mg L^{-1}).
- *: No reaction occurred.
- Metal loading: 16mg/20mL, Fe/Pd (Pd = 2.3 wt %) nanoparticles in PAA/PVDF membrane.

Catalytic activity as a function of Pd coating content

In order to understand the role of Pd as the second dopant, the batch dechlorination rates of PCB 4 were measured as a function of Pd coating content (Figure 4.36). The k_{SA} is 0.017 L h^{-1} m^{-2}, 0.068 L h^{-1} m^{-2} and 0.166 L h^{-1} m^{-2} for Fe/Pd nanoparticles with 0.6, 2.3 and 5.6 wt% Pd respectively. Once again, in all these three different Fe/Pd nano systems, direct formation of biphenyl was achieved while PCB 1 was detected only in the trace level. It should be noted that Fe^0 nanoparticles without Pd showed insignificant dechlorination (less than 0.2 mg L^{-1} PCB 1 was formed after 5 days and no biphenyl was detected) at the same batch reaction conditions. In the bimetallic system, the role of Fe is to generate hydrogen by corrosion reaction, while Pd serves as the catalyst and the chlorine atom in PCB 4 is mainly replaced by hydrogen on the Pd surface (Xu and Bhattacharyya, 2005b; Lowry and Johnson, 2004). Therefore the Pd atoms are considered as the surface reactive sites for the dechlorination of DiCB. The variation of the k_{SA} as a function of Pd content is due to the difference of reactive sites. By normalizing the k_{SA} in terms of Pd content (reactive sites), we found the same reaction rate of Fe/Pd nanoparticles. The following reaction model developed by Johnson et al. (1996) provided a better way to understand and quantify the effect of variation in reactivity of different metal system (E4.2).

$$-\frac{dC}{dt} = k_{SA}\rho_m a_S C = k_2 \Gamma a_s \rho_m C \qquad \text{(E4.2)}$$

Where k_2 is the second order rate constant at a particular type of site (L h^{-1} mol^{-1}) and Γ is the surface concentration of reactive sites (mol m^{-2}). In this model, k_{SA} is expressed as the product of k_2 and Γ, which is more reasonable when dechlorination reaction preferentially occurs at the reactive catalytic surface sites (bimetallic system).

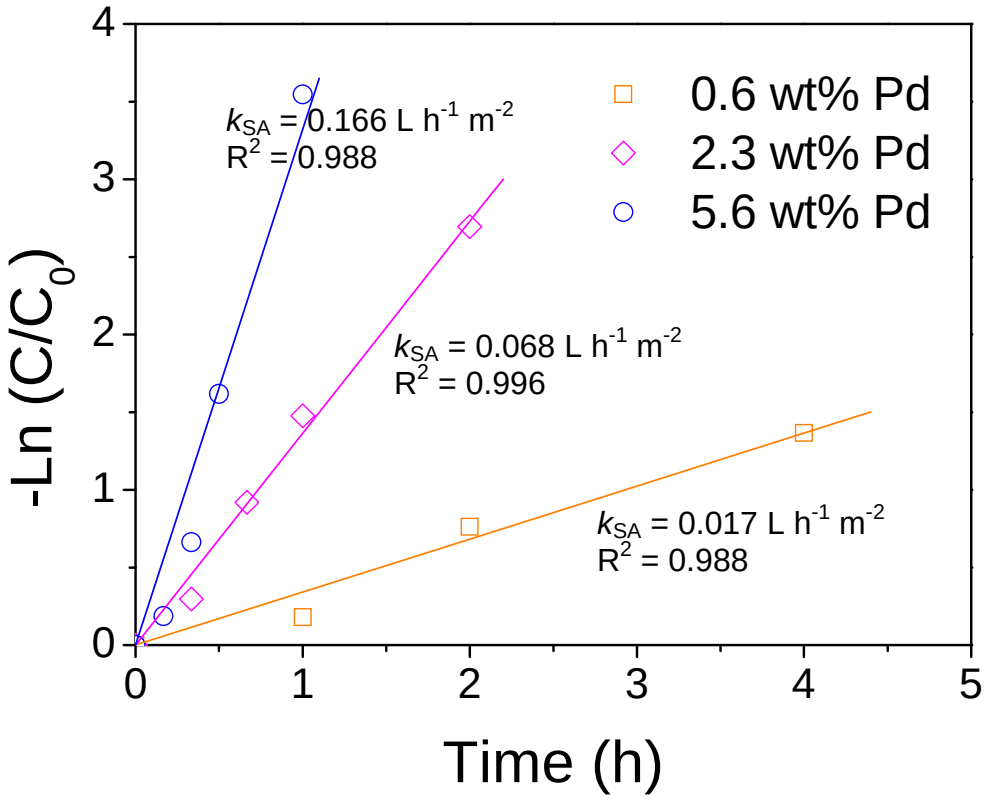

Figure 4.36 Best linear fit of k_{SA} for dechlorination of PCB 4 with various Fe/Pd nanoparticles in pore-filled PAA/PVDF membranes. Metal loading: 16mg/20mL (Xu and Bhattacharyya, 2007).

Based on the 30 nm average diameter of nanoparticles, we calculated the Pd coverage and surface Pd atoms for different Fe/Pd nanoparticles by using a Pd atom cross-sectional area of 0.0787 nm^2 (Nutt et al., 2005). Our calculations indicate that Fe/Pd nanoparticles with 0.6, 2.3, and 5.6 wt % Pd have 0.1, 0.4, and 0.97 layers of Pd atoms, respectively. Since maximum Pd coverage is less than one layer, all the Pd atoms are considered as surface reactive sites. Γ for the three different nanoparticles with 0.6, 2.3, and 5.6 wt % Pd is 2.20×10^{-6} mol m^{-2}, 8.43×10^{-6} mol m^{-2} and 2.05×10^{-5} mol m^{-2}, respectively. It should be noted that total surface area was used in all k_{SA} calculations. By applying the Γ into the equation 3, the k_2 was determined to be 7,727 L h^{-1} mol^{-1}, 8,066 L h^{-1} mol^{-1} and 8,098 L h^{-1} mol^{-1} respectively. The enhanced reaction rate (k_{SA}) is only due to the increase of surface Pd atoms.

High resolution STEM-EDS mapping images were also acquired in Figure 4.37 to compare the Pd atoms distribution for different Pd coating nanoparticles. The STEM-EDS mapping technique presents us a 2-D image of 3-D sample in transmission (Williams and Carter, 1996). All the Fe/Pd nanoparticles show a core/shell structure with Fe rich in the core region and Pd rich in the shell region. More Pd atoms were deposited on the iron surface and the Pd shell layer became denser with the increase Pd content. In spite of the limited spatial resolution in the EDS mapping, the distribution of Pd atoms is still in qualitative agreement with the result based on the calculation. This result implies that a uniform Pd coating with controllable thickness can be obtained by post reduction of Pd^{2+} with Fe nanoparticles immobilized in membrane phase.

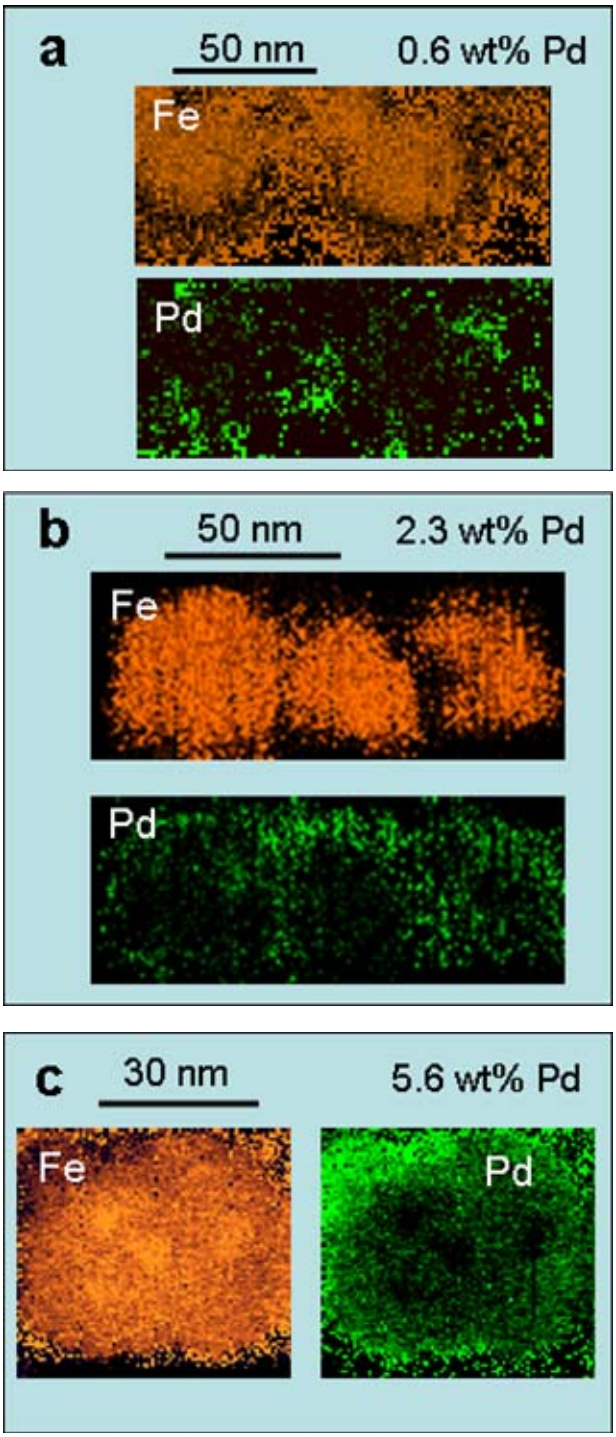

Figure 4.37 STEM-EDS Mapping Fe/Pd nanoparticles. (a): 0.6 wt% Pd; (b): 2.3 wt% Pd; (c): 5.6 wt% Pd (Xu and Bhattacharyya, 2007).

In our previous results where commercial PAA was dip-coated on the PVDF surface, we reported k_{SA} of 0.10 L h^{-1} m^{-2} for Fe/Pd (Pd = 1 wt%) nanoparticles synthesized on the membrane surface. It is about 9 times higher than the k_{SA} reported in this paper. The higher k_{SA} is due to the lower mass transfer resistance since Fe/Pd nanoparticles were located at the membrane surface. While in this study, PAA was prepared inside the PVDF membrane pores. Fe^{2+} was bound to PAA and reduced to nanoparticles inside the membrane pores. Since the reaction occurs only at the nanoparticle surface, the organics must diffuse through the membrane pores which can control the reaction rate. However, the diffusion control can be avoided by operating at high convective flow mode. Compared with the previous study (dip-coating), this new synthesis method (pore-filled) provides a more stable membrane matrix because PAA is cross-linked and immobilized inside the porous network structure instead of physically sitting on top of the membrane surface. Higher PAA and metal loading is achieved since the membrane pore surfaces are fully utilized.

Effect of Temperature

In an effort to achieve a deeper insight into the mechanism of Pd catalyzed dechlorination, the dependence of batch reaction rate on temperature was investigated to obtain the activation energy (E_a, kJ mol^{-1}). The E_a is the measure of minimum energy required to complete the reaction. In general, the role of the catalyst is to reduce the E_a by changing the reaction pathway and thus enhance the reaction rate. It has been found that complete dechlorination of PCBs in aqueous solution by monometallic bulk size Fe^0 (no catalyst) requires high temperature (400 °C) (Chuang et al., 1995). But E_a was not measured in the literature for this type of process. The reduction of PCBs by Ni-Mo catalyst with supplied H_2 in non-aqueous phase was observed at relatively mild conditions (82~91% conversion at 250 °C) (Gryglewicz et al., 2006). Earlier research reported the E_a of 124 kJ mol^{-1} (Gryglewicz et al., 2006) for 2, 3-dichlorobiphenyl by non-catalytic process and 93 kJ mol^{-1} (Murena et al., 2000) for 3-chlorobiphenyl by the Ni-Mo catalyst with supplied H_2 in non-aqueous phase. The dependence of rate constant on the temperature was modeled in Figure 4.38 by the Arrhenius equation. Based on the

best linear fitting, the E_a for DiCB degradation by membrane supported Fe/Pd nanoparticles was determined to be 24.5 kJ mol^{-1}. It is about five times lower than the non-catalytic process (Gryglewicz et al., 2006) and nearly four times lower than the Ni-Mo catalyzed dechlorination (Murena et al., 2000) in non-aqueous phase with supplied H_2 gas. This indicates the high catalytic property of Pd which is effective in the hydrodechlorination of PCBs from water at room temperature. It is reported in the literature (Su and Plus, 1999) that diffusion-controlled reactions in solution have low activation energies (E_a < 21 kJ mol^{-1}), whereas E_a values for reaction on surfaces are usually in the order of 84 kJ mol^{-1}. These E_a values indicate the diffusion control for membrane-supported Fe/Pd system.

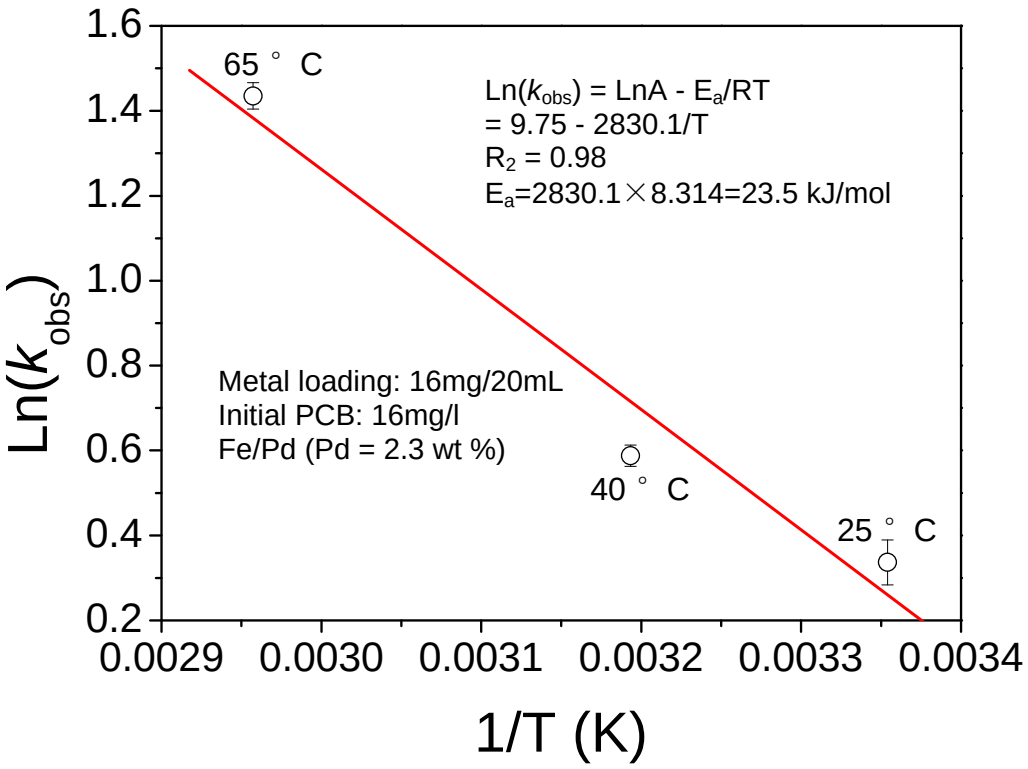

Figure 4.38 Best linear fit of E_a for dechlorination of PCB 4 with membrane supported Fe/Pd (Pd = 2.3 wt %) nanoparticles at various temperature (Xu and Bhattacharyya, 2007).

Stability of Fe/Pd reactivity

One of the important issues for the PCBs dechlorination by membrane supported Fe/Pd nanoparticles is the decrease in the reactivity due to the consumption of iron as a reactant, oxidation of iron surface, formation of iron (II, III) hydroxide on the particle surface and possibility of leaching of Pd or Fe^0 from the membrane. An eight-cycle dechlorination experiment was conducted in a 20 ml batch solution containing 64 mg membrane supported Fe/Pd nanoparticles (Pd = 2.3 wt%) with repeated spiking of concentrated DiCB solution. After each cycle, the DiCB concentration was raised to ~ 16 mg L^{-1} after adding concentrated DiCB solution. More than 90% dechlorination was achieved after first 4 cycles, while only about 50% dechlorination was obtained after 8 cycles, indicating the decline of catalytic activity. There are only two possibilities for the decline of reactivity: deactivation of Fe or deactivation of Pd. Hydrogen production from the reaction was measured to understand the possibility of iron deactivation. As shown in the Figure 4.39, the hydrogen gas still can be produced by iron even after 26 hours, indicating that the decline of dechlorination rate is not due to the iron deactivation.

It is well known that Pd and chloride have a strong interaction, which may cause the Pd deactivation. In order to prove this hypothesis, dechlorination experiment was conducted in 40 mg L^{-1} Cl^- solution using fresh membrane supported Fe/Pd nanoparticles. No obvious decline of nanoparticle reactivity was observed. This indicates that Pd is not deactivated by Cl^- ions formed from the PCB dechlorination. In order to further investigate the decrease in the catalytic activity, STEM-EDS mapping analysis on the nanoparticles (no membrane) was used to examine the distribution of Fe and Pd after the 8 cycles. In comparison with fresh Fe/Pd nanoparticles in which Pd were deposited on the Fe surface, it was found that Pd was completely covered by thick layers of iron and oxygen after the reaction (Figure 4.40), suggesting the deposition of iron hydroxide which deactivated Pd surface. The final metal ion concentrations in the solution were found to be 0.4 mg l^{-1} for iron and Pd leaching was not detected, indicating Fe/Pd nanoparticles remains stable inside the PAA/PVDF membrane matrix.

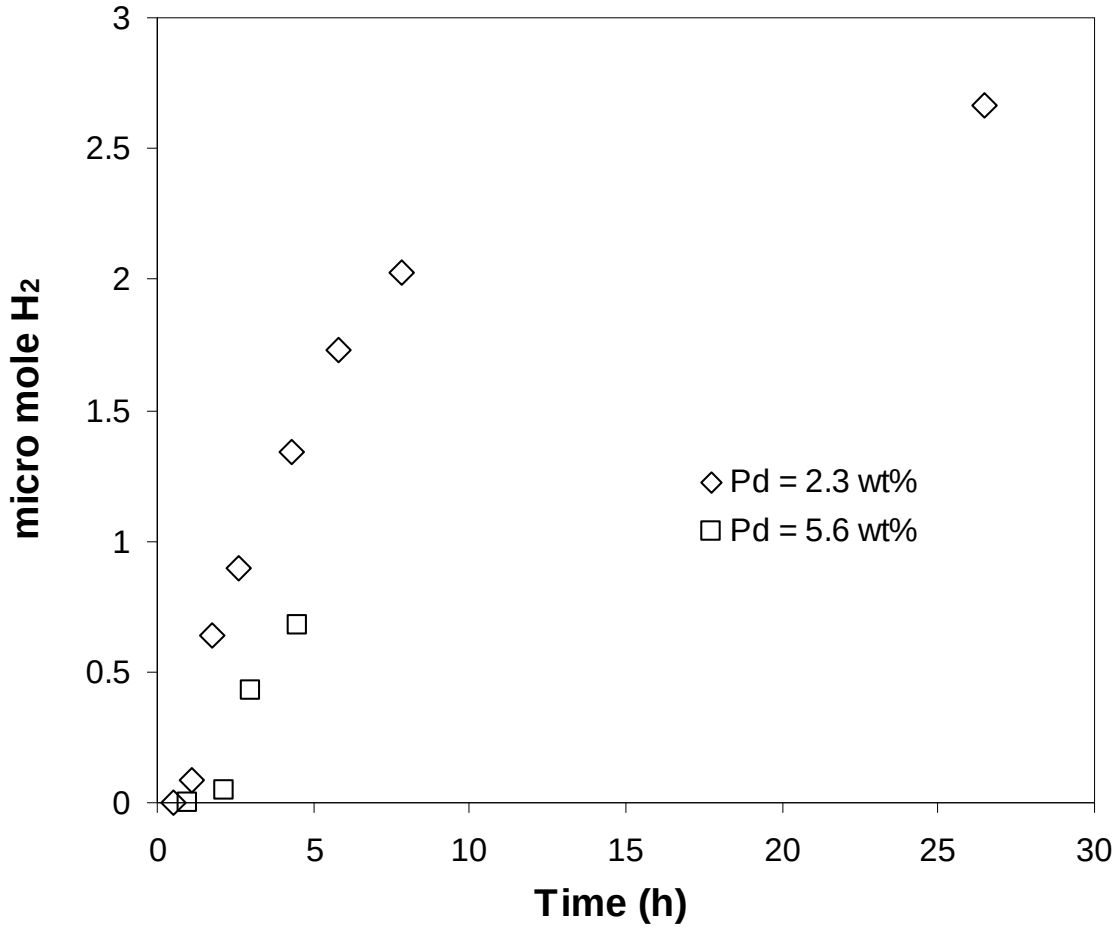

Figure 4.39 Plots of hydrogen gas (micro mol) produced during DiCB dechlorination reaction at pH 6 with PAA/PVDF membrane supported Fe/Pd nanoparticles, measured by static headspace analysis using GC-TCD (0.1 ~ 1 mL of headspace sampled, 16 mg Fe/Pd loading in 20 mL vials, initial DiCB concentration: 16 mg L^{-1} in 50/50 vol.% ethanol/water).

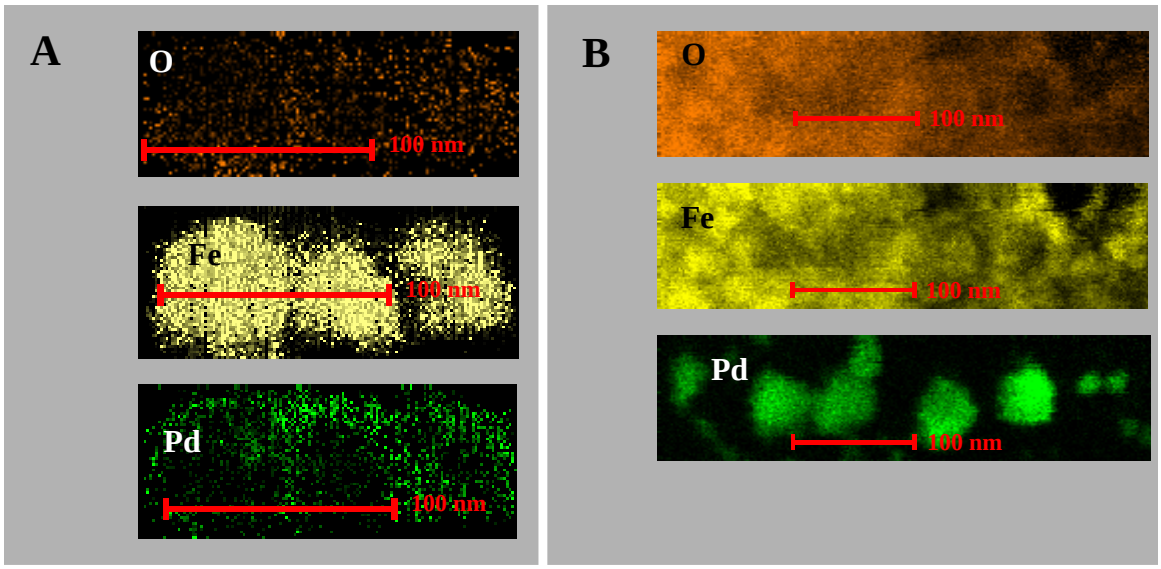

Figure 4.40 STEM-EDS Mapping Fe/Pd nanoparticles. (A): Fresh Fe/Pd nanoparticle (B): Fe/Pd nanoparticle after 4 cycles of dechlorination of 2,2'-dichlorobiphenyl. O = oxygen

4.5.5 Dechlorination of 3, 3', 4, 4'-Tetrachlorobiphenyl (PCB 77) by Bimetallic Nanoparticles in Pore-filled PAA/PVDF Membranes

Toxicity studies of PCB77 (3, 3', 4, 4'-tetrachlorobiphenyl, non-ortho-chlorinated PCB) have received extensive attention in recent years due to the specific structure-activity relationship. It has been reported that the major part of PCB toxicity is due to the chlorine atoms in non-ortho position. These compounds having chlorinated substitutents in both para positions and any/all meta positions are known as coplanar PCBs which are highly toxic. PCB77 is among the most commonly found coplanars in the environment. Thus, it is important to study and quantify the degradation kinetics and mechanism of PCB77 using bimetallic nanoparticles (Fe/Pd).

Figure 4.41 shows the dechlorination of 15.6 mg/L PCB 77 in 65/35 vol.% ethanol/water solution with Fe/Pd (Pd: 2.3 wt%) immobilized inside pore-filled PAA/PVDF membranes. High concentration of ethanol in the solution matrix was used because of the lower solubility of PCB 77 in water. As shown in the figure, the membrane supported Fe/Pd nanoparticles exhibit extremely fast dechlorination rate. Complete degradation of PCB 77 by Fe/Pd in PAA/PVDF membrane was achieved within 2 hours. Biphenyl was formed as the main dechlorination product. PCB77 was completely transformed to biphenyl after 2 hours. The degradation of PCB77 by Fe/Pd nanoparticles occurred in a sequential reduction pathway (Figure 4.42), which is indicated by the detected less chlorine intermediates. All the PCB intermediates were only identified in the low concentration level within 1 hour. It has been proven in the literature (Lowry et al. 2004) that non-ortho-chlorinated PCB congeners dechlorinate faster than the ortho-chlorinated isomers due to the effect of higher steric hindrance for ortho-position. The reactivity of the chlorine substitutents decreases in the order para ≈ meta > ortho (Noma et al. 2003). Due to the increasing torsion angles with the increase of ortho substitution, non-ortho substituted congeners could adsorb in a closed planar position with nanoparticles, which is beneficial for the reductive dechlorination. The more positive reduction potentials measured in the literature (Huang and Rusling, 1995) also support the increased reactivity of non-ortho substituted congeners.

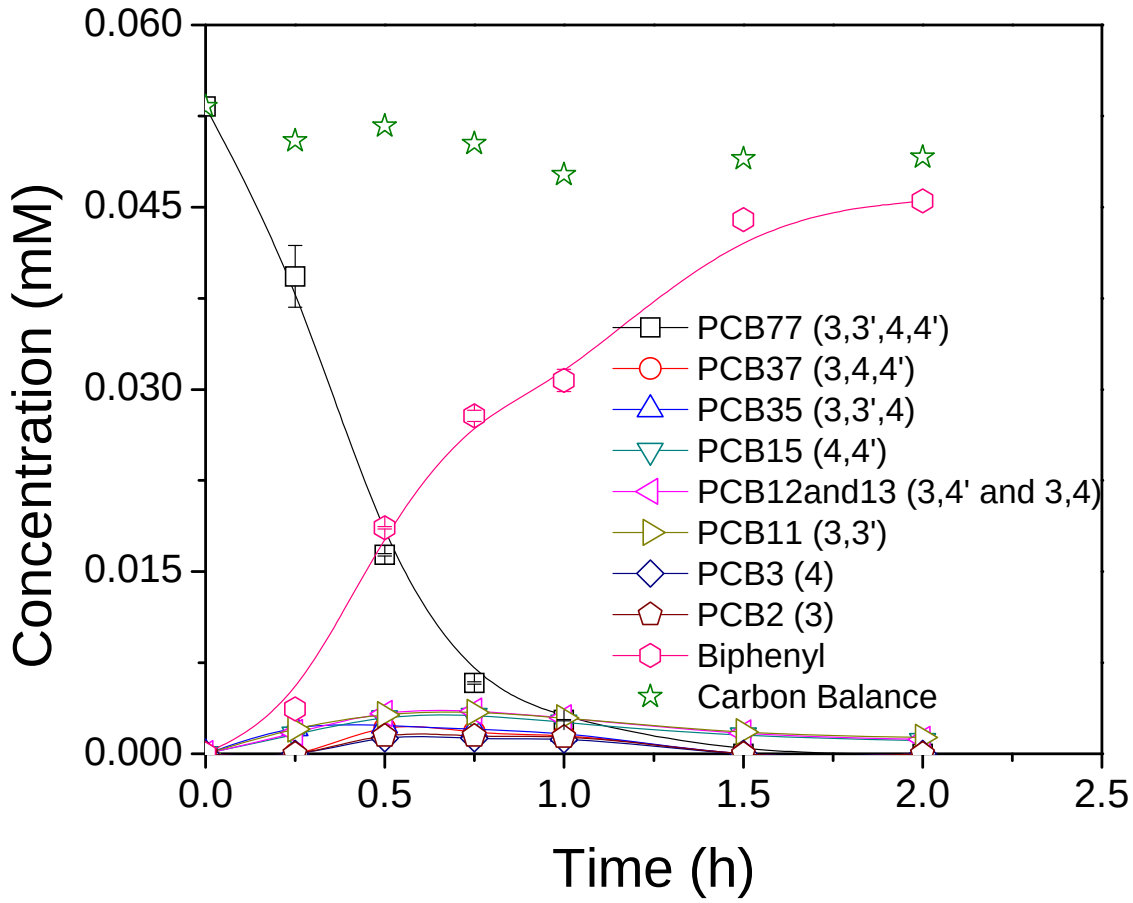

Figure 4.41 Batch reaction of PCB77 with Fe/Pd (Pd = 2.3 wt%) in pore-filled PAA/PVDF membrane. Metal loading: 0.8 g L^{-1}. Initial PCB77 concentration: 15.6 mg L^{-1}.

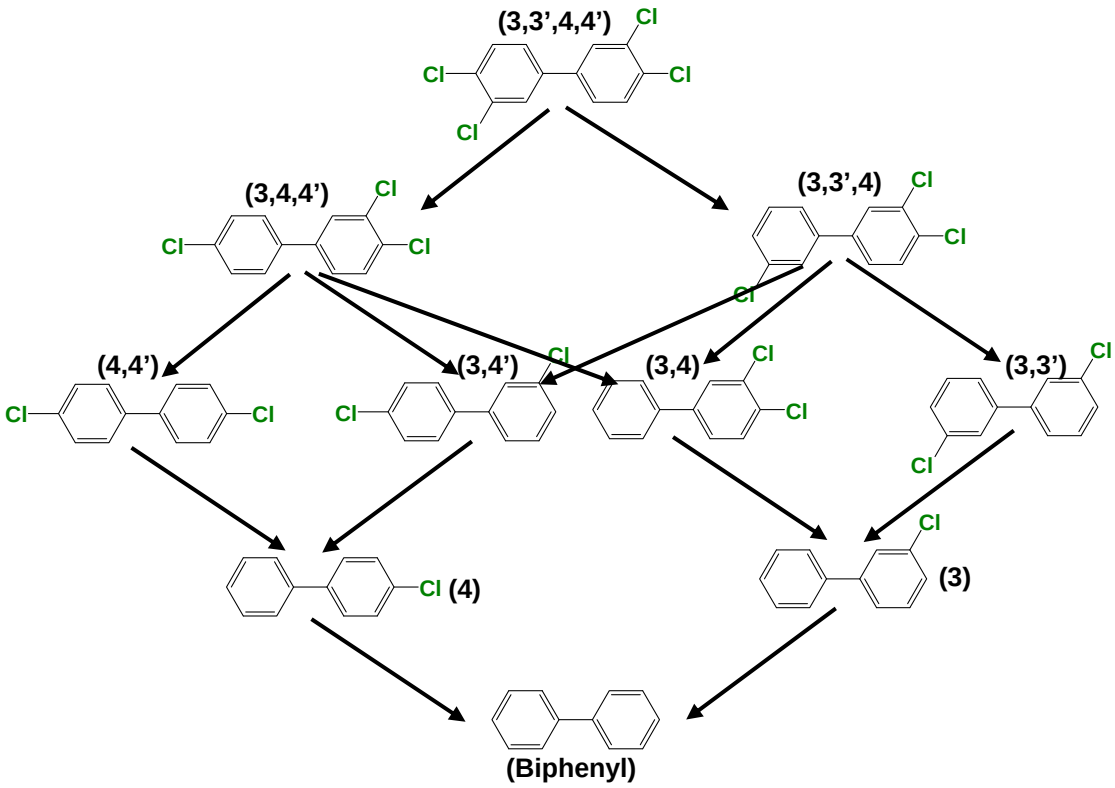

Figure 4.42 Reductive dechlorination pathway of 3,3',4,4'-tetrachlorobiphenyl (PCB 77) by Fe/Pd nanoparticles.

Best linear fit to the experimental data (R^2 = 0.97), the k_{obs} and k_{SA} (PCB77) determined to be 2.82 h^{-1} and 0.141 L h^{-1} m^{-2}. Since PCB 77 does not have any chlorine in the ortho position, the k_{SA} is more than two times higher than that for the degradation of PCB 4 which contains only ortho position chlorines. This result is consistent with the observation reported in the literature (Lowry et al. 2004) that higher-chlorinated and nonortho-substituted congeners dechlorinate faster than lower-chlorinated and ortho-substituted congeners. The degradation for PCB 77 in this study showed all eight intermediates which can occur in theory by reductive pathway. All the intermediates appeared in the close concentration level. This can be explained by the little difference of reactivity between para and meta chlorines substitutents. The carbon mass balance based on the sum of remaining PCB 77, intermediates and biphenyl was about ~95% of the initial amount of PCB 77. The ~ 5% mass losses are due to the extraction equilibrium.

In order to obtain a better understanding and quantification of PCB 77 dechlorination, Figure 4.43 plots the selectivity for biphenyl and the intermediates as a function of PCB 77 conversion. All the eight different intermediates were added together as the total intermediates. The conversion and selectivity were calculated based on the following equations:

$$X_{PCB77} = \frac{C_{PCB77} - C^0{}_{PCB77}}{C^0{}_{PCB77}} \tag{E4.3}$$

$$S_{Biphenyl} = \frac{C_{Biphenyl} - C^0{}_{Biphenyl}}{C^0{}_{PCB77} - C_{PCB77}} \tag{E4.4}$$

$$S_{Intermediate} = \frac{C_{Intermediatel} - C^0{}_{Intermediate}}{C^0{}_{PCB77} - C_{PCB77}} \tag{E4.5}$$

Where, X is the conversion; S is the selectivity and C is the concentration (mM). It can be seen that although each single intermediate was observed in low level compared to the biphenyl formation, the selectivity of the total intermediates is almost equal to the biphenyl selectivity. The selectivity of the total intermediates remained unchanged when the PCB 77 conversion was increased from 20% to 70%, while the biphenyl selectivity increased from 30% to 50%. After 70% conversion, the intermediate selectivity decreases rapidly. This indicates that the degradation of PCB 77 does not result in the correspondingly equal amount formation of biphenyl. Before 70% PCB 77 degradation,

the main dechlorination reactions are the conversion of PCB 77, tri- and di-chlorobiphenyls to monochlorobiophenyl and the formation of biphenyl. After 70% conversion, the main reactions are the conversion of mono-chlorobiphenyl to biphenyl.

During dechlorination with Fe/Pd nanoparticles, the iron is oxidized and Fe (II, III) species may be released from the membrane. The PAA functionalized membranes have the capability of capturing these dissolved Fe (II, III) ions. The aqueous phase analysis after the dechlorination showed (Figure 4.44) negligible amount of Fe in the solution 0.03 mg (0.18 wt % of initial Fe). In order to measure Fe ions in membrane phase, ion exchange with Ba^{2+} (0.05 M) was performed to transfer captured Fe ions from membrane phase to aqueous phase. The aqueous phase analysis after Ba^{2+} ion exchange shows 1.2 mg Fe (2% of the initial Fe) captured by membrane. The recaptured Fe ions by membrane can be subsequently regenerated using $NaBH_4$.

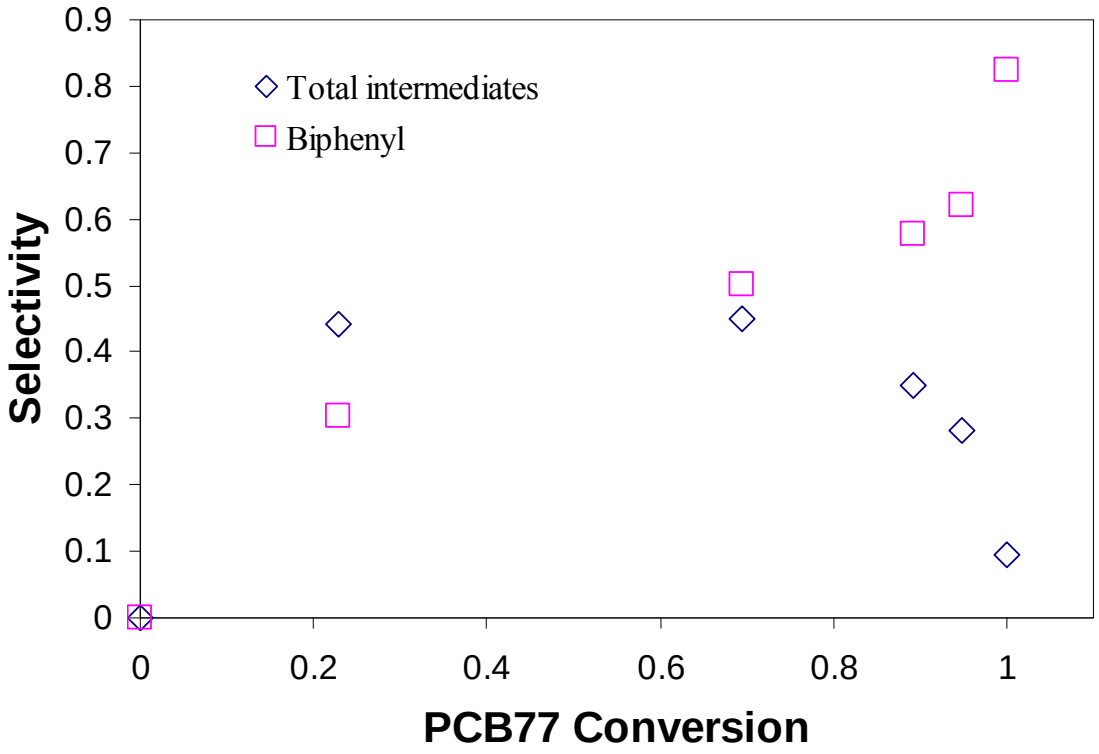

Figure 4.43 Selectivity for biphenyl and the intermediates as a function of PCB 77 conversion.

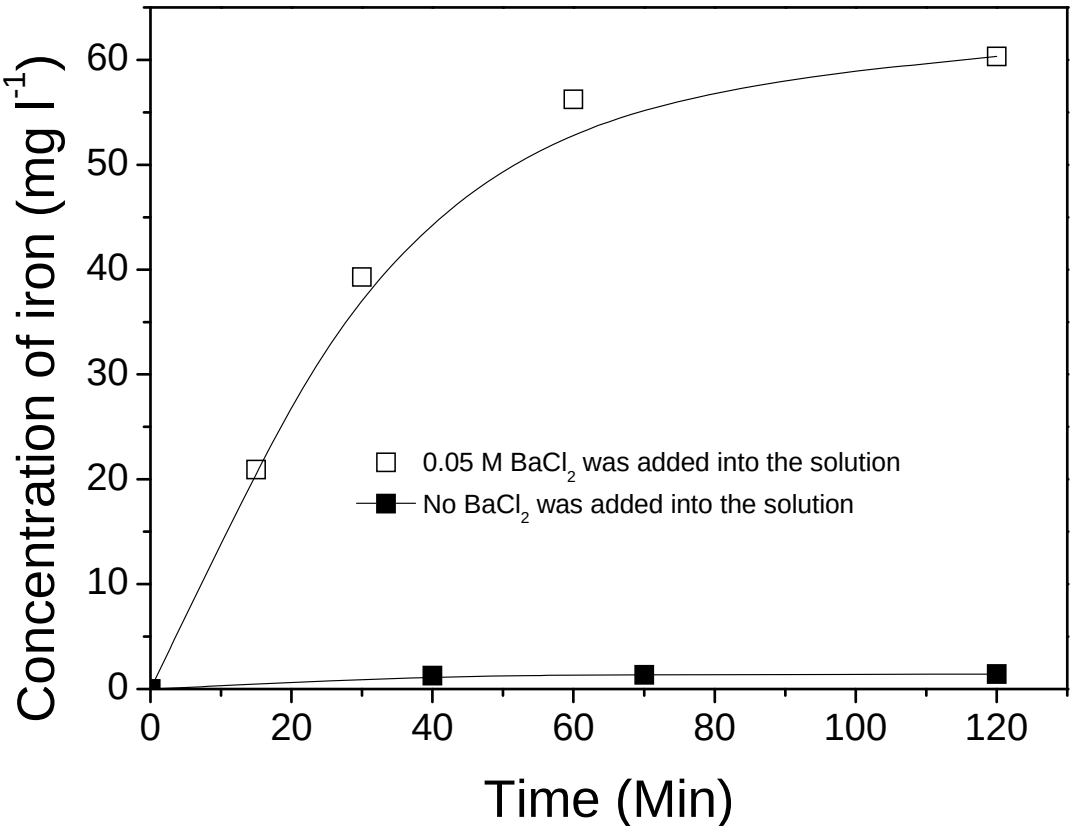

Figure 4.44 Dissolution of Fe nanoparticles in PAA/PVDF membranes. Fe loading: 16 mg/20 ml, Volume of the solution: 20 ml.

Chapter 5 Membrane Reactor Model

This chapter mainly consists of the studies of reductive dechlorination of PCB by Fe/Pd nanoparticles in pore-filled PAA/PVDF membrane under convective flow mode. A two-dimensional mathematical model for the mass transfer and reaction inside membrane pores is presented. The parameters used in the model simulation such as pore size and PCB diffusivity were obtained from dextran rejection and diffusion experimental data. The 2-D model considers convection, diffusion, and reaction kinetics on the membrane reactor module. The influence of membrane pore size, reaction rate varied by changing Pd composition, and PCB diffusivity was evaluated and then compared with the experimental data.

5.1 Formulation of Membrane Reactor Model

The catalytic hydrodechlorination by membrane supported bimetallic (Fe/Pd and Fe/Ni) nanoparticles in the batch mode has been extensively reported in the previous chapter. The reaction mechanism can be described by the reduction of chlorinated organics to non-toxic (or less toxic) hydrocarbons in the presence of the second catalytic metal (Pd or Ni) by substitution of chlorine with hydrogen generated from Fe^0 corrosion. This chapter presents the modeling and experimental studies of dechlorination with the same membrane supported bimetallic nanoparticles under convective mode. In this study, 2, 2'-dichlorobiphenyl (DiCB, PCB 4) was used as the model compound. We have investigated and quantified reaction pathway and kinetics for the DiCB dechlorination in the batch mode. We have also correlated the normalized reaction rate (k_{SA}) with the Pd coating composition in terms of reactive sites.

The dechlorination reaction of PCBs inside the pore-filled PAA/PVDF membrane containing Fe/Pd nanoparticles under convective flow mode was described by a two-dimensional reactor model. Figure 5.1 presents a schematic diagram showing the mass-transfer and reaction phenomenon of PCBs inside the PAA/PVDF membrane pores. The PCBs solution are transferred through the membrane by applied pressure, diffused and

reacted with Fe/Pd nanoparticles immobilized inside PAA layer. The following assumptions are adopted for the model development.

- The system is operated isothermally and at steady state.
- The membrane pores are assumed to be cylindrical and uniform size.
- Constant density, viscosity and diffusivity are considered for the dilute PCBs solution.
- Fully developed laminar flow is assumed for the liquid inside the membrane pores, and there is no flow in the radial direction.
- The model assumes homogeneous distribution of Fe/Pd nanoparticles in the PAA layer.
- The reaction only occurs in the PAA layer (no reaction in the pore region).
- The reaction at the membrane surface is negligible.
- PCBs are transferred through membrane pores by convection and diffusion, and transferred into PAA layer only by radial diffusion.

Based on the above the assumptions, the mathematical equations for the mass transfer and reaction inside the membrane pore and PAA region can be described as follows (Figure 5.1).

① *Membrane pore region*

$$U_z \frac{\partial C}{\partial z} = D_s \frac{1}{r} \frac{\partial C}{\partial r}\left(r \frac{\partial C}{\partial r} \right) + D_s \frac{\partial^2 C}{\partial z^2} \tag{E5.1}$$

with the boundary conditions

$$z = 0,\ C = C_0 \tag{E5.1a}$$

$$r = 0,\ \frac{\partial C}{\partial r} = 0 \tag{E5.1b}$$

The model equation (E5.1) includes the expression for the convective flux and diffusion in axial and radial direction. Since the nanoparticles are assumed to be in the PAA region, there is no reaction term in the E5.1. C is the concentration of PCB (mM), and C_0 is the initial PCB concentration (mM). D_s is the diffusion coefficient of the bulk PCB in the membrane pores ($m^2\ s^{-1}$). Ds is calculated from the Wilke and Chang equation (Wilke and Chang 1995):

$$D_s = \frac{\left(117.3\times10^{-18}\right)\left(\varphi M_B\right)^{0.5}T}{\mu v_A^{\,0.6}} \qquad \text{(E5.1c)}$$

M_B is the molecular weight of solvent (g mol^{-1}); T is the temperature (K); μ is the viscosity of solvent (kg m^{-1} s^{-1}); v_A is the molar volume of PCB (m^3 kmol^{-1}, v_A for DiCB is 0.161 m^3 kmol^{-1}).ϕ is the association factor for solvent (2.26 for water as the solvent and 1.5 for ethanol as solvent). Based on the calculation, D_s for DiCB is 8.50 $\times$ 10^{-10} m^2 s^{-1} in water and 6.53 $\times$ 10^{-10} m^2 s^{-1} in ethanol. Since the solvent matrix contains 50% vol ethanol and 50% vol water, average D_s of 7.5 $\times$ 10^{-10} m^2 s^{-1} was used in the model calculation.

U_z is the velocity along the z-axis (m s^{-1}). The fully developed laminar flow profile along the z-axis is described by:

$$U_z = 2U_0\left(1-\left(\frac{r}{r_1}\right)^2\right) \qquad \text{(E5.1d)}$$

Where U_0 is the mean velocity (m s^{-1}), r and z are the radial and axial coordinates (m). r_1 is the mean pore radius after the PAA modification (m). r_1 is calculated from the observed membrane rejection of various dextran by using the Ferry-Faxen equation (Ferry 1936; Lindau et al., 1998):

$$(1-R)=\left(1-\frac{r_s}{r_1}\right)^2\cdot\left(1-0.104\frac{r_s}{r_1}-5.21\left(\frac{r_s}{r_1}\right)^2+4.19\left(\frac{r_s}{r_1}\right)^3+4.18\left(\frac{r_s}{r_1}\right)^4-3.04\left(\frac{r_s}{r_1}\right)^5\right) \qquad \text{(E5.1e)}$$

R is the rejection of dextran. r_s is the hydraulic radius of the dextran molecule (m), which can be determined from the following correlation with the molecular weight of dextran:

$r_s = 0.27\times10^{10}\,M^{0.498}$ (Hagel 1988; Lindau et al., 1998) (E5.1f)

M is the molecular weight of dextran.

② *PAA layer containing Fe/Pd nanoparticles*

$$D_m\frac{1}{r}\frac{\partial C}{\partial r}\left(r\frac{\partial C}{\partial r}\right)+D_m\frac{\partial^2 C}{\partial z^2}+(-k_{in}\rho a_s\cdot C)=0 \qquad \text{(E5.2)}$$

with the boundary conditions:

$$r=r_1,\ D_s\frac{\partial C}{\partial r}=k_m(C_2-HC_1) \qquad \text{(E5.2a)}$$

$$r = r_2,\ \frac{\partial C}{\partial r} = 0 \qquad \text{(E5.2b)}$$

The model equation (E5.2) describes the dechlorination reaction and axial and radial diffusion in the PAA region. C_1 is the concentration of PCB (mM) in the pore region at the pore/PAA layer interface, and C_2 is the concentration of PCB (mM) in the PAA layer at the pore/PAA layer interface. k_{in} is the surface area normalized reaction rate at convective flow mode (L m^{-2} s^{-1}). It has been discussed in the previous chapter that k_{in} can be expressed as the product of k_2 and Γ ($k_{in} = k_2 \cdot \Gamma$). k_2 is the second order rate constant at the Pd (reactive) site (L s^{-1} mol^{-1}) and Γ is the surface concentration of reactive (Pd) sites (mol m^{-2}). ρ is the density of Fe/Pd (g L^{-1}). a_s is the surface area per unit mass of Fe/Pd (m^2 g^{-1}). H is the PCB partitioning coefficient. D_m is the PCB diffusion coefficient through the PAA layer (m^2 s^{-1}). r_2 is the initial PVDF membrane pore size (110×10^{-6} m). H and D_m are determined from the PCB diffusion experiments, which will be discussed later. k_m is the mass transfer coefficient (m s^{-1}) determined from Sherwood number (Sh) correlations for membrane filtration system at laminar flow condition (Tu et al., 2001 and 2005). Wiley et al. (1985) and van den Berg et al. (1989) used the following correlation for membrane filtration systems operating under fully developed laminar flow condition (Re <2,000).

$$Sh = \frac{k_m d}{D_s} = 1.86\,\mathrm{Re}^{0.5}\, Sc^{0.33}\left(\frac{d}{L}\right)^{0.33} \qquad \text{(E5.2c)}$$

d is the membrane pore diameter after PAA modification (m). Re is the Reynolds number ($Re = \rho U_0 d/\mu$); Sc is the Schmidt number ($Sc = \mu/\rho D_s$); L is the membrane thickness (125×10^{-6} m). Peclet (Pe) number is another dimensionless number relating the rate of convection of a flow to its rate of diffusion. Pe is defined by the ratio of characteristic diffusion time over residence time. There are two Pe number in the system: Pe_r (radial) and Pe_z (axial).

$$Pe_r = \frac{r_1^2 / D_s}{L / U_0} \qquad \text{(E5.2d)}$$

$$Pe_z = \frac{L^2 / D_s}{L / U_0} \qquad \text{(E5.2e)}$$

Pe_{r} is a measure of radial diffusion resistance and Pe_z is a measure of axial diffusion resistance at certain conditions (flow rates).

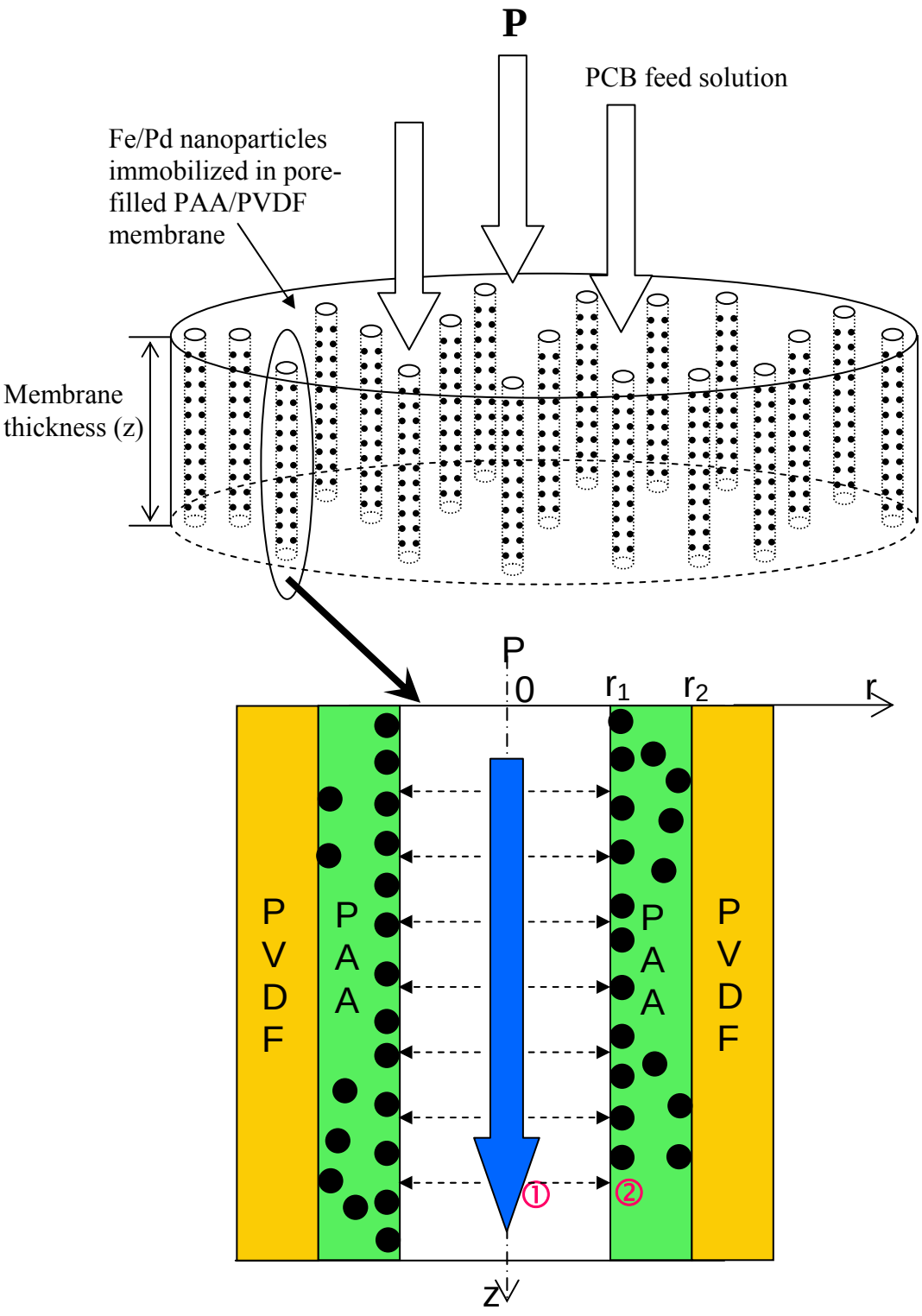

Figure 5.1 Schematic diagram showing the mass transfer and reaction taking place inside the membrane pores.

The modeling protocol developed in this work is summarized in Figure 5.2. In this model, the convective flow membrane reactor can be characterized by the following membrane parameters: membrane pore size and porosity (r and ε, determined from dextran rejection), membrane thickness (L, 125×10^{-6} m), system parameters: PCB solution density and viscosity, PCB diffusivity in bulk solution (D_s, calculated from Wilke and Chang equation E5.1c), PCB diffusivity and partitioning coefficient (D_m and H, determined form diffusion experiments), reaction parameters: nanoparticle surface area, Pd composition (Γ, reactive sites), metal loading, intrinsic reaction rate constant, and operating parameters: volumetric flux and initial PCB concentration (C). Since the reaction rate constant from batch reaction is the observed rate which includes the effect of diffusion, the observed batch rate constant is not suitable for the convective flow model calculation. The intrinsic rate constant could be obtained from batch reaction with Fe/Pd nanoparticles without membrane. However, it is quite difficult to prepare the same Fe/Pd nanoparticles in solution without the support of membrane. Therefore, the intrinsic rate constant (k_{in}) has been determined by fitting the model with the experimental data. k_{in} is the only parameter that was taken as fitting parameters for model validation and simulation. All other parameters were determined by independent calculations or experiments.

The two steady-state partial differential equations (E5.1 and E5.2) were integrated together to obtain the PCB concentration profiles along the z-axis of the membrane. Direct formation of biphenyl for the degradation of 2,2'-dichlorobiphenyl is assumed since the chlorinated intermediate (2-chlorobiphenyl) was detected in trace level. The concentration profile for biphenyl was calculated from the mass balance (neglecting the formation of 2-chlorobiphenyl). Femlab™ (COMSOL, version 3.0a) was used to solve the two sets of partial differential equations (E5.1 and E5.2). Multiphysics axial symmetry modules of convection–diffusion were applied to the two-phase regions. The membrane pore and PAA region were partitioned into about 57,000 finite element cells to ensure accurate calculation of concentration profile along the membrane pore axis. This model provides useful and convenient method to study and simulate the effect of designing and operating parameters such as membrane properties, catalyst properties and loading, flow rate on the performance of the reactor.

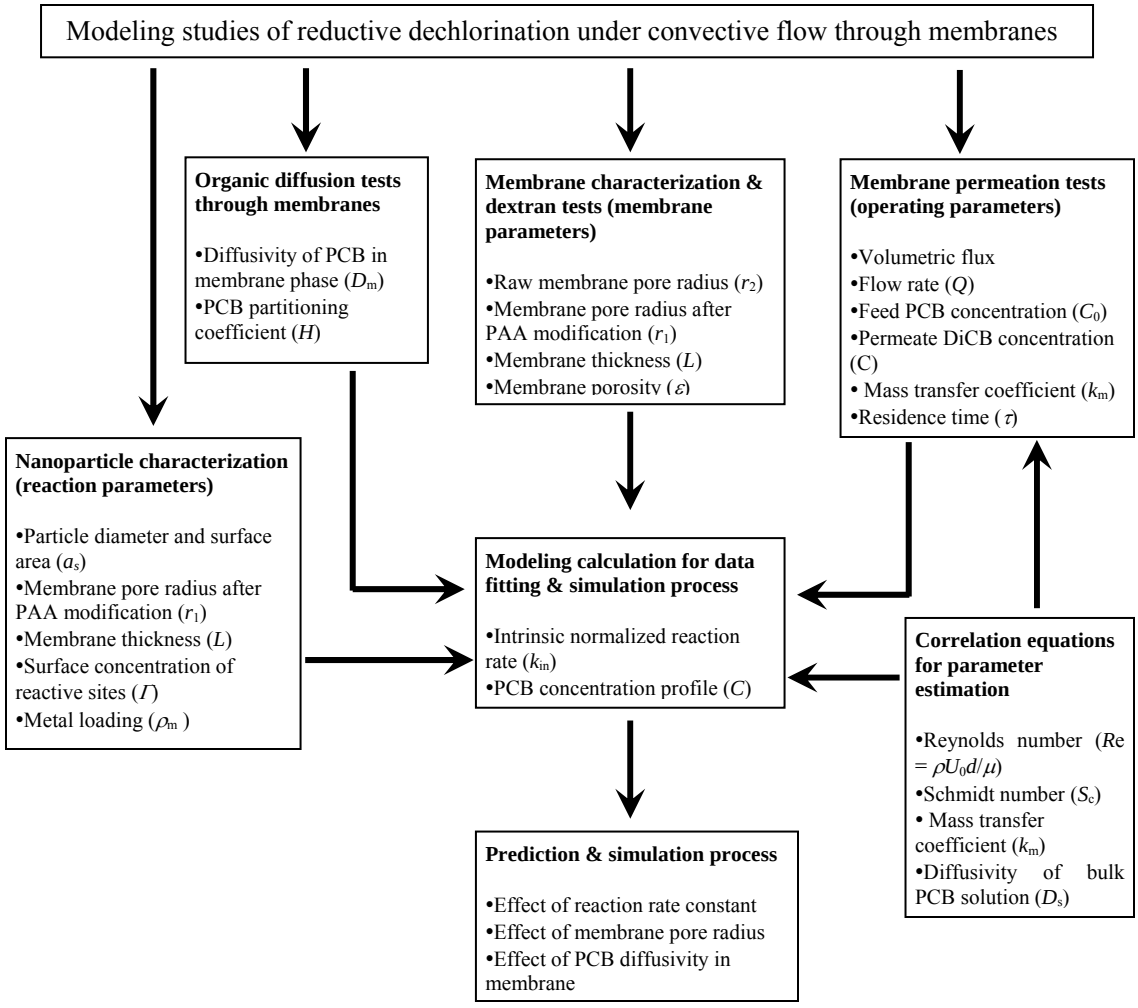

Figure 5.2 Protocol and phase diagram for modeling studies of reductive dechlorination under convective flow.

5.2 Determination of Diffusion (D_m) and Partitioning (H) Coefficient of 2, 2'-Dichlorobipheny (DiCB, PCB 4) through PAA/PVDF Membrane

After the formulation of membrane reactor, the next important stage is to obtain the model parameters. Although some model parameters such as mass transfer coefficient and PCB diffusivity in solution can be determined by calculation. The diffusivity and partitioning coefficient of DiCB through PAA/PVDF membrane were investigated by the diffusion experiments.

The diffusion study experimental set-up is shown in the Figure 5.3. The PAA/PVDF membrane was immersed into the DIFU water and purged with O_2 for 12 hours to deactivate the iron nanoparticles. Then the membrane was mounted in the middle of a stainless steel diffusion cell to separate the two compartments (feed side and permeation side). Each compartment in the diffusion cell has the volume of 500 mL. The membrane area separating the two compartments has the area of 3.5 cm^2. Each compartment was stirred vigorously during the experiment. Solution of 0.6 mM DiCB was added into the feed side compartment, and the same amount of solution without DiCB was placed in the permeation side compartment. The DiCB concentration in the permeation side was measured versus time by GC-MS. To obtain the sample for GC analysis, two mL solution was drawn from each compartment and extracted with 2-mL hexane for 2 hours respectively. Since the change of DiCB concentration in the feed compartment is negligible, the DiCB concentration in feed side (C_{10}) is assumed to be constant. The DiCB concentration in the permeation compartment (C_1) is always much less than that in the feed side (C_{10}). The data can be analyzed by the following equation developed by Yang et al. (2002) to determine the diffusion and partitioning coefficient of DiCB in membrane.

$$\frac{C_0}{C_{10}} = \left[\frac{D_m H}{L}\left(\frac{A}{V}\right)\right]\left(t - \frac{L^2}{6D_m}\right) \qquad \text{(E5.3)}$$

Where A is the membrane area (m^2); L is the membrane thickness (m); V is the volume of the permeation side (m^3); and t is time (s); H is the DiCB partitioning coefficient through the membrane; D_m is the DiCB diffusivity through the membrane ($m^2\ s^{-1}$)

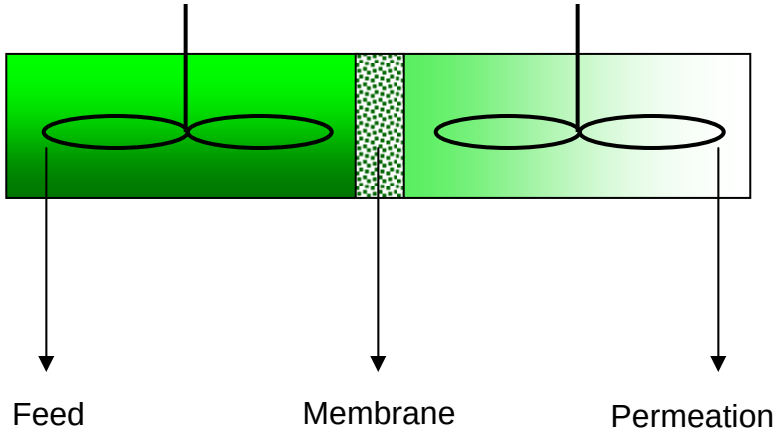

Figure 5.3 Experimental apparatus of diffusion study. Two well-stirred volumes are separated by PAA/PVDF membrane containing deactivated Fe nanoparticles. DiCB diffuses from left to right across the membrane.

The experimental results for DiCB diffusion through the PAA/PVDF membrane containing deactivated Fe nanoparticles are shown in the Figure 5.4. As shown in the figure, the DiCB concentration in the permeation cell (C_1) increase linearly with time. By fitting the data with equation E5.3, the partitioning coefficient (H) was determined to be 1.16. This is very close to one since the PAA is swollen with water. The diffusion coefficient (D_m) was found to be 6.5×10^{-11} m^2 s^{-1}. This value is less than that in water (7.5×10^{-10} calculated from equation E5.1c). The lower number is expected since the polymer chain should restrain the diffusion of DiCB.

5.3 Determination of Pore Size of PAA/PVDF Membrane Containing Fe/Pd Nanoparticles

The next important parameter for the model calculation is the membrane pore size. The mean pore size was determined by measuring the retention of various molecule weight of dextran using the Ferry-Faxen equation (E5.1e). The dextran rejection result is shown in the Figure 5.5. The pH of the dextran solution (800 mg L^{-1}) was kept at ~7 to keep the PAA chain in extended form. As expected, with the increase of dextran molecular weight, we observe the increase of rejection. The rejection is 95% for the dextran with the molecular weight of 2,000,000. The mean pore size is determined to be 64 nm by using the Ferry-Faxen equation (E5.1e). Therefore, the thickness of the PAA layer is calculated to be 46 nm. Initially, the unmodified PVDF membrane has the porosity of 75%. The porosity after modification is determined based on the assumption that the membrane pores are all cylindrical and uniform and PAA is homogeneously coated on the pore surface. The calculated membrane porosity after PAA modification is 25.4%. The calculated total PAA layer volume per membrane is 0.0825 cm3. The weight of total PAA is calculated to be 0.086 g. The dry PAA weight measured by mass difference before and after in-situ polymerization is 0.067 g. The variation is due to the uniform PAA thickness assumption for calculation and the wet and dry state difference. The residence time (τ) then can be obtained from dividing the membrane pore volume by the flow rate. And the mean velocity U_0 can be determined based on the membrane thickness and the residence time.

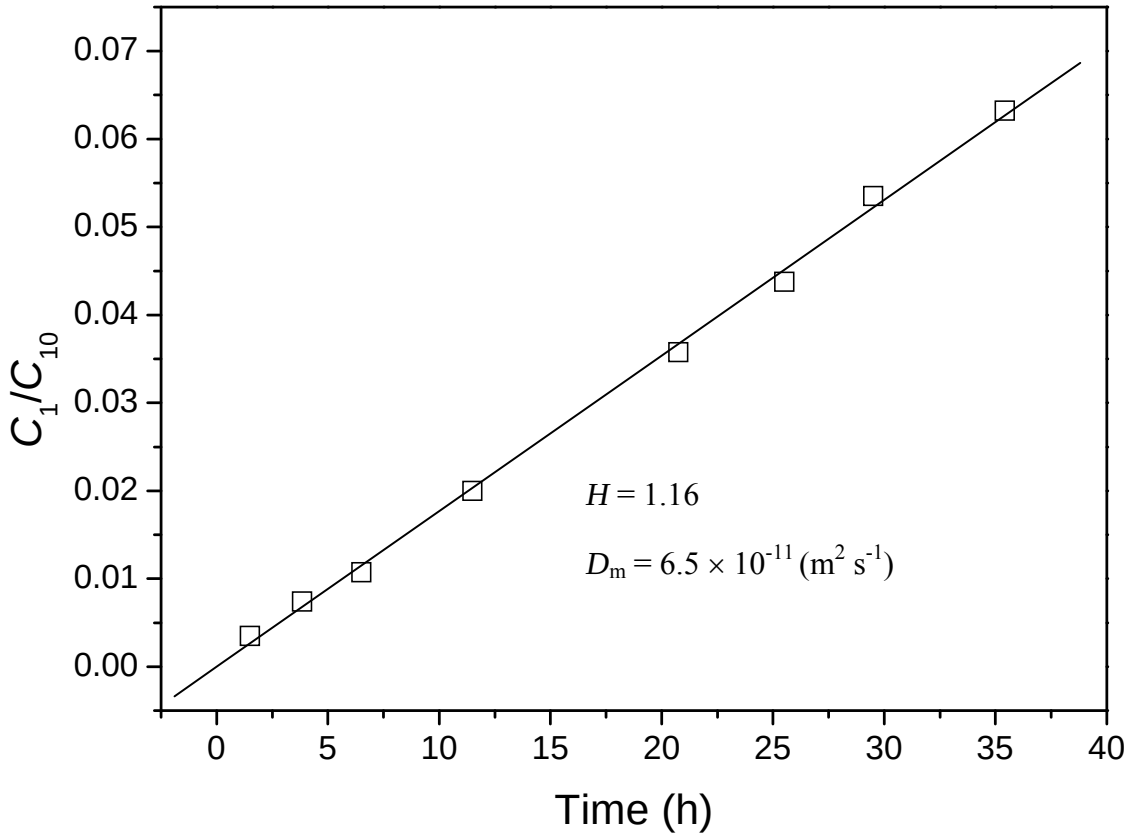

Figure 5.4 Experimental values of DiCB diffusion through PAA/PVDF membrane containing deactivated Fe nanoparticles. Membrane thickness: 125 × 10-6 m. Membrane area: 3.5 cm^2.

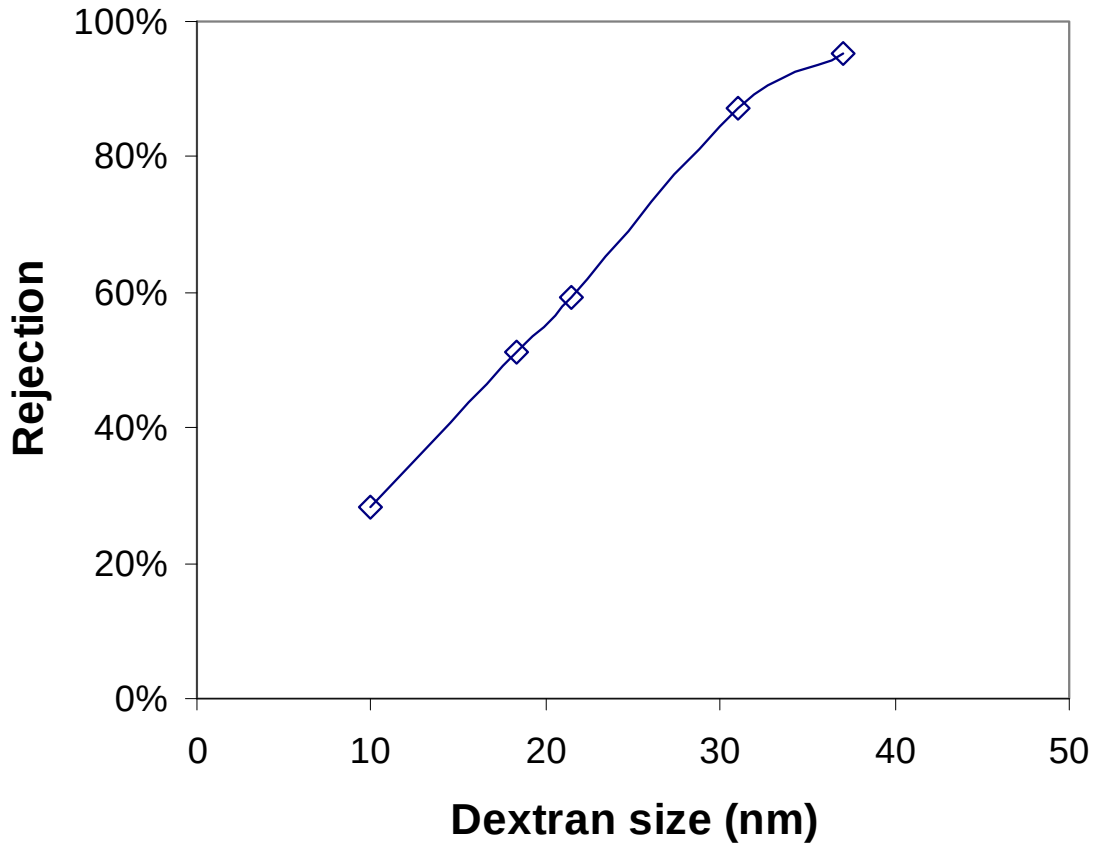

Figure 5.5 The rejection of different molecular weight dextran by pore-filled PAA/PVDF membrane containing Fe/Pd nanoparticles.

5.4 Modeling Results and Membrane Performance under Convective Flow Mode

Figure 5.6 shows the degradation of DiCB as a function of residence time (τ) for the PAA/PVDF membrane reactor containing Fe/Pd nanoparticles under convective flow mode. The membrane had 0.15 g Fe-Pd/cm^3 (Pd = 2.3 wt %) of loading evenly in the PAA layer. The membrane area is 13.2 cm^{-2} and 125 μm thickness. The plots in the Figure 5.6 correlated the model equation with the experimental data to obtain the intrinsic reaction rate. The intrinsic surface area normalized reaction rate (k_{in}) was adjusted to minimize the sum of squares between the model and experimental values. Based on the model fitting (R^2 = 0.97), k_{in} is determined to be 0.11 L m^{-2} h^{-2}, which is about 1.6 times higher than that in batch mode (0.068 L m^{-2} h^{-1}). This value seems reasonable because the rate we obtained in batch mode is the observed reaction rate which contains both the reaction and mass transfer (diffusion) term. However, the mass transfer and reaction are separate in the convective flow membrane reactor model, which results in the intrinsic reaction rate. Table 5.1 summarizes the model parameters used for the calculation of PAA/PVDF membrane reactor. As shown in the figure, the concentration of DiCB at the membrane outlet decrease with the increase of the residence time. This is as expected, longer residence means longer reaction time and higher DiCB conversion.

Figure 5.7 plots the experimental data and model prediction for the dechlorination products formation (biphenyl and intermediate) at different residence time. Biphenyl was the dominating product and 2-chlorobiphenyl was only detected in trace level. Since only trace amount of 2-chlorobiphenyl was observed, direct formation of biphenyl by replacing two chlorines simultaneously is assumed for the model calculation. The equations and boundary conditions used were given in below:

① *Membrane pore region*

$$U_z \frac{\partial C_B}{\partial z} = D_s \frac{1}{r} \frac{\partial C_B}{\partial r}\left(r \frac{\partial C_B}{\partial r} \right) + D_s \frac{\partial^2 C_B}{\partial z^2} \qquad \text{(E5.4)}$$

with the boundary conditions

$z = 0,\ C_B = 0$ (E5.4a)

$r = 0,\ \frac{\partial C_B}{\partial r} = 0$ (E5.4b)

② *PAA layer containing Fe/Pd nanoparticles*

$$D_m \frac{1}{r}\frac{\partial C_B}{\partial r}\left(r\frac{\partial C_B}{\partial r}\right) + D_m \frac{\partial^2 C_B}{\partial z^2} + (k_{in}\rho a_s \cdot C_{DiCB}) = 0 \qquad \text{(E5.5)}$$

with the boundary conditions:

$$r = r_1,\ D_s \frac{\partial C_B}{\partial r} = k_m (C_{B2} - HC_{B1}) \qquad \text{(E5.5a)}$$

$$r = r_2,\ \frac{\partial C_B}{\partial r} = 0 \qquad \text{(E5.5b)}$$

The model equations and boundary conditions for biphenyl are similar to those for DiCB calculation. C_B is the biphenyl concentration (mM). The diffusivity for biphenyl is assumed to be same as that for DiCB for simplification. k_{in} is determined to be 0.11 L m^{-2} h^{-2} based on the DiCB data fitting. As shown in the figure, the biphenyl model prediction matches the experimental data very well. This also verifies the previous model and data fitting. Due to the partitioning of PCBs in the membrane, the carbon balance in the permeate solution is about 85% ~ 90%.

The concentration profile inside the membrane reactor calculated at two different residence time is shown in Figure 5.8 and Figure 5.9. About 80% degradation of DiCB was achieved at the residence of 15 seconds. As shown in the figure, there is no significant concentration difference in the radial direction. This is due to the large ratio of membrane thickness (125 μm) over pore radius (64 nm). It is important to point out that Pe_r is determined to be 10^{-6} ~ 10^{-7}, while Pe_z is in the range of 1 to 25. This also confirms that radial variation can be neglected when $Pe_z >> Pe_r$. So the equations actually can be simplified to one dimension. In order to make the model general for different applications, we keep the model in 2-D form for the simulation. In order to show the radial variation effect, the membrane thickness was deliberately decreased to 125 nm to give the similar Pe_r and Pe_z. When the thickness is changed to 125 nm (all other parameters are kept the same), the Pe_r is determined to be 2×10^{-4} ~ 6×10^{-3}, while Pe_z is in the range of 1×10^{-3} ~ 2.5×10^{-2}. Since the membrane is extremely thin, the DiCB conversion is very low at the low residence. But the radial effect can be clearly seen in the figure.

Table 5.1 Parameters used for modeling PAA/PVDF membrane reactor containing Fe/Pd nanoparticles

Parameter	Units	Value
Membrane thickness, (reactor length, z)	(m)	1.25×10^{-4}
Membrane Pore size, (radius, r)	(m)	6.4×10^{-8}
PAA layer width	(m)	4.6×10^{-8}
Fe/Pd density, ρ	(g cm^{-3})	0.15
Fe/Pd nanoparticle size	(nm)	30
Fe/Pd nanoparticle surface area, S_a	(m^2 g^{-1})	25
Residence time, τ	(s)	0~25
DiCB partitioning coefficient, H	-	1.16
DiCB diffusion coefficient in membrane, D_m	(m^2 s^{-1})	6.5×10^{-11}
DiCB diffusion coefficient in bulk solution, D_s	(m^2 s^{-1})	7.5×10^{-10}

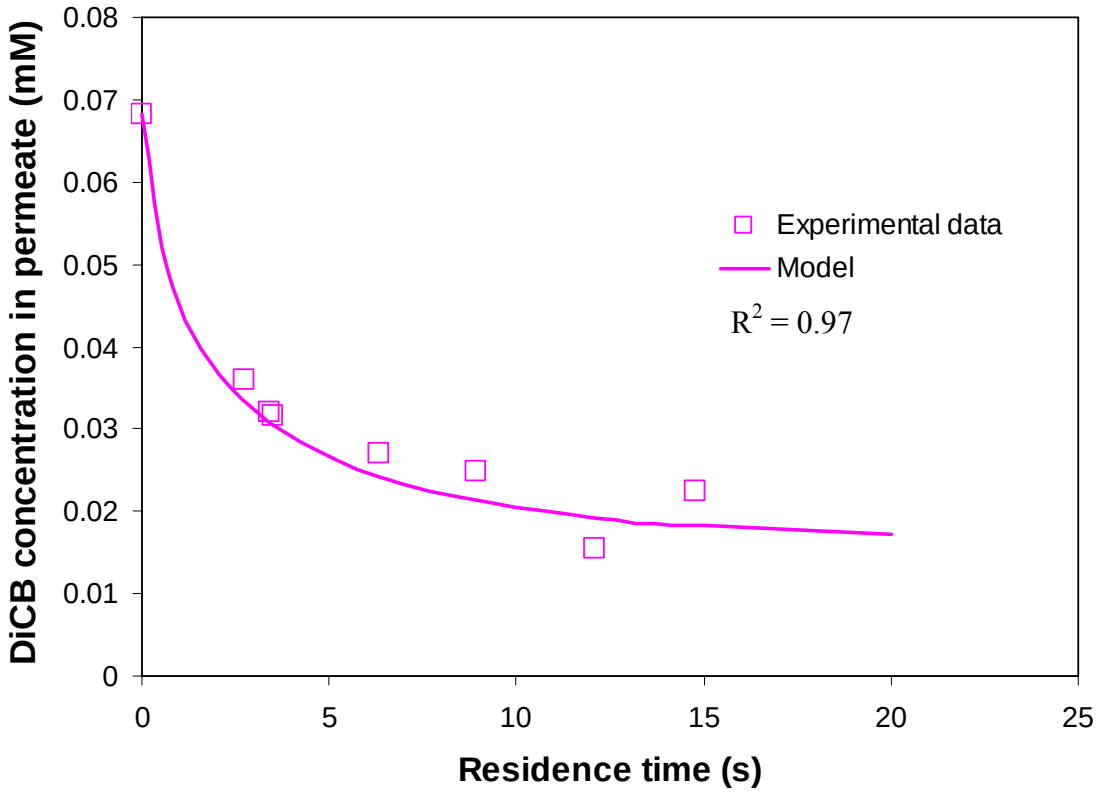

Figure 5.6 Plot of the molar concentration of DiCB in the PAA/PVDF membrane reactor outlet at difference residence time. Fe/Pd (Pd = 2.3 wt %) loading in the PAA layer: 0.15 g cm^{-3}.

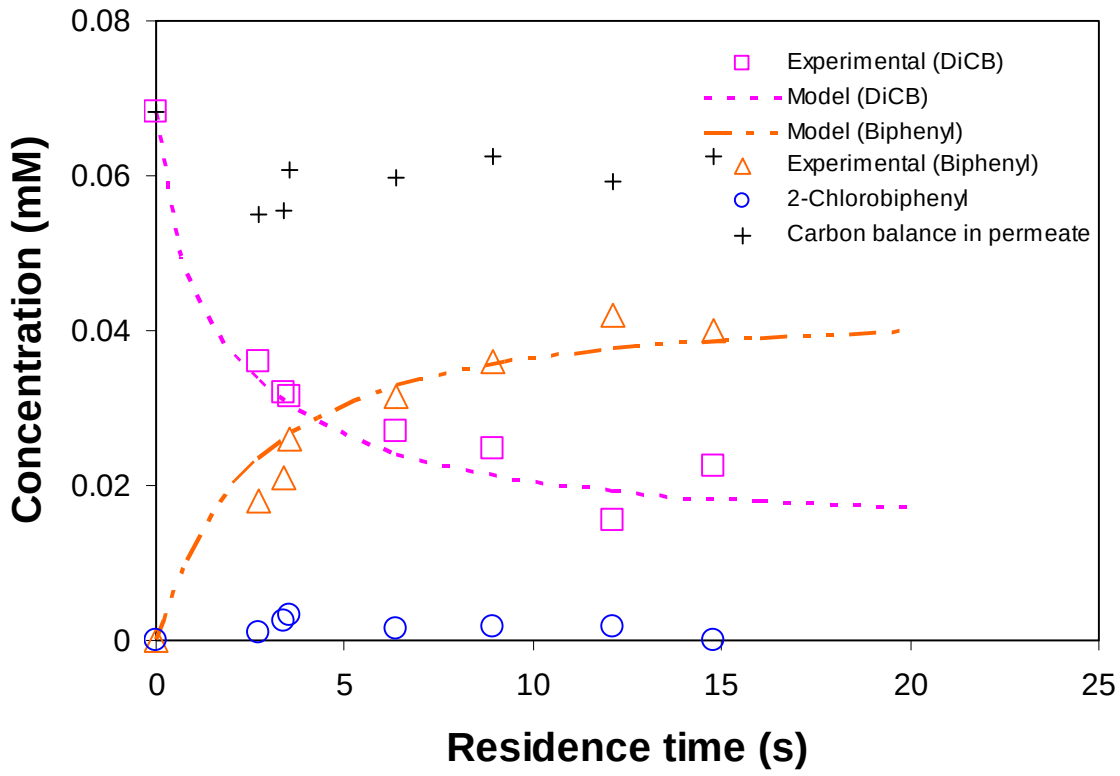

Figure 5.7 Degradation of DiCB by membrane supported Fe/Pd nanoparticles under convective flow mode. Plot of the molar concentration of DiCB, 2-chlorobiphenyl and biphenyl in the PAA/PVDF membrane reactor outlet at difference residence time. Fe/Pd (Pd = 2.3 wt %) loading in the PAA layer: 0.15 g cm^{-3}.

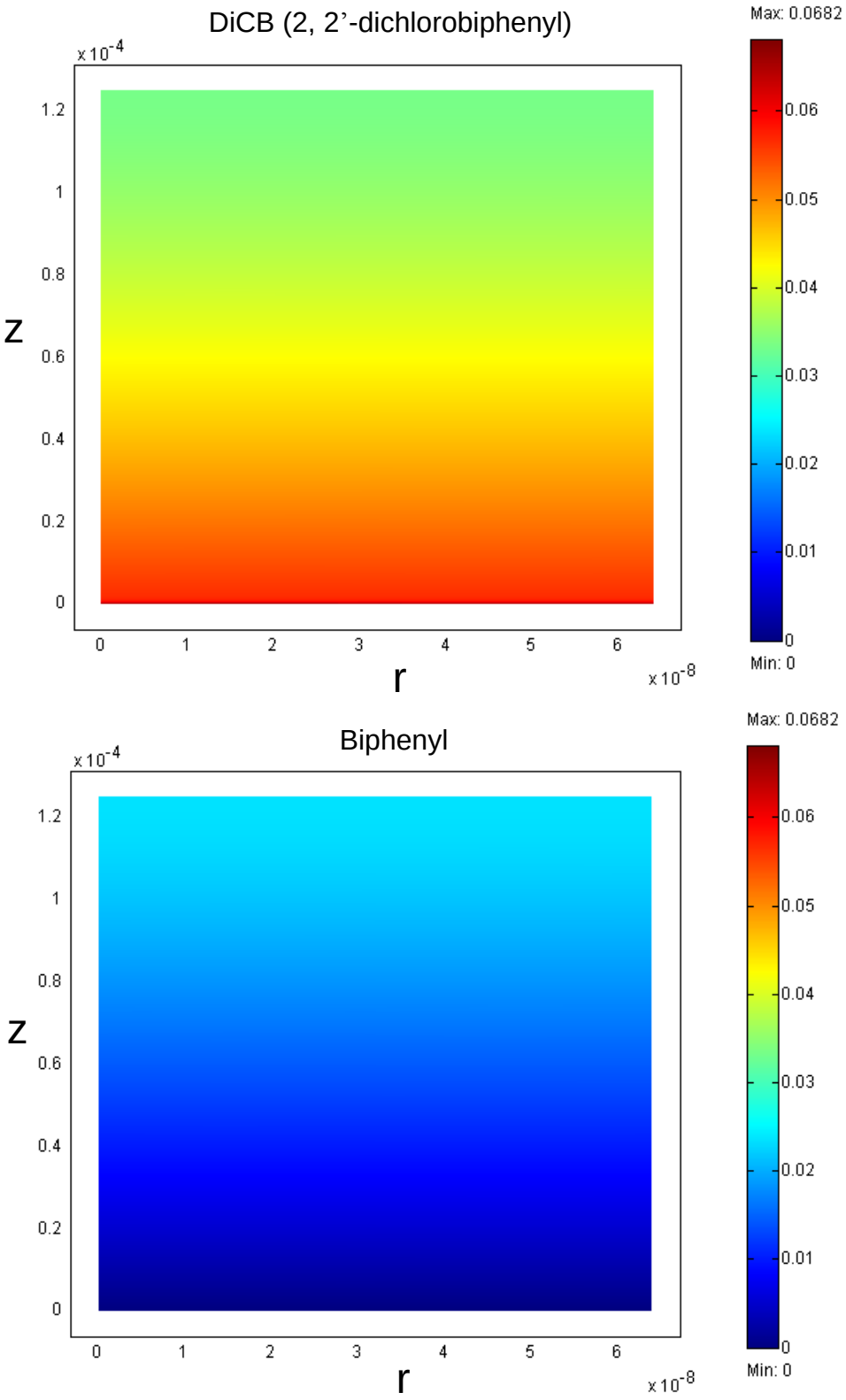

Figure 5.8 Concentration profile for DiCB degradation in the PAA/PVDF membrane reactor at residence time of 2.7 seconds. ($Pe_r = 2 \times 10^{-6}$, $Pe_z = 7.7$)

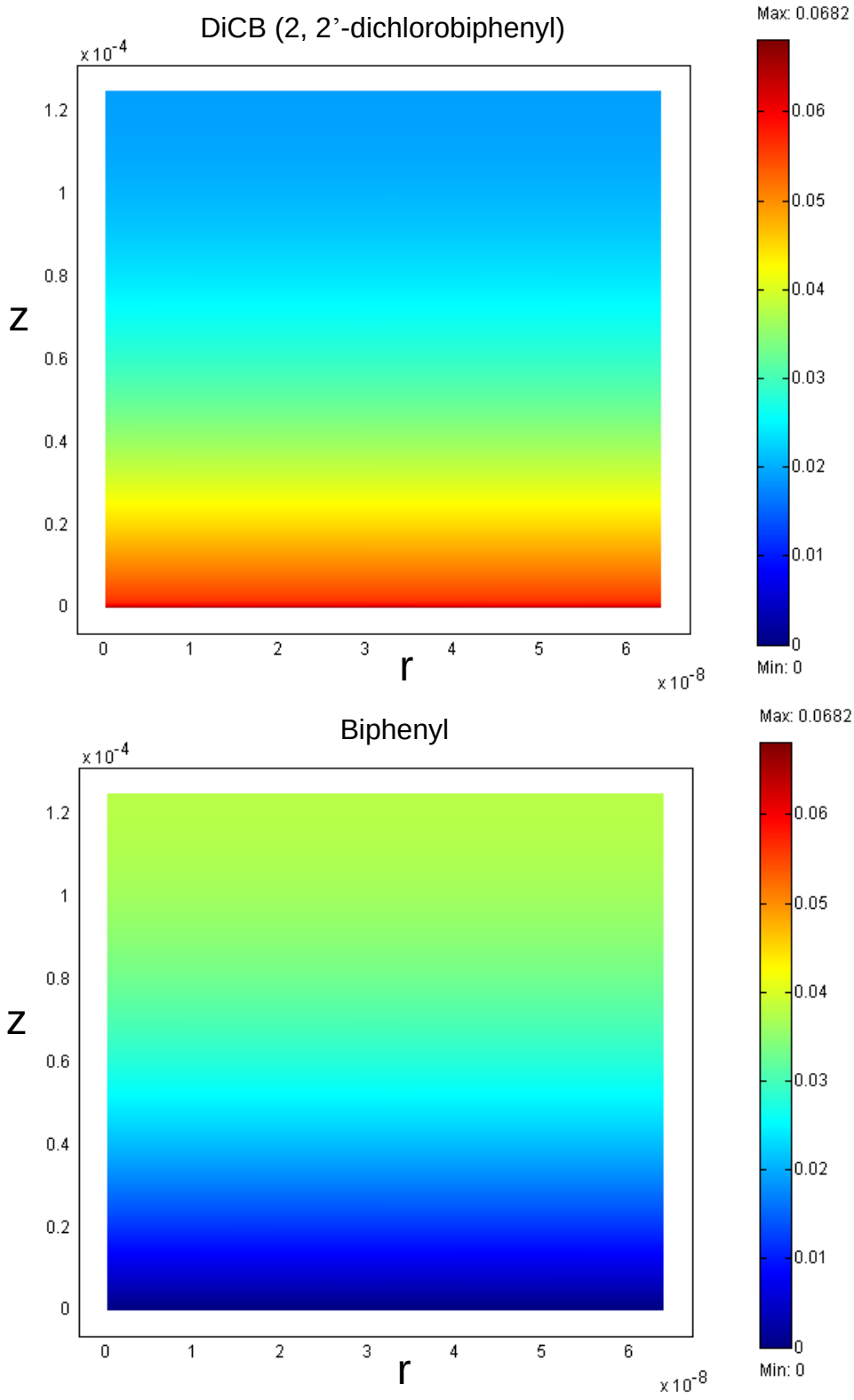

Figure 5.9 Concentration profile for DiCB and biphenyl in the PAA/PVDF membrane reactor at residence time of 12.1 seconds ($Pe_r = 4.4 \times 10^{-7}$, $Pe_z = 1.7$).

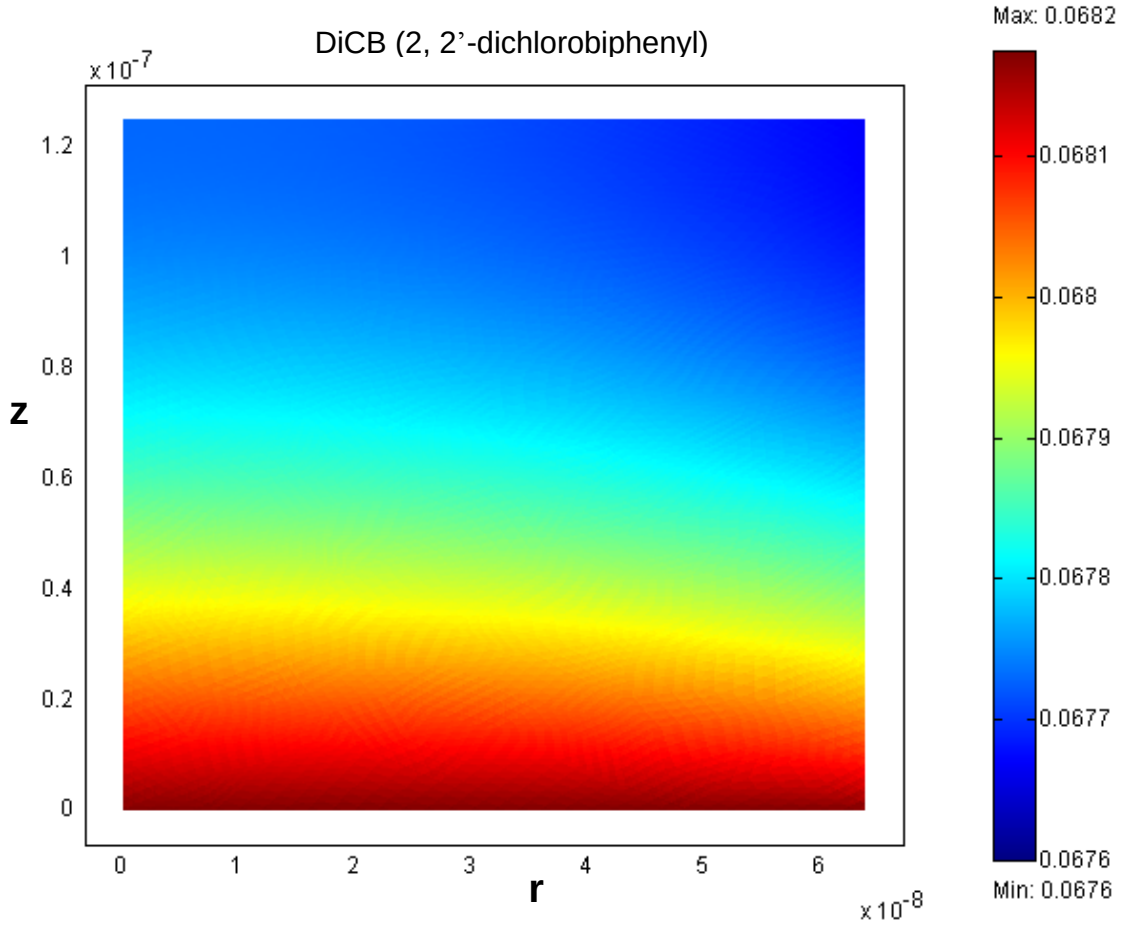

Figure 5.10 Plot of DiCB concentration variance in the radial direction. The membrane thickness was deliberately decreased 125 nm ($Pe_r = 4.4 \times 10^{-4}$, $Pe_z = 1.7 \times 10^{-3}$). The flow rate is the as that in the Figure 5.9.

In the previous chapter, the mean Fe/Pd nanoparticle size was determined to be 30 nm with the standard deviation of 6.7 nm. The deviation of particles size can lead to the variance in the particle surface area calculation, which eventually can result in the deviation of observed reaction rate. The deviation of the observed reaction rate is calculated to be 20% based on the 6.7 nm nanoparticle size deviation. Therefore, it is important to understand the effect of the deviation of the observed reaction rate on the model simulation.

Figure 5.11 shows the effect of observed reaction rate variation due to the nanoparticle size deviation. As shown in the figure, there is no significant variation caused by this deviation in the modeling results. The errors between the model and experimental results are also well matched within the modeling deviation.

Previously we assumed that there is no convective flow in the PAA layer for the model development and PCBs can enter into PAA layer only by diffusion. This assumption is reasonable since flow is preferentially through the pores at low operating pressure. However the actual flow may not be zero although it is much lower than the pore region because PAA is a highly hydrophilic and the PAA layer is not completely dense. In order to study the influence of the flow through the PAA layer, we performed the model calculation based on flow through the PAA layer. In this case, it becomes a homogeneous model where PAA and membrane pore are not in the separate domain. PAA containing Fe/Pd nanoparticles and membrane pore channel can be considered as one homogeneous domain. One equation including convection, diffusion and reaction can be used to describe this homogeneous model. The simulation result for the homogeneous model is shown in the Figure 5.12. The homogeneous model consider 100% convective flow pass through the PAA. The overall residence time is defined by membrane pore volume/volumetric flux. In the zero flow through PAA domain, the residence time is for flow through pores, but the actual reaction time is the diffusion time in PAA layer which is much longer than overall residence time. However in the convective flow through PAA mode (homogeneous model), the residence time is the actual reaction time. So as it can be seen in the figure, at high flow rate, the DiCB degradation in convective flow mode is less than zero flow through PAA mode. This is because reaction is the rate-controlling step at high flow rate (short reaction time results in less conversion). The insignificant

diffusion resistance can be confirmed by the high peclet number (Pez = 3 ~ 25) at high flow rate. But at low flow rate, diffusion becomes the rate-controlling step (low peclet number (Pez < 2 also indicates the high diffusion resistance) and convective flow through PAA shows high DiCB conversion rate than zero flow through PAA due to the less diffusion resistance.

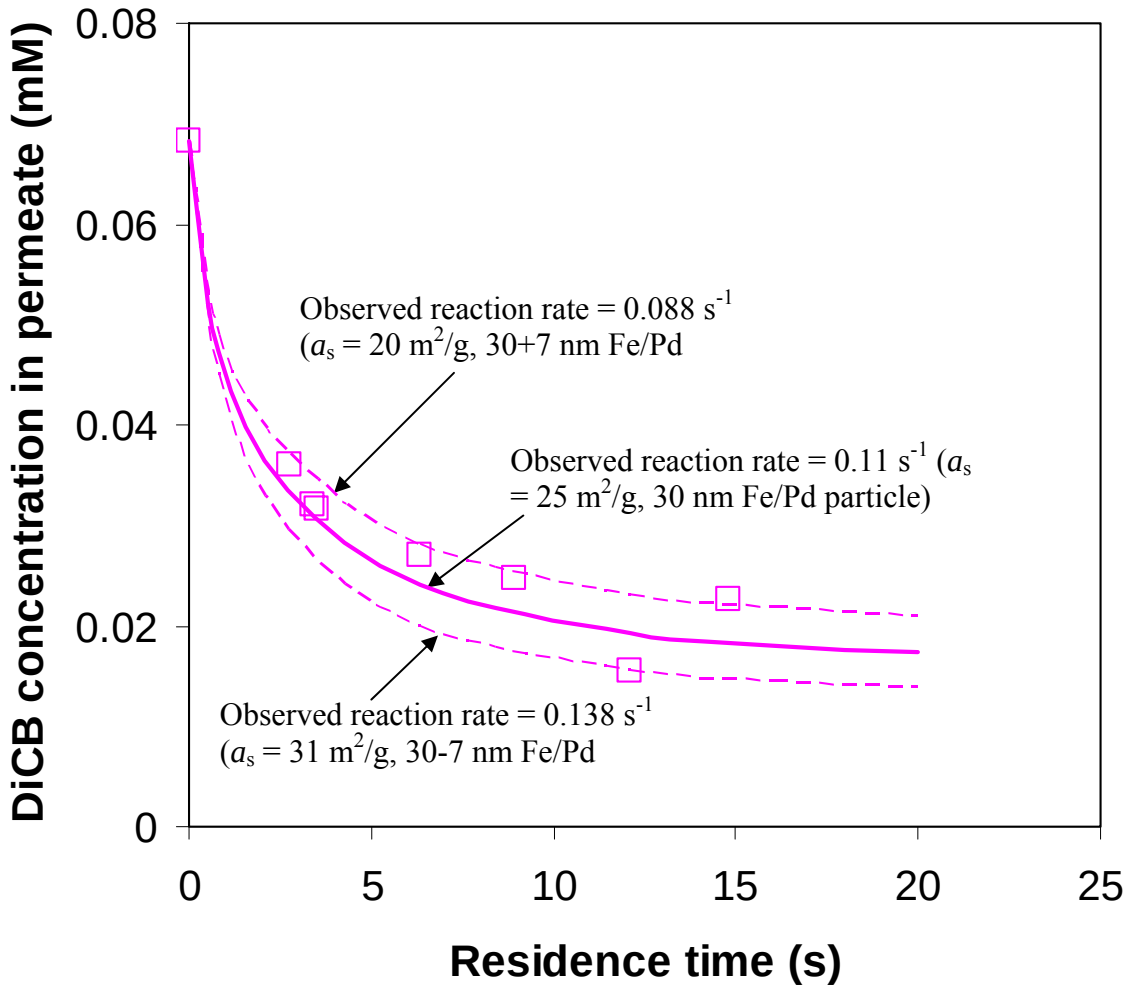

Figure 5.11 Influence of nanoparticle size standard deviation on the model prediction. Variation of molar concentration of DiCB in the PAA/PVDF membrane reactor outlet due to the deviation of nanoparticle size. Nanoparticle loading in the PAA layer: 0.15 g cm^{-3}.

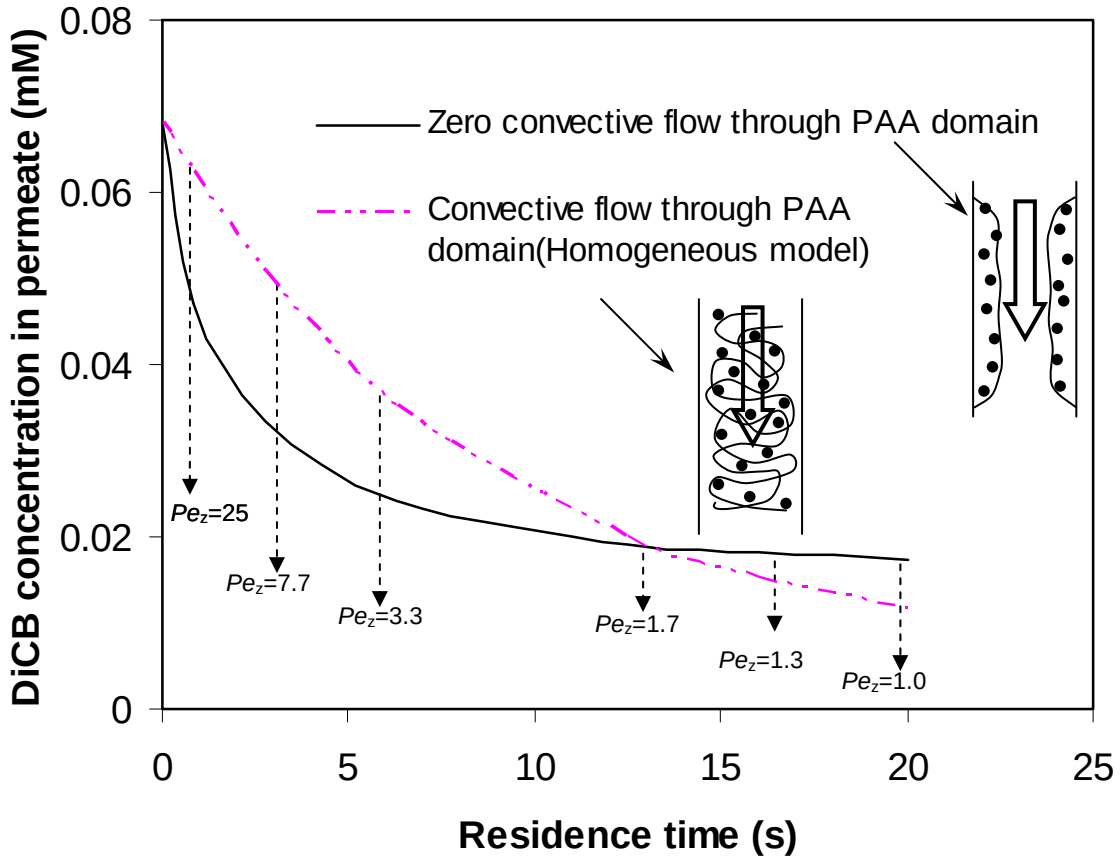

Figure 5.12 Modeling comparison for zero flow and convective flow through the PAA domain.

Influence of Pd composition

After solving the 2-D mass transfer and reaction equation for the membrane reactor, we start to use the model to simulate and predict the reaction under different conditions and parameter. First we can get a faster reaction by changing the reaction rate. Increasing the nanoparticles loading is the obvious way to obtain higher reaction rate. In the Chapter 4, we studied the effect of three different Pd coating compositions (0.6 wt%, 2.3 wt%, 5.6 wt%) on the reactivity of Fe/Pd nanoparticles in batch reactions. We found that the surface normalized reaction rate (k_{SA}) was enhanced with the increase of Pd coating. And k_{SA} can be expressed by $k_2 \cdot \Gamma$. k_2 is the same for the three different Pd coating system, and increased reaction rate is only due to the increase of Γ (Pd sites). Thus, we can change the reaction rate by changing the Pd coating composition (Γ). By comparing the Γ and k_{in} (Pd = 2.3 wt%), we can easily determine the k_{in} at the Pd coating of 0.6 wt% and 5.6 wt% to be 0.268 L m^{-2} h^{-1} and 0.0275 L m^{-2} h^{-1}, respectively. Figure 5.13 shows the modeling and experimental results of DiCB degradation at different Pd coating compositions under convective flow mode. The figure shows a significant increase of DiCB degradation at the higher Pd coating as well as a significant decrease of reaction at the lower Pd coating. About 90% conversion of DiCB was achieved at the residence time 15 seconds for the Pd coating composition of 5.6 wt%. Again, biphenyl was the dominating product, and 2-chlorobiphenyl was only detected in trace level. It can be seen that there is good agreement between the model prediction and experimental data. It is important to point out that the new reaction rate constants at higher Pd loading and lower Pd loading were obtained by the previous correlation between k_2 and Γ not by model fitting. The new rate constants were used to predict the reaction and compare with the experimental data.

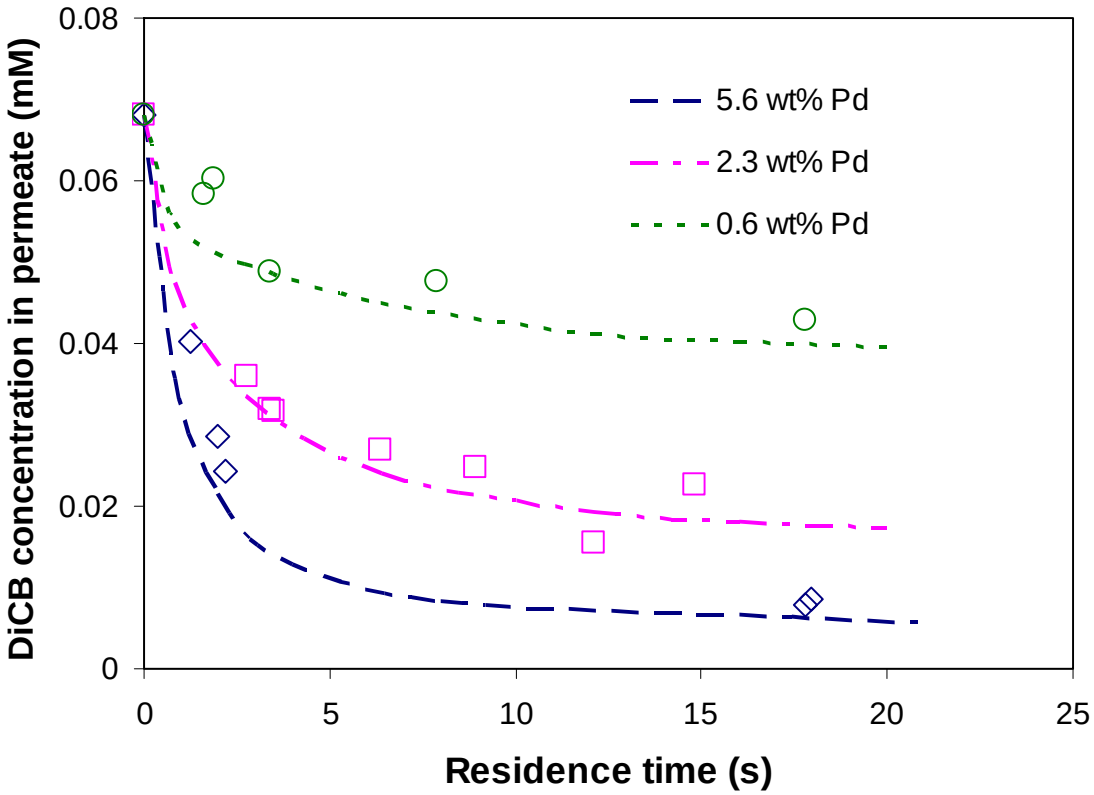

Figure 5.13 Modeling and experimental results of the effect of Pd coating composition on the dechlorination under convective flow. Plot of the molar concentration of DiCB in the PAA/PVDF membrane reactor outlet with different Pd coating at difference residence time. Nanoparticle loading in the PAA layer is the same for different Pd coating system: 0.15 g cm^{-3}. Note: the symbols represent the experimental data, while the lines represent model prediction.

Influence of membrane pore size

The membrane pore size is another important parameter in the design of the membrane reactor. In theory, the membrane pore size can be varied by either using different pore size support membranes (keeping the same amount of PAA functionalization) or changing the thickness of PAA layer. In this study, different sizes of PVDF support membranes were used to vary the pore size. Figure 5.14 shows the simulation results of DiCB degradation at different residence time for different membrane pore sizes. The experimental data for the 179 nm membrane pore were also plotted in the figure for comparison with the model prediction. As shown in the figure, there is a good agreement between the model prediction and experimental data, considering the simplification of uniform membrane pore distribution and experimental error. It can be seen that higher DiCB conversion was achieved in narrower membrane pores while the wider membrane pore would result in the lower DiCB conversion. This is due to the larger metal loading per unit pore volume in the narrower membrane pore size even though the metal loading per membrane is kept the same. The narrower pore channel also shortens the DiCB diffusion length and thus benefits the reaction.

Effect of PCB diffusivity through membrane

The diffusion coefficient (D_m) of PCB in membrane is determined by the property of the polymer and the degree of cross-linking. D_m is one of the system parameters that affect the PCB dechlorination results. Since PAA has been used as the functional polymer to immobilized bimetallic nanoparticles, D_m is a function of the density of PAA cross-linking. It is known that D_m usually decreases significantly as the cross-linking density increases (Reinhart and Peppas, 1983). The main purpose of this paper is to synthesize bimetallic nanoparticles in PAA functionalized membrane and study the catalytic dechlorination reactivity. Although PAA cross-linking density was not varied by experiment, we still can use the model to simulate the dechlorination reaction at different diffusion coefficient. Figure 5.15 shows modeling prediction of the effect of the D_m on the DiCB dechlorination under convective flow. Since PCBs must diffuse through PAA

layer before they can be adsorbed and then dechlorinated on the Fe/Pd nanoparticle surface, lower PCB diffusivity results in the higher diffusion resistance and thus decreases the reaction efficiency. As expected, the decrease of diffusivity led to a negative effect on the overall membrane reactor performance. As shown in the Figure, when $D_m > 6.5 \times 10^{-12}$ m^2 s^{-1}, the effect of D_m is significant while when $D_m < 6.5 \times 10^{-12}$ m^2 s^{-1}, the effect is much less sensitive to the variation of D_m.

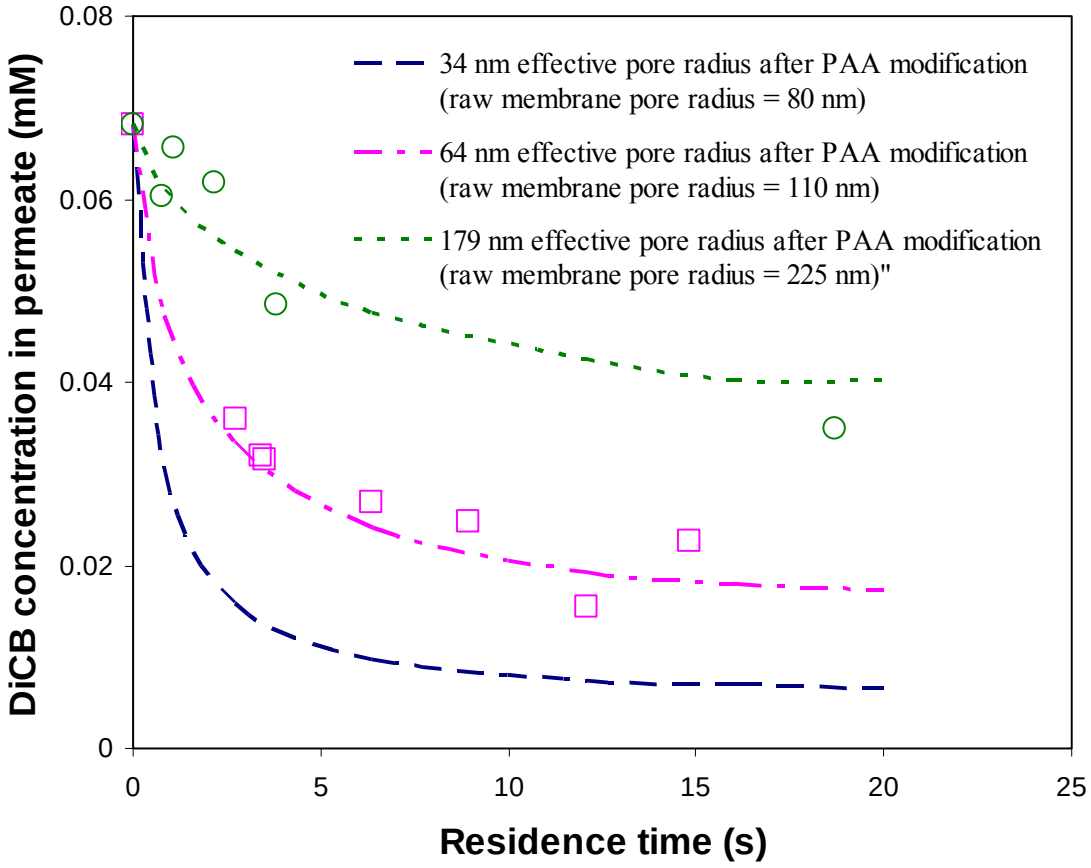

Figure 5.14 Modeling and experimental results of the effect of membrane pore size on the dechlorination under convective flow. Plot of the molar concentration of DiCB in the PAA/PVDF membrane reactor outlet with different membrane pore size at difference residence time. Fe/Pd (Pd = 2.3 wt%) nanoparticle loading in the PAA layer is the same : 0.15 g cm^{-3}. Note: the symbols represent the experimental data, while the lines represent model prediction.

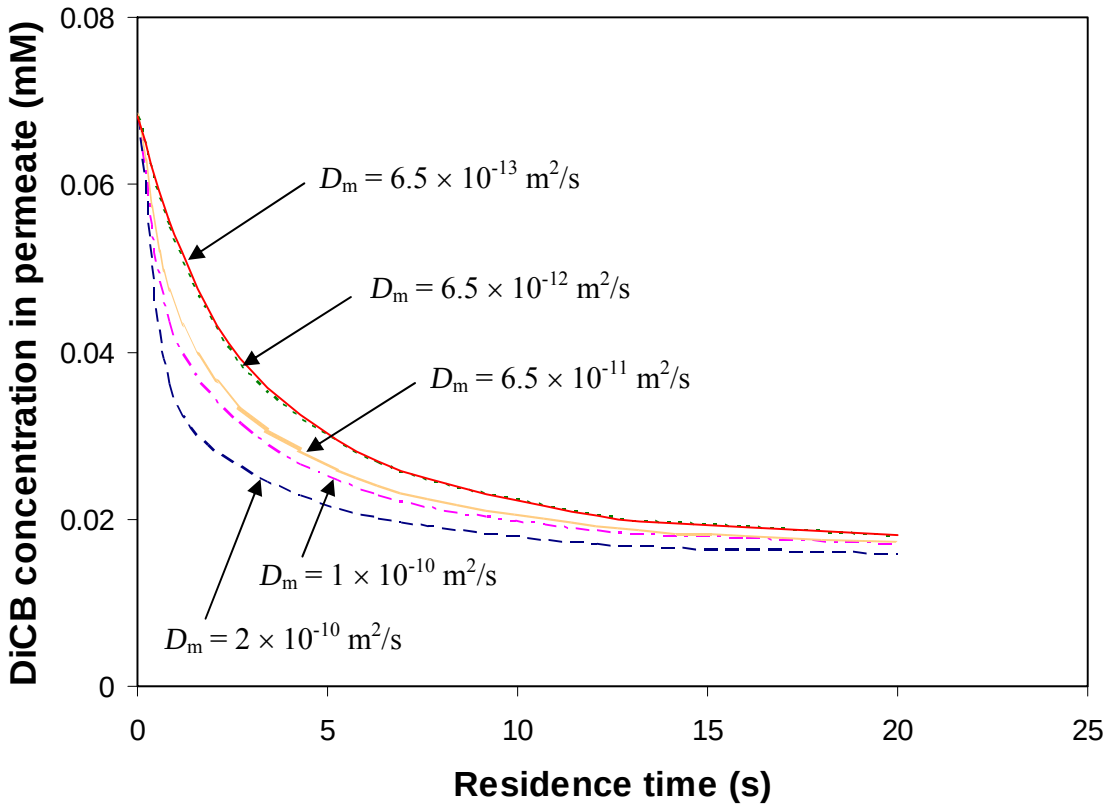

Figure 5.15 Effect of DiCB diffusivty through the membrane on the dechlorination under convective flow from the model simulation. Plot of the molar concentration of DiCB in the PVDF/PAA membrane reactor outlet with different DiCB diffusivity in membrane at difference residence time. Fe/Pd nanoparticle (Pd = 2.3 wt%) loading in the PAA layer is the same : 0.15 g cm^{-3}.

Chapter 6 Conclusion

The primary work in this dissertation has been focused on the experimental and modeling studies of reductive degradation of chlorinated organics using prepared membrane-based bimetallic nanoparticles. The overall conclusions involve the contributions and accomplishments in the following areas: nanoparticle synthesis & characterization, dechlorination kinetics & mechanism, and mathematical modeling simulation. This work has demonstrated successful in-situ synthesis of highly reactive bimetallic nanoparticles with controllable size, distribution and structure in the functionalized membrane matrix. The membrane immobilized nanostructured bimetallic materials (Fe/Ni and Fe/Pd) exhibited fast and complete reduction capability towards both chlorinated aliphatics and conjugated aromatics. The normalized reaction rate for TCE degradation by membrane supported Fe/Ni nanoparticles is about 5 times higher than the rate for Fe/Ni synthesized in solution, 200 times higher than the rate for nanoscale iron particles, and 400 times higher than the rate for bulk iron particles. With complete conversion to biphenyl, the normalized reaction rate for PCB dechlorination with membrane supported Fe/Pd nanoparticles in this study is 10,000 fold higher than that reported in the literature. A mathematical model including convection, diffusion and reaction was developed to describe and predict the organic dechlorination at different conditions inside membrane pores. The experimental data showed a good agreement with the model simulation results. Our work has led to significant improvement of current chlorinated organics degradation and advancement of high reactive nanostructured materials development.

Fundamental Science and Engineering Advancements:

- High loading of ion-exchange groups inside membrane pores can be achieved by in-situ polymerization of acrylic acid to capture metal ions as nanoparticle precursors.
- Well dispersed nanoscale particles can be synthesized in microporous membranes by ion-exchange and in-situ reduction processes.

- High resolution STEM-EDS mapping can be used to localize the PAA functionalization, characterize bimetallic nanoparticle structure and correlate it with reactivity
- Deposition of second metal (Ni or Pd) on iron can greatly enhance the reaction rate by changing the dechlorination pathway from electron transfer to catalytic hydrodechlorination.
- The normalized batch reaction rate for membrane supported bimetallic system is a function of reactive sites and hydrogen production
- Metal leaching from reaction can be minimized by recapture with ion-exchange groups in the membrane.

The specific conclusions and significances drawn from this work are summarized below.

6.1 Membrane Functionalization and Nanoparticle Synthesis

The hypothesis for membrane supported nanoparticles synthesis in this work is based on the chelation metal ions with ion-exchange groups in membrane followed by reduction of chelated metal ions. The membrane modification with ion-exchange groups for metal ions capture was achieved by two different methods: PAA dip-coating followed by thermal cross-linking with ethylene glycol; in-situ polymerization of acrylic acid inside membrane pores. Both methods have showed successful immobilization of PAA in MF membrane. PAA was mainly located on the membrane surface by dip-coating method, while in-situ polymerization resulted in homogenous distribution of PAA inside membrane pores. The membrane morphology and structure difference after PAA modification were characterized by SEM and TEM. The chelation interaction of metal ions and carboxylic acid was quantified by ICP analysis and EDS analysis. Especially, STEM-EDS mapping technique was successfully used to localize PAA functional domain from the PVDF substrate and illustrate the binding interaction between metal ions and PAA.

Bimetallic nanoparticles were synthesized in-situ by reduction of metal ions chelated with PAA in membrane. The PAA functionalized membrane provides a good

platform to immobilize and control the nanoparticles. SEM, TEM, HRTEM, EDS mapping were performed to characterize the size, structure and distribution of membrane supported bimetallic nanoparticles. The nanoparticles showed uniform size (~30 nm) and distribution in PAA domain without agglomeration due to the protection from polymer chains and chelation interaction. It has been proven the size and the nanoparticles can be manipulated within the membrane matrix. This is achieved by the control of the spacing distance between chelated metal ions by altering the metal loading. We have demonstrated that the bimetallic Fe/Ni nanoparticles can have an alloy or core/shell structure depending on the simultaneous reduction or sequential reduction of two metal ions. The alloy or core/shell structure were confirmed and illustrated by STEM-Mapping. High resolution EDS mapping also allows for understanding and correlating the nanoparticle structure and dopant metal composition with dechlorination reactivity.

6.2 Reductive Dechlorination by Membrane Supported Bimetallic Nanoparticles

In order to obtain high accurate analysis for reaction kinetics studies, we have established protocols to analyze various organics (TCE, PCB and complete intermediates and final product analysis), metal ions and chloride ions using EPA suggested methods. The synthesized Fe/Ni and Fe/Pd bimetallic nanoparticles in PAA functionalized MF membranes showed high reactivity towards the degradation of various chlorinated organics. Typically, complete degradation of TCE can be achieved within 1 hour by membrane based Fe/Ni nanoparticles. Complete conversion of ethane was observed in headspace, but no other chlorinated intermediate byproducts were found in both aqueous and headspace phase. The normalized reaction rate is about 5 times higher than the rate for Fe/Ni synthesized in solution, 200 times higher than the rate for nanoscale iron particles, and 400 times higher than the rate for bulk iron particles. The significant enhancement of the reaction rate is due to the reaction pathway shift from electron transfer (single Fe system) to catalytic hydrodechlorination. The role of water is to generate electrons and hydrogen gas from iron corrosion reaction. The hydrogen gas can be enriched on the Ni or Pd surface and decomposed into highly reactive atomic H to replace chlorine.

Fast and complete degradation of PCBs were also obtained using membrane supported Fe/Pd nanoparticles. Compared to the slower rate and incomplete dechlorination reported in the literature, our membrane based Fe/Pd system resulted in about 10,000-fold enhancement on the normalized reaction rate and complete conversion to biphenyl. The reaction rate is a function of the second metal composition because of the effect on the concentration of available active sites and the hydrogen production. Our correlation between the Pd composition and reaction rate indicates that the enhancement of the reaction rate is only due to the increase of Pd sites when Pd coating is less than one monolayer. The bimetallic nanoparticle structure also had a great effect on the reactivity. At the same amount of Ni coating, core/shell structure system led to 3-fold increase in the TCE degradation rate over the alloy structure Fe/Ni system. This enhancement is also due to the higher available active sites in the core/shell Fe/Ni system. The high resolution mapping benefits the understanding and quantification of the reactivity with structure and composition.

6.3 Mathematical Modeling of PCB Dechlorination by Membrane Based Fe/Pd Nanoparticles under Convective Flow

In order to predict results at different conditions, we have developed and applied a 2-D mathematical model for the PCB degradation by membrane supported Fe/Pd nanoparticles under convective flow mode. This model incorporates convection, diffusion and reaction kinetics to describe mass transfer and reaction in the membrane reactor module. In this model, the membrane reactor was characterized by the following four types of parameters: (1) membrane parameters: membrane pore size and porosity and membrane thickness; (2) system parameters: PCB solution density and viscosity, PCB diffusivity, PCB diffusivity and partitioning coefficient; (3) reaction parameters: nanoparticle surface area, Pd composition (Γ, reactive sites), metal loading, intrinsic reaction rate constant; (4) operating parameters: volumetric flux and initial PCB concentration. The intrinsic rate constant (k_{in}) has been determined by fitting the model with the experimental data. k_{in} is the only parameter that was taken as fitting parameters

for model validation and simulation. All other parameters were determined by independent calculations or experiments.

We have demonstrated the effects of varying membrane pore size, reaction rate constant and diffusivity by both the proposed model calculation and performed experiments. A good fitting of the experimental data has been obtained with the modeling simulation results. This model is a useful tool for the prediction and evaluation of PCB degradation at various conditions. For the variables investigated, the PCB degradation under convective flow benefited form narrow pore size, high intrinsic reaction rate.

Nomenclature

a_s = specific surface area ($m^2\ g^{-1}$)

A = membrane area (m^2)

C = organic (TCE or PCB) concentration (mM)

C_1 = organic (TCE or PCB) concentration in membrane pore region (mM)

C_2 = organic (TCE or PCB) concentration in PAA domain (mM)

C_B = Biphenyl concentration (mM)

D_s = diffusion coefficient of the bulk PCB solution ($m^2\ s^{-1}$)

D_m = diffusion coefficient of PCB in membrane phase ($m^2\ s^{-1}$)

d = membrane pore diameter (m)

H = PCB partitioning coefficient

k_m = mass transfer coefficient ($m\ s^{-1}$)

k_{SA} = normalized reaction rate ($L\ m^{-2}\ h^{-1}$)

k_{in} = intrinsic normalized reaction rate ($L\ m^{-2}\ h^{-1}$)

k_2 = second order rate constant at a particular type of site ($L\ h^{-1}\ mol^{-1}$)

M_B is the molecular weight of solvent ($g\ mol^{-1}$)

L = membrane thickness (m)

r = radial coordinate (m)

r_1 = mean membrane pore radius after the PAA modification (m)

r_2 = unmodified PVDF membrane mean pore radius (m)

r_s = hydraulic radius of the dextran molecule (m)

Pe_r = peclet number in the radial direction, $(r_1^2/D_s)/(L/U_0)$

Pe_r = peclet number in the axial direction, $(L^2/D_s)/(L/U_0)$

R = the rejection of dextran

Re = Reynolds number ($Re = \rho U_0 d/\mu$)

Sc = Schmidt number ($Sc = \mu/\rho D_s$)

T = temperature (K)

t = time (h)

U_z = the velocity along the z-axis (m s^{-1})

V = volume of the feed and permeation side for diffusion experiment (m^3)

U_0 = the mean velocity along the z-axis (m s^{-1})

z = axial coordinates (m)

Greek letters

ε = membrane porosity

ϕ = association factor for solvent

μ = viscosity of PCB solution (kg m^{-1} s^{-1})

ρ = density of PCB solution (kg m^{-3})

ρ_m = mass concentration of metal (g L^{-1})

τ = residence time (s)

ν_A = molar volume of PCB (m^3 $kmol^{-1}$)

Γ = surface concentration of reactive sites (mol m^{-2})

Chemical / polymer symbols

AA: Acrylic acid

PAA: Polyacrylic acid

DiCB: 2, 2’-dichlorobiphenyl

PCB: Polychlorinated biphenyl

PES: Polyether sulfone

PVDF: Polyvinylidene fluoride

TCE: Trichloroethylene

TMPTA: 1,1,1-trimethylolpropane triacrylate

References

Ahuja, D., Bachas, L., and Bhattacharyya D., Modified fenton reaction for trichlorophenol dechlorination by enzymatically generated H_2O_2 and gluconic acid chelate, Chemosphere, 2007, 66, 2193–2200.

Aiken III, J.D., Finke, R.G., A review of modern transition-metal nanoclusters: their synthesis characterization, and applications in catalysis, Journal of Molecular Catalysis A: Chemical, 1999, 145, 1-44.

Akamatsu, K., Deki, S., Nanoscale metal particles dispersed in polymer matrix, NanoStructured Materials, 1997, 8, 1121-1129.

Arnold, W.A., Roberts, A. L., Pathways of chlorinated ethylene and chlorinated acetylene reaction with Zn (0), Environ. Sci. Technol., 1998, 32, 3017-3025.

Arnold, W.A., Ball, W.P. and Roberts, A.L., Polychlorinated ethane reaction with zero-valent zinc: pathways and rate control, Journal of Contaminant Hydrology, 1999, 40, 183-200.

Avramescu, M.E., Sager, W.F.C., Wessling, M., Functionalised ethylene vinyl alcohol copolymer (EVAL) membranes for affinity protein separation., J. Membr. Sci., 2003, 216, 177-193.

Basu, S., Wei, I.W., Advanced chemical oxidation of 2,4,6-trichlorophenol in aqueous phase by Fenton's reagent-part I: effects of the amounts of oxidant and catalyst on the treatment reaction, Chem. Eng. Comm., 1998, 164, 111-137.

Bhattacharyya, D., Hestekin, J.A., Brushaber, P., Cullen, L., Bachas, L.G. and Sikdar, S.K., Novel poly-glutamic acid functionalized Microfiltration membranes for sorption of heavy metals at high capacity, J. Membr. Sci., 1998, 141, 121-135.

Bhattacharyya, D. and Butterfield, A., New Insights into Membrane Science and Technology : Polymeric, Inorganic and Biofunctional Membranes, Elsevier Science, 2003.

Bodnariuk, P., Coq, B., Ferrat, G., Figueras, F. Carbon-chlorine hydrogenolysis over PdRh and PdSn bimetallic catalysts. J. Catal., 1989, 116, 459-466.

Boronina, T.N., Lagadic, I., Sergeev, G.B., Klabunde, K.J., Activated and nonactivated forms of zinc power: reactivity towards chlorocarbons in water and AFM studies of surface morphologies, Environ. Sci. Technol., 1998, 32, 2614-2622.

Brown, C.A., Catalytic hydrogenation. V. Reaction of sodium borohydride with aqueous nickel salts. P-1 nickel boride, a convenient, highly active nickel hydrogenation catalyst, J. Org. Chem. 1970, 35, 1900-1904.

Brown, C.A., Brown H.C., The reaction of sodium borohydride with nickel acetate in aqueous solution-A convenient synthesis of an active nickel hydrogenation catalyst of low isomerizing tendency, J. Am. Chem. Soc. 1963, 85, 1003-1005.

Burrow, P.D., Aflatooni, K., Gallup, G.A., Dechlorination rate constants on iron and the correlation with electron attachment energies, Environ. Sci. Technol., 2000, 34, 3368-3371.

Carpenter, E. E., Calvin, S., Stroud, R. M., Harris, V. G., Passivated iron as core-shell nanoparticles, Chem. Mater., 2003, 15, 3245-3246.

Choe, S., Lee, S.H., Chang, Y.Y., Hwang, K.Y., Khim, J., Rapid reductive destruction of hazardous organic compounds by nanoscale Fe^0. Chemosphere. 2001, 42, 367-372.

Choi, H.S., Hino, T., Shibata, M., Negishi, Y., Ohya, H., The characteristics of a PAA-PSF composite membrane for separation of water ethanol mixtures through Pervaporation, J. Membr. Sci., 1992, 72, 259-266.

Chuang, F., Larson, R.A., Wessman, M.S., Zero-valent iron-promoted dechlorination of polychlorinated biphenyls, Environ. Sci. Technol. 1995, 29, 2460-2463.

Ciebien, J.F., Cohen, R.E. and Duran, A., Membrane catalysts for partial hydrogenation of 1, 3-butadiene: catalytic properties of palladium nanoclusters synthesized within diblock copolymer films, Materials Science and Engineering C 7, 1999, 45-50.

Corbierre, M. K., Cameron, N. S., Lennox, R. B., Polymer-stabilized gold nanoparticles with high grafting densities, Langmuir, 2004, 20, 2867-2873.

Cwiertny, D. M., Bransfield, S. J., Roberts, A. L., Influence of the oxidizing species on the reactivity of iron-based bimetallic reductants, Environ. Sci. Technol., 2007, 41, 3734-3740.

Damle, C., Biswas, K., Sastry, M., Synthesis of Au-core/Pt-shell nanoparticles within thermally evaporated fatty amine films and their low-temperature alloying. Langmuir, 2001, 17, 7156-7159.

Delaunois, F., Petitjean, J.P., Lienard, P., Jacob-Duliere, M., Autocatalytic electroless nickel-boron plating on light alloys. ATB Metallurgie, 2001, 41, 10-13.

Ferry, J.D., Statistical evaluation of sieve constants in ultrafiltration. J. Gen. Physiol., 1936, 20, 95-104.

Fukasawa, T., Suetsuna, T., Harada, K., Suenaga, S., Catalytic performance of metal nanoparticles supported by ceramic composite produced by partial reduction of solid solution with dopant. J. Am. Ceram. Soc., 2005, 88, 2938-2941.

Gabriel, E. M., Gillberg, G. E., In situ modification of microporous membranes, J. Appl. Poly. Sci., 1993, 48, 2081-2090.

Geismann, C., and Ulbricht, M., Photoreactive functionalization of poly (ethylene terephthalate) track-etched pore surfaces with ‘‘smart’’ polymer systems., Macromol. Chem. Phys., 2005, 206, 268–281.

Glavee, G.N., Klabunde, K.J., Sorensen, C.M., Hadjipanayis, G.C., Chemistry of borohydride reduction of iron (II) and iron (III) ions in aqueous and nonaqueous media. formation of nanoscale Fe, FeB and Fe_2B powders, Inorg. Chem., 1995, 34, 28-35.

Gonsalves, K.E., Li, H., Perez, R., Santiago, P. and Jose-Yacaman, M., Synthesis of nanostructured metals and metal alloys from organometallics, Coordination Chemistry Reviews, 2000, 206-207, 607-630.

Gotpagar, J., Grulke, E., Tsang, T., Bhattacharyya, D., Reductive dehalogenation of trichloroethylene Using Zero-Valent Iron, Environ. Prog.,1997, 16, 137-143.

Gotpagar, J.K., Grulke, E.A. and Bhattacharyya, D., Reductive dehalogenation of trichloroethylene: kinetic models and experimental verification, Journal of Hazardous Materials, 1998, 62, 243-264.

Gotpagar J., Lyuksyutov S., Cohn R., Grulke E. and Bhattacharyya D., Reductive dehalogenation of trichloroethylene with zero-valent iron: surface profiling microscopy and rate enhancement studies, Langmuir 1999, 15, 8412-8420.

Grittini C., Malcomson M., Fernando Q. and Korte N., Rapid dechlorination of polychlorinated biphenyls on the surface of a Pd/Fe bimetallic system, Environ. Sci. Technol., 1995, 2898.

Gryglewicz, G., Stolarski, M., Gryglewicz, S., Klijanienko, A., Piechocki, W., Hoste, S., Van Driessche, I., Carleer, R., Yperman, J. Hydrodechlorination of dichlorobiphenyls over Ni–Mo/Al2O3 catalysts prepared by spray-drying method. Chemosphere, 2006, 62, 135-141.

Haber, F., and Weiss J., The catalytic decompotition of hydrogen peroxide by iron salts, Proc. R. Soc. London, 1934, A147, 332-351.

Hagel, L., Aqueous-size-exclusion chromatography. J. Chrom. Library, 1988, 40, 119-155.

He, F., Zhao, D. Preparation and characterization of a new class of starch-stabilized bimetallic nanoparticles for degradation of chlorinated hydrocarbons in water. Environ. Sci. Technol. 2005, 39, 3314-3320.

He, F., Zhao, D., Liu, J., Roberts, C. B., Stabilization of Fe-Pd nanoparticles with sodium carboxymethyl cellulose for enhanced transport and dechlorination of trichloroethylene in soil and groundwater, Ind. & Eng. Chem. Res., 2007, 46, 29-34.

He, J., Ichinose, I., Kunitake, T., Nakao, A., In situ synthesis of noble metal nanoparticles in ultrathin TiO2-gel films by a combination of ion-exchange and reduction processes. Langmuir, 2002, 18, 10005-10010.

He, J., Ichinose, I., Kunitake, T., Nakao, A., Shiraishi, Y., Toshima, N., Facile fabrication of Ag-Pd bimetallic nanoparticles in ultrathin TiO2-Gel films: nanoparticle morphology and catalytic activity. J. Am. Chem. Soc., 2003, 125, 11034-11040.

Helland, B.R., Alvarez, P.J.J. and Schnoor, J.L., Reductive dechlorination of carbon tetrachloride with elemental iron, Journal of Hazardous Materials, 1995, 41, 205-216.

Henry, C.R., Growth, structure and morphology of supported metal clusters studied by surface science techniques, Cryst. Res. Technol., 1998, 33, 1119-1140.

Hestekin, J.A., Bachas, L. G., Bhattacharyya, D., Poly (amino acid) - functionalized cellulosic membranes: metal sorption mechanisms and results, Ind. Eng. Chem. Res. 2001, 40, 2668-2678.

Hierso, J.C., Feurer, R. Poujardieu, J., Kihn, Y., Kalck, P., Metal-organic chemical vapor deposition in a fluidized bed as a versatile method to prepare layered bimetallic nanoparticles, Journal of Molecular Catalysis A: Chemical, 1998, 135, 321-325.

Ho, W. and Sirkar, K. K., Membrane handbook, Van Nostrand Reinhold, 1992, New York.

Hong, S. U., Bruening, M. L., Separation of amino acid mixtures using multilayer polyelectrolyte nanofiltration membranes., J. Membr. Sci., 2006a, 280, 1-5.

Hong, S.U., Miller, M. D., Bruening, M. L., Removal of dyes, sugars, and amino acids from NaCl solutions using multilayer polyelectrolyte nanofiltration membranes., Ind. Eng. Chem. Res., 2006b, 45, 6284-6288.

Huang, J., Guo,Q., Ohya, H., Fang, J., The characteristics of crosslinked PAA composite membrane for separation of aqueous organic solutions by reverse osmosis, J.Membr.Sci., 1998, 144, 1-11.

Huang, Q., Rusling, J. F., Formal reduction potentials and redox chemistry of polyhalogenated biphenyls in a bicontinuous microemulsion, Environ. Sci. Technol. 1995, 29, 98-103.

Ikeda, S., Akamatsu, K., Nawafune, H., Nishino, T., Deki, S., Formation and growth of copper nanoparticles from ion-doped precursor polyimide layers. J. Phys. Chem. B., 2004, 108, 15599-15607.

Jain, P. K., Lee, K. S., El-Sayed, I. H., El-Sayed, M. A., Calculated absorption and scattering properties of gold nanoparticles of different size, shape, and composition: applications in biological imaging and biomedicine. J. Phys. Chem. B. 2006, 110, 7238-7248.

Jiang, C., Markutsya, S., Pikus, Y., Tsukruk, V., Freely suspended nanocomposite membranes as highly sensitive sensors. Nature Mater., 2004, 3, 721-728.

Johnson, T.L., Scherer, M.M., Tratnyek, P.G., Kinetics of halogenated organic compound degradation by iron metal, Environ. Sci. Technol. 1996, 32, 2634-2640

Kiadambi, S., Bruening M.L., Multilayered polyelectrolyte films containing palladium nanoparticles: synthesis, characterization, and application in selective hydrogenation. Chem.Mater., 2005, 17, 301-307.

Kim, Y.H. and Carraway E.R., Reductive dechlorination of TCE by zero valent bimetals, Environ. Tech., 2003, 24, 69-75.

Kiwi, J., Lopez, A., Nadtochenko, V., Mechanism and kinetics of the OH-radical intervention during Fenton oxidation in the presence of a significant amount of radical scavenger (Cl-). Environ. Sci. Technol.,2000,34, 2162-2168.

Konishi, S., Saito, K., Furusaki, S. and Sugo, T., Binary metal-ion sorption during permeation through chelating porous membranes, J. Membr. Sci., 1996, 111, 1-6.

Korte, N. E., West, O. R., Liang, L., Gu, B., Zutman, J. L., Fernando, Q., The effect of solvent concentration on the use of palladized-iron for the step-wise dechlorination of polychlorinated biphenyls in soil extracts, Waste Management, 2002, 22, 343-349.

Kwan, W.P., Voelker, B.M., Decomposition of hydrogen peroxide and organic compounds in the presence of dissolved iron and ferrihydrite, Environ. Sci. Technol., 2002, 36, 1467-1476.

Legrand, J.-C., Diamy, A.-M., Riahi, G., Randriamanantenasoa, Z., Polisset-Thfoin, M., Fraissard, J., Application of a dihydrogen afterglow to the preparation of zeolite-supported metallic nanoparticles. Catalysis Today, 2004, 89, 177-182.

Li, F., Vipulanandan, C., Mohanty, K. K. Microemulsion and solution approaches to nanoparticle iron production of degradation of trichloroethylene. Colloids Surf., A 2003, 223, 103-112.

Li, Y.C., Bachas, L. G., Bhattacharyya, D., Kinetics Studies of Trichlorophenol destruction by chelate-based Fenton reaction. Environ. Eng. Sci., 2005, 22, 756-771.

Lien, H.L., Zhang, W.X., Nanoscale iron particles for complete reduction of chlorinated ethenes. Colloids and Surfaces A: Physicochemical and Engineering Aspects, 2001,191, 97-105.

Lindau, J., Jönsson; Bottino, A., Flux reduction of ultrafiltration membranes with different cut-off due to adsorption of a low-molecular-weight hydrophobic solute-correlation between flux decline and pore size. J. Membr. Sci., 1998, 149, 11-20.

Liu, Y., Majetich, S.A., Tilton, R.D., Sholl, D.S., Lowry G.V., TCE dechlorination rates, pathways, and efficiency of nanoscale iron particles with different properties. Environ. Sci. Technol., 2005, 39, 1338-1345.

Liu, Y., Lowry, G. V., Effect of particle age (Fe^0 Content) and solution pH on NZVI reactivity: H_2 evolution and TCE dechlorination. Environ. Sci. Technol., 2006, 40, 6085-6090.

Liu, Z., Ling, X. Y., Su, X., Lee, J. Y., Carbon-supported Pt and PtRu nanoparticles as catalysts for a direct methanol fuel cell. J. Phys. Chem. B., 2004, 108, 8234-8240.

Lowry, G. V., Johnson, K. M., Congener-specific dechlorination of dissolved PCBs by microscale and nanoscale zerovalent iron in a water/methanol solution, Environ. Sci. Technol., 2004, 38, 5208-5216.

Macalady, D. L., Tratnyek, P. G., Grundl, T. J., Abiotic reduction reactions of anthropogenic organic chemicals in anaerobic systems: a critical review, J. Contam. Hydrol., 1986, 1, 1-28.

Mandal S., Selvakannan, P.R., Pasricha, R., Sastry M., Keggin ions as UV-switchable reducing agents in the synthesis of Au core-Ag shell nanoparticles, J. Am. Chem. Soc., 2003, 125, 8440-8441.

Matheson, L.J., Tratnyek, P.G., Reductive dehalogenation of chlorinated methanes by iron metal, Environ. Sci. Technol., 1994, 28, 2045-2053.

Meyer, D. E., Williams, M., and Bhattacharyya, D., Reverse osmosis in Kirk-Othmer encyclopedia of chemical technology, John Wiley, 2006.

Moharram, M. A. and Khafagi, M. G., Thermal behavior of poly(acrylic acid)–poly(vinyl pyrrolidone) and poly(acrylic acid)–metal–poly(vinyl pyrrolidone) complexes, J. Appl. Poly. Sci., 2006, 102, 4049–4057.

Morris, P. J., Mohn, W. W., Quensen, J F, III; Tiedje, J. M., Boyd, S. A., Establishment of polychlorinated biphenyl-degrading enrichment culture with predominantly meta dechlorination, Appl. Environ. Microbiol., 1992, 58, 3088-3094.

Murena, F., Schioppa, E., Gioia, F. Catalytic hydrodechlorination of a PCB dielectric oil. Environ. Sci. Technol. 2000, 34, 4382-4385.

Nakano, Y., Okawa, K., Nishijima, W., Okada, M., Ozone decomposition of hazardous chemical substance in organic solvents, Water Res., 2003, 37, 2595-2598.

Nutt, M., Hughes, J.B., Wong, M., Designing Pd-on-Au bimetallic nanoparticle catalysts for trichloroethene hydrodechlorination. Environ. Sci. Technol., 39, 2005, 1346-1353.

Ohya, H., Shibata, M., Negishi, Y., Guo, Q.H., Choi, H.S., The effect of molecular weight cut-off of PAN ultrafiltration support layer on separation of water-ethanol mixtures through Pervaporation with PAA-PAN composite membrane, J.Membr.Sci., 1994, 90, 91-100.

Orth, W.S., Gillham, R.W., Dechlorination of trichloroethene in aqueous solution using Fe^0, Environ. Sci. Technol., 1996, 30 66-71.

Papp, S., Szel, J., Oszko, A., Dekany, I., Synthesis of polymer-stabilized nanosized rhodium particles in the interlayer space of layered silicates. Chem. Mater., 2004, 16, 1674-1685.

Park, K.T., Klier, K., Wang, C.B., Zhang, W.X. Interaction of tetrachloroethylene with Pd (100) studied by high-resolution X-ray photoemission spectroscopy. J. Phys. Chem. B., 1997, 101, 5420-5428.

Patolsky, F., Weizmann, Y., Williner I., Actin-based metallic nanowires as bio-nanotransporters. Nature Mater., 2004, 3, 692-695.

Paul, S., Pearson, C., Molloy, A., Cousins, M. A., Green, M., Kolliopoulou, S., Dimitrakis, P., Normand, P., Tsoukalas, D., Petty, M. C., Langmuir-blodgett film deposition of metallic nanoparticles and their application to electronic memory structures. Nano Letters, 2003, 3, 533-536

Pera-Titus, M., Garcia-Molina, V., Banos, M. A., Gimenez, J., Esplugas, S., Degradation of chlorophenols by means of advanced oxidation processes: a general review**,** Appl. Catal., B., 2004, 47, 219-256.

Perez, M., Torrades, F., Domenech, X., Peral, J., Fenton and photo-Fenton oxidation of textile effluents, Water Res., 2002, 36, 2703-2710.

Philippot, K., Chaudret, B., Organometallic approach to the synthesis and surface reactivity of noble metal nanoparticles, Comptes Rendus Chimie, 2003, 6, 1019-1034.

Pignatello, J.J., Oliveros, E., MacKay, A., Advanced oxidation processes for organic contaminant destruction based on the Fenton reaction and related chemistry. Critical Reviews in Environ. Sci. Technol., 2006, 36, 1-84.

Pivin, J. C., Sendova-Vassileva, M., Lagarde, G., Singh, F., Podhorodecki, A., Optical activation of Eu^{3+} ions by Ag nanoparticles in ion exchanged silica-gel films. J. Phys. D: Appl. Phys., 2006, 39, 2955-2958.

Powell, R.M., Powell, P.D., Puls, R.W., Economic analysis of the implementation of permeable reactive barriers for remediation of contaminated Groundwater EPA/600/R-

02/034, Environmental Protection Agency, U.S. Office or Research and Development: Cincinnati, June 2002.

Reinhart C. T., Peppas, N. A., Solute diffusion in swollen membranes. Part II. Influence of crosslinking on diffusive properties, J.Membr.Sci., 1983, 18, 227-239.

Rhim, J.W., Sohn, M.Y., Joo, H.J. and Lee, K.H., Pervaporation separation of binary organic-aqueous liquid mixtures using crosslinked PVA membrane. I. Characterization of the reaction between PVA and PAA, J.Appl.Polym.Sci., 1993, 50, 679-684.

Rhim, J.W., Kim, H.K. and Lee, K.H., Pervaporation separation of binary organic-aqueous liquid mixtures using crosslinked poly (vinyl alcohol) membranes. IV. Methanol-water mixtures, J.Appl.Polym.Sci., 1996, 61, 1767-1771.

Rhim, J.W., Park, H.B., Lee, C.S., Jun, J.H., Kim, D.S., Lee, Y.M., Crosslinked poly (vinyl alcohol) membranes containing sulfonic acid group: proton and methanol transport through membranes, J.Membr.Sci., 2004, 238, 143-151.

Ritchie, S.M.C., Bachas, L.G., Olin, T., Sikdar, S.K., Bhattacharyya, D., Surface modification of silica-and cellulose-based microfiltration membranes with functional polyamino acids for heavy metal sorption, Langmuir, 1999, 15, 6346-6357.

Ritchie, S.M.C., Kissick, K.E., Bachas, L.G., Sikdar, S.K., Parikh, C., Bhattacharyya, D., Polycysteine and other polyamino acid functionalized microfiltration membranes for heavy metal capture, Environ. Sci. Technol. 2001, 35, 3252-3258

Rivas, B.L., Pereira, E.D. and Moreno-Villoslada, I., Water-soluble polymer-metal ion interactions, Prog. Polym. Sci., 2003, 28, 173-208

Roberts, A. L., Totten, L. A., Arnold, W. A., Burris, D. R., Campbell, T. J., Reductive elimination of chlorinated ethylenes by zero-valent metals, Environ. Sci. Technol. 1996, 30, 2654-2659.

Sao-Joao, S., Giorgio, S., Penisson, J. M., Chapon, C., Bourgeois, S., Henry, C., Structure and deformations of Pd-Ni core-shell nanoparticles. J. Phys. Chem. B., 2005, 109, 342-347.

Scherer, M.M., Balko, B.A., Gallagher, D.A., Tratnyek, P.G., Correlation analysis of rate constants for dechlorination by zero-valent iron, Environ. Sci. Technol., 1998, 32, 3026-3033.

Schnarr, M., Truax, C., Farquhar, G., Hood, E., Gonullu, T., and Stickney, B., Laboratory and controlled field experiments using potassium permanganate to remediate trichloroethylene and perchloroethylene DNAPLs in porous media, J. Contam. Hydrol., 1998, 29, 205-224.

Schrick, B., Blough, J.L., Jones, A.D., Mallouk, T.E., Hydrodechlorination of trichloroethylene to hydrocarbons using bimetallic nickel-iron nanoparticles. Chem.Mater. 2002, 14, 5140-5147

Schwarzenbach, R. P., Gschwend, P. M., Imboden, D. M., Environmental organic chemistry, 1993, Wiley-Interscience, New York.

Scott, R. W. J., Wilson, O. M., Crooks, R. M. Synthesis, characterization, and applications of dendrimer-encapsulated nanoparticles. J. Phys. Chem. B. 2005, 109, 692-704.

Shah, T. N., Ritchie, S. M. C., Esterification catalysis using functionalized membranes., Applied Catalysis, A: General, 2005, 296, 12-20.

Shaub, W.M., Tsang, W., Dioxin formation in incinerators, Environ. Sci. Technol., 1983, 17, 721-730.

Smuleac, V., Butterfield, D., A., and Bhattacharyya, D., Layer-by-layer assembled microfiltration membranes for biomolecule immobilization and enzymatic catalysis, Langmuir, 2006, 22, 10118-10124.

Son, S. U., Jang, Y., Park, J., Na, H. B., Park, H. M., Yun, H. J., Lee, J., Hyeon, T., Designed synthesis of atom-economical Pd/Ni bimetallic nanoparticle-based catalysts for sonogashira coupling reactions. J. Am. Chem. Soc., 2004, 126, 5026-5027.

Steuck, M.J. inventor. Millipore Corp., assignee., Membrane having radiochemically crosslinked hydrophilic coating for use in filtration. United States patent, 1990, US 4944879.

Su, C., Plus, R. W. Kinetics of trichloroethene reduction by zerovalent iron and tin: pretreatment effect, apparent activation energy, and intermediate products. Environ. Sci. Technol. 1999, 33, 163-168.

Tamara, M.L. and Butler, E.C., Effects of iron purity and groundwater characteristics on rates and products in the degradation of carbon tetrachloride by iron metal, Environ. Environ. Sci. Technol, 2004, 38, 1866-1876.

Tannenbaum, R., Metal cluster growth limited by polymer surface interactions, Current Trends in Polymer Science, 1998, 3, 81-98.

Tada, H., Soejima, T., Ito, S., Kobayashi, H., Photoinduced desorption of sulfur from gold nanoparticles loaded on metal oxide surfaces, J. Am. Chem. Soc., 2004, 126, 15952-15953.

Tarr, M.A. Chemical degradation methods for wastes and pollutants, Marcel Dekker Inc. 2003, Chapter 9, 371-421.

Tee, Y-H., Grulke, E., and Bhattacharyya, D., Role of Ni/Fe Composition on the Degradation of Trichloroethylene from Water, Ind. Eng. Chem. Res., 2005, 44, 7062-7072.

Tee Y.H., Destruction study of toxic chlorinated organics using bimetallic nanoparticles and membrane reactor: synthesis, characterization and modeling, Dissertation, 2006.

Teel, A.L., Warberg, C.R., Atkinson, D.A., Watts, R.J., Comparison of mineral and soluble iron Fenton's catalysts for the treatment of trichloroethylene, Water Res., 2001, 35, 977-984.

Teranishi, T. and Miyake, M., Novel synthesis of monodispersed Pd/Ni nanoparticles, Chem. Mater. 1999, 11, 3414-3416.

Tsutsumi, K., Funaki, Y., Hirokawa, Y., Hashimoto, T., Selective incorporation of palladium nanoparticles into microphase-separated domains of poly (2-vinylpyridine)-block-polyisoprene, Langmuir 1999, 15, 5200-5203.

Tomida, T., Hamaguchi, K., Tunashima, S., Katoh, M., Masuda, S., Binding properties of a water-soluble chelating polymer with divalent metal ions measured by ultrafiltration. poly (acrylic acid), Ind. Eng. Chem. Res. 2001, 40, 3557-3562.

Tu, S.C., Ravindran, V., Den, W., Pirbazari, M., Predictive membrane transport model for nanofiltration processes in water treatment, AIChE J. 2001, 47, 1346–1362.

Tu, S. C. ; Ravindran, V. ; Pirbazari, M., A pore diffusion transport model for forecasting the performance of membrane processes, J.Membr.Sci., 2005, 265, 29-50.

Ulbricht, M., Yang, H., Porous polypropylene membranes with different carboxyl polymer brush layers for reversible protein binding via surface-initiated graft copolymerization, Chem. Mater., 2005, 17, 2622-2631.

van den Berg, G. B., Racz, I. G., Smolders, C. A., Mass transfer coefficients in cross-flow ultrafiltration, J. Membr. Sci., 1989, 47, 25.

Vogel, T. M., Criddle, C. S., McCarty, P. L., Transformations of halogenated aliphatic compounds, Environ. Sci. and Technol., 1987, 21, 722-736

Wang, C.B. and Zhang, W.X., Synthesizing nanoscale iron particles for rapid and complete dechlorination of TCE and PCBs, Environ. Sci. Technol., 1997, 31 2154-2156.

Wang, T.C., Rubner, M.F., Cohen, R.E., Polyelectrolyte multilayer nanoreactors for preparing silver nanoparticle composites: controlling metal concentration and nanoparticle size, Langmuir, 2002, 18, 3370-3375.

Watts, R.J., Teel, A.L., Chemistry of modified Fenton's reagent (catalyzed H_2O_2 propagations-CHP) for in situ soil and groundwater remediation, J. Environ, Eng., 2005, 131, 612-622.

Wei, J., Xu, X., Liu, Y., Wang, D. Catalytic hydrodechlorination of 2,4-dichlorophenol over nanoscale Pd/Fe: Reaction pathway and some experimental parameters. Water Res. 2006, 40, 348-354.

Westrick, J. J., Mello, J. W., Thomas, R. F. The groundwater supply survey, Journal - American Water Works Association, 1984, 76, 52-59.

Wiley, D. E., Fell, C. J. D., Fane, A. G., Optimization of membrane module design for brackish water desalination, Desalination, 1985, 52, 249.

Wilke, C. R. and Chang, P., Correlation of diffusion coefficients in dilute solutions, AIChE J, 1955, 1: 264.

Williams D. B., Carter C. B., Transmission electron microscopy, volume (4): Spectrometry, Kluwer Academic Pub, 1996.

Worden, J. G., Dai, Q., Shaffer, A. W., Huo, Q., Monofunctional group-modified gold nanoparticles from solid phase synthesis approach: solid support and experimental condition effect. Chem. Mater., 2004, 16, 3746-3755.

Xu, J., Dozier A. and Bhattacharyya, D., Synthesis of nanoscale bimetallic particles in polyelectrolyte membrane matrix for reductive transformation of halogenated organic compounds, J. Nanoparticle Res., 2005a, 7, 449-467.

Xu, J. and Bhattacharyya, D., Membrane-based bimetallic nanoparticles for environmental remediation: synthesis and reactive properties, Environ. Prog., 2005b, 24, 358-366.

Xu, J., and Bhattacharyya, D., Fe/Pd nanoparticle immobilization in microfiltration membrane pores: synthesis, characterization, and application in the dechlorination of polychlorinated biphenyls, Ind. Eng. Chem. Res., 2007, 46, 2348-2359.

Xu, Y.F., Huang, R.Y.M., Pervaporation separation of ethanol-water mixtures using ionically crosslinked blended polyacrylic acid (PAA)-Nilon-6 membranes, J.Appl.Polym.Sci., 1988, 36, 1121.

Yakushiji, K., Ernult, F., Imamura, H., Yamane, K., Mitani, S., Takanashi, K., Takahashi, S., Maekawa, S., Fujimori H., Enhanced spin accumulation and novel magnetotransport in nanoparticles. Nature Mater. 2005, 4, 57-61.

Yang, C.; Nuxoll, E. E.; Cussler, E. L., Reactive barrier films., AIChE J., 2001, 47, 295-302.

Yang, J., Lee, J.Y., Chen, L.X., Too, H.-P., A phase-transfer identification of core-shell structures in Ag-Pt nanoparticles. J. Phys. Chem. B., 109, 2005, 5468-5472.

Ying, L., Yu, W.H., Kang, E.T., Neoh, K.G., Functional and surface-active membranes from poly (vinylidene fluoride)-graft-poly (acrylic acid) prepared via RAFT-mediated graft copolymerization, Langmuir, 2004, 20, 6032-6040.

Zepp, R.G., Faust, B.C., Hoigne, J., Hydroxyl radical formation in aqueous reactions (pH 3-8) of iron (II) with hydrogen peroxide: the photo-Fenton reaction, Environ. Sci. Technol., 1992, 26, 313-319.

Zhang, W.X., Wang, C.B., Lien, H.L., Treatment of chlorinated organic contaminants with nanoscale bimetallic particles. Catalysis Today. 1998, 40, 387-395.

Vita

Jian Xu was born on July 1, 1975, in Zhenjiang, China. He graduated from Suzhou High School in Jiangsu Province, China in 1993. He received his Bachelor of Science degree in Chemical Engineering from Beijing University of Chemical Technology in 1997. Then he worked for Suzhou Thermal Engineering Research Institute as a research engineer. In 1999 he attended East China University of Science and Technology to pursue his Master of Science degree in Chemical Engineering. After he received his M.S degree in 2002, he joined the Ph.D. program in Chemical Engineering at the University of Kentucky.

Awards:

- Outstanding Poster Paper Award in North American Membrane Society (NAMS) Annual Meeting, Orlando, Florida, USA (2007)
- Second Prize Winner in Oral Presentation at Eastern Regional Chemical & Materials Engineering Graduate Symposium (2006)
- Outstanding Paper Award in North American Membrane Society (NAMS) Annual Meeting, Providence, RI, USA (2005)
- First Place Winner of Graduate Student Paper Award in the national paper contest conducted by AIChE Environmental Division. (2004)
- First Place Poster Paper Award in Advances in Membranes and Fuel Cells Technology at AIChE Annual Meeting (Separations Division), San Francisco, CA, USA (2003)

Publications:

- Venkatachalam K., Arzuaga X., Chopra Nitin., Gavalas V. G., Xu J., Bhattacharyya D., Hennig B., and Bachas, L. G., Reductive dechlorination of 3,3',4,4'-tetrachloro biphenyl (PCB) using palladium or palladium/iron nanoparticles and assessment of

the reduction in toxic potency in vascular endothelial cells, Submitted to J. Hazard. Mater., 2007 (Accepted).

- Xu, J. and Bhattacharyya, D., Fe/Pd nanoparticle immobilization in microfiltration membrane pores: synthesis, characterization and application in dechlorination of polychlorinated biphenyls, Ind. Eng. Chem. Res., 46, 2348-2359 (2007).
- Xu, J. and Bhattacharyya, D., Membrane-based bimetallic nanoparticles for environmental remediation: synthesis and reactive properties, Environ. Prog., 24(4), 358-366 (2005).
- Xu, J., Dozier A. and Bhattacharyya, D., Synthesis of nanoscale bimetallic particles in polyelectrolyte membrane matrix for reductive transformation of halogenated organic compounds, J. Nanopart. Res, 7(4/5), 449-467, (2005).
- Xu, J. and Xu, Z.L., Poly (vinyl chloride) (PVC) hollow fiber ultrafiltration membranes prepared from PVC/additives/solvent, J. Membr. Sci., 208, 203-212 (2002).

Presentations:

- Xu, J. and Bhattacharyya D., Catalytic dechlorination of polychlorinated biphenyl (PCBs) in water by Fe/Pd nanoparitcles in polyacrylic acid functionalized membranes, presented at the annual North American Membrane Society (NAMS) Meeting, Orlando, Florida, May 12-16, 2007.
- Xu, J. and Bhattacharyya D., Reductive degradation of chlorinated organics by membrane-supported nanoparticles: synthesis, characterization and modeling Study, presented at the annual American Institute of Chemical Engineers (AIChE) Meeting, San Francisco, CA, November 12-17, 2006.
- Xu, J. and Bhattacharyya D., Catalytic dechlorination of polychlorinated biphenyls from contaminated water by Fe/Pd nanoparticles synthesized in functionalized PVDF

membranes, presented at the annual North American Membrane Society (NAMS) Meeting, Chicago, IL, May 12-17, 2006.

- Xu, J., Bachas, L.G., and Bhattacharyya, D., Nanotechnology/membrane applications of dechlorination of toxic organics, presented at the NIEHS-SBRP Annual Meeting, New York, Jan 11-13, 2006.
- Xu, J. and Bhattacharyya D., Bimetallic nanoparticles synthesis in membrane matrix: nanoparticle structure and reactive properties, presented at the annual American Institute of Chemical Engineers (AIChE) Meeting, Cincinnati, OH, October 30-November 4, 2005.
- Xu, J. and Bhattacharyya D., Membrane-based bimetallic nanoparticle synthesis for reductive dechlorination of organics: synthesis, characterization and kinetic study, presented at the annual North American Membrane Society (NAMS) Meeting, Providence, Rhode Island, June 11-15, 2005.
- Xu, J. and Bhattacharyya D., Kinetic and mechanistic study of trichloroethylene and polychlorinated biphenyl (PCBs) reduction with nanoscale catalyzed Fe^0 immobilized in polyelectrolyte membrane, presented at the annual AIChE Meeting, Austin, TX, November 7-12, 2004.
- Xu, J. and Bhattacharyya D., Membrane-based nanoparticle synthesis for organic detoxification, presented at International Workshop on Nanomaterials, Lexington, KY, September 20-21, 2004.
- Xu, J. and Bhattacharyya, D., Nanoscale bimetallic particles synthesis in polyelectrolyte membrane matrix for organic dechlorination, presented at the NAMS 2004 Meeting, Honolulu, Hawaii, June 26-30, 2004.
- Xu, J. and Bhattacharyya, D., Transformation of halogenated organic compounds by nanoscale bimetallic particles immobilized in polyelectrolyte membrane matrix, presented at the 227th ACS National Meeting, Anaheim, CA, March 28-April 1, 2004.

- Xu, J. and Bhattacharyya D., Synthesis of nanoscale metal particles for reductive transformation of halogenated compounds, presented at the 2003 Annual AICHE Meeting, San Francisco, CA (2003).